Dynamics, Robust Control, and Power Management of Voltage-Source Converters in Hybrid Multiterminal AC/DC Grids

by

Masoud Davari

A thesis submitted in partial fulfillment of the requirements for the degree of

Doctor of Philosophy

in

Energy Systems

Department of Electrical and Computer Engineering
University of Alberta

Abstract

The electric energy sector is moving toward extensive integration of clean and renewable energy sources, energy storage units, and modern loads via highly efficient and flexible multiterminal dc grids integrated within the traditional ac grid infrastructure in both transmission and distribution levels. A voltage-source converter (VSC) is the main technology enabling the interconnection of dc and ac grids. In such demanding applications, effective and robust integration of ac and dc grids, in the presence of coupling nonlinear dynamics, parametric uncertainties, and disturbances, is crucial to maintain the stability and robust performance of the overall ac/dc dynamic system. Motivated by this objective, this thesis addresses the dynamics, robust control, and power management of VSCs in hybrid multiterminal ac/dc grids.

Firstly, a robust multi-objective dc-link voltage controller is developed for a bi-directional VSC regulating the dc-link voltage of a multiterminal dc grid; i.e., the VSC operates as a dc-voltage power-port. The proposed controller ensures excellent tracking performance, robust disturbance rejection, and robust stability against operating point and parameter variation with a simple fixed-parameter low-order controller. A disturbance rejection controller is designed, based on the singular-values μ-synthesis approach, to achieve robustness against variation in the converter operation point. Further, the effect of parametric uncertainty in the effective dc-link capacitance is mitigated by modifying the robust disturbance rejection controller, via the polynomial method, to ensure that the closed-loop poles are allocated in the pre-defined region in the complex plane even under parameter variation.

Secondly, the dynamics and control of VSCs considering the instantaneous power of both ac- and dc-side filters and dc grid uncertainties are addressed in the this thesis. Consequently, a detailed small-signal model of the dc-link dynamics in grid-connected VSCs considering the instantaneous power of both ac- and dc-side energy storage components and a robust optimal dc-link voltage controller is presented in this thesis. The proposed controller ensures excellent tracking performance, robust disturbance rejection, and robust performance against operating point and parameter variation with a simple fixed-parameter controller.

Thirdly, this thesis presents a natural-frame variable-structure-based nonlinear control system for the master VSC applied in multiterminal grids to overcome problems associated with

conventional dc-link voltage controllers, which are suffering from stability and performance issues, mainly attributed to the small-signal-based control design approach and the use of cascaded control structure based on the power balance framework that yields unmodeled nonlinear dynamics. The proposed controller accounts for the complete nonlinear dynamics of the master VSC without any cascaded control structure, and it globally stabilizes the nonlinear dynamics via a passivity-based design approach.

Fourthly, this thesis presents a robust vector-controlled VSC that facilitates full converter power injection at weak and very weak ac grid conditions (i.e., when the short-circuit capacity ratio is one). The controller overcomes problems related to the stability and performance of conventional vector-controlled VSCs integrated into very weak ac grids (high impedance grids) because of the increased coupling between the converter and grid dynamics, via the phase-locked loop (PLL). As a result, a detailed dynamic model for the ac-bus voltage dynamics, including the PLL dynamics, is developed and validated in this thesis. Then, the model is used to design a robust optimal ac-bus voltage controller to stabilize the dynamics under operating point variation and grid impedance uncertainty. Because the developed model includes the PLL dynamics, the developed controller inherently mitigates the negative impact of the PLL on the converter stability.

Fifthly, this thesis addresses the challenges associated with a dc-voltage-controlled VSC interfacing a wind turbine into a dc grid, which is gaining widespread acceptance under weak grid connection or isolated operation. Under weak grid connection or isolated operation, the machine-side VSC regulates the dc-link voltage via changes in the generator speed. However, several control difficulties are yielded; important among these are: 1) the nonlinear plant dynamics with a wide range of operating point variation; 2) the control lever is mainly the generator speed, which complicates the dc-link voltage control dynamics; 3) the presence of uncertain disturbances associated with dynamic loads (e.g., power-converter-based loads) connected to the dc grid and wind speed variation; and 4) the presence of parametric uncertainty associated with the equivalent dc-link capacitance due to connecting/disconnecting converter-based loads. This thesis proposes a robust parallel distributed control strategy as a simple and robust solution to handle a large variation of the operating point of the wind turbine system. The proposed controller is based on the robust structured singular values μ-synthesis approach as well as a functional fuzzy model.

Finally, this thesis presents a robust power sharing and dc-link voltage regulation controller for grid-connected VSCs in dc grids applications to overcome difficulties and problems related to the dynamics and stability of a grid-connected VSC with dc power sharing droop control. Major difficulties are: 1) ignoring the effect of the outer droop loop on the dc-link voltage dynamics when the dc-link voltage controller is designed, which induces destabilizing dynamics, particularly under variable droop gain needed for optimum economic operation, energy management, and successful network operation under converter outages and contingencies; 2) uncertainties in the dc grid parameters (e.g., passive load resistance and equivalent capacitance as viewed by the dc side of the VSC); and 3) disturbances in the dc grid (i.e., power absorbed or injected from/to the dc grid), which change the operating point and the converter dynamics by acting as a state-dependent disturbance. A detailed dynamic model that considers the droop controller dynamics and the impact of the effective dc-side load parameters and disturbances imposed on the VSC is developed. Then, a robust controller that preserves system stability and robust performance is developed.

A theoretical analysis and comparative simulation and experimental results are presented in this thesis to show the validity and effectiveness of the developed models and proposed control structures.

Preface

This thesis is an original work by Masoud Davari. As detailed in the following, some chapters of this thesis have been published, submitted, or will be submitted for publication as scholarly articles in which Prof. Yasser A.-R. I. Mohamed was the supervisory author and has contributed to concepts formations and the manuscript composition.

Chapter 2 of this thesis has been published as M. Davari and Y. A.-R. I. Mohamed, "Robust multi-objective control of DC-voltage power port in VSC-based hybrid AC/DC micro-grids," *IEEE Transactions on Smart Grid*, vol. 3, no. 4, pp. 1597-1612, September 2013.

Chapter 3 of this thesis has been published as M. Davari and Y. A.-R. I. Mohamed, "Dynamics and robust control of a grid-connected VSC in multiterminal DC grids considering the instantaneous power of DC and AC side filters and DC grid uncertainty," *IEEE Transaction on Power Electronics*, vol. 31, no. 3, pp. 1942-1958, March 2016.

Chapter 4 of this thesis has been published as M. Davari and Y. A.-R. I. Mohamed, "Variable-structure-based nonlinear control for the master VSC in DC-energy-pool multiterminal grids," *IEEE Transactions on Power Electronics*, vol. 29, no. 11, pp. 6196-6213, November 2014.

Chapter 5 of this thesis has been published as M. Davari and Y. A.-R. I. Mohamed, "Dynamics and Robust Vector Control of a Very Weak Grid-Connected Voltage-Source Converter Considering the Phase Locked Loop Dynamics," *IEEE Transaction on Power Electronics*, fully accepted on Dec. 28th 2015, in press.

Chapter 6 of this thesis has been submitted for possible publication as M. Davari and Y. A.-R. I. Mohamed, "Robust DC-Link Voltage Control of a Voltage-Source Converter Interfacing a Wind Turbine into DC-Grids," *IEEE Transaction on Power Electronics*, and conditionally, it has been accepted with some revisions.

Paper out of Chapter 7 of this thesis is in preparation and will be submitted for possible publication.

Dedication

I dedicate my dissertation work to my dearest and loved one, valued Neda, and my family. A special feeling of gratitude to my loving parents, Abed and Shahin, whose words of encouragement, immense support, selfless sacrifice, and push for tenacity always ring in my ears. My sister, Shekoufeh, and my brothers, Behnam and Mohammad, have never left my side and are very special.

I also dedicate this dissertation to many friends of mine. Last and absolutely not least, I dedicate this work and give special thanks to my first teacher in my life, Ms. Maryam Modarres.

Abū-Muhammad Muslih al-Dīn bin Abdallāh Shīrāzī, سعدی شد یرازی ,

"All human beings are members of one frame, Since all, at first, from the same essence came.
When time afflicts a limb with pain The other limbs at rest cannot remain.
If thou feel not for other's misery A human being is no name for thee."

William Shakespeare, "*There is nothing either good or bad but thinking makes it so."*

Sigmund Freud, *"Unexpressed emotions will never die. They are buried alive and will come forth later in uglier ways."*

Bertrand Russell, *"I should like to say two things; one intellectual and one moral.*

The intellectual thing I should want to say to them is this: When you are studying any matter, or considering any philosophy, ask yourself, only, what are the facts and what is the truth that the facts bear out. Never let yourself be diverted either by what you wish to believe, or by what you think would have beneficent social effects if it were believed. But look only, and solely, at what are the facts. That is the intellectual thing that I should wish to say.

The moral thing I should wish to say to them is very simple: I should say love is wise, hatred is foolish. In this world, which is getting more and more closely interconnected, we have to learn to tolerate each other; we have to learn to put up with the fact that some people say things that we don't like. We can only live together in that way and if we are to live together and not die together, we must learn a kind of charity and a kind of tolerance which is absolutely vital to the continuation of human life on this planet."

Charles Chaplin, *"...I should like to help everyone – if possible – Jew, Gentile – black man – white.... We want to live by each other's happiness – not by each other's misery... The way of life can be free and beautiful, but we have lost the way. Greed has poisoned men's souls, has barricaded the world with hate, has goose-stepped us into misery and bloodshed.... We think too much and feel too little. More than machinery, we need humanity. More than cleverness, we need kindness and gentleness. Without these qualities, life will be violent and all will be lost. ... Don't give yourselves to these unnatural men - machine men with machine minds and machine hearts! You are not machines,... You have the love of humanity in your hearts! ..."*

Acknowledgments

I would like to express my deep gratitude and special thanks to my dear supervisor and mentor, Prof. Yasser Abdel-Rady I. Mohamed, for his countless hours of reflecting, reading, encouraging, and most of all patience throughout the entire process. His excitement and willingness to provide feedback made the completion of this research an enjoyable experience. This research and dissertation would not have been possible without his continuous guidance, encouragement and support.

I would like to thank my committee members, Prof. Venkata Dinavahi, Prof. Yasser Abdel-Rady I. Mohamed, Prof. Sahar Pirooz Azad, Prof. Dewei (David) Xu, and Prof. Qing Zhao, for their constructive feedback and comments. I would like also to thank many faculty and staff members at the Electrical and Computer Engineering Department, University of Alberta for their support.

I would also like to acknowledge the financial support provided by the Natural Sciences and Engineering Research Council of Canada (NSERC), and Alberta Innovates – Technology Futures Graduate Student Scholarship**.**

Table of Contents

List of Figures

List of Acronyms

AC	Alternating Current
DC	Direct Current
DOF	Degree of Freedom
EP	Equilibrium Point
EtoE	Equilibrium-to-Equilibrium
HOT	High Order Term
HVDC	High Voltage Direct Current
MTDC	Multiterminal DC
PCC	Point of Common Coupling
PLL	Phase Lock Loop
PMSG	Permanent Magnet Synchronous Generator
RHP	Right-Half-Plane
SCC-R	Short-Circuit Capacity Ratio
VSC	Voltage Source Converter
VSC-*m*	Master Voltage Source Converter

Chapter 1

Introduction

This chapter presents the concepts and definitions that will be frequently referred to in the rest of this thesis, the literature survey, research motivations, research objectives, and thesis contributions and outline.

1.1 AC Grids and DC Grids

Electric power was initially generated in late nineteenth century using dc generators. Distribution and utilization of electric power were also based on dc systems. However, dc systems lost ground to ac systems for various technical and economic reasons as the power systems developed [1]. AC grids benefit from utilizing existing ac-power grid infrastructures, control strategies, protection, and standards; however, they suffer from complicated control strategies in the synchronization process, reduced power quality, and stability issues. Furthermore, ac grids need additional power electronic devices, such as dc/dc boosters and dc/ac inverters, in order to interface dc-based distributed energy resources (DERs) with upstream ac power and/or loads.

In transmission systems, dc technology was again re-introduced in a different form in 1954 for undersea high voltage direct current (HVDC) power transmission [2]; The HVDC technology is used today for long distance power transmission and for asynchronous connection of ac power systems [3].

On the other hand, new electric power networks such as smart grids and supper grids are receiving widespread acceptance nowadays [4]-[6]. In such networks, multiterminal dc (MTDC) systems are playing a vital role in integrating different renewable energy resources as well as feeding both types of ac and dc loads. Furthermore, the interest in dc micro-grids employed in distribution systems is recently significant. The benefits of dc grids again appear in distribution systems due to 1) potential dc DERs, such as photovoltaic and solar systems; and 2) the high penetration level of dc loads in modern future distribution systems, such as data centers, communication centers, light-emitting diode (LED) lighting systems, and present electric or

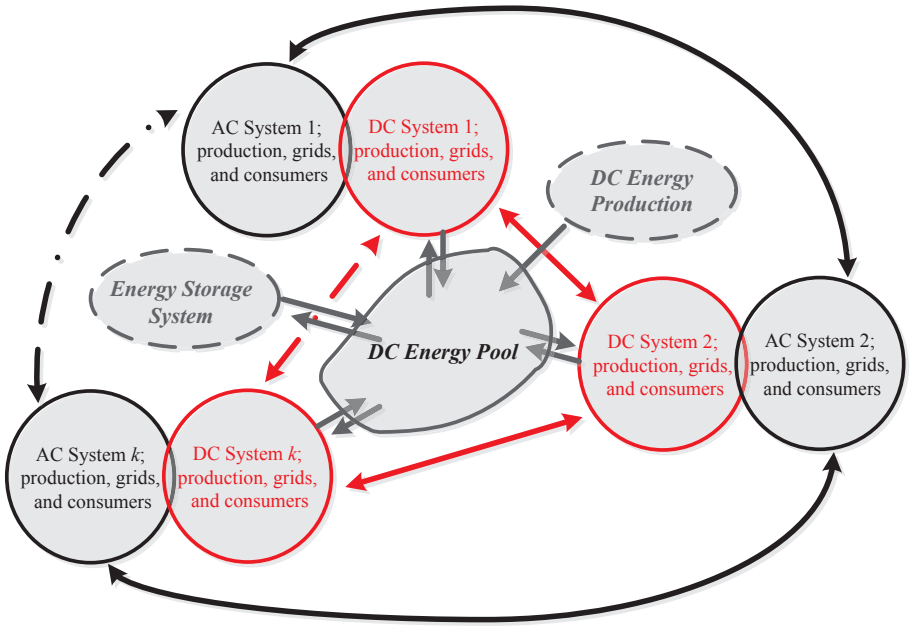

Fig. 1.1. Hybrid multiterminal ac/dc grid based on dc-energy pool concept.

hybrid vehicles [7]-[11]. In fact, dc micro-grids can take advantage of the dc power generated by most of DERs in addition to offering good power quality and transformer-less voltage levels that results in the improvement of efficiency, size, and cost of the distribution network [12]-[29]. However, there are new challenges that should be considered to facilitate effective implementation of dc grids and dc micro-grids [24]-[26].

To combine the benefits of both ac grid and dc grid, hybrid ac/dc grids are recently proposed as an emerging topology in future electric power network [27]-[29]. In fact, the interest in MTDC grids, or generally hybrid ac/dc grids, employed in both transmission and distribution systems, is increasing with no signs of slowing down under the smart-/super-grid paradigm. Electric power is fed/extracted into/from a central inner dc grid called dc-energy pool. DC sources and loads can be directly connected to the dc-energy pool, whereas one or more ac networks can be interfaced to the dc-pool via bidirectional VSCs to increase the supply reliability. Such a topology facilitates flexibility and high reliability and reduces the number of energy conversion stages. Further, the stability of the overall system can be remarkably improved, as compared to pure ac micro-grid systems, under the high penetration of renewable resources. Fig. 1.1 shows the conceptual design of a multiterminal hybrid ac/dc grid. Figs. 1.2 and 1.3 show typical high-voltage multiterminal grids implemented in the transmission level.

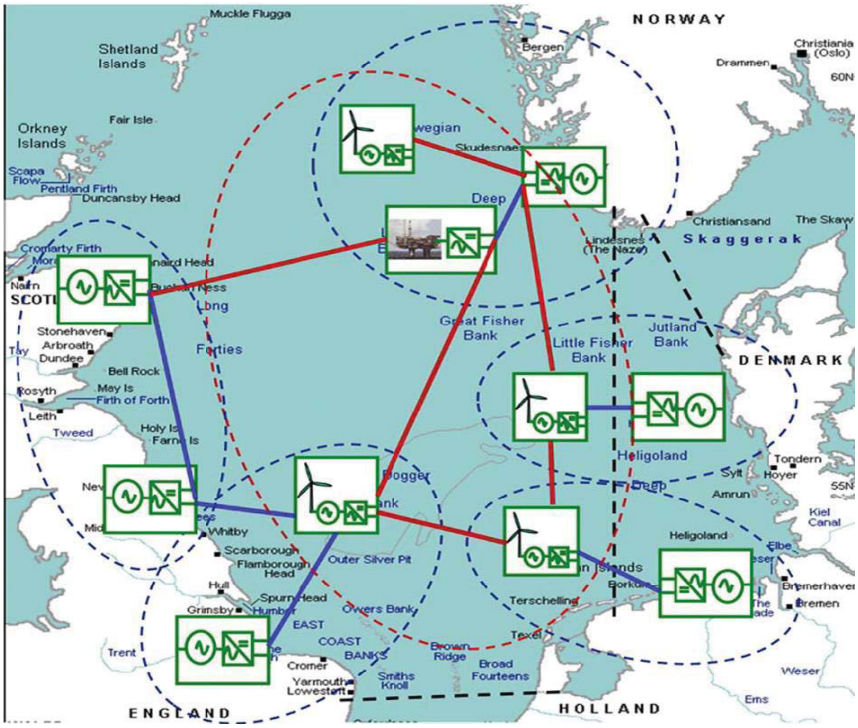

Fig. 1.2. "*Meshed North Sea HVDC grid scenario: blue lines show early state developments and red lines show later stage development).* [*66*]"

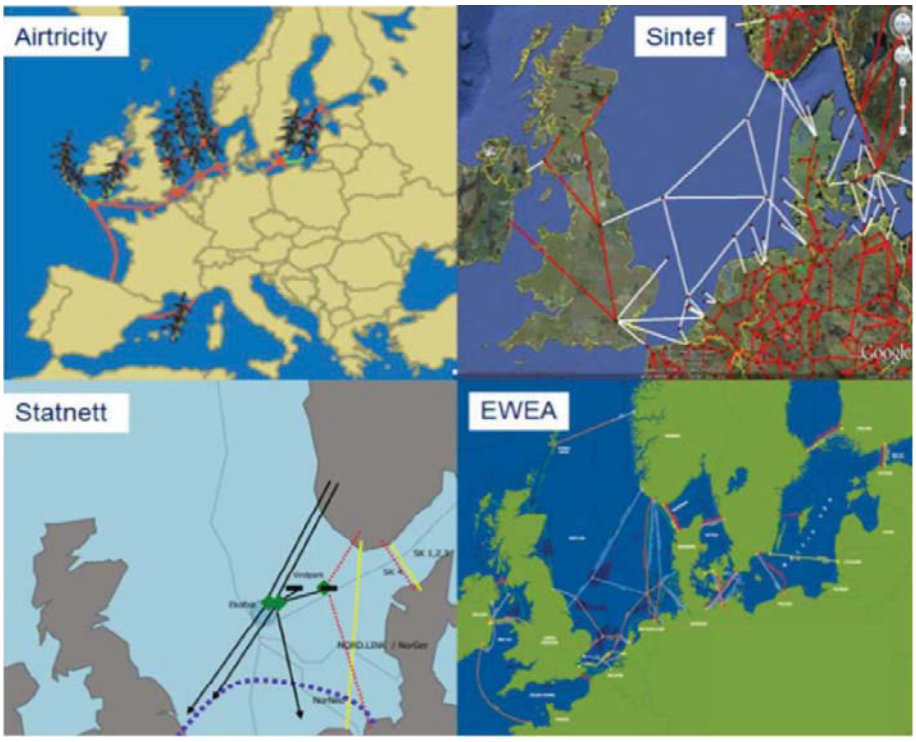

Fig. 1.3. "*North Sea supergrid proposal by Airtricity (top left), Sintef (top right), Statnett (bottom left), and the European Wind Energy Association (bottom right).* [*66*]"

1.2 Technical Challenges Related to MTDC Grids

In MTDC grids, the dc-energy pool is the core part of the overall electric network, and it works like the heart of an MTDC grid. Indeed, all entities are sharing electric power with that central unit whose stability and performance affect the stability and performance of other sections connected to an MTDC grid. Hence, effective control of the dc-bus voltages of the dc-energy pool is very critical to ensure both stability and acceptable performance of the whole dynamic system.

The dynamics and uncertain nature of an MTDC grid challenge the control and stability of the overall hybrid ac/dc system. The fact that a typical MTDC is faced with unavoidable disturbances and uncertainties complicates the control design of a practical system applicable in many working conditions and scenarios. In a typical MTDC grid, power converters can operate in different modes and can be subjected to different types of uncertainties and disturbances. Key operating modes are:

1) One master VSC (VSC-m) stabilizes the dc-link voltage of the dc-energy pool via controlled bi-directional active power exchange with a host ac grid. The ac grid stiffness remarkably affects the stability and performance of the master VSC, which in turns affects the stability and performance of the overall hybrid ac/dc grid. Therefore, the dynamics and control aspects of the master VSC in both stiff and weak grids connections should be considered.
2) The dc-link voltage regulation task is shared between several power converters in the MTDC grid via power versus dc voltage droop control. Therefore, the dynamics and control aspects of VSCs with dc droop feedback should be investigated.
3) At the dc side of the master VSC, an inductive energy storage component, hereinafter called the dc side inductance, may appear due to many practical and possible scenarios, such as the presence of a second order LC dc filter and unceranitiey in cables inductances. Therefore, the dynamics and control aspects of the master VSC should be revisited under the presence of such additional dynamics and uncertainty.
4) A full-scale wind turbine system can be directly connected to the dc-energy pool via a VSC. The interfacing VSC needs to control the dc-link voltage via controlled changes in the generator speed to facilitate wind turbine integration in weak or isolated grids. Several control challenges and difficulties need to be addressed to facilitate effective integration.

The control difficulties related to these modes and the drawbacks of the existing solutions are summarized in the following section.

1.3 Literature Survey

In this section, a literature survey on the control of VSCs in MTDC grids under different possible operating modes is presented.

1.3.1 Control of the Master VSC under Stiff AC Grid: A Linear Approach

DC-link voltage control in VSCs has been addressed in several studies such as [12], [13], [15], [17], [27], and [28]. Controllers are usually designed in the small-signal sense to synthesize linear fixed-parameter controllers, which are suitable for easy implementation in industrial applications. However, the applied controllers are designed mainly for a single converter and are based on certain assumptions that might not be satisfied in emerging high-power hybrid ac/dc networks. Key drawbacks of previous methods can be summarized as follows.

1) Simplified dc voltage power port model that ignores the dependency of the dc-link voltage dynamics on the operating mode of VSCs, i.e., rectification, inversion or reactive power injection. However, the dependency of the dc-link voltage dynamics on the operating mode of the VSC affects the stability of the entire closed-loop system by generating a right-half-plane (RHP) zero, i.e., a non-minimum phase zero. This dependency can be a crucial factor affecting the converter stability, particularly in high power converters, where the instantaneous power of the ac-side inductor filter cannot be ignored due to the relatively large inductance of the filter associated with the relatively low switching frequency, and high converter current. In [30]-[31], a PI-lead controller is proposed to stabilize the dc-link voltage dynamics at worst operating point when an operating-point-dependent dc-link voltage control model is used. However, the stability cannot be guaranteed under large and fast variation of the operating point due to the nonlinear behavior of the dc-link voltage dynamics. Further, robustness and effectiveness of disturbance rejection cannot be guaranteed with a PI-lead controller acting on a nonlinear plant with large and dynamic variation in the operating point.
2) External power signals imposed on the dc-link voltage dynamics are assumed as an exogenous disturbance. In fact, external power input drives change in the operating point to

achieve power balance. Therefore, robust disturbance rejection at different operating points is essential.

3) External power signals are assumed available, via measurement and/or communication of the dc-link currents, for feed-forward control in the dc-power port controller [30]-[31]. Due to cost and reliability issues associated with the additional sensor requirements, it is highly desirable to develop an external power sensor-less-control scheme with effective disturbance rejection. The dependency of the plant dynamics on the external disturbance complicates this objective and demands a carefully-designed robust control scheme.
4) Accurate system parameters are assumed. In particular, the effective capacitance of the dc-link is assumed to be constant. However, connection/disconnection of resources/loads to/from dc-energy pool directly affects the effective dc-link capacitance and the control performance might be affected under such uncertainties.

1.3.2 Control of the Master VSC under Stiff AC Grid and DC Side Inductance: A Linear Approach

Several aspects related to the dynamics and controls of VSCs such as current control, ac-bus voltage control, dc-link voltage control, grid synchronization and islanding detection, are addressed in the current literature [5]-[30]. However, some important aspects, which directly affect the stability and the performance of a master VSC in a typical MTDC system, are not addressed. These issues are summarized as follows.

1) As the penetration level of dc grids increases in modern distribution and transmission networks, dc grid stability and power quality become crucial objectives. The use of a dc-side choke to reduce the input-line harmonics to meet IEEE 519 limits, suppress voltage/current spikes, reduce ac ripple on the dc-bus, reduce dv/dt and di/dt rates, solve nuisance tripping, and reduce dc-bus transient overvoltages becomes essential in such demanding VSC applications [32]. However, an ac-side filter is essential to ensure a grid connection with high power quality. Moreover, the dc-side energy storage components affect the instantaneous power flow in the converter, which in turns affects the dynamics of the dc-link voltage. Similarly, the instantaneous power of the ac-side filter affects the dc-link voltage small-signal dynamics by creating an operating point-dependent zero that changes the system

dynamics from minimum phase to non-minimum phase in the rectification mode [31]. To the best of my knowledge, modeling and analysis of grid-connected VSCs considering the instantaneous power of both ac- and dc-side energy storage components are not addressed in the current literature.

2) In dc and hybrid ac/dc grids, VSCs can be connected to different entities, such as dc sources and dc loads with their front-end filters and converters. The connection and disconnection of such devices with their frequency-dependent output impedances directly affect the performance and stability of the dc-link voltage dynamics of the interfacing VSC. For example, current source converters are interfaced to dc grids with an inductive dc filter (choke) [33], and advanced dc hub configurations connecting several renewable resources to dc grids [34] and *Z*-source converters are interfaced to dc grids via an *LC* network [35]. Therefore, the development of a robust dc link voltage controller, considering the impact of the energy storage components in the dc and ac sides and possible uncertainties, demands special attention.
3) When the instantaneous power of both ac and dc energy storage components is considered, it can be shown that the dc-link voltage dynamics become highly dependent on the converter operation point (i.e., converter power or current levels, which vary in a wide negative to positive range owing to the bidirectional power nature of VSCs interfacing active dc grids to ac grids). Therefore, the dc-link voltage controller should be robust against operating point variation; i.e., to provide robust stability against operating point variation.

1.3.3 Control of the Master VSC under Stiff AC Grid: A Nonlinear Approach

DC-link voltage control in VSCs has been addressed in several studies such as [12], [13], [15], [17], [27], and [28]. However, existing controllers have the following drawbacks.

1) Several controllers are commonly synthesized in the small-signal sense of the power-balance equation across the dc-link capacitor, and they are based on the commonly used grid-voltage-oriented *dq*-frame [30] and [36]. In spite of its simplicity, small-signal-based controllers lack global stability [68], which is an essential requirement in complex MTDC grids.
2) The models used for dc-link voltage control suffer from incomplete plant dynamics due to ignoring the dependency of the converter dynamics on the converter operating point.

Furthermore, recently, the impact of the inner current control loop on the dc-link voltage regulation is addressed and it has been shown that ignoring the current dynamics remarkably affects the stability of the dc-voltage-controlled converter [37]. In other words, a practical converter system has complicated dynamics due to existing coupling between the outer controller, the inner controller, and the PWM process, which degrades the overall system stability as well as performance.

3) In the conventional *dq*-frame control, a complex control structure is needed to reduce the second-harmonic component induced on the dc-link voltage under unbalanced conditions (e.g., unsymmetrical faults or unbalance) in the ac-grid [63].

1.3.4 Control of the Master VSC under Weak AC Grid and Negligible DC Side Inductance: A Linear Approach

It has been shown, recently, that a VSC with the standard vector control strategy suffers from stability and performance issues when connected to a weak ac grid (i.e., a high impedance grid) [38]-[46]. For technical and economic reasons, distributed generation units and renewable energy resources can be located in remote areas, and hence, they can be connected to utility grids via high impedance lines [39], [40]. Furthermore, in VSC-based HVDC systems, a weak ac grid can be supported by an HVDC-link [41], [42]. In such applications, the grid stiffness remarkably affects the VSC system stability [38]-[48].

The grid stiffness in power converter integration studies can be characterized by the short-circuit capacity ratio (SCC-R) [38]-[42], which is defined as the grid short-circuit capacity at the point of common coupling (PCC) to the rated power of the VSC. In [38], it is reported that, with a significant tuning effort, the active power injection capability should be reduced to 0.5-0.6 per-unit to preserve the converter stability under very weak grid condition (SCC-R=1). In [45], the power injection is limited to 0.4 pu at SCC-R=1 to maintain the converter stability. The impact of the converter control parameters and grid stiffness on the VSC stability are addressed in [41], [43]. It has been shown that the phase-locked-loop (PLL), which is an essential element in the standard vector control strategy, remarkably contributes to the converter instability in the weak grid conditions. This finding matches the interesting findings in [47]; the PLL increases the negative real part of the converter impedance and increases undesirable interactions with the grid

impedance. Regardless of the PLL type, its impact on the converter output impedance is negative [43]. The work in [41] suggests a large reduction in the PLL gains to reduce its negative impact. However, reducing the PLL gains is limited by the converter performance constraints. Tuning both the PLL and the dc voltage controller parameters in a weak-grid connected VSC is used in [44] to improve the converter performance. It should be noted that the main converter controllers (e.g., the PLL, ac-bus voltage control, current control, dc-link voltage control, etc.) are mainly designed to meet the tracking and disturbance rejection performances. Therefore, relying on the main converter control parameters (e.g., by applying large reductions in the PLL gains) to shape the converter impedance and mitigate undesirable dynamic interactions with the host grid yields limited solutions. To enhance the performance of a weak-grid-connected vector-controlled VSC, a gain-scheduled-based controller is reported in [42], where an H_∞ control design methodology is used to tune the controller parameters. However, eight control parameters should be tuned under different grid conditions to enhance the converter performance.

To improve the converter control performance under weak grid conditions, PLL-less controllers are recently developed; e.g., [38], [46]. The interesting power-synchronization approach [38] forces the VSC to emulate the performance of synchronous machines. By this way, the need for the PLL is eliminated, and effective control performance can be yielded under very weak grid conditions. However, the control structure does not match the standard vector control strategy that is the state-of-the-art controller in the power converter industry. Therefore, the development of a simple and robust vector controller for weak grid-connected VSCs demands a special attention.

In the current literature, the impact of the PLL is usually ignored when the converter controllers are designed. The small-signal analysis of weak-grid connected VSCs shows that the dominant eigenvalues affecting the converter stability are strongly related to the states of the PLL and ac-bus voltage at the PCC [43], [45]. Therefore, while ignoring the PLL dynamics can be accepted under stiff grid conditions, it yields unmodelled dynamics under weak grid conditions. Such unmolded dynamics is the main cause of instability under weak grid condition. To the best of the author's knowledge, the development of a robust yet simple vector controller that includes the PLL dynamics for very weak grid-connected VSCs is not reported in the current literature.

1.3.5 Control of a Full-scale Wind Turbine Direcly Connected to a DC Grid

Wind-based power generation has a very high potential for increased penetration in power networks. However, the integration of full-scale wind power converters in dc grids demands special attention. Wind power generation can be directly connected to a dc grid via a VSC, especially, in dc distribution systems, which can be more frequently employed in the future smart grids with high penetration of dc loads. Using wind power generation in future hybrid ac/dc grids is a promising, practical, and beneficial approach in dc distribution systems which can be far from the main transmission system and have a good potential of wind power generation, such as rural areas supplied with wind power and energy storage systems [49]-[50]. Further, in multiterminal dc grids in the transmission system, multi-converters can share the dc voltage regulation task via dc-voltage versus dc-power droop mechanism. Integrating wind power generation into a dc grid has its own challenges, particularly when the dc voltage is controlled by a variable-speed wind turbine [51]-[52]. Few papers addressed the dc-link voltage control via changing the generator speed in a full-scale wind turbine [51]-[52]. The control objectives reported in [51]-[52] are the integration of wind turbines in weak grids and fault-ride-through in grid-connected turbines, respectively. However, direct control of the dc-link voltage by a wind turbine in dc grids yields several control problems that are not thoroughly addressed in the current literature. Such problems include the highly nonlinear system dynamics, harsh variation in the system operating point, uncertainties in system parameters, and the presence of state-dependent disturbances. In particular, control problems occur in the following ways.

1) In a directly connected wind turbine to a dc grid, there is only one control lever that is the rotational speed of the permanent magnet synchronous generator (PMSG). This fact complicates the dc-link voltage control dynamics, where the mechanical dynamics should be considered in the control design. The resulting dynamics is highly nonlinear with uncertainties associated with the wind turbine power characteristics that vary with the wind speed and pitch angle.
2) Different static and dynamic loads (e.g., power converter-based loads) can be connected to a dc grid. Thus, it is a must to have a dc-link voltage dynamic model that is controllable by the rotational speed of the PMSG, and can model the effects of different static and dynamic loads. The modeling approach presented in [51]-[52] is not practical for a dc grid with both

static and dynamic loads. The approach presented in [51] suffers from an incomplete linearization around one operating point. The approach presented in [52] lacks the controllability in dc grid applications where a grid-side converter is needed to inject the acceleration power into an ac grid.

3) With dc-link voltage control via the generator speed, the control lever (i.e., the generator speed) causes harsh variation in the operating point that challenges the control performance and stability. The controller developed in [51] has two main drawbacks for dc grids application. Firstly, the controller is not synthesized to ensure stability at different operating points. Secondly, the controller is not robust against variations in the operating point as well as static and dynamic loads.

4) In dc grids, several static loads can be connected/disconnected to/from the dc grid, and thus affecting the open-loop time-constant of the dc-link voltage dynamics of the dc-voltage controlled wind-turbine. Therefore, robustness against system parameter variation is essential in the dc-link voltage controller.

1.3.6 Control of VSCs with DC Droop Power Management Strategy

Power sharing among different VSCs connected to a dc grid with multiple ac terminals is essential to share the power economically among different ac terminals. To avoid the reliability and cost issues associated with communication-based power sharing methods (e.g., centralized approaches based master/slave control and its variants [53]-[57]) dc-voltage droop control is a common and cost-effective method for power sharing control [58]-[62]. In this method, only the local information is used to realize the power sharing function.

Recently, some of the stability and dynamics aspects of droop-controlled VSCs in dc grids have been addressed in the current literature. To optimize the economic operation of a multiterminal dc grid, variable droop gains are generated by a supervisory energy management controller [59]-[60]. However, the findings in [61]-[62] show that the stability of the VSC with dc-droop function significantly depends on the droop gains, and this necessitates using adaptive droop mechanism. However, some important aspects that directly affect the performance and stability of grid-connected VSCs with dc droop control function are not addressed in the current literature. These issues are summarized as follows:

1) The dc-link voltage control is designed without considering the impact of the droop feedback on the overall converter dynamics. In fact, the droop mechanism affects the dc-link voltage dynamics. The dc-link dynamics already depends on the converter operating point when the instantaneous power of the inductor ac filter is considered. With power sharing via droop control, this dependency is increased as the operating point of the converter varies according to the droop feedback mechanism. Therefore, destabilizing dynamics can be generated, particularly under variable droop gain needed for optimum economic operation, energy management, and successful network operation under converter outages and contingencies.
2) The dc grid parameters as viewed by the dc-link of a VSC (e.g., equivalent passive load resistance, equivalent dc-link capacitance and dc grid power disturbances set by other converters connected to the dc grid) are subjected to a large range of variation and uncertainties; this significantly affects the stability and performance not only due to operating point variation but also due to changes in the plant parameters.
3) In droop-controlled VSCs, the dc-link voltage varies in a relatively large range due the droop mechanism; therefore, the dc-link voltage controller should offer robustness against variation in the converter set point, active and reactive operating points as well as system uncertainties and disturbances.

1.4 Research Motivations

A detailed literature survey indicates the urgent need to develop robust controllers for VSCs in MTDC grids to stabilize and enhance the overall MTDC grid system considering the complicated nonlinear converter-grid dynamics and the presence of uncertainties and disturbances in a typical MTDC system. Specifically, there is a need to

1) Develop a robust linear dc-link voltage controller that addresses the dependency of the converter dynamics on the converter operating point.
2) Characterize the converter dynamics and develop a robust dc-link voltage controller for the master VSC in the presence of an uncertain dc side inductance.
3) Improve the performance of the standard vector-controlled VSC under weak and very weak ac grid conditions.

4) Facilitate direct connection of a dc-voltage controlled wind turbine into dc grids.
5) Develop a robust dc-link voltage controller for droop-controlled VSCs in MTDC grids.

1.5 Research Objectives

This research aims at developing new models, and robust control and power management algorithms for VSCs to stabilize and enhance the performance of MTDC grids without exact a priori knowledge on the MTDC structure and parameters. The main objectives of this thesis are as follows.

1) Developing a robust multi-objective dc-link voltage controller for a bi-directional VSC regulating the dc-link voltage of an MTDC grid. The proposed controller is designed to ensure excellent tracking performance, robust disturbance rejection, and robust stability against operating point and parameter variation with a simple fixed-parameter low-order controller.
2) Investigating the dynamics and robust control aspects of VSCs considering the instantaneous power of both ac- and dc-side filters and dc grid uncertainties.
3) Developing a natural-frame variable-structure-based nonlinear control system for the master VSC applied in dc-energy pool multiterminal grids to overcome problems associated with conventional dc-link voltage controllers, which are suffering from stability and performance issues, mainly attributed to the small-signal-based control design approach and the use of cascaded control structure based on the power balance framework that yields unmodeled nonlinear dynamics.
4) Developing a robust vector-controlled VSC that facilitates full converter power injection at weak and very weak ac grid conditions (i.e., when the short-circuit capacity ratio is one).
5) Addressing the control challenges associated with a dc-voltage-controlled VSC interfacing a wind turbine into a dc grid, which is gaining widespread acceptance under weak grid connection or isolated operation.
6) Developing a robust power sharing and dc-link voltage regulation controller for grid-connected VSCs in dc grid applications to overcome difficulties and problems related to the dynamics and stability of a grid-connected VSC with dc power sharing droop control.

1.6 Thesis Contributions and Outline

The remainder of this thesis is structured as follows.

Chapter 2 presents a robust multi-objective controller for the master VSC in MTDC grids. The proposed controller ensures excellent tracking performance, robust disturbance rejection, and robust stability against operating point and parameter variation with a simple fixed-parameter low-order controller. A two-degree-of-freedom control structure is proposed, where feed-forward tracking and base-line robust disturbance rejection controllers are employed to decouple disturbance rejection and tracking objectives. A disturbance rejection controller is designed, based on the singular-values μ-synthesis approach, to achieve robustness against variation in converter operation point. Further, the effect of parametric uncertainty in the effective dc-link capacitance is mitigated by modifying the robust disturbance rejection controller, via the polynomial method, to ensure that the closed-loop poles are allocated in the pre-defined region in the complex plane even under parameter variation. A theoretical analysis and comparative simulation and experimental results are presented to show the effectiveness of the proposed control structure.

Chapter 3 presents 1) a detailed small-signal model of the dc-link dynamics in grid-connected VSCs considering the instantaneous power of both ac- and dc-side energy storage components, and 2) a robust optimal dc-link voltage controller. The proposed controller ensures excellent tracking performance, robust disturbance rejection, and robust performance against operating point and parameter variation with a simple fixed-parameter controller. A theoretical analysis, comparative simulation studies, and experimental results are presented to show the effectiveness of the proposed control structure.

Chapter 4 presents a natural-frame variable-structure-based nonlinear control system for the master VSC applied in dc-energy pool multiterminal grids. The proposed controller accounts for the complete nonlinear dynamics of the master VSC without any cascaded control structure, and it globally stabilizes the nonlinear dynamics via a passivity-based design approach. Analysis and comparative simulation as well as experimental results are presented to show the effectiveness of the proposed controller.

Chapter 5 presents a robust vector-controlled VSC that facilitates full converter power injection at weak and very weak grid conditions (i.e., when the short-circuit capacity ratio is

one). To realize the controller, firstly, a detailed dynamic model for the ac-bus voltage dynamics, including the PLL dynamics, is developed and validated in Chapter 5. Secondly, the model is used to optimally design a robust ac-bus voltage controller to stabilize the dynamics under operating point variation and grid impedance uncertainty. Because the developed model includes the PLL dynamics, the developed controller inherently stabilizes the negative impact of the PLL on the converter stability. A theoretical analysis and comparative simulation and experimental results are provided to show the effectiveness of the proposed controller.

Chapter 6 addresses the challenges associated with a dc-voltage-controlled VSC interfacing a wind turbine into a dc grid and proposes a robust parallel distributed control strategy as a simple and robust solution to handle a large variation of the operating point of the wind turbine system. The proposed controller is based on the robust structured singular values μ-synthesis approach as well as a functional fuzzy model. Analysis and comparative simulation results are presented to show the effectiveness of the proposed controller.

Chapter 7 presents a robust power sharing and dc-link voltage regulation controller for grid-connected VSCs in dc grids applications. A detailed dynamic model that considers the droop controller dynamics and the impact of the effective dc-side load parameters and disturbances imposed on the VSC is developed. Then, a robust controller that preserves system stability and robust performance is developed. A mathematical analysis as well as simulation results is provided to show the effectiveness of the proposed controller.

Finally, the summary of this thesis and direction for future work are detailed in Chapter 8.

Chapter 2

Robust DC-Link Voltage Regulation of the Master VSC in MTDC Grids

2.1 Introduction

This chapter presents a robust multi-objective controller for a stiff ac grid connected master VSC in MTDC grids/micro-grids. A two DOF control structure is proposed, where feed-forward tracking and base-line robust disturbance rejection controllers are employed to decouple the design objectives of disturbance rejecting and reference tracking. The main contributions of this chapter to the research field can be highlighted as follows.

1) The development of a robust disturbance rejection controller based on an accurate dc-link voltage dynamic model that considers the dependency of the dc-link voltage dynamics on the operating point of the VSC. The disturbance rejection controller is designed, based on the singular-values μ-synthesis approach, to achieve robustness against variation in converter operation point.
2) The development of an external-power-sensorless-control scheme with effective disturbance rejection. The proposed controller achieves excellent disturbance rejection without any feed-forward control of external power disturbances imposed on the dc-link.
3) The development of a robust controller against uncertainty in the equivalent dc-link capacitance. The robust disturbance rejection controller is modified, via the polynomial method, to ensure that the closed-loop poles are allocated in a pre-determined region in the complex-plane even under parameter variation.
4) The developed controller has a simple structure, low order and fixed-parameters, which makes it very attractive for industrial applications.

A theoretical analysis and comparative simulation and experimental results are presented to demonstrate the effectiveness of the proposed controller.

2.2 Modeling of the Master VSC

Fig. 2.1 shows a grid-connected converter that is responsible for regulating the dc-link voltage in an MTDC by balancing the powers injected and absorbed from the dc-link. The method employed to model dc voltage power port is based on the space vector theory [30]. Because it is neither practical nor realistic to design the dc-link voltage controller of the using an exact dc grid model, an equivalent uncertain model of the MTDC system as viewed from the master VSC is adopted. As shown in Fig. 2.1, the model consists of an equivalent variable current source modeling the variable power injection/absorption of other converters connected to the MTDC grid, an equivalent resistor to model passive loads connected to the MTDC grid, and an equivalent capacitance modeling the dc-link capacitances of power converters connected to the MTDC grid [115]. A strong ac grid is assumed and the dc grid series inductance is assumed to be negligible.

An accurate dc-link voltage model is used in this chapter, which considers the instantaneous power of the ac-side filter, L shown in Fig. 2.1. The effect of the instantaneous power of the ac filer inductance L is neglected in low-power VSC applications (due to the small filter inductance associated with high switching frequencies); however, it adds additional dynamics in high power VSCs, which results in different dynamics of the dc-link voltage at different operating points.

The power balance across the dc-link capacitor in Fig. 2.1 can be represented by (2-1)

$$P_{ext} - P_{loss} - \frac{d}{dt}(0.5C_{eq}V_{DC}^2) = P_{DC} \tag{2-1}$$

where V_{DC} is the dc-link voltage, C_{eq} is the equivalent dc-link capacitance at the dc terminal of the VSC that is equivalent to parallel combination of the equivalent dc grid capacitance $C_{DC\text{-}eq}$ and the dc-link capacitance C, i.e., $C_{eq}=C_{DC\text{-}eq}+C$, P_{ext} is the external power whose positive reference is injection into the dc-energy pool, P_{loss} is the power losses of the converter, and P_{DC} is the net power as shown in Fig. 2.1 which is equal to the VSC ac-side terminal power, P_t.

If the instantaneous power of the ac filter, i.e., L shown in Fig. 2.1, is not considered, the terminal power P_t is equal to the ac-side power P_s as it has been assumed in [12], [17], [28]-[27], which yields a dc-voltage power port model that is independent of the operation point of the converter [23] and [29]. After mathematical manipulation, the relation between P_t, P_s and Q_s can be obtained as

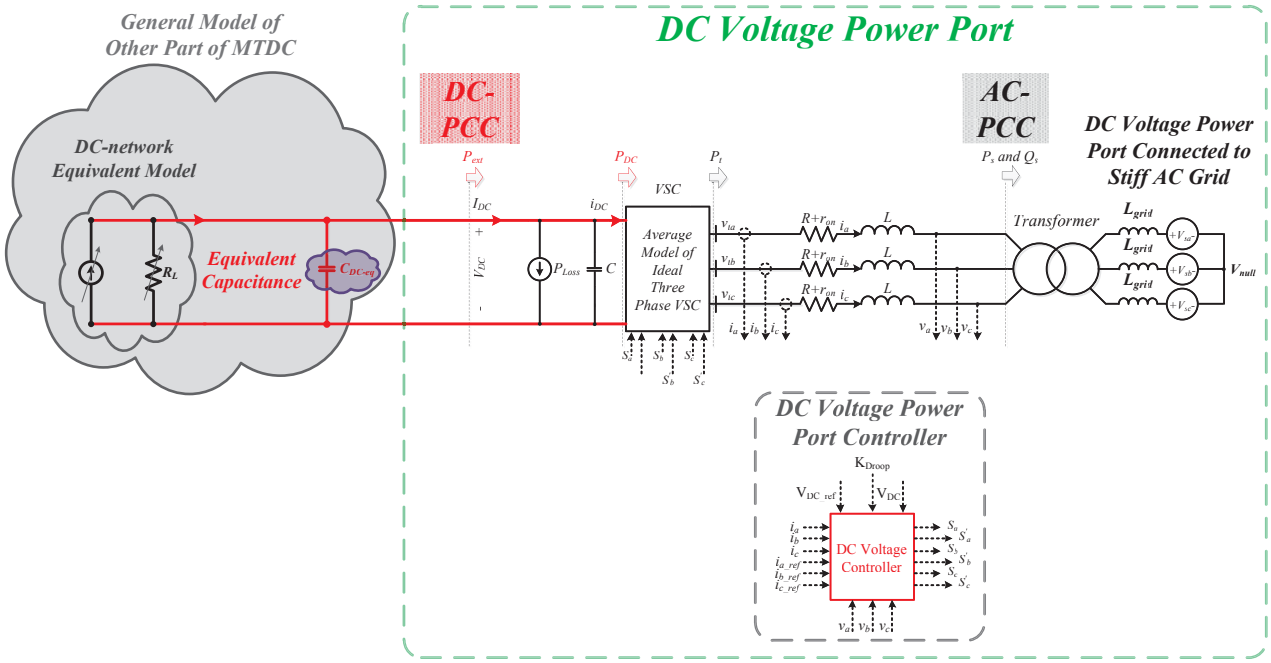

Fig. 2.1. Master VSC configuration.

$$\begin{aligned} &P_{ext} - P_{loss} - \frac{d}{dt}(0.5C_{eq}V_{DC}^2) = P_{DC} \\ &\Rightarrow \frac{d}{dt}(0.5C_{eq}V_{DC}^2) = P_{ext} - P_{DC} - P_{loss} \end{aligned} \quad . \tag{2-2}$$

P_{loss} can be modeled as a resistance R_p in parallel with the dc terminals. This approach is usually adopted in high-power converters to augment the converter losses as a passive element that can be reflected to the model of the VSC [30].

$$P_{loss} = \frac{V_{DC}^2}{R_p} \tag{2-3}$$

Therefore,

$$P_{DC} = P_t \tag{2-4}$$

where P_t is the instantaneous power delivered to the ac terminals.

Thus, in the *dq* reference frame, the instantaneous power is

$$P_t = 1.5(V_{td}I_d + V_{tq}I_q) \tag{2-5}$$

If the energy stored in the interface reactors is ignored, then the power balance equation can be written as (2-6).

$$V_{DC}^2 + 0.5R_pC_{eq}\frac{d}{dt}(V_{DC}^2) = R_pP_{ext} - 1.5R_pV_{sd}I_d \tag{2-6}$$

After linearization around an operating point, one reaches (2-7).

$$\begin{aligned}\tilde{V}_{DC}^2(s) &= R_p\frac{1}{(0.5R_pC_{eq}s+1)}\tilde{P}_{ext} - 1.5R_pI_{d0}\frac{1}{(0.5R_pC_{eq}s+1)}\tilde{V}_{sd}(s)\\ &-1.5R_pV_{sd0}\frac{1}{(0.5R_pC_{eq}s+1)}\tilde{I}_d(s)\end{aligned} \tag{2-7}$$

When the energy stored in the interface reactors is considered, the power balance equation becomes

$$\begin{aligned}P_t &= P_L + P_R + P_s\\ P_L &= \frac{d}{dt}(0.5Li_a^2 + 0.5Li_b^2 + 0.5Li_c^2)\\ P_R &= 3\times 0.5R\,|\,I\,|^2\\ P_s &= 1.5V_{sd}I_d + 0\end{aligned} \tag{2-8}$$

where P_L is the instantaneous power of the inductor, P_R is the power losses in the filter inductor, and P_s is the grid side power. The q-component of the grid voltage at the PCC is zero, i.e., V_{sq}=0 due to the operation of the voltage-oriented vector control scheme.

Provided that a balanced three phase ac currents are considered at a given operating point, the converter currents can be represented by (2-9).

$$\begin{cases} i_a = I\cos(\omega t)\\ i_b = I\cos(\omega t - \dfrac{2\pi}{3}) \Rightarrow 0.5Li_a^2 + 0.5Li_b^2 + 0.5Li_c^2 = 0.75LI^2 = 0.75L\,|\,I\,|^2\\ i_c = I\cos(\omega t - \dfrac{4\pi}{3})\end{cases} \tag{2-9}$$

As a result, equation (2-10) can be written

$$P_t = 1.5(V_{td}I_d + V_{tq}I_q) = \frac{d}{dt}(0.75L\,|\,I\,|^2) + 1.5R\,|\,I\,|^2 + 1.5V_{sd}I_d \tag{2-10}$$

where $|I|$ is the amplitude of the converter line current, and it is equal to

$$|\,I\,| = \sqrt{I_{td}^2 + I_{tq}^2} \tag{2-11}$$

Consequently, the dc-link voltage control dynamics is governed by equation (2-12)

$$\frac{d(0.5C_{eq}V_{DC}^2)}{dt} = P_{ext} - \frac{V_{DC}^2}{R_P} - \frac{3L}{4}\left(\frac{dI_d^2}{dt} + \frac{dI_q^2}{dt}\right) - \frac{3R}{2}(I_d^2 + I_q^2) - \frac{3}{2}V_{sd}I_d \tag{2-12}$$

Equation (2-12) describes the nonlinear dynamics of the dc-link voltage considering the instantaneous power of the ac filter [30].

The current dynamics, represented by equations (2-13) and (2-14); (2-13) and (2-14), are the dynamics of the control lever of the dc-link voltage controller in a cascaded control system

$$L\frac{dI_d}{dt} = L\omega I_q - (R + r_{on})I_d + 0.5V_{DC}m_d - V_{sd} \tag{2-13}$$

$$L\frac{dI_q}{dt} = -L\omega I_d - (R + r_{on})I_q + 0.5V_{DC}m_q - V_{sq} \tag{2-14}$$

where (I_d, I_q), (V_{sd}, V_{sq}), and (m_d, m_q) are dq-components of the VSC output current, grid voltages and converter modulation index, respectively [30]; and r_{on} is the equivalent average conduction resistance of the VSC [30].

The outer loop dynamics, i.e., equation (2-12), can be linearized around an operating point, (I_{d0}, I_{q0}) as expressed in (2-15).

$$\begin{aligned}\tilde{V}_{DC}^2(s) = &-\frac{1.5R_PLI_{d0}s + 1.5R_P(V_{sd0} + 2RI_{d0})}{0.5R_PC_{eq}s + 1}\tilde{I}_d(s) - \frac{1.5LR_PI_{q0}s + 3RR_PI_{q0}}{0.5R_PC_{eq}s + 1}\tilde{I}_q(s) \\ &-1.5\frac{R_PI_{d0}}{0.5R_PC_{eq}s + 1}\tilde{V}_{sd} \\ &+\frac{R_P}{0.5R_PC_{eq}s + 1}\tilde{P}_{ext}(s)\end{aligned} \tag{2-15}$$

where "~" denotes small-signal variable and subscript "0" denotes an operating point signal.

Fig. 2.2 shows a block diagram of the dc-link voltage dynamics including the feedback controller. Conventionally, P_{ext} is used for feed-forward control in the dc voltage controller ([23], [27], [30] and [31]) to enhance its performance as shown in Fig. 2.2 (a). However, the proposed controller gives better disturbance rejection performance without using any feed-forward control of P_{ext} as shown in Fig. 2.2 (b). This feature eliminates the need for additional measurement and sensor requirements to measure P_{ext}, which enhances the reliability and cost measures of the proposed controller. Fig. 2.2 (b) shows the control structure for the dc-link voltage dynamics based on the detailed model in (2-15).

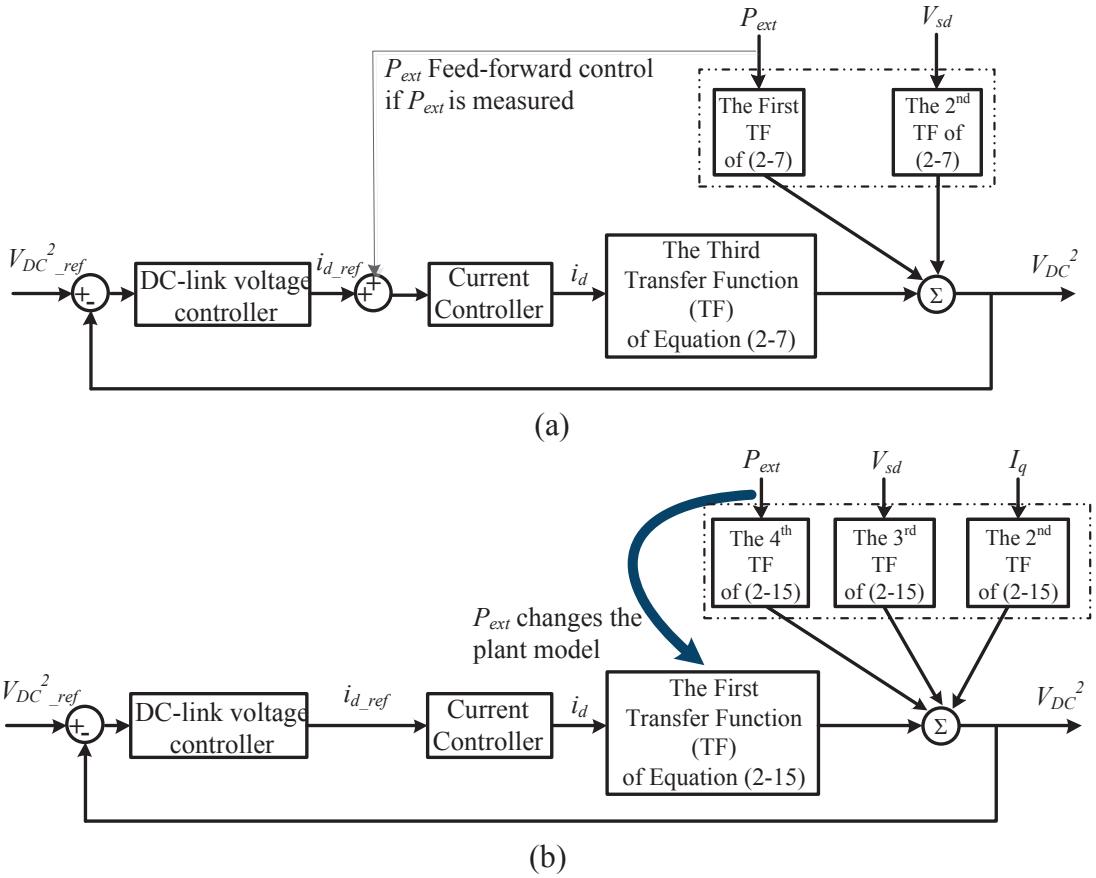

Fig. 2.2. Block diagram of the dc-link voltage control dynamics. a) conventional control used in previous work b) proposed control system.

2.3 Proposed DC-Link Voltage Control Design

By inspecting (2-15), it can be seen that V^2_{DC} is the output, I_d is the input, P_{ext}, V_{sd}, and I_q are the disturbances affecting the output. The ac-grid voltage V_{sd} is an external disturbance that impacts the plant output without affecting the plant model or the transfer function connecting V_{sd} to the output. However, I_q and P_{ext} cannot be considered as external disturbances. As I_q changes due to variation of the VSC operating point (I_{d0}, I_{q0}), the transfer function connecting I_q to the output changes, and accordingly it impacts the output due to the additional dynamics (the second term in equation (2-15)) imposed on the dc-link voltage dynamics. The worst case happens for the disturbance P_{ext}; when P_{ext} changes, it affects the output not only with its frequency distribution but also with its effect on the plant model form the input I_d to the output V^2_{DC}. In other words, plant model variation associated with operating point changes coincide with P_{ext} variation as P_{ext} affects P_{DC}, P_t, P_s, and I_d. From the control theory point of view, the model is dependent on the

disturbance changes; therefore the controller should reject a disturbance that changes the nominal plant model. Furthermore, the first term of (2-15) shows that the plant model changes from minimum phase system to the non-minimum system as the VSC operating mode changes from inversion to the rectification, which dramatically affects the phase response due to the non-minimum-phase zero. On the other hand, uncertainty in system parameters (e.g., changes of equivalent dc- link capacitance due to connection/disconnection of dc-energy sources/loads) might be yielded and should be considered in the control design.

Motivated by the aforementioned limitations, a robust control scheme for the dc-voltage power port is proposed in this chapter. The conceptual design of the proposed controller is to split the control objectives over two simple fixed-parameter controllers to ensure perfect tracking and robust performance. The controllers are augmented in a sequential design approach to ensure overall stability and robust performance under operating point variation, parametric uncertainty, and the occurrence of disturbances. Fig. 2.3 depicts the overall structure of the proposed controller.

2.3.1 Controller Synthesis: Reference Tracking

Generally, it is desirable to decouple the reference-tracking and disturbance rejection objectives in controller synthesis. This approach creates a two-degree-of-freedom controller, which enables the design of a robust disturbance rejection controller without affecting the tracking performance in a way that is not possible with conventional PI controllers.

A general non-minimum phase strictly proper stable system is modeled by

$$G(s)=\frac{K_{DC}N(s)}{D(s)}=\frac{K_{DC}N_{MP}(s)N_{N-MP}(s)}{D(s)} \tag{2-16}$$

where K_{DC} is the dc gain if the polynomials $N(s)$ and $D(s)$ have their coefficients adjusted to have 1 as their zero-degree coefficient, and $N_{N\text{-}MP}(s)$, $N_{MP}(s)$, and $D(s)$ are the non-minimum phase, minimum-phase, and stable polynomials, respectively. To realize a 2-DOF control structure for minimum-phase systems, a model-based feed-forward control approach can be adopted [79]. Fig. 2.4(a) describes the whole controller structure of a 2-DOF controller. Fig. 2.4 (a) describes the case when the entire plant $G(s)$ is invertible, therefore $G(s)=G_i(s)$. However, this is not always the case, similar to the present control design problem, as the plant can have a non-minimum

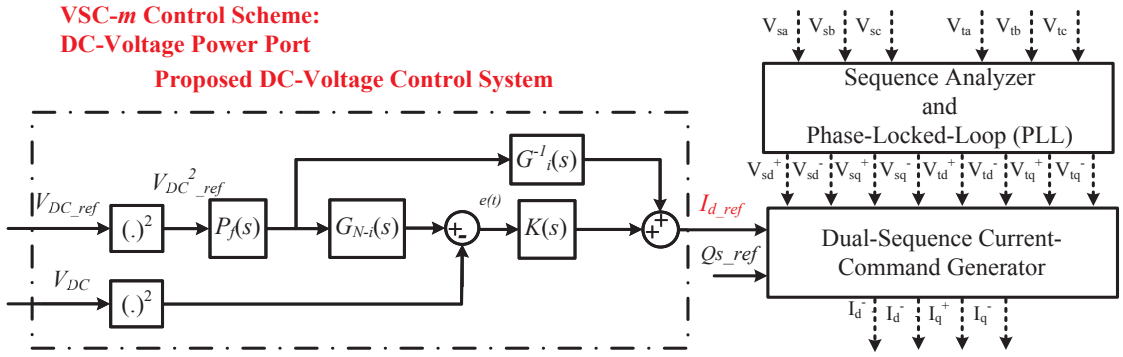

Fig. 2.3. Proposed control scheme for the dc-voltage power-port in MTDC grid.

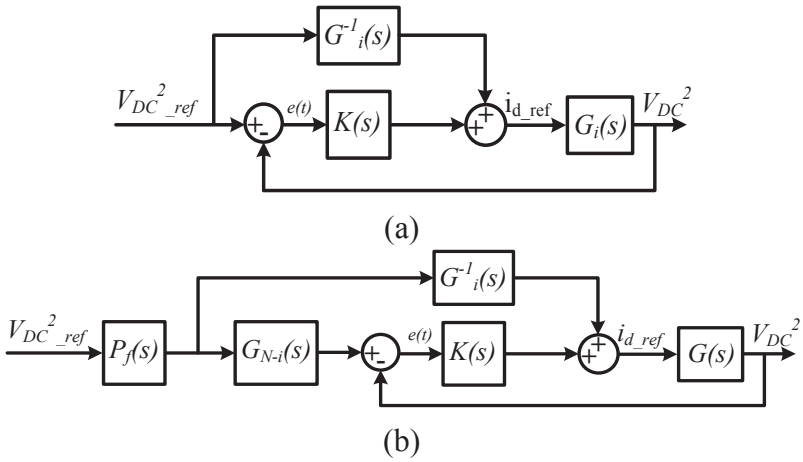

Fig. 2.4. Model-based feed-forward reference tracking controller for (a) the minimum-phase system, (b) non-minimum phase system.

phase zero. In this case, Fig. 2.4 (b) is proposed, where $G_i(s)$ is the invertible part of the transfer function of total plant, $G(s)$, and $G_{N\text{-}i}(s)$ is the noninvertible part of $G(s)$ based on the decomposition of equation (2-16). Note that the feed-forward path employed in the controller is the internal feed-forward path of the dc-voltage controller, and it is not like the conventional feed-forward of the external power P_{ext} to enhance the control performance. Indeed, P_{ext} is the power injected or absorbed to or from the dc link which is not always measurable in the large-scale ac/dc hybrid micro-grids based on the dc-energy pool.

With the configuration shown in Fig. 2.4 (a), the following sensitivity function $S(s)$ and complementary sensitivity function $T(s)$ can be obtained:

$$S(s) = \frac{G_i^{-1}(s)G_i(s)}{1+G_i(s)K(s)} - \frac{1}{1+G_i(s)K(s)} = 0 \tag{2-17}$$

$$T(s) = 1 \tag{2-18}$$

As it is obvious from (2-17) and (2-18), this method is not realizable for non-minimum phase strictly proper systems. The non-minimum phase feature results in internal instability, and strictly proper system with unrealizable inverse; therefore, it is impossible to implement with a physical system. This problem exactly exists in Youla parameterization of all stabilizing controllers for the non-minimum phase strictly-proper stable LTI systems [80].

To overcome this problem, only the minimum-phase part is extracted to build all stabilizing controllers; and a pre-filter is used to make the improper inverse transfer function proper [80]. The modified feed-forward controller is shown in Fig. 2.4 (b), where $G_i(s)$, is the invertible part of the total plant, and $G_{N\text{-}i}(s)$ is the noninvertible part of the total plant. In Fig. 2.4 (b), the sensitivity function and complementary sensitivity function are 0 and $P_f(s)G_{N\text{-}i}(s)$, respectively. Hence, $P_f(s)$ should be stable, and the relative degree of $P_f(s)$ should be greater than or equal to the relative degree of $G_i(s)$. Besides, $P_f(0)=1$. By meeting these conditions, both feed-forward paths will be stable and proper transfer functions. $G(s)$ is the first transfer function of (2-15), and $G_i(s)$ is its invertible part based on the decomposition shown by (2-16).

Under exact model matching, the tracking transfer function is unity. Thus, using the control structure in Fig. 2.4 (b), the feedback controller $K(s)$ can be designed mainly for disturbance rejection, whereas the pre-filter in the tracking controller dictates the tracking dynamics. It should be noted that model mismatch in the feed-forward tracking controller leads to uncertainty in the system, which will be also rejected by the feedback controller (i.e., the feedback controller also contributes to the tracking performance under model mismatch conditions). Further, if the feedback controller is designed with robustness against uncertainties, as proposed in this chapter, the overall robustness with respect to tracking, disturbance rejection, operating point variation and parametric uncertainties can be remarkably improved. With this control structure, it is possible to design the feed-forward controller using the nominal small-signal dynamics without a need to adaptively tune the feed-forward controller.

2.3.2 Controller Synthesis: Disturbance Rejection

As mentioned earlier, the main disturbance that affects the output (V^2_{DC}) is P_{ext}. As a result, the controller $K(s)$ should be designed to reject the disturbance P_{ext} under all possible operating points of the VSC. It should be mentioned that P_{ext} changes the operating point of the converter; and accordingly, it changes the plant dynamics. Furthermore, controlling the dc-voltage power

port without using the measured value of P_{ext} is a privilege to avoid extra measurements devices. Therefore, effective disturbance rejection without feed-forward control of P_{ext} is a key feature in the proposed controller.

The H_∞ optimization approach may result in robust stabilization against unstructured system perturbations and nominal performance requirements as discussed in [84]. It is though possible that by applying appropriate weighting functions some robust performance requirements can be achieved; satisfactory designs have been reported, in particular when using the H_∞ loop-shaping design method [81]-[84]. Instead of H_∞ loop-shaping design approaches, design methods based on the structured singular value μ can be used in order to achieve robust performance in addition to robust stability. Indeed, H_∞ design of two DOF controller is not able to simultaneously guarantee both robust stability and robust performance of the closed-loop system. Consequently, μ-synthesis approach is used to induce both robust stability and robust performance in closed-loop system. There are two key iterative μ-synthesis methods which are *DK*-iteration and μK-iteration methods. In this thesis, the *DK*-iteration is employed.

One of the best ways to reject the disturbance effect on the output is minimizing the H_∞ norm from filtered P_{ext} to filtered output in the presence of weighted uncertainty, or designing the controller based on the structured singular values μ-analysis [81]-[84]. The μ-synthesis controller leads to better robust performance as compared to the H_∞ controller. This feature allows the design of a disturbance rejection controller that preserves the robustness and stability under operating point variation.

Based on the current controller implemented in *dq* frame using a PI controller and feed-forward decoupling signals, the closed-loop current control dynamics can be given by

$$G_c(s) = \frac{1}{\tau_i s + 1} \tag{2-19}$$

where $1/\tau_i$ is the closed-loop current control bandwidth.

Using Fig. 2.2, the total transfer function for the dc-voltage control dynamics at an operating point (I_{d0}, I_{q0}) can be given by

$$G_T(s) = -\frac{1.5R_P L I_{d0} s + 1.5R_P (V_{sd0} + 2RI_{d0})}{0.5R_P C_{eq} s + 1} \times \frac{1}{\tau_i s + 1} \tag{2-20}$$

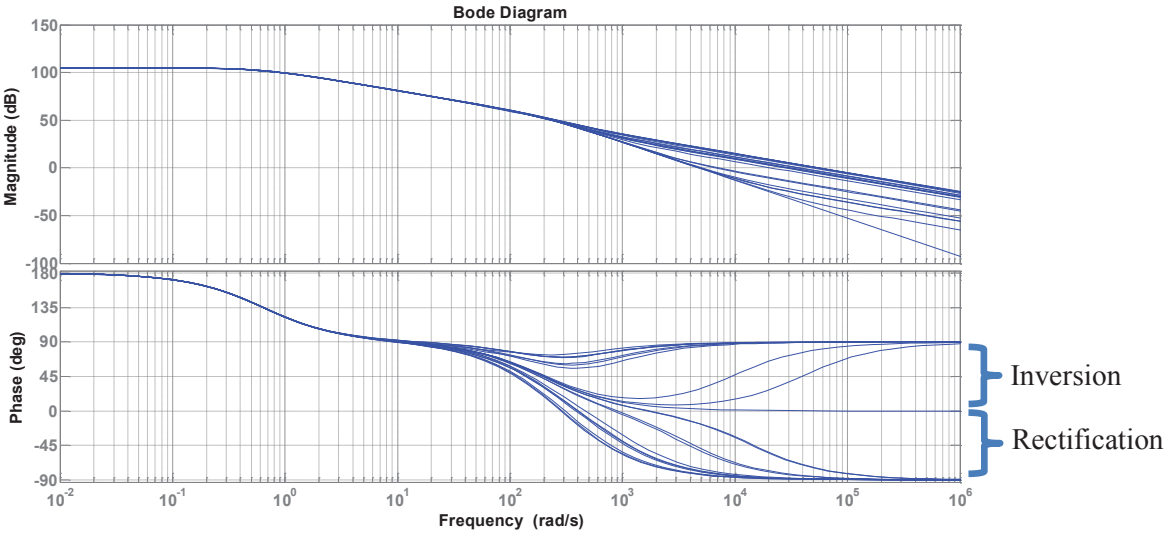
Bode Diagram
Magnitude (dB)
Phase (deg)
Frequency (rad/s)
Inversion
Rectification

(a)

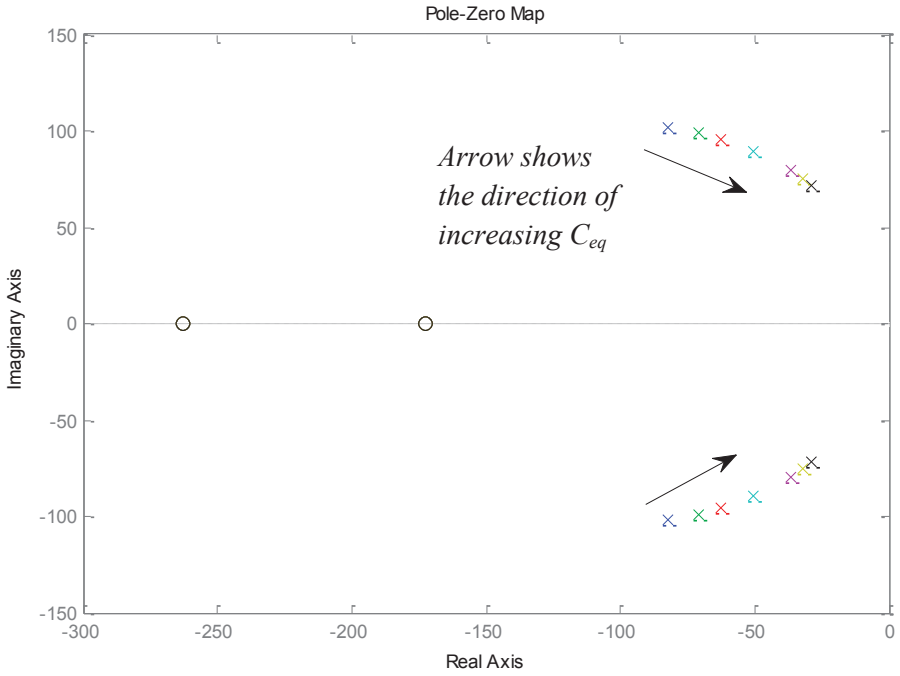
Pole-Zero Map
Arrow shows
the direction of
increasing C_{eq}
Imaginary Axis
Real Axis

(b)

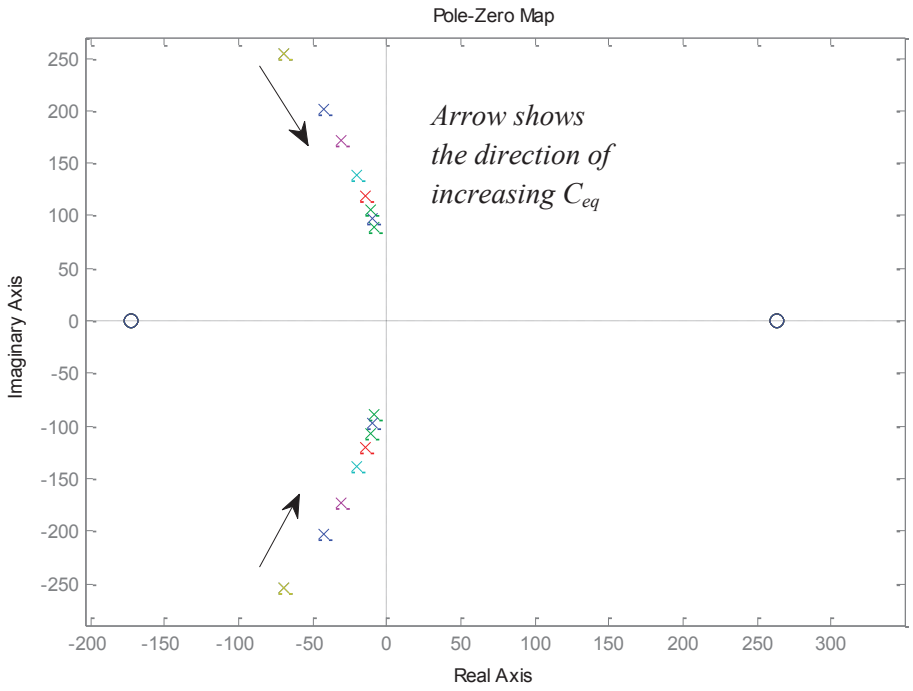

(c)

Fig. 2.5. (a) Frequency response of (2-15) at different operating modes. (b) Pole-zero map of the closed-loop system with PI controller and variable C_{eq} (12.5 mF to 100 mF) at rated power in inversion mode. (c) at rated power in the rectification mode.

Fig. 2.5(a) shows the frequency response of $G_I(s)$ for the complete range of VSC-*m* operating points. It is clear that the magnitude of the linearized plant at an operating point is the same in both inversion and rectification modes at the same power; however, the phase is dramatically reduced at the same power in the rectification mode due to the RHP zero. Further, by considering (2-20), it can be seen that the pole of the transfer function of the open loop system from $I_d(s)$ to V^2_{DC} is a function of C_{eq} which shows that C_{eq} affects the pole of the closed-loop system. Fig. 2.5 (b) shows the closed-loop zero-pole map of with a conventional PI controller (with a bandwidth of 40 Hz) at different values of C_{eq} (12.5 mF to 100 mF) at rated power in the inversion mode (i.e., left-hand zero). It clearly shows that the PI controller is not robust against variation in the equivalent capacitance. The relative stability is affected due to uncertainty in C_{eq}. Fig. 2.5 (c) shows the pole-zero map under the same range of C_{eq} when the converter works at full power in rectification mode. The non-minimum phase behavior of the system along with uncertainties yields to lower stability margin at parametric uncertainties. Therefore, the development of a robust controller that yields robust stability and robust control

performance at variation in both the operating point and equivalent capacitance demands special attention.

Although designing switched controllers for different operating point is feasible [85], designing one controller with robust performance at different operating points benefits from lower complexity and better stability. Besides, there are other design approaches based on polynomial methods which are feasible and practical to design a controller for nonlinear plants having different transfer functions for different operating points in order to fix the closed-loop poles in a specific region D to have better stability margin [86]. However, the problem is that polynomial method offers only sufficient condition based on linear matrix inequalities (LMIs) to find the controller coefficients; this might yield infeasible solution under wide range of operating point variation, which is a typical case in VSC operation. Another problem is finding an appropriate central polynomial where, in the present case, it could be found based on H_∞ or μ-synthesis optimal controller for a base-line controller designed based on maximum rated power in the rectification mode. Therefore, the robust optimal control approach is adopted in this chapter to design the disturbance rejection controller to yield effective disturbance rejection under the complete range of operating point variation, which can be considered as unstructured (weighted) uncertainty.

For robust control design, the dc-link voltage control dynamics should be modeled as an uncertain transfer function affected by operating point variation. If the instantaneous power of the ac-side filter is ignored, the dynamics in (2-20) converges to the conventional simplified dc-link voltage control dynamics, i.e., equation (2-21) [12]-[17], [27]-[29].

$$G_T(s) \to -1.5V_{sd0}\frac{1}{0.5C_{eq}s}\times\frac{1}{\tau_i s+1} \tag{2-21}$$

In this case, both multiplicative and additive uncertainty modeling are allowed to be employed in designing robust controller; however, only additive uncertainty can be employed if the accurate model in (2-20) is used since, due to RHP zero, multiplicative uncertainty modeling leads to unstable transfer function for the uncertain part [84]. As a result, the additive uncertainty modeling is employed for designing robust performance controllers.

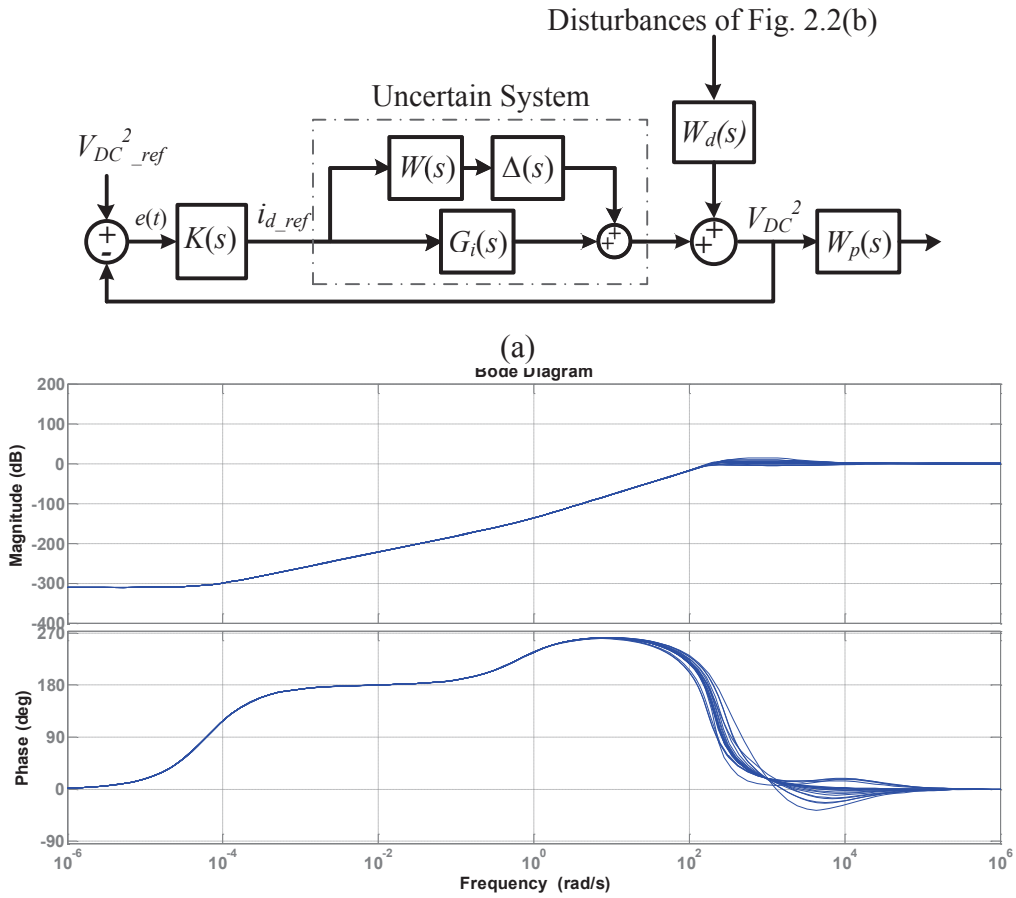

Fig. 2.6. (a) Structure used to design feedback controller. (b) Disturbance rejection performance with the proposed controller at different operating points.

In order to deal with the operating point variation problem in high-power VSCs, a robust controller design using the μ-synthesis approach, which uses *DK*-iteration [82], is adopted. In other words, the operating point variation is modeled as an unstructured uncertainty $\Delta(s)$ weighted by a transfer function $W(s)$; then, the robust stability theory is applied to synthesize a stabilizing LTI controller for all the plant models parameterized by the uncertain plant model, which reflects operating point variation using $W(s)\Delta(s)$. Also, the performance objective is introduced as a weighted sensitivity minimization problem using filters $W_d(s)$ and W_p(s) as shown in Fig. 2.6(a). By this way, operating point variationin high power VSCs can be seen as an LTI control synthesis problem which includes both robust performance and stability properties. In order to have one structure that models all operating point variations, the transfer function $G(s)$ is considered as $G_I(s)$ (in (5-9)) evaluated at the maximum power in rectifier mode. Then, the robust controller can be designed by using the following weighted filters:

$$W(s) = -\frac{1.5R_p L I_{d0} s}{(0.5R_p C_{eq} s + 1)} \times \frac{1}{\tau_i s + 1} \tag{2-22}$$

$$W_d(s) = \frac{1 \times 10^6 R_p}{(0.5R_p C_{eq})s + 1} \times \frac{1}{s + 10^{-4}} \times \frac{1}{\frac{1}{2\omega_0} s + 1} \tag{2-23}$$

$$W_p(s) = \frac{1}{s + 10^{-4}} \tag{2-24}$$

By choosing $W(s)$ as (2-22), the controller guarantees robust performance and stability during I_{d0} variation. $W_d(s)$ is selected as (2-23) to reject P_{ext} during normal operation and fault conditions in ac grid. The selection of this bandwidth as $2\omega_0$ is found satisfactory under balanced and unbalanced conditions. $W_p(s)$ is selected as (2-24) to help the feed-forward paths in reference tracking due to the fact that transfer functions of the feed-forward paths are changing during operating point variation. Hence, this approach eliminates the need for employing identification and adaptation methods to update feed-forward paths at different operating points, and facilitates simple controller design with appropriate performance.

Applying the robust controller design approach via the μ-synthesis MATLAB toolbox and model order reduction leads to the following robust disturbance rejection controller, which ensures effective disturbance rejection at different operating points even during transient conditions:

$$K(s) = \frac{y(s)}{x(s)} = \frac{-4.179 \times 10^4 s^3 - 1.711 \times 10^7 s^2 - 2.813 \times 10^9 s - 2.01 \times 10^{11}}{s^4 + 3.842 \times 10^5 s^3 + 2.894 \times 10^9 s^2 + 3.389 \times 10^5 s + 10.79} \tag{2-25}$$

The controller has a simple structure with fixed parameters; therefore, it can be efficiently implemented. Fig. 2.6(b) shows the disturbance rejection performance of the proposed controller at different operating points. It is clear that high disturbance rejection performance can be obtained at nominal conditions and it can be preserved at different operating point of the converter without using disturbance feed-forward control.

2.3.3 Controller Synthesis: Robustness against Parameter Variations

In Section 2.3.2, the designed controller guarantees robust stability and disturbance rejection under operating point variation. In this section, the disturbance rejection controller is modified to ensure robustness against parameter variation as well. In particular, the uncertainty in the

equivalent dc-link capacitance is considered due to possible variation in this parameter due to connection/disconnection of dc-sources and loads.

It is possible to consider the parameter variation during the design of the disturbance rejection controller using the μ-synthesis approach. However, the synthesized controller will be of high-order and complexity. Further, the non-minimum phase nature of the plant only allows the consideration of additive uncertainty. While disturbance can be reasonably modeled as additive uncertainty [82], parametric uncertainties involve both multiplicative and additive [81]-[84]. Moreover, it is highly desirable to ensure robust stability margins in power networks by ensuring that the closed-loop poles will be allocated in a specific region even under parametric uncertainties. To achieve these objectives, the polynomial method is adopted to design the robust controller based on the base-line controller developed in Section 2.3.2. By employing the polynomial method, it can be guaranteed that all closed loop poles are located in a pre-determined region in the complex-frequency domain. Among the advantages of this method is simplicity and the resulting controller has the same order, or relatively closer, to the base-line controller.

From the control theory point of view, the problem is finding a fixed-order robust controller for a polytopic system to guarantee that the poles of the closed loop system are laid on a desired region, D, defined by (2-26), where its one-dimensional boundary, $\partial\mathcal{D}$, is defined by (2-27), where a, b, and c are the parameters defining the rejoin D; s is the complex operator; and "*" denotes complex conjugate.

$$D=\left\{ s\in C:\begin{bmatrix}1 & s^*\end{bmatrix}\underbrace{\begin{bmatrix}a & b\\ b^* & c\end{bmatrix}}_{S}\begin{bmatrix}1\\ s\end{bmatrix}<0\right\} \quad \text{where} \quad S=\begin{bmatrix}a & b\\ b^* & c\end{bmatrix} \tag{2-26}$$

$$\partial D=\left\{ s\in C: a+bs+b^*s^*+css^*=0\right\} \tag{2-27}$$

The polytopic system has n given vertices G_1,.., G_n produced by parameter variation and/or operating point variation. In fact, the roots of the closed-loop characteristic polynomial for all possible values of its coefficients should be laid in the region D, so it is called D stability criteria. D can be any region in the complex plane; e.g., left half plane (LHP), unit disk, or any other region. The goal is to find the coefficients of the controller $K(s)$ to guarantee that all poles of the closed-loop system are laid in D. Generally speaking, this is a non-convex problem based on the

coefficients of polynomials; however, by the method proposed in [86], the non-convex stability domain is approximated by a convex one which is inner in the non-convex region. Thus, the LMI approach is used to find the solution of the problem formed by the coefficients polynomials. Strictly positive real (SPR) polynomials and their relation with positive polynomials are the key point for designing robust controller based on polynomial methods [86]-[87].

Assume that $G_T(s)$ and controller $K(s)$ are written as

$$G_T(s) = \frac{b(s,\lambda)}{a(s,\lambda)} \tag{2-28}$$

$$K(s) = \frac{y(s)}{x(s)} \tag{2-29}$$

where $G_T(s)$ is polytopic, or even multi-linear, uncertain transfer function in the parameter vector λ belonging to a polytope Λ [86]-[88]. Hence, all possible polytopic characteristic polynomials are satisfying (2-30).

$$c(s,\lambda) = a(s,\lambda)x(s) + b(s,\lambda)y(s) \tag{2-30}$$

Thus, robust D stability is equivalent to laying roots of all possible $c(s,\lambda)$ in region D as long as λ belongs to a polytope Λ by finding appropriate $y(s)$ and $x(s)$ as polynomial with fixed degree.

The sufficient condition for the mentioned problem is stated at the following theorem [86].

"Theorem 1: Given a stable polynomial matrix D(s) of size n and degree d, referred to as central polynomial, polynomial matrix N(s) is stable if there is a symmetric matrix of degree d, $P=P^*$, satisfying the LMI (2-31)

$$D^*N + N^*D - H(P) > 0 \tag{2-31}$$

where $\mathrm{H(P)} = \Pi^*(\mathrm{S}\otimes\mathrm{P})\Pi$, $\otimes$ *is tensor product and* Π *is matrix of size* $2dn \times n(d+1)$ *with appropriate distribution of the identity and zero matrices. More details on Theorem 1 can be found in* [86]."

Using system parameters, $G_T(s)$ can be given by

$$G_T(s) = \frac{0.1125I_{d0}s + 2.625I_{d0} + 177{,}375}{0.625C_{eq}s^2 + (0.005 + 125C_{eq})s + 1} \tag{2-32}$$

Using the base-line robust disturbance rejection controller in (2-25) and system parameters, the following $c(s, \lambda_0)$ can be obtained:

$$c(s,\lambda_0) = 0.0113s^6 + 4324.5s^5 + 146183272s^4 + 5.8095\times10^9 s^3 + 1.5959\times10^{12}s^2 + 3.7957\times10^{14}s + 3.3585\times10^{16} \quad (2\text{-}33)$$

For a given range of equivalent capacitance variation at full power in the rectification mode, and by using *Theorem* 1 and the *Yalmip* toolbox in Matlab [89], the base-line controller can be modified to

$$K(s) = \frac{-4.9379\times10^{-18}s^3 - 1.8506\times10^{-15}s^2 - 1.8747\times10^{-13}s - 8.3792\times10^{-12}}{1.3586\times10^{-20}s^4 + 5.5176\times10^{-17}s^3 + 3.2832\times10^{-13}s^2 + 5.5176\times10^{-17}s} \quad (2\text{-}34)$$

The controller employs the robust disturbance rejection feature (as designed in Section 2.3.2) along with fixing the closed-loop poles in a pre-determined region *D* under parameter variation; therefore, both robust disturbance rejection and robust stability are guaranteed.

2.3.4 Controller Synthesis: Mitigation of DC-Voltage Ripples under Unb alanced Conditions or Asymmetrical Faults

When the ac-grid voltages are unbalanced, 2nd harmonic voltage ripples are induced in the dc-link voltage [30]. To reject the effect of unbalanced condition on the dc-link voltage, the dc voltage controller is augmented with a dual-sequence controller that utilizes the sequence component of the grid voltage to generate the reference sequence current components needed to attenuate dc-voltage ripple and satisfying the positive-sequence active and reactive power requirements simultaneously. For example, the reference current generation for the VSC-PQ can be obtained by

$$\begin{bmatrix} I_d^{+*} \\ I_q^{+*} \\ I_d^{-*} \\ I_q^{-*} \end{bmatrix} = \frac{2}{3}\begin{bmatrix} V_{sd}^{+} & V_{sq}^{+} & V_{sd}^{-} & V_{sq}^{-} \\ -V_{sq}^{+} & V_{sd}^{+} & -V_{sq}^{-} & V_{sd}^{-} \\ -V_{tq}^{-} & V_{td}^{-} & V_{tq}^{+} & -V_{td}^{+} \\ V_{td}^{-} & V_{tq}^{-} & V_{td}^{+} & V_{tq}^{+} \end{bmatrix}^{-1}\begin{bmatrix} p_s^{*} \\ q_s^{*} \\ 0 \\ 0 \end{bmatrix} \quad (2\text{-}35)$$

where I_d^{+}, I_d^{-}, I_q^{+}, and I_q^{-} are the *dq* components of positive and negative sequence VSC currents, respectively; V_{sd}^{+}, V_{sd}^{-}, V_{sq}^{+}, and V_{sq}^{-} are *dq* components of positive and negative sequence of PCC voltage, respectively; V_{td}^{+}, V_{td}^{-}, V_{tq}^{+}, and V_{tq}^{-} are *dq* components of positive and negative sequence of the VSC voltage, respectively; and p_s^{*} and q_s^{*} are the reference values of active and reactive powers required at the PCC, respectively. In a similar way, the reference currents of VSC-*m* can be obtained to attenuate the effect of grid-voltage unbalance on the dc-link voltage as shown in Fig. 2.3.

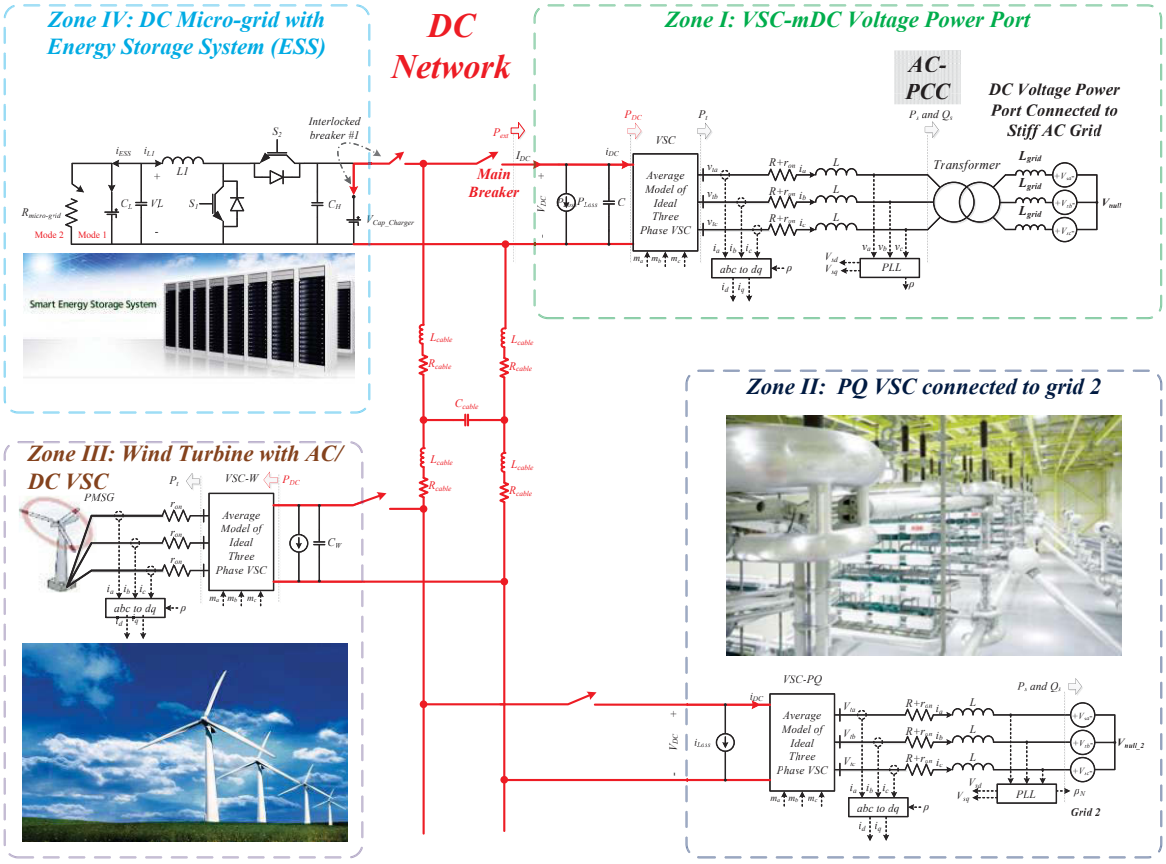

Fig. 2.7. Hybrid network system under study.

2.4 Simulation Results

A typical four-terminal MTDC grid, shown in Fig. 2.7, is simulated in the MATLAB/Simulink environment. The controller structure of Zone I is the same as Fig. 2.3; also, the circuit and controller parameters of Zone II, -III, and -IV are given in Section 2.6. The converters and network parameters are based on the practical guidelines given in [30].

The average model of VSCs in Zones I, II and III is used to reduce the computational burden without loss of accuracy. A switching model of the bi-directional dc/dc converter system (Zone IV) is implemented to test the control performance under typical high-frequency disturbances associated with converter switching. To evaluate the performance of the proposed voltage control scheme, several scenario and events are simulated. Key results are reported as follows. For the sake of performance comparison, the proposed controller is compared to three controllers: 1) the conventional PI controller, which is designed based on the simplified dynamics in equation (2-21). 2) PI-lead controller without feed-forward control of external

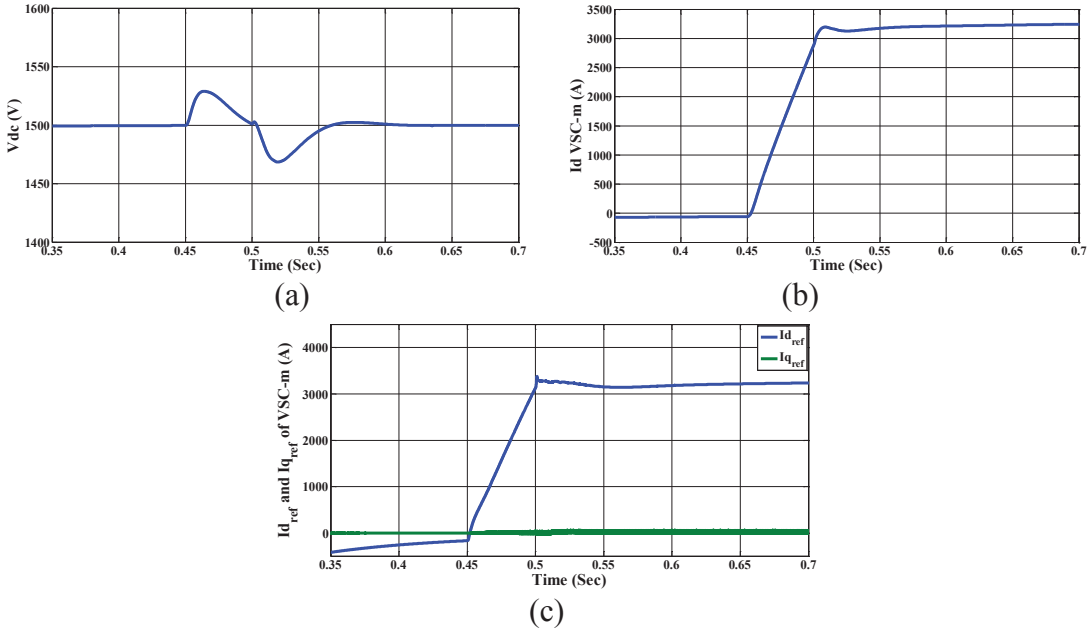

Fig. 2.8. Event I with the proposed controller: (a) DC-link voltage at VSC-*m*, b) *d* component of the VSC-*m* current, (c) *dq* reference current components of the VSC-*m*.

power P_{ext}; the controller is designed based on the accurate model in (2-20) at the worst case operating point, i.e., full power at rectification mode. The lead part is designed to compensate for the phase reduction due to the RHP in the rectification mode at the worst operating point. 3) The aforementioned PI-lead controller is designed with feed-forward control of P_{ext}, as shown in Fig. 2.2(a), to enhance the disturbance rejection performance of the controller, which demands measurement of P_{ext}. Both PI and PI-lead controllers are designed to yield a bandwidth of 200rad/s and phase margin of 50^o. Using nominal system parameters in Section 2.6, the PI and PI-lead controllers are given by

$K_{pi}(s)$=-0.0028-0.4839/s, and $K_{pi\text{-}lead}(s)$=-2.632((s+19)/(s^2+2077s)).

The simulated events are as follows.

1) Event I: At t=0.45 s, the rated active power, 2.5 MW at unity power factor, is absorbed from Zone II and injected to Zone I. VSC-*m* is operating in the inversion mode at the rated power. Fig. 2.8 shows the control performance in this case with the proposed controller. Fig. 2.8(a) shows the dc-link voltage. The maximum over/under-shoot voltage is less than 30 V (2%) with a recovery time of 0.1 s. Fig. 2.8(b) shows the *d*-component of the line current of VSC-*m*, whereas Fig. 2.8(c) shows the reference *dq* current components. The proposed controller

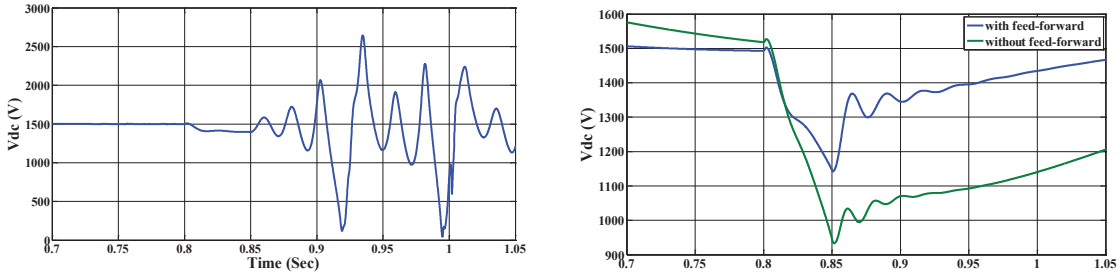

(a) (b)

Fig. 2.9. Event II: DC-link voltage control with (a) PI and (b) PI-lead controllers.

quickly and accurately generates the *d*-component of the reference current to reject the power disturbance and minimize its impact on the dc-link voltage without any feed-forward control of external power disturbances.

2) Event II: At t=0.8 s, the rated active power, 2.5 MW at unity power factor, is absorbed from Zone I and is pumped to Zone II. VSC-*m* is operating as rectifier at rated power, which is the worst case scenario from stability point of view. Fig. 2.9(a) shows the dc-link voltage control performance with the PI controller. The system becomes unstable, at t=0.8s, when VSC-*m* operates as a rectifier at rated power due to the effect of the un-modeled dynamics. To overcome this stability issue, the PI-lead controller is adopted. Fig. 2.9(b) shows the control performance of the PI-lead controller with and without feed-forward control of P_{ext} when VSC-*m* operates as a rectifier at rated power at t=0.8s. It can be seen that stable performance is yielded; however, the robustness in terms of disturbance rejection is weak yielding to large voltage dips around 500 V when feed-forward control is disabled and around 300 V with feed-forward control. Further, the voltage recovery dynamics is oscillatory in both cases with a recovery time around 0.2s. Fig. 2.10 shows the performance of the proposed controller under the same event. In this harsh power reversal scenario, the operating point is dynamically changed from I_{d0}=+3000 A to I_{d0}=-3000 A. In spite of this large-signal power disturbance, the proposed controller yields over/under-shoot voltage that is less than 50V (3.3%) with a recovery time of 0.1s as shown in Fig. 2.10(a). Significant performance improvement can be obtained as compared to the PI and PI-lead controllers even with P_{ext} feed-forward control.

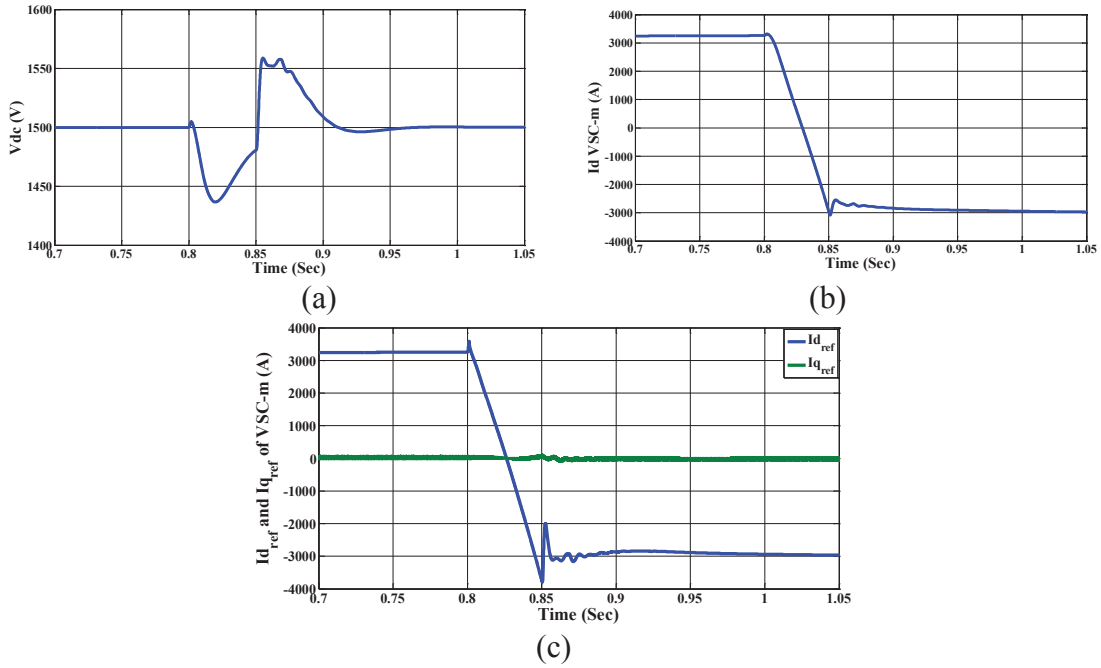

Fig. 2.10. Event II with the proposed controller: (a) DC-link voltage at VSC-*m*, (b) *d*-component of the VSC-*m* current, (c) *dq* reference current components of the VSC-*m*.

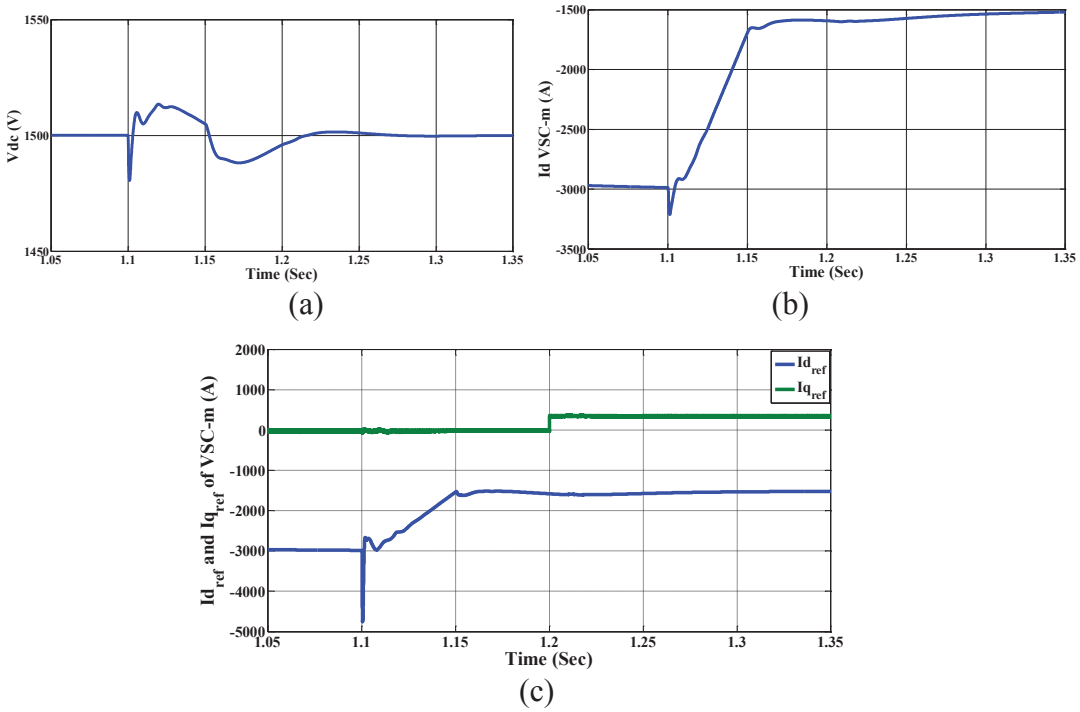

Fig. 2.11. Event III with the proposed controller: (a) DC-link voltage at VSC-*m*, (b) *d* component of the VSC-*m* current, (c) *dq* reference current components of the VSC-*m*.

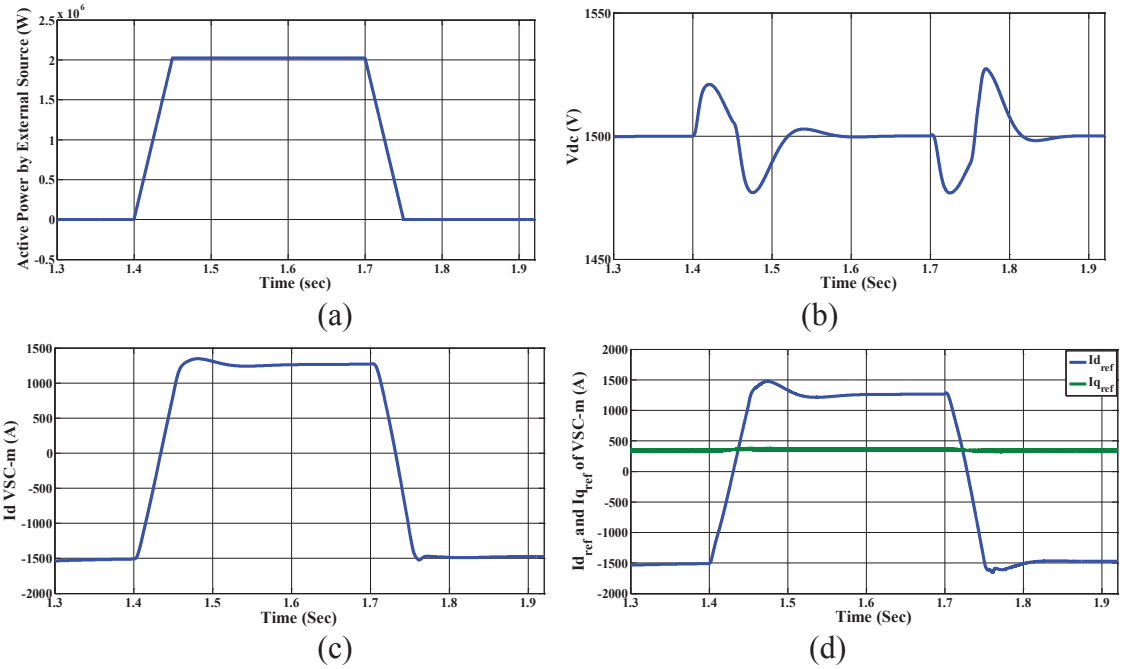

Fig. 2.12. Event IV with the proposed controller: (a) External source power. (b) DC-link voltage at VSC-*m*, (c) *d* component of the VSC-*m* current, (d) *dq* reference current components of the VSC-*m*.

3) Event III: At t=1.1 s, the active power absorbed from Zone I and pumped to Zone II is decreased from 2.5 MW to 1.25 MW, whereas the reactive power command is increased from 0 to 0.25 Mvar injected to grid 1 at t=1.2 s. Again, VSC-*m* is operating in the rectifier mode. Fig. 2.11 shows the control performance of the proposed controller in this case.
4) Event IV: At t=1.4 s, Zone III is connected to the dc-energy pool to pump 2 MW at unity power factor, then it is disconnected at t=1.7 s. Fig. 2.12 shows the control performance of the proposed controller in this case. Fig. 2.12(a) shows the power injected by Zone III. In spite of the large power disturbance and the uncertainty in the equivalent dc-link capacitor, "seen" by VSC-*m*, due to the connection of the wind-turbine VSC with local dc-link capacitor of 3000 μF, robust voltage control performance is yielded with over/under-shot voltage that is less than 25 V (1.67%) and recovery time around 0.1 s.
5) Event V: With the power levels as in event III, Zone IV is connected to the dc-energy pool using interlocked breaker #1 at t=1.95 s, then it is disconnected at t=2.85 s. Initially, the dc-micro-grid load is disconnected and the ESS is controlled in the boost mode to inject power

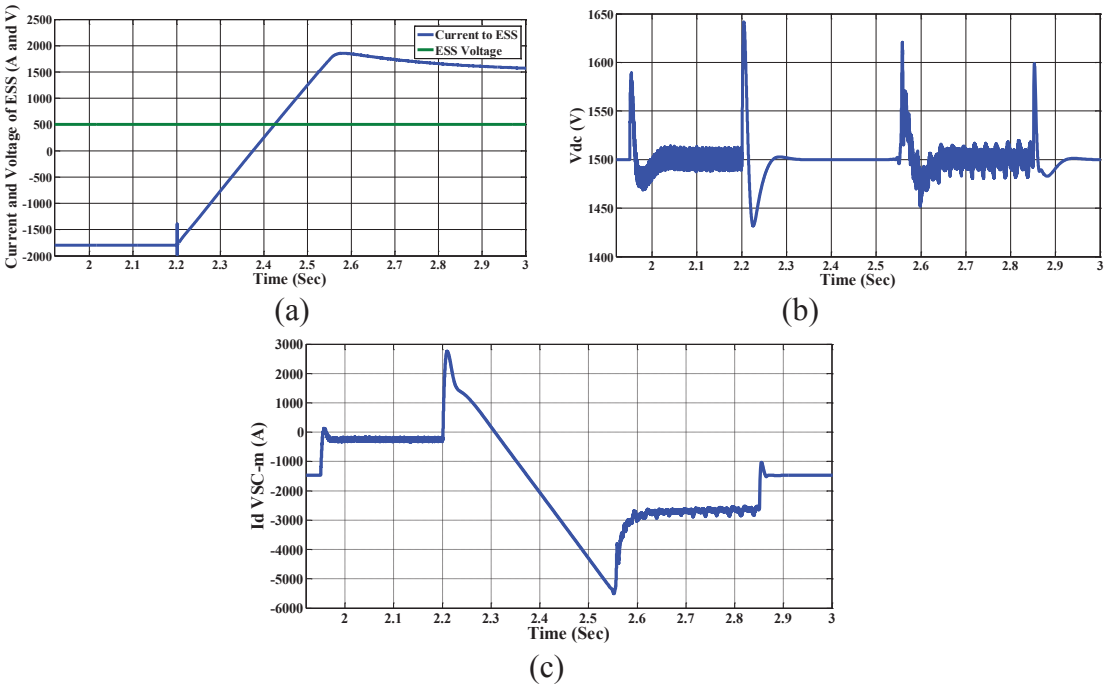

Fig. 2.13. Event V with the proposed controller: (a) DC-link voltage at VSC-*m*, (b) *d*-component of the VSC-*m* current, (c) *dq* reference current components of the VSC-*m*.

to the dc-energy pool by controlling the inductor current i_{L1} in Fig. 1 via a simple PI controller. Hence, I_d of VSC-*m* is increased from -1250 A to approximately -250 A. At t=2.2 s, the dc-micro-grid load is connected to the bi-directional dc/dc converter and the battery is disconnected to model a contingency event and test the robustness of the proposed controller under overload conditions. Accordingly, the dc/dc converter is commanded to suddenly change its control mode from boost to buck to transfer power from dc energy pool to the dc-micro-grid load. The power reversal time is approximately 0.35 s. At t=2.85 s, Zone IV is disconnected. Fig. 2.13(a) shows the output current of the dc/dc converter and the ESS voltage. Fig. 2.13(b) shows the dc-link voltage. In spite of the harsh transient conditions, which drift the operating point outside the rated power range, the maximum over/under-shoot voltage is 9.3% with recovery time 0.1 s.

Further, the proposed controller successfully ensures robust voltage control performance in the presence of dynamic interactions between the dc/dc converter and the dc-energy pool. Fig. 2.13(c) shows the corresponding *d*-component of the line current of VSC-*m*.

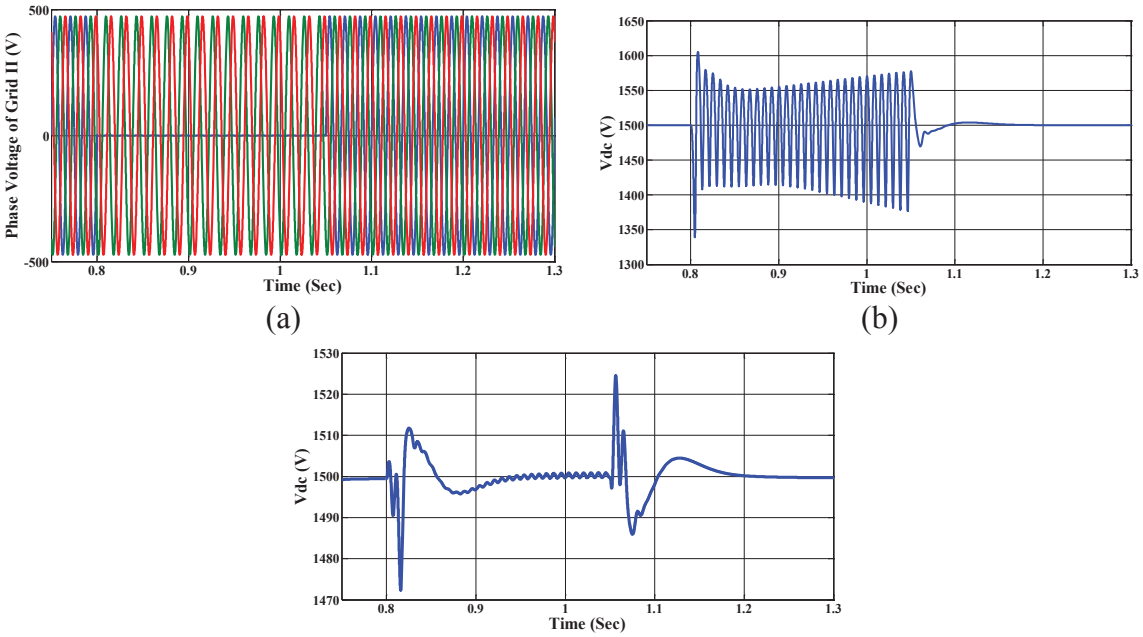

Fig. 2.14. Event VI with the proposed controller: (a) Grid 2 voltages, (b) DC-link voltage with positive sequence controller. (c) DC-link voltage with dual-sequence controller.

6) Event VI: With the power level as in event III, an asymmetric line-to-ground (LG) fault occurs in the grid II from t=0.8 s to t=1.05 s. Fig. 2.14(a) shows grid II voltages. Fig. 2.14(b) shows the dc-link voltage with only a positive-sequence voltage controller. As expected, 2nd harmonic voltage ripple appears due the unsymmetrical fault conditions. Fig. 2.14(c) shows the control performance with the dual-sequence controller. The voltage ripple can be effectively mitigated by controlling both the positive and negative sequence components of the VSC current. Further, the proposed controller robustly regulates the dc-link voltage even in the presence of large disturbances associated with fault conditions with maximum voltage rise/dip of less than 30 V (i.e., 2%) with a recovery time around 0.1 s.

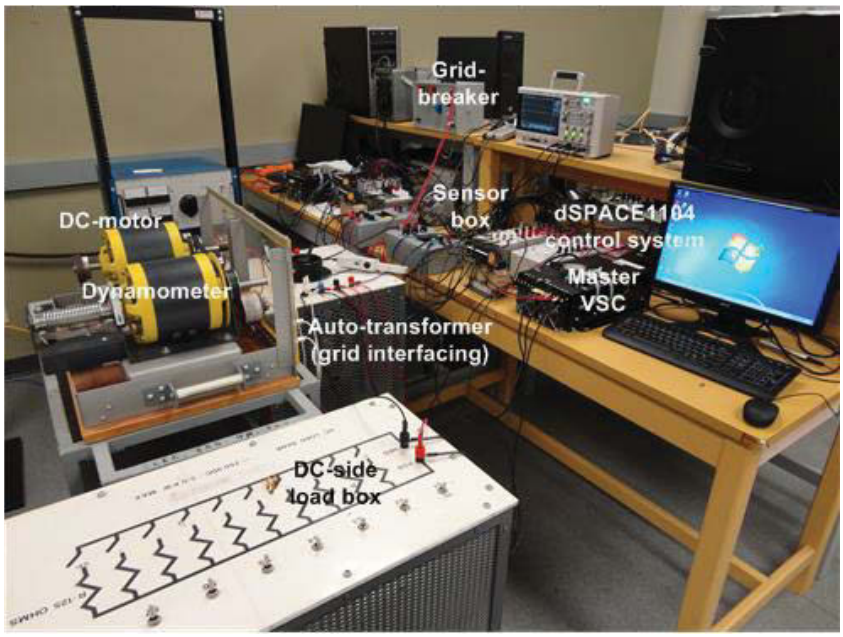

Fig. 2.15. A view of the experimental setup.

2.5 Experimental Results

For further evaluation of the proposed controller, an experimental test system, shown in Fig. 2.15, is employed.

The experimental system is composed of a grid-connected VSC, which operates as a dc-voltage power port (master VSC), and dc-side static and dynamic load modeling a dc micro-grid. The VSC is controlled in the rectification mode, which yields the worst operating conditions with respect to dc-link voltage stability. A Semistack intelligent power module, which includes gate drives, six insulated gate bipolar transistors (IGBTs), and protection circuit, is used to implement the master VSC. The switching frequency is 10 kHz, which indicates that the proposed compensator can be effectively implemented under high sampling frequency. The ac-side filter inductance and resistance are 1.2 mH and 0.06 Ω, respectively. The dc-link capacitance is 2.04 mF. The VSC is rated at 35 A, 208 V. However, at the rated conditions of this low-power VSC, the zero of the dc-link voltage dynamics is located at $-(V_{sd0}+2RI_{d0})/LI_{d0}$ = 2760 s^{-1}, which indicates that the non-minimum phase behavior in low-power converters is negligible. Therefore, operating the low-power VSC at rated conditions does not provide the exact operating-point dependent dc-link dynamics that appear in a typical high-power converter. To emulate the performance of a typical high-power VSC with ratings 580 V, 2500 A, 0.3 mH-

ac-filter inductor, equivalent filter and converter resistance R=10 mΩ and 2.04 mF dc-link capacitance, the laboratory scale converter is de-rated to 0.7 kW, 20 V, 20 A. At these new rated conditions, the rated non-minimum phase zero will be located at 381 s^{-1}, which is the same zero of the high power converter. Both converters will have the same pole due to the same dc-link capacitance. By such similarity study, the dynamic performance of the low-power VSC will be very similar to that of the high-power converter. The VSC inductor currents are measured by HASS-50-S current sensors whereas the voltages are measured by LEM-V-25-400 voltage sensors. The converter is interfaced to a dSPACE1104 control card via a CMOS/TTL interfacing circuit. The VSC current and dc-link controllers, *dq* orientation and the PWM generation are implemented on the dSPACE1104 control card supported with a TMS320F240-DSP coprocessor structure for PWM generation. The dSPACE1104 interfacing board is equipped with eight digital-to-analogue channels and eight analogue-to-digital channels to interface the measured signals to/from the control system. The software code is generated by the Real-Time-WorkShop under a Matlab/Simulink environment. The dc-side load is composed of a resistive load-box and a dynamic load, which can be used as effective mean to emulate a dc-micro-grid with both static and dynamic loads. The dynamic load is composed of a Lab-Volt® dc-motor loaded by a dynamometer.

The control performance of the proposed controller is compared to that of the conventional PI-lead controller with feed-forward control to enhance the disturbance rejection. The PI-lead controller is designed in the rectification mode and at the maximum converter current (20 A). The proposed controller is designed following the detailed procedure presented in Section 2.3. Key results are reported as follows. In all oscilloscope waveforms shown in Fig. 2.16-Fig. 2.21, the top trace (channel 3) shows the per-unit dc-link voltage, the middle trace (channel 2) shows one-phase ac-line current in A, whereas the bottom trace (channel 1) shows the per-unit I_d-current generated by the dc-link voltage controller.

Fig. 2.16 shows the control performance of the master VSC with PI-lead dc-link voltage controller in the rectification mode during the start-up of the dc micro-grid. As can be seen, during large and dynamic variation of the operating point of the converter, instability is yielded due to the large and fast drift in the operating point induced by the starting of the dynamic load. It should be noted that instability occurs even when the converter current is less than the rated current. This indicates that system instability can be yielded under fast and large changes of the

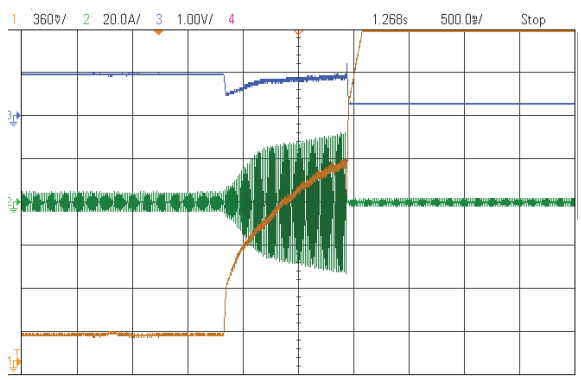

Fig. 2.16. Experimental results of the PI-lead controller during starting of the dc micro-grid load (dc motor load); Channel 3 (top): V_{dc} in per-unit Channel 2 (middle): one phase ac-line current; Channel 1 (bottom): I_d in per-unit generated by PI-lead controller.

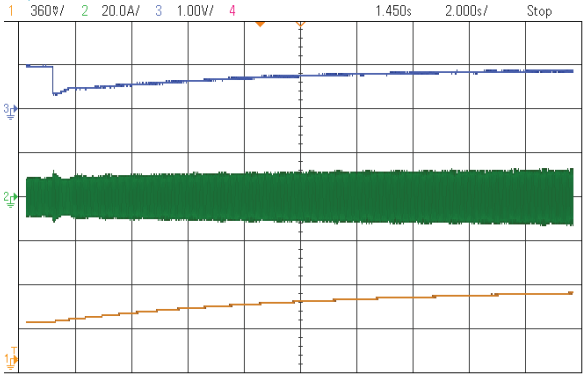

Fig. 2.17. Experimental results of the PI-lead controller with moderate changes of the dc micro-grid load (dc motor load); Channel 3 (top): V_{dc} in per-unit, Channel 2 (middle): one phase ac-line current; Channel 1(bottom): I_d in per-unit generated by PI-lead controller.

operating point even if the PI-lead controller is designed at the rated current. The phenomenon is attributed to the nonlinearity of the dc-link voltage dynamics (i.e., the system does not exhibit small-signal dynamics that can be stabilized by a simple PI-lead controller). The dc-link voltage collapses and the converter is tripped due to control system instability. Fig. 2.17 shows the control performance with the PI-lead controller when the load current is changing moderately, in terms of magnitude and ramp rate by controlling the dynamometer load. As the PI-lead controller is designed with a lead-filter, stable control performance is yielded even at the rated load current and when the load is increasing gradually. However, the disturbance rejection performance in terms of the voltage dip and recovery time is weak. To test the robustness of the PI-lead controller against variation in the effective dc-link capacitance, the effective dc-link capacitance is doubled.

Fig. 2.18 shows the control performance under this parametric uncertainty condition and with the PI-lead controller. As predicted by the theoretical analysis in Fig. 6, the conventional PI-lead controller cannot preserve system stability under parametric uncertainty. The dc-link voltage oscillations are in the range of 40rad/s, which is in-line with the theoretical analysis in Fig. 6(b). The results in Fig. 2.16 and Fig. 2.18 show that the conventional PI-lead controller cannot guarantee system stability under wide-range of operating point variation and parametric uncertainty in the effective dc-link capacitance.

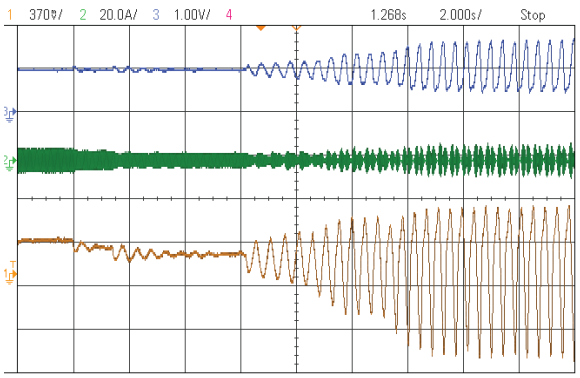

Fig. 2.18. Experimental results of the PI-lead controller with uncertainty in the dc-link capacitance; Channel 3 (top): Vdc in per-unit, Channel 2 (middle): one phase ac-line current; Channel 1(bottom): I_d in per-unit generated by PI-lead controller.

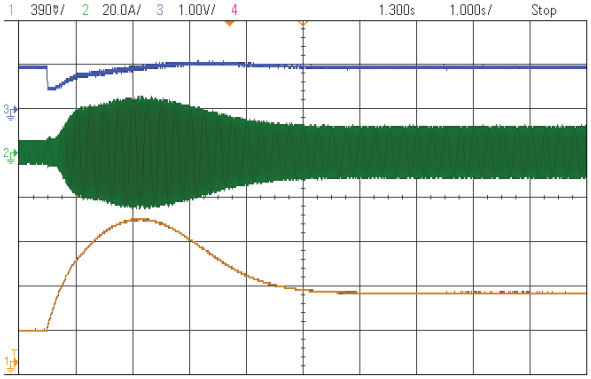

Fig. 2.19. Experimental results of the proposed controller during starting of the dc micro-grid load (dc motor load); Channel 3 (top): V_{dc} in per-unit, Channel 2 (middle): one phase ac-line current; Channel 1(bottom): I_d in per-unit generated by proposed controller.

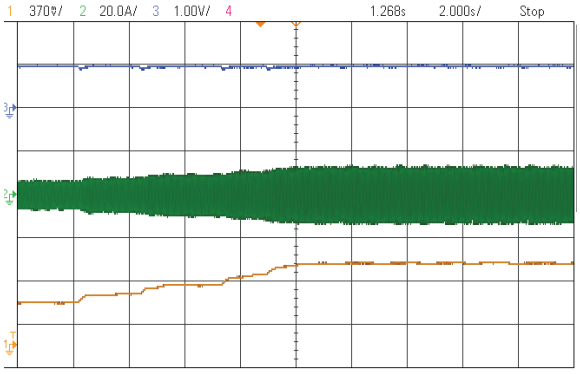

Fig. 2.20. Experimental results of the proposed controller with uncertainty in the dc-link capacitance and operating point variation; Channel 3 (top): V_{dc} in per-unit, Channel 2 (middle): one phase ac-line current; Channel 1(bottom): I_d in per-unit generated by proposed controller.

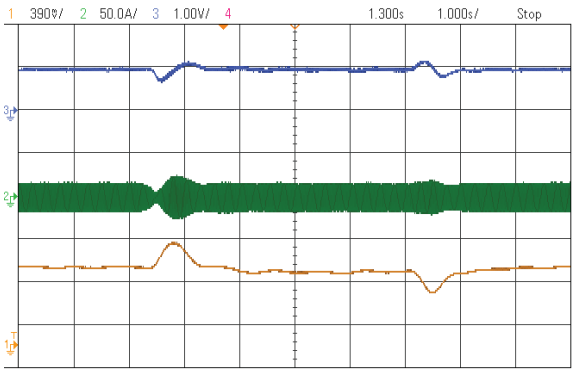

Fig. 2.21. Experimental results of the proposed controller with variation in reactive-current reference (-1.0pu to 1.0pu to -1.0 pu); Channel 3 (top): V_{dc} in per-unit, Channel 2 (middle): one phase ac-line current; Channel 1(bottom): I_d in per-unit generated by proposed controller.

Fig. 2.19 shows the control performance of the master VSC with the proposed dc-link voltage controller in the rectification mode during the start-up of the dc micro-grid. In spite of the dynamic and large variation in the dc micro-grid load current (motor starting current), the proposed controller offers robust stability against operating point variation and preserves the

stability of the dc-link voltage. As compared to the PI-lead controller [Fig. 2.16], the proposed controller remarkably contributes to the network stability under the occurrence of dynamic and large changes in the operating point. Further, a robust control performance is yielded where the voltage dip and recovery times are remarkably smaller than the corresponding values obtained with the PI-lead controller [see Fig. 2.18]. It should be noted that the proposed controller does not use any feed-forward control of the external power disturbance. To test the robustness of the proposed controller against parametric uncertainty in the equivalent dc-link capacitance, the effective dc-link capacitance is doubled. Fig. 2.20 shows the control performance of the proposed controller under such parametric uncertainty. The system is excited by successive increase of the dc-side load. Due to the proposed robust pole placement design, the proposed controller shows robust control performance. Fig. 2.21 shows the control performance of the proposed controller during variation in the reactive power setting. The reactive current command is changed from -1.0 pu to +1.0 pu and then to -1.0 pu again. Due to uncertainty in the effective ac-side inductance and the finite bandwidth of the current controller, coupling between active and reactive power exists. Power coupling can be reduced by using deadbeat inner current control loop and robust decoupling scheme [90], [91]. The proposed controller, however, provides close regulation of the dc-link voltage during the disturbances associated with active-reactive power coupling.

2.6 Parameters of Simulated System in Fig. 2.7

Zone I, II, III: VSC-*m*, VSC-W, and VSC-PQ: Rated Power=2.5 MVA, Grid 1, Grid 2 Voltage=580 V at 60 Hz; R_p=250 Ω; R=3.5 mΩ; L=300 μH; C=2×C_{eq}=25,000 μF, C_W=6000 μF, Switch resistance=1.0 mΩ; Diode resistance=1.0 mΩ; Current controller K_p=0.06 Ω ; K_i=0.7 Ω/s.; Zone IV: Power rating =1 MW, ESS and load voltage 500 V-dc, C_L=1000 μF, C_H=6000 μF, L_1=100 mH, R_{DC}=0.3214 Ω, K_p(mode1)=0.4, K_i(mode1)=4×10^{-4}, K_p(mode2)=0.0133, K_i(mode2)=0.0533, V_{L_Ref}=500 V, i_{L_Ref}=1800 A. DC-pool: Rated voltage=1,500 V, dc-cable length=20 km, R_{cable}=0.82 mΩ/km, C_{cable}= 0.014 μF/km, L_{cable}=0.98 μH/km

2.7 Conclusion

A robust controller with a simple fixed-parameter low-order structure has been proposed for the master VSC in an MTDC grid. The salient features of the proposed controller are 1) robust disturbance rejection performance under wide range of large and fast dynamic changes in the converter operating points and large-signal disturbances (e.g., power reversal at rated and over-load (contingency) conditions; low-impedance unsymmetrical fault conditions; and connection/disconnection of loads/sources in the dc grid); 2) the controller eliminates the need of using external power disturbance feed-forward control, which improves the reliability and cost measures by creating a dc-power (or dc-current) sensor-less robust disturbance rejection controller; 3) robust control performance under possible variation in the equivalent dc-link capacitance due to connection/disconnection of dc loads and/or sources in the dc grid; and 4) simple fixed-parameter low-order linear control structure with robust performance in spite of the highly nonlinear dc-link voltage control dynamics. With these features, the proposed controller remarkably contributes to the stability and reliability of multiterminal ac/dc networks. A theoretical analysis and comparative simulation and experimental results have shown the robustness and effectiveness of the proposed controller.

Chapter 3

Dynamics and Robust Control of the Master VSC in Multiterminal DC Grids Considering the Instantaneous Power of DC- and AC-side Filters and DC Grid Uncertainty

3.1 Introduction

Motivated by the difficulties mentioned in Section 1.3.2, this chapter presents a detailed small-signal model of a grid-connected VSC considering the impact of the instantaneous power of both ac and dc filters on the dc-link voltage dynamics. A sensitivity study is conducted to gauge the impact of parametric uncertainty associated with energy storage components and operating point variation on the dc-link voltage dynamics. To ensure robust dc-link voltage control performance, a robust controller is synthesized considering possible uncertainties in the dc filter components. Furthermore, the controller is synthesized to yield robust performance and stability against EtoE maneuver resulting from operating point variation [63]-[64]. The controller is optimally synthesized using the μ-synthesis approach employing the *DK*-iteration algorithm owing to the fact that external active and reactive powers affect the dc-link voltage dynamics as exogenous disturbances. Therefore, by minimizing the H_∞ norm from exogenous disturbance to the output, which is the dc-link voltage, optimal disturbance rejection is achieved in the proposed controller. A theoretical analysis, comparative simulation studies, and experimental results are presented to show the effectiveness of the proposed control structure.

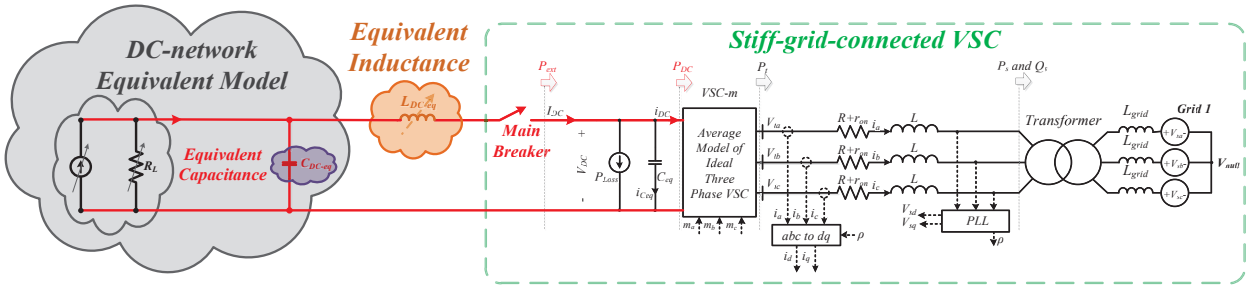

Fig. 3.1. DC voltage power port connected to a stiff ac grid with dc-side inductance.

3.2 Modeling of Grid-Connected VSC with DC LC-Filter

A typical 2.5 MW, 580 V_{ac}, 1500 V_{dc}, 60 Hz grid-connected VSC for dc grid applications with uncertain dc inductor and ac-side inductive filter is shown in Fig. 3.1. The system parameters are given in Section 3.7. In Fig. 3.1, $L_{DC\text{-}eq}$ and C_{eq} are the equivalent inductance and capacitance, respectively, reflected to the dc side of the grid-connected VSC, and R_{res} is the filter damping resistor to suppress possible resonance in the *LC*-dc filter. Both $L_{DC\text{-}eq}$ and C_{eq} are subjected to uncertainty in their nominal values, which is a practical assumption owing to the uncertainty associated with the operation of the dc grid and the connection and disconnection of dc generators and loads with their front-end converters and filters, which affect the equivalent values of $L_{DC\text{-}eq}$ and C_{eq}. An *L*-based ac filter with equivalent inductance *L* (representing the summation of filter and transformer leakage) and equivalent resistance *R*, which is commonly used in high-power converters, is adopted. Furthermore, if high-order ac-side filters are adopted—e.g., *LC* or *LCL* filter—it has been found that their impact on the dc-link voltage dynamics is negligible owing to the frequency-scale separation between the *LCL* filter dynamics and dc-link voltage dynamics. In other words, the bandwidth of the dc-link voltage control loop is usually less than the fundamental frequency (in the range of 20 Hz to 50 Hz); in this range, the ac-side filter behaves mainly as an *L* filter [92]. Therefore, the use of an *L* filter in this analysis is not a restricting assumption. The internal losses of the VSC are modeled by equivalent resistance r_{on} on the ac side and a current source on the dc side to model the power loss P_{loss} due to the reverse recovery and tailing current processes of the power switches. The dc grid is modeled by 1) a variable current source representing external power P_{ext} that can be delivered or absorbed from the dc grid by dc generators and/or converter-based loads with regulated output power (i.e., active loads), and 2) an equivalent resistance R_{Load} representing equivalent passive loads in the dc

grid. It should be noted that it is extremely difficult and impractical to design the converter control system based on the overall exact system dynamics, which contain both the dc and ac grid dynamics. Therefore, the equivalent models of both grids (i.e., a Thevenin's equivalent circuit model of the ac grids and Norton's equivalent circuit of the dc grid) are usually assumed during the analysis and control design stages [63]. A standard grid-oriented vector control scheme is adopted in this study owing to its widespread acceptance in the power converter industry. In this scheme, two proportional-integral (PI) current controllers (inner controllers) and an outer dc-link voltage controller are adopted. The dc-link voltage controller generates the *d*-axis reference current component whereas the q-axis reference current component is set to zero to yield unit power factor operation. A standard *dq*-based three-phase phase-locked loop (PLL) is adopted to extract the synchronization angle (ρ).

According to Fig. 3.1, an accurate model of the dc-link dynamics can be obtained when the total instantaneous power in the storage devices—i.e., $L_{DC\text{-}eq}$ and C_{eq}—is considered. The power balance across the dc-link capacitor can be given by

$$P_{ext} - P_{loss} - \frac{V_{DC}^2}{R_L} - D(0.5L_{DC-eq}I_{DC}^2) - D(0.5C_{eq}V_{DC}^2) = P_{DC} = P_t \tag{3-1}$$

where V_{DC} is the dc-link voltage, I_{DC} is the current flowing into dc inductor, C_{eq} is the equivalent dc-link capacitance seen from the grid-connected VSC's dc side, which includes the main dc-link capacitance and the paralleled filter capacitance, hence $C_{eq}= C_{DC\text{-}eq}+C$, $L_{DC\text{-}eq}$ is the equivalent inductance of the dc-inductor which may vary from the nominal value due to uncertainties, P_{ext} is the external power injected to the dc side, P_{loss} is the power losses in the converter circuit, R_L is the equivalent static resistance reflected at the VSC's dc-side, P_{DC} is the net power as shown in Fig. 1, which is equal to the VSC ac-side terminal power, P_t, and D is the time-derivative operator, i.e., $Dx=d(x)/dt$. It should be noted that P_t is not the same as the power injected into the grid, i.e., P_s, due the presence of the ac-side filter.

In (3-1), V_{DC} is considered as the controlled output, whereas P_{DC} or P_t can be regarded as the input to this dynamic model. Therefore, the term I_{DC} should be expressed based on the output, i.e., either V_{DC} of V^2_{DC}, and input signal, P_{DC}. Using Kirchhoff's current law (KCL), based I_{dc} can be given by

$$\left.\begin{aligned} I_{DC} &= i_{Ceq} + i_{DC} \\ i_{Ceq} &= C_{eq}DV_{DC} \end{aligned}\right\} \Rightarrow DI_{DC} = C_{eq}D^2V_{DC} + Di_{DC} \tag{3-2}$$

where i_{Ceq} is the current flowing into the dc filter's capacitor, i_{DC} is the injected current into the VSC's dc side after the equivalent capacitor C_{eq}, and D^2 stands for second derivative over time, i.e., $D^2x = d^2x/dt^2$.

Using (3-2) in (3-1), the instantaneous power in $L_{DC\text{-}eq}$ can be given by

$$\begin{aligned} 0.5L_{DC}DI_{DC}^2 = {} & L_{DC-eq}C_{eq}^2 DV_{DC}D^2V_{DC} + L_{DC-eq}C_{eq}Di_{DC}DV_{DC} \\ & + L_{DC-eq}C_{eq}i_{DC}D^2V_{DC} + L_{DC-eq}i_{DC}Di_{DC} \end{aligned} \tag{3-3}$$

where i_{DC} can be expressed based P_{DC} and V_{DC} as $i_{DC}=P_{DC}/V_{DC}$. Consequently,

$$Di_{DC} = \frac{V_{DC}DP_{DC} - P_{DC}DV_{DC}}{V_{DC}^2} \tag{3-4}$$

Now, let $x_1=V_{DC}$ and $x_2=DV_{DC}$, and using (3-1), (3-3), (3-4), the following power balance equation can be obtained:

$$\begin{aligned} & P_{ext} - P_{loss} - \frac{x_1^2}{R_L} - L_{DC-eq}C_{eq}^2 x_2 Dx_2 - L_{DC-eq}C_{eq}\frac{x_2}{x_1}x_2 DP_{DC} \\ & + L_{DC-eq}C_{eq}\frac{x_2^2}{x_1^2}P_{DC} - L_{DC-eq}C_{eq}\frac{P_{DC}}{x_1}Dx_2 - L_{DC-eq}\frac{P_{DC}}{x_1^2}DP_{DC} + L_{DC-eq}\frac{x_2}{x_1^3}P_{DC}^2 \\ & - C_{eq}x_1x_2 - P_{DC} = F(x_1, x_2, Dx_2, P_{DC}, DP_{DC}, P_{ext}, P_{loss}) = 0 \end{aligned} \tag{3-5}$$

The nonlinear dynamics in (3-5) can be linearized using Taylor series expansion on the dynamic function F around one equilibrium point (EP) as given by (3-6).

$$\begin{aligned} & F(x_1, x_2, Dx_2, P_{DC}, DP_{DC}, P_{ext}, P_{loss}) = \\ & F|_{(E.P.)} + \frac{\partial F}{\partial P_{ext}}|_{(E.P.)}\tilde{P}_{ext} + \frac{\partial F}{\partial P_{loss}}|_{(E.P.)}\tilde{P}_{loss} \\ & + \frac{\partial F}{\partial x_1}|_{(E.P.)}\tilde{x}_1 + \frac{\partial F}{\partial x_2}|_{(E.P.)}\tilde{x}_2 + \frac{\partial F}{\partial (Dx_2)}|_{(E.P.)}\tilde{Dx}_2 \\ & + \frac{\partial F}{\partial P_{DC}}|_{(E.P.)}\tilde{P}_{DC} + \frac{\partial F}{\partial (DP_{DC})}|_{(E.P.)}\tilde{DP}_{DC} + (HOT) \end{aligned} \tag{3-6}$$

where ~ expresses the perturbed signal around their EP, and high order terms (HOT) are ignored in order to linearize (3-5).

Furthermore, the EP can be expressed by (3-7) considering that all variables are static at the equilibrium state.

$$\begin{aligned} EP &= (x_{1-0}, x_{2-0}, Dx_{2-0}P_{DC-0}, DP_{DC-0}, P_{ext-0}, P_{loss-0}) \\ &= (V_{DC-nominnal}, 0, 0, P_{DC-0}, 0, P_{ext-0}, P_{loss-0}) \end{aligned} \tag{3-7}$$

where subscript "0" denotes the value of the variable at the EP

After mathematical manipulation, the linearized small-signal dynamics of (3-5) can be given by

$$\tilde{P}_{ext} - \tilde{P}_{loss} - \tilde{P}_{DC} - L_{DC-eq}C_{eq}\frac{P_{DC-0}}{V_{DC-nominnal}}\tilde{D}x_2 - L_{DC-eq}\frac{P_{DC-0}}{V^2_{DC-nominnal}}\tilde{D}P_{DC}$$
$$+L_{DC-eq}\frac{P^2_{DC-0}}{V^3_{DC-nominnal}}\tilde{x}_2 - C_{eq}V_{DC-nominnal}\dot{\tilde{x}}_2 - \frac{2V_{DC-nominnal}}{R_p}\tilde{x}_1 = 0 \quad (3\text{-}8)$$

Equation (3-8) reveals that it is a must to find the relation between P_{DC} and the main control input (lever) I_d, i.e., the *d*-component of the ac current injected or absorbed from the ac grid, in order to reach a linear time-invariant (LTI) model describing the relation between the output V_{DC} and the control input I_d. Similar process should be applied to $D\widetilde{P_{DC}}$ as shown in (3-8) . In this regard, considering the total power balance on the ac side is essential to account for the effect of the instantaneous power of the ac-side filter as well. Equation (3-9) describes this power balance:

$$P_{DC} = P_t = P_{loss\_R} + P_{filter\_L} + P_s \quad (3\text{-}9)$$

where, P_{loss_R} is total instantaneous power losses in the equivalent resistance of the inductor L, P_{loss_L} is the total instantaneous power of the ac-side inductor L, and P_s is total instantaneous power, which have to be absorbed/injected from/to the point of common coupling (PCC) in order to stabilize the dc-link voltage constant.

Owing to the fact that a standard vector-current-controlled-based VSC is employed as the actuator of active and reactive powers at the PCC, all equations should be expressed based on current components in the synchronous *dq*-frame, which is the most common framework for analysis and control of power converters [36]. Hence, all terms of (3-2) should be expressed based on *dq*-components of the current space vector $\vec{I}$, which has active and reactive components I_d and I_q. To start this conversion process, the total instantaneous power absorbed by a three-wire three-phase network can be expressed by

$$P_{3-wire\ 3-phase\ network} = Re\{1.5\vec{v}(t)\vec{i}^{*}(t)\} \quad (3\text{-}10)$$

where $\vec{v}$ and $\vec{\imath}$ and represent the space vectors of the applied voltage and feeding current into the three-wire three-phase network. Using (3-10), the following equations can be reached for all terms of (3-9).

$$\begin{aligned} P_{loss\_R} &= Re\{1.5\vec{v}_R(t)\vec{i}_R^*(t)\} = Re\{1.5R\vec{I}(t)\vec{I}^*(t)\} \\ &= 1.5R\left|I\right|^2 = 1.5R((I_d)^2 + (I_q)^2) \end{aligned} \tag{3-11}$$

where (I_d, I_q) are the *dq* components of the VSC output current, and R is the equivalent filter resistance.

The total stored energy in the three-phase inductor L is expressed by

$$W_L = 0.5L(i_a^2 + i_b^2 + i_c^2) \tag{3-12}$$

where i_a, i_b, and i_c are three-phase current injected into three-phase inductor L; they are assumed to be in the form of (3-13) at one general operating point:

$$\begin{cases} i_a^2 = I^2\cos^2(\omega t - \varphi_i) \\ i_b^2 = I^2\cos^2(\omega t - \varphi_i - \dfrac{2\pi}{3}) \Rightarrow i_a^2 + i_b^2 + i_c^2 = 1.5I^2 \\ i_c^2 = I^2\cos^2(\omega t - \varphi_i - \dfrac{4\pi}{3}) \end{cases} \tag{3-13}$$

where I and φ are the amplitude and phase of the space vector $\vec{I}$, respectively. Consequently, (3-14) is reached for the instantaneous power of three-phase inductor L.

$$P_{filter\_L} = 0.75LD((I_d)^2 + (I_q)^2) \tag{3-14}$$

Under unity power factor operation (i.e., I_q=0) and/or perfect synchronization (i.e., V_q=0), P_s can be given by

$$P_s = 1.5I_dV_{d_s} \tag{3-15}$$

where V_{ds} is the *d*-component of the voltage space vector at the PCC.

Using (3-9)-(3-15), the relation between P_{DC}, I_d, and other signals, which are treated as disturbances can be given by

$$\begin{aligned} &P_{DC} - 0.75LD(I_d)^2 - 1.5R(I_d)^2 - 1.5I_dV_{d_s} - 0.75LD(I_q)^2 - 1.5R(I_q)^2 \\ &= G(I_d, DI_d, I_q, DI_q) = 0 \end{aligned} \tag{3-16}$$

Consequently, (3-16) can be used in (3-8) to find perturbed signal $\widetilde{P_{DC}}$. Again, because of the fact that (3-16) is a nonlinear equation, it is possible to employ Taylor series expansion on the dynamic function G around one EP as follows:

$$\begin{aligned} &G(I_d, DI_d, I_q, DI_q) = \\ &G|_{(E.P.)} + \frac{\partial G}{\partial I_d}|_{(E.P.)}\,\tilde{I}_d + \frac{\partial G}{\partial DI_d}|_{(E.P.)}\,\tilde{DI}_d \\ &+G|_{(E.P.)} + \frac{\partial G}{\partial I_d}|_{(E.P.)}\,\tilde{I}_q + \frac{\partial G}{\partial DI_q}|_{(E.P.)}\,\tilde{DI}_q + (HOT) \end{aligned} \tag{3-17}$$

The EP of (3-16) can be expressed by

$$\begin{aligned} (EP) &= (I_{d-0}, DI_{d-0}, I_{q-0}, DI_{q-0}) \\ &= (I_{d-0}, 0, I_{q-0}, 0) \end{aligned} \tag{3-18}$$

After mathematical manipulation, (3-19) can be reached. It should be noted that all terms related to $\tilde{I}_q$ and $\widetilde{DI_q}$ are lumped into the function $g(\tilde{I}_q, \widetilde{DI_q})$, as shown in (3-19), owing to the fact these signals are treated, in control terminology, as disturbance signals affecting the output signal. From the physical point of view, the dc-link energy, and hence the output V_{DC}, are mainly affected by active current component I_d:

$$\tilde{P}_{DC} = 1.5LI_{d-0}\tilde{DI}_d + 3RI_{d-0}\tilde{I}_d + 1.5V_{d_s}\tilde{I}_d + g(\tilde{I}_q, \tilde{DI}_q) \tag{3-19}$$

In addition to (3-19), $D\widetilde{P_{DC}}$ is also required to find the explicit transfer function between I_d and V_{DC} using (3-8). Using (3-16), DP_{DC} and its EP can be given by

$$\begin{aligned} &DP_{DC} - 1.5L(DI_d)^2 - 1.5LI_d D^2 I_d - 3RI_d DI_d - 1.5V_{d_s} DI_d \\ &-1.5L(DI_q)^2 - 1.5LI_d D^2 I_q - 3RI_d DI_q = \\ &H(I_d, DI_d, D^2 I_d, I_q, DI_q, D^2 I_q) = 0 \end{aligned} \tag{3-20}$$

$$\begin{aligned} (E.P.) &= (I_{d-0}, DI_{d-0}, D^2 I_{d-0}, I_{q-0}, DI_{q-0}, D^2 I_{q-0}) \\ &= (I_{d-0}, 0, 0, I_{q-0}, 0, 0) \end{aligned} \tag{3-21}$$

Using Taylor series expansion on the dynamic function H in (3-20), $D\widetilde{P_{DC}}$ can be given by

$$\begin{aligned} D\tilde{P}_{DC} &= 1.5LI_{d-0}D^2\tilde{I}_d + 3RI_{d-0}D\tilde{I}_d + 1.5V_{d_s}D\tilde{I}_d \\ &+ h(I_q, DI_q, D^2 I_q) \end{aligned} \tag{3-22}$$

Equations (3-8), (3-19), and (3-22) are combined to reach the final transfer function describing the relation between I_d and V_{DC} as (3-23).

$$\tilde{V}_{DC} = \frac{as^2+bs+e}{As^2+Bs+E}\tilde{I}_d - R\frac{Dist(\tilde{I}_q, s\tilde{I}_q.s^2\tilde{I}_q)}{As^2+Bs+E} - \frac{\tilde{P}_{loss}}{As^2+Bs+E} - \frac{\tilde{P}_{ext}}{As^2+Bs+E}$$

$$a \triangleq -1.5L_{DC-eq}L\frac{P_{DC-0}I_{d-0}}{V^2_{DC-nominnal}}$$

$$b \triangleq -L_{DC-eq}\frac{P_{DC-0}}{V^2_{DC-nominnal}}(3RI_{d-0}+1.5LI_{d-0}+1.5V_{sd})-1.5LI_{d-0}$$

$$e \triangleq -3RI_{d-0}-1.5V_{sd}$$

$$A \triangleq L_{DC-eq}C_{eq}\frac{P_{DC-0}}{V_{DC-nominnal}}$$

$$B \triangleq (C_{eq}V_{DC-nominnal} - L_{DC-eq}\frac{P^2_{DC-0}}{V^3_{DC-nominnal}})$$

$$E \triangleq (\frac{2}{R_L}V_{DC-nominnal}) \quad (3\text{-}23)$$

where *Dist* is a linear function of set $\{\tilde{I}_q, s\tilde{I}_q, s^2\tilde{I}_q\}$, and according to equations (3-9) to (3-15) , $P_{DC\text{-}0}$ equals to: $P_{DC-0} = 1.5(RI^2_{d-0} + RI^2_{q-0} + V_{sd}I_{d-0})$

Furthermore, from (3-16), $P_{DC\text{-}0}$ at EP can be obtained from the corresponding current components ($I_{d\text{-}0}$,$I_{q\text{-}0}$) as

$$P_{DC-0} = 1.5R(I_{d-0})^2 + 1.5I_{d-0}V_{d_s} + 1.5R(I_{q-0})^2 \quad (3\text{-}24)$$

Finally, (3-23) presents linearized LTI model of the dc-link dynamics considering the instantaneous power of all energy storage devices in a VSC with *LC* dc filter and *L* ac filter.

To complete the model, the current control dynamics need to be included. In vector-controlled VSCs, the current control is conducted in the *dq*-frame with feed-forward and decoupling terms. Therefore, the closed-loop current control dynamics can be represented by the following transfer function [63]:

$$TF_{current} = \frac{1}{T_i s + 1} \quad (3\text{-}25)$$

where T_i is the time-constant of the current controller.

Therefore, the overall transfer function between $\tilde{V}_{DC}$ and $\tilde{I}_d$ can be given by

$$\tilde{V}_{DC}(s)=\frac{as^2+bs+e}{As^2+Bs+E}\times\frac{1}{T_is+1}\tilde{I}_d(s)=\frac{as^2+bs+e}{AT_is^3+(BT_i+A)s^2+(ET_i+B)s+E}\tilde{I}_d(s) \tag{3-26}$$

For the sake of performance comparison, two additional small-signal models of the dc-link voltage dynamics are considered. The first model is a simplified and conventional one that completely ignores the impact of the instantaneous powers of the ac and dc filter components. In this case the dc-link voltage dynamics will be related to the control input by [63].

$$\tilde{V}^2_{DC}(s)=-1.5V_{sd}\frac{1}{0.5C_{eq}s}\times\frac{1}{T_is+1}\tilde{I}_d(s) \tag{3-27}$$

In this idealized case, the dc-link voltage dynamics model is independent of the converter operating point without any possible non-minimum phase behavior.

In the second case, the instantaneous power of the ac-filer is considered whereas the impact of the dc filter is completely ignored. In this case the dc-link voltage small-signal dynamics can be given by [30] and [63]-[64].

$$\tilde{V}^2_{DC}(s)=-1.5\frac{R_LLI_{d-0}s+R_L(V_{sd}+2RI_{d-0})}{0.5R_LC_{eq}s+1}\times\frac{1}{T_is+1}\tilde{I}_d(s) \tag{3-28}$$

It should be pointed out that the output is V^2_{DC} in (3-28) and it is V_{DC} in (3-29). For the sake of comparison of (3-28) with (3-26), ((3-29) can be derived from (3-28) to have the same output signal in both (3-29) and (3-26), i.e., V_{DC}. Then,

$$\tilde{V}_{DC}(s)=-1.5\frac{R_LLI_{d-0}s+R_L(V_{sd}+2RI_{d-0})}{R_LC_{eq}V_{DC-nominnal}s+2V_{DC-nominnal}}\times\frac{1}{T_is+1}\tilde{I}_d(s) \tag{3-29}$$

In either (3-28) or (3-29), it is clear that the magnitude of the linearized plant at an operating point is the same in both inversion and rectification modes at the same power; however, the phase is dramatically reduced at the same power in the rectification mode due to the right-hand-plane (RHP) zero, which is generated in the rectification mode and affects the overall system stability and performance if the controller is designed based on the idealized model. Because of the fact that (3-29) includes only the dynamics of the ac side's filter, (3-26) should converge to (3-29) if $L_{DC\text{-}eq}$ equals to zero. If $L_{DC\text{-}eq}$ equals to zero, (3-29) becomes a special case of (3-26) ; the values of a, b, e, A, B, and E are given in (3-30) for $L_{DC\text{-}eq}$=0.

$$a = 0$$
$$b = -1.5LI_{d-0}$$
$$e \triangleq -3RI_{d-0} - 1.5V_{sd}$$
$$A = 0 \qquad \text{then}$$
$$B = C_{eq}V_{DC-nominnal}$$
$$E = \frac{2}{R_L}V_{DC-nominnal}$$

$$\tilde{V}_{DC} = \frac{-1.5LI_{d-0}s - 1.5V_{sd} - 3RI_{d-0}}{C_{eq}V_{DC-nominnal}s + \frac{2}{R_L}V_{DC-nominnal}}\tilde{I}_d - Disturbance\ Signals \qquad (3\text{-}30)$$

Equation (3-26) shows that the dc-link voltage dynamics is remarkably different from the conventional simplified dc-link voltage dynamics (3-27) and when only the impact of the ac-filter is considered (3-28). Equation (3-26) reveals that considering $L_{DC\text{-}eq}$ adds additional zero and pole to the dynamics in (3-27); at different operating points and uncertainty in system parameters, the zero can lead to non-minimum phase dynamics whereas the pole can be unstable. Physically, the impact of $L_{DC\text{-}eq}$ cannot be simply reflected to the ac side of the converter as an equivalent ac-side inductance to simplify the modeling. Similarly, the ac-side inductance L cannot be reflected to the dc side of the converter as an equivalent dc-side inductance. Indeed, both inductances and capacitances interact via the energy conversion process across the converter. The impact of different system parameters on the dynamic characteristics of (3-26) is discussed in the following section.

3.3 Discussion about DC Side Dynamics of Grid-connected VSC

The impact of different parameters on the stability as well as performance of the dc-link voltage dynamics is investigated. This sensitivity study is important to identify the most critical system parameters and provide guidelines to design a robust dc-link voltage controller. The sensitivity study is conducting with respect to the dc-side filter parameters, $L_{DC\text{-}eq}$, C_{eq}, and the power level of active and static loads on the dc grid represented by (P_{ext} and R_L in Fig. 3.1, respectively).

3.3.1 Mathematical Analysis

Considering (3-26), one can mathematically analyze the location of the zeroes and poles of the

linearized transfer function around one specific operating point using the Routh–Hurwitz criterion. Accordingly, the impact of different operating points as well as parameter variation on the location of the zeroes and poles can be quantified. If T_i=0, the denominator of (3-26) becomes a second order polynomial, and the Routh–Hurwitz criterion is simplified as follows: if all coefficients *a*, *b*, and *e* have the same sign, then (3-26) does not has right-hand plane (RHP) zero. In addition, if all coefficients *A*, *B*, and *E* have the same sign, then (3-26) is stable.

1) Inversion Mode

Firstly, suppose that the converter is operating in the inversion mode. Consequently, both $P_{DC\text{-}0}$ and *A* are positive, and in order to have a stable transfer function in (3-26), *B* and *E* should be positive too. If positive values of R_L, (i.e., passive resistive dc-side load), *E* is always positive**.** Consequently, the value of *B* is important in the inversion mode; if (3-31.a) is satisfied, then (3-26) is stable in the inversion mode, and if (3-31.b) is satisfied, then (3-26) is unstable in the inversion mode.

$$L_{DC-eq} < C_{eq}\frac{V_{DC-nominnal}^4}{P_{DC-0}^2} \Rightarrow L_{DC-eq} < C_{eq}\frac{V_{DC-nominnal}^4}{(1.5(RI_{d-0}^2 + RI_{q-0}^2 + V_{sd}I_{d-0}))^2} \quad (3\text{-}31.a)$$

$$L_{DC-eq} > C_{eq}\frac{V_{DC-nominnal}^4}{P_{DC-0}^2} \Rightarrow L_{DC-eq} > C_{eq}\frac{V_{DC-nominnal}^4}{(1.5(RI_{d-0}^2 + RI_{q-0}^2 + V_{sd}I_{d-0}))^2} \quad (3\text{-}31.b)$$

Thus, since the maximum value of $P_{DC\text{-}0}$ is equal to the capacity of the converter ($VSC_{Capacity}$), (3-31) can be translated to (3-32) as a rule of thumb in the design procedure to the have a stable system in the inversion mode.

$$L_{DC-eq} < C_{eq}\frac{V_{DC-nominnal}^4}{VSC_{Capacity}^2} \quad (3\text{-}32.a)$$

⇒ VSC is always stable in the inversion mode

$$L_{DC-eq} > C_{eq}\frac{V_{DC-nominnal}^4}{VSC_{Capacity}^2} \quad (3\text{-}32.b)$$

⇒ VSC is always unstable in the inversion mode

About the location of zeroes, it is found out that the sign of a, b, and e are all negative because of the fact that the sign of both $P_{DC\text{-}0}$ and $I_{d\text{-}0}$ are the same provided that $RI^2_{q\text{-}0}$ is very

negligible as compared to $RI^2_{d\text{-}0}+ V_{sd}I_{d\text{-}0}$, which is the case in all industrial and practical VSCs to have as lowest as possible losses associated with series resistance of inductive filter. Consequently, there will be no RHP zero in the inversion mode.

2) Rectification Mode

Secondly, suppose that the converter is operating in the rectification mode. Consequently, $P_{DC\text{-}0}$ and A are negative, and in order to have a stable transfer function in (3-26), B and E should be negative too. Again, if R_L is positive, E is always positive and (3-26) is unstable. Consequently, the value of B is important in that scenario in the rectification mode; if (3-33.a) is satisfied, then (3-26) is stable in the rectification mode, and if (3-33.b) is satisfied, then (3-26) is unstable in the rectification mode.

$$L_{DC-eq} > C_{eq}\frac{V^4_{DC-nominnal}}{P^2_{DC-0}} \Rightarrow L_{DC-eq} > C_{eq}\frac{V^4_{DC-nominnal}}{(1.5(RI^2_{d-0}+RI^2_{q-0}+V_{sd}I_{d-0}))^2} \tag{3-33.a}$$

$$L_{DC-eq} < C_{eq}\frac{V^4_{DC-nominnal}}{P^2_{DC-0}} \Rightarrow L_{DC-eq} < C_{eq}\frac{V^4_{DC-nominnal}}{(1.5(RI^2_{d-0}+RI^2_{q-0}+V_{sd}I_{d-0}))^2} \tag{3-33.b}$$

Thus, since the maximum value of $P_{DC\text{-}0}$ is equal to the capacity of the converter, equations (3-33) can be translated to equations (3-34) as a rule of thumb in the design procedure to the have a stable system in the rectification mode and supplying dynamic fixed power loads.

$$L_{DC-eq} > C_{eq}\frac{V^4_{DC-nominnal}}{VSC^2_{Capacity}} \tag{3-34.a}$$

⇒ VSC is always stable in the rectification mode and supplying dynamic fixed power loads

$$L_{DC-eq} < C_{eq}\frac{V^4_{DC-nominnal}}{VSC^2_{Capacity}} \tag{3-34.b}$$

⇒ VSC is always unstable in the rectification mode and supplying dynamic fixed power loads

About the location of zeroes, it is found out that the sign of a is always negative because of the fact that the sign of both $P_{DC\text{-}0}$ and $I_{d\text{-}0}$ are the same as it is discussed before. Consequently, the sign of b and e should also be negative to prevent RHP zero in the rectification mode. Equations (3-35) express the conditions under which there will be no RHP zero in the rectification mode.

$$\begin{cases} L_{DC-eq} < \dfrac{1.5LI_{d-0}}{(3RI_{d-0}+1.5LI_{d-0}+1.5V_{sd})}\dfrac{V_{DC-nominnal}^2}{P_{DC-0}} \\ +3RI_{d-0}+1.5V_{sd}>0 \\ L_{DC-eq}>0 \Rightarrow 3RI_{d-0}+1.5LI_{d-0}+1.5V_{sd}>0 \\ P_{DC-0}<0 \text{ and } I_{d-0}<0 \end{cases} \Rightarrow \quad (3\text{-}35)$$

$$\begin{cases} L_{DC-eq} < \dfrac{1.5LI_{d-0}}{(3RI_{d-0}+1.5LI_{d-0}+1.5V_{sd})}\dfrac{V_{DC-nominnal}^2}{P_{DC-0}} \\ \dfrac{-1.5V_{sd}}{3R+1.5L} < I_{d-0} < 0 \end{cases}$$

3.3.2 The Threshold Point of Stability (Instability)

As equation (3-31) and equation (3-33) reveal, there in one threshold value of $L_{DC\text{-}eq}$ which makes the VSC stable/unstable depending on the VSC operating point, nominal value of V_{DC}, i.e., $V_{DC\text{-}nominal}$, and the value of C_{eq}, and for that specific threshold value, VSC is unstable either in rectification mode or inversion mode as equation (3-31) and equation (3-33) demonstrate. Fig. 3.2 shows the threshold value of $L_{DC\text{-}eq}$ at different values of the VSC power at the rated values of $V_{DC\text{-}nominal}$ and C_{eq}. A typical 2.5 MW, 580 V_{ac}, 1500 V_{dc}, 60 Hz grid-connected VSC with parameters given in Section 3.7 is used in the numerical analysis [30], [63]. It should be noted that $V_{DC\text{-}nominal}$ is changing from the possible minimum value, $2V_{sd}$, to 1500 V, to show the effect of different possible nominal values of V_{DC} on the stability of the VSC. The obtained expressions provide useful guidelines to find the stability-related ranges of the dc-side inductance, which can vary in a wide range owing to system uncertainties.

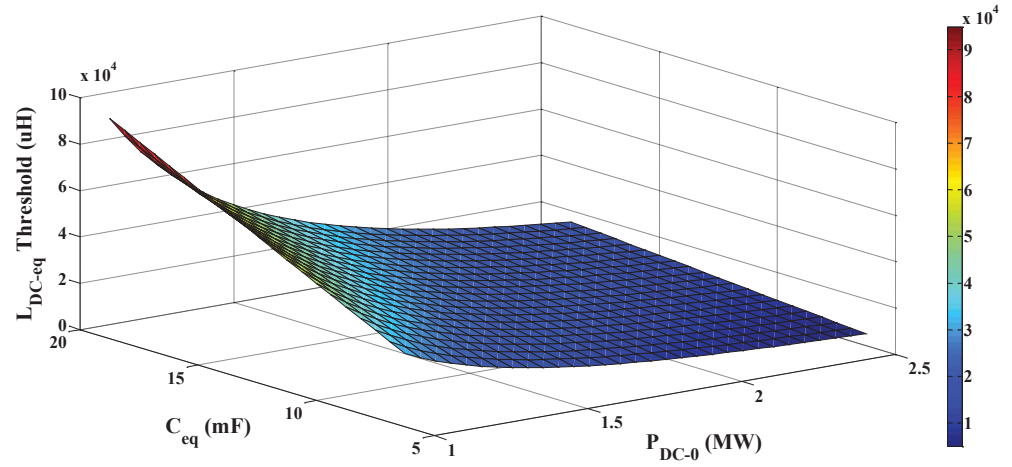

(a)

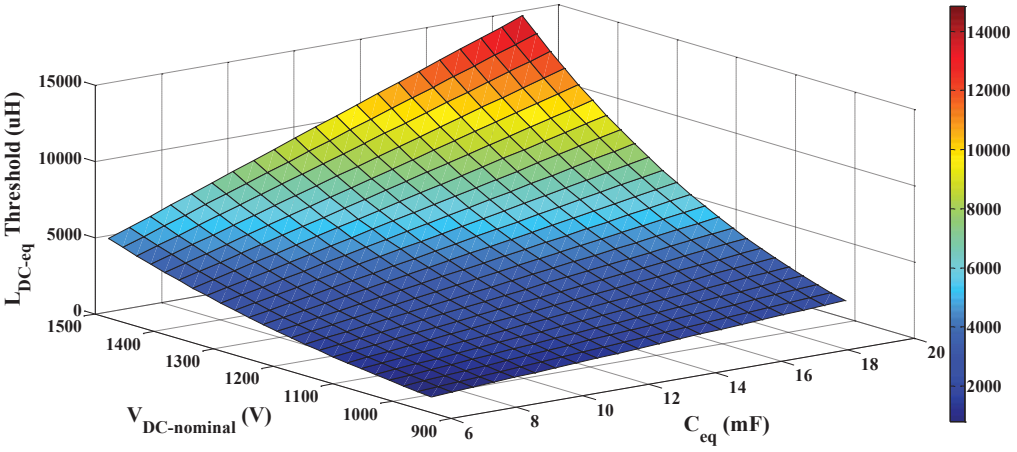

(b)

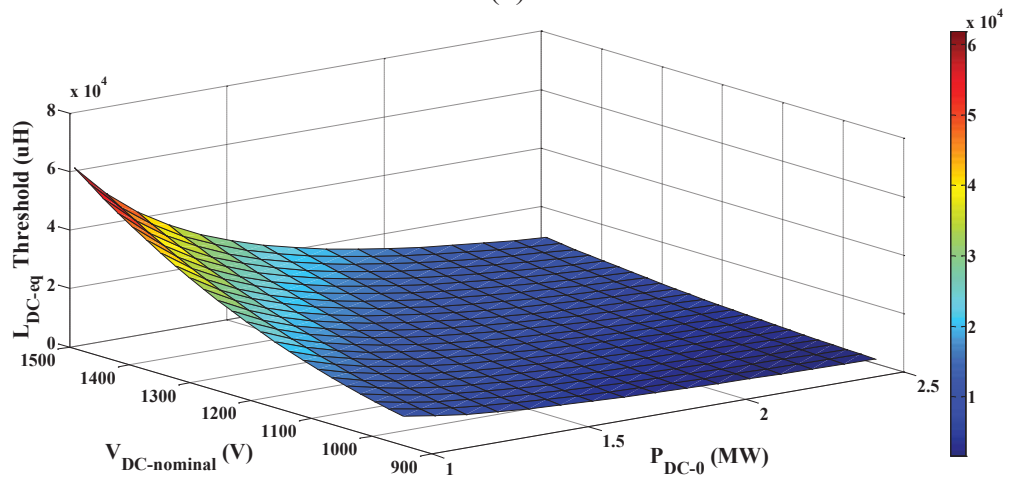

(c)

Fig. 3.2. The threshold value of $L_{DC\text{-}eq}$ for having stable/unstable transfer function (3-26) in inversion/rectification mode. As (3-31) and (3-33) shows, the 3D-plot is symmetrical for negative values of $P_{DC\text{-}0}$; the effect of (a) $P_{DC\text{-}0}$ and C_{eq} (b) $V_{DC\text{-}nominal}$ and C_{eq} (c) $V_{DC\text{-}nominal}$ and $P_{DC\text{-}0}$.

3.3.3 Eigen Analysis and Frequency Responses

The frequency response of (3-26) is shown in Fig. 3.3 to show the effect of different values of $P_{DC\text{-}0}$ on the transfer function while $L_{DC\text{-}eq}$ is fixed on 150 (μH). The transfer function is unstable for some operating points; the poles related to each operating point along with $L_{DC\text{-}eq}$ = 150 μH are given in Table 3.1. Moreover, the pole locations change when $P_{DC\text{-}0}$ varies from the maximum rectification mode to the maximum inversion mode. Fig. 3.3 (b) shows the trajectory of the fast pole whereas Fig. 3.3 (c) shows the trajectory of the slow pole when $P_{DC\text{-}0}$ varies from the maximum rectification mode to the maximum inversion mode.

TABLE 3.1: POLES OF TRANSFER FUNCTION (3-26)

$P_{DC\text{-}0}$ (MW)	$L_{DC\text{-}eq}$ (μH)	Pole #1	Pole #2
-2.5	150	6074.304	-0.649
-2.0	150	7636.865	-0.646
-1.5	150	10252.624	-0.643
-1.0	150	15554.333	-0.641
-0.5	150	32160.057	-0.640
0.0	150	-461346.775	-0.640
+0.5	150	-28080.059	-0.640
+1.0	150	-14417.290	-0.642
+1.5	150	-9658.104	-0.644
+2.0	150	-7231.582	-0.647
+2.5	150	-5756.041	-0.650

In addition, Fig. 3.4 shows the effect of different values of $L_{DC\text{-}eq}$ on the poles of (3-26) when $P_{DC\text{-}0}$ is fixed at –2.5 MW. It should be noted that the transfer function is unstable for all values of $L_{DC\text{-}eq}$ as predicted from (3-33). The corresponding poles are given in Table 3.2. The pole locations change when
$L_{DC\text{-}eq}$ varies from zero to the maximum value of 1500 μH as shown in Fig. 3.4.

The values of R_L and C_{eq} dramatically affect the location of the poles/zeros of the small-signal dynamics in (3-26). Fig. 3.5 shows the frequency response of (3-26) due to change in R_L and C_{eq}; Tables 3.3 and 3.4 reveal the location of poles for changes in R_L and C_{eq} as well.

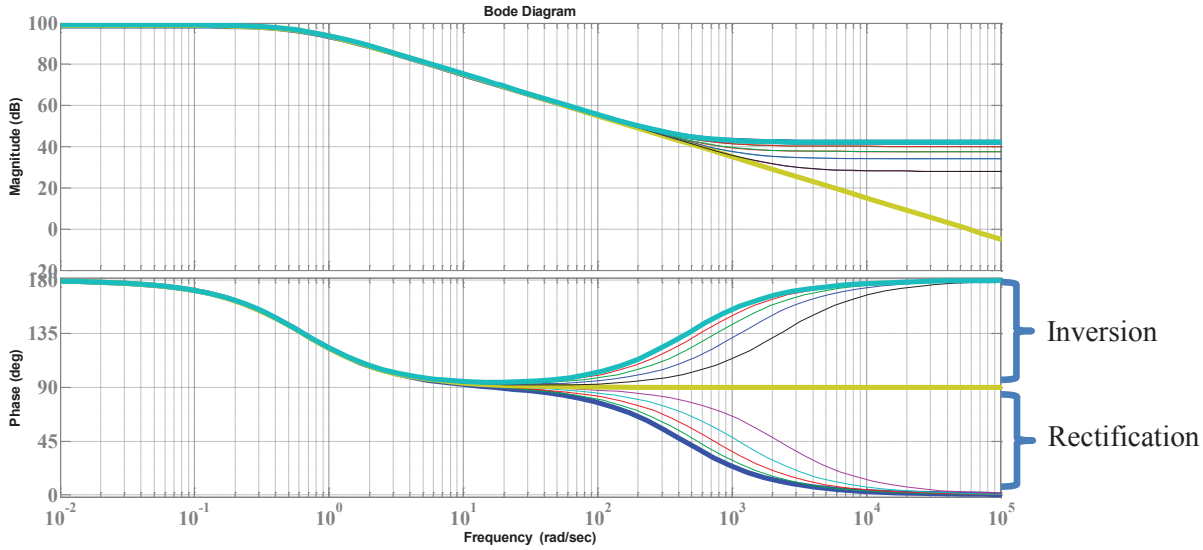
Bode Diagram
Magnitude (dB)
Phase (deg)
Frequency (rad/sec)
Inversion
Rectification

(a)

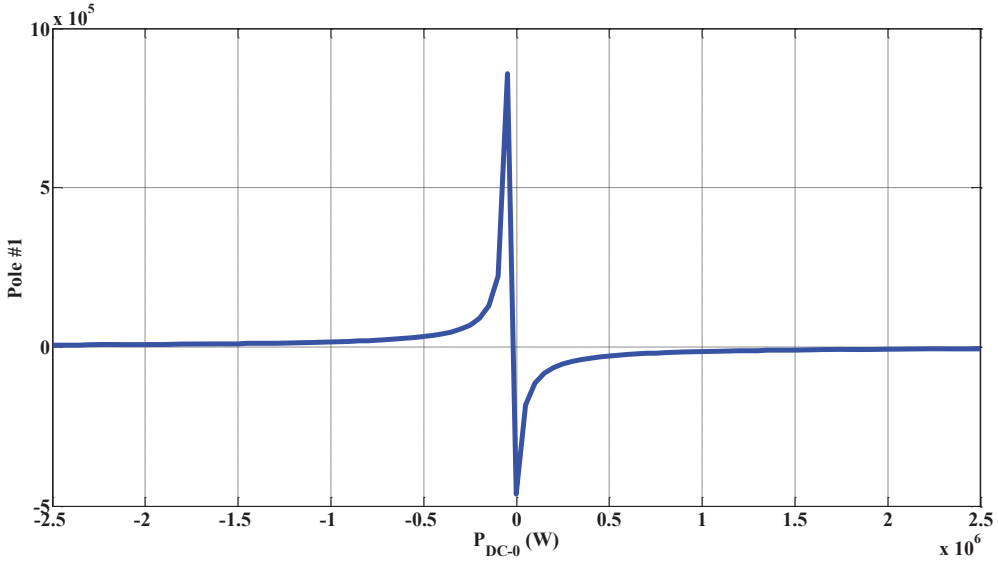
x 10^5
Pole #1
P_DC-0 (W)
x 10^6

(b)

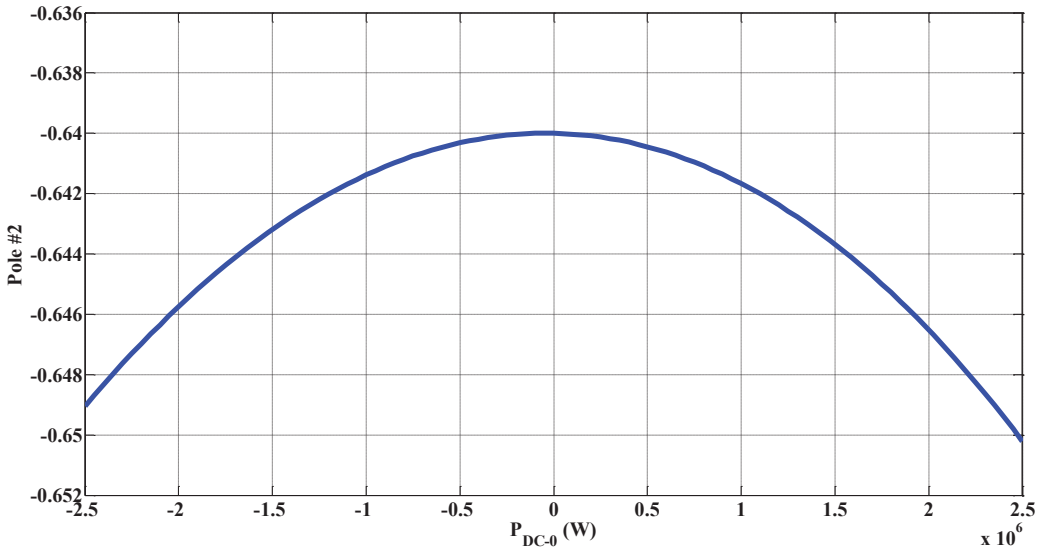

(c)

Fig. 3.3. (a) The bode diagram of transfer function (3-26) for all operating points from maximum rectification mode to the maximum inversion mode. (b) The effect of P_{DC-0} on the fast unstable pole, pole #2. (c) The effect of P_{DC-0} on the slow stable pole, pole #1.

TABLE 3.2: POLES OF TRANSFER FUNCTION (3-26)

P_{DC-0} (MW)	L_{DC-eq} (μH)	Pole #1	Pole #2
-2.5	0	-0.640	-0.640
-2.5	150	6074.304	-0.649
-2.5	300	2994.198	-0.658
-2.5	450	1967.502	-0.668
-2.5	600	1454.159	-0.678
-2.5	750	1146.158	-0.688
-2.5	900	940.827	-0.698
-2.5	1050	794.166	-0.709
-2.5	1200	684.172	-0.720
-2.5	1350	598.625	-0.732
-2.5	1500	530.190	-0.744

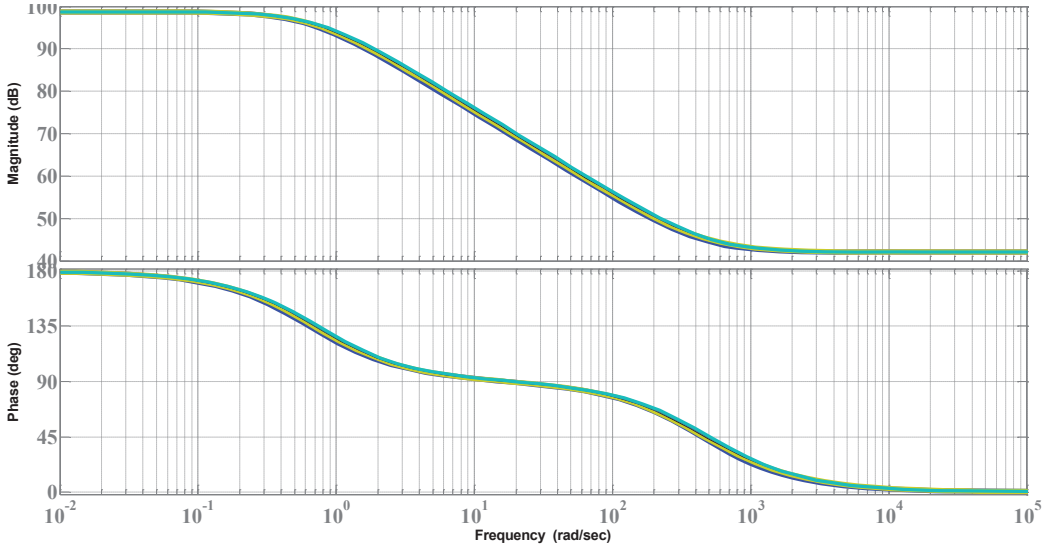
Magnitude (dB)
Phase (deg)
Frequency (rad/sec)

(a)

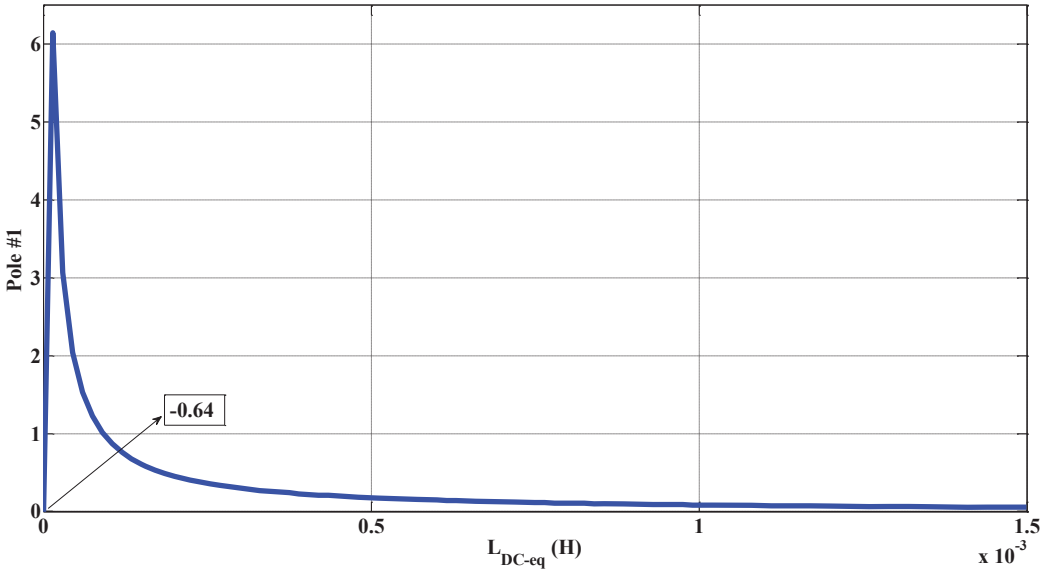
Pole #1
-0.64
L DC-eq (H)
x 10-3

(b)

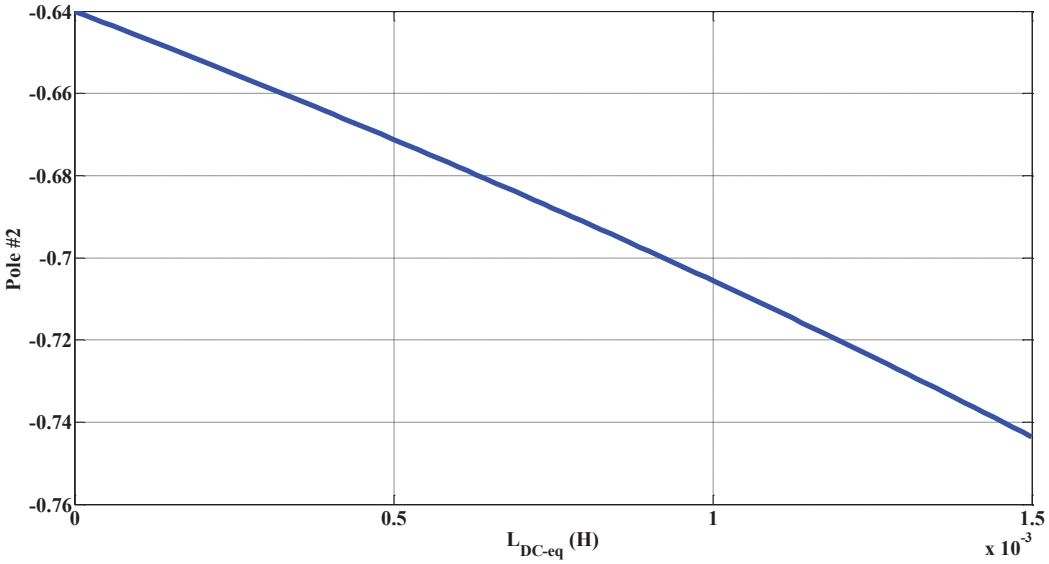

(c)

Fig. 3.4. (a) The bode diagram of transfer function (3-26) for changes in the value of $L_{DC\text{-}eq}$ from 0 to 1500 µH. (b) The effect of $L_{DC\text{-}eq}$ on the fast unstable pole, pole #2. (c) The effect of $L_{DC\text{-}eq}$ on the slow stable pole, pole #1.

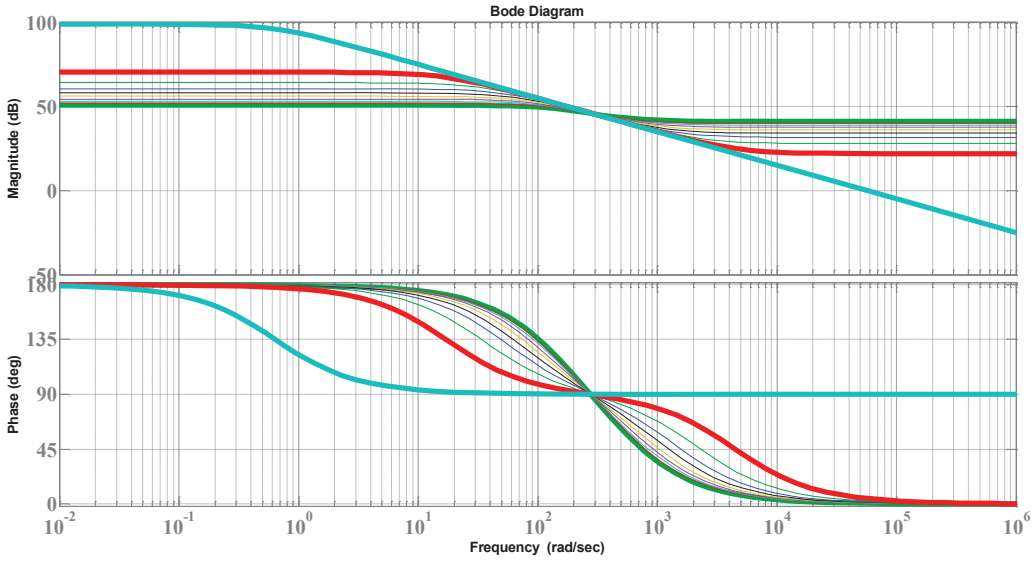

(a)

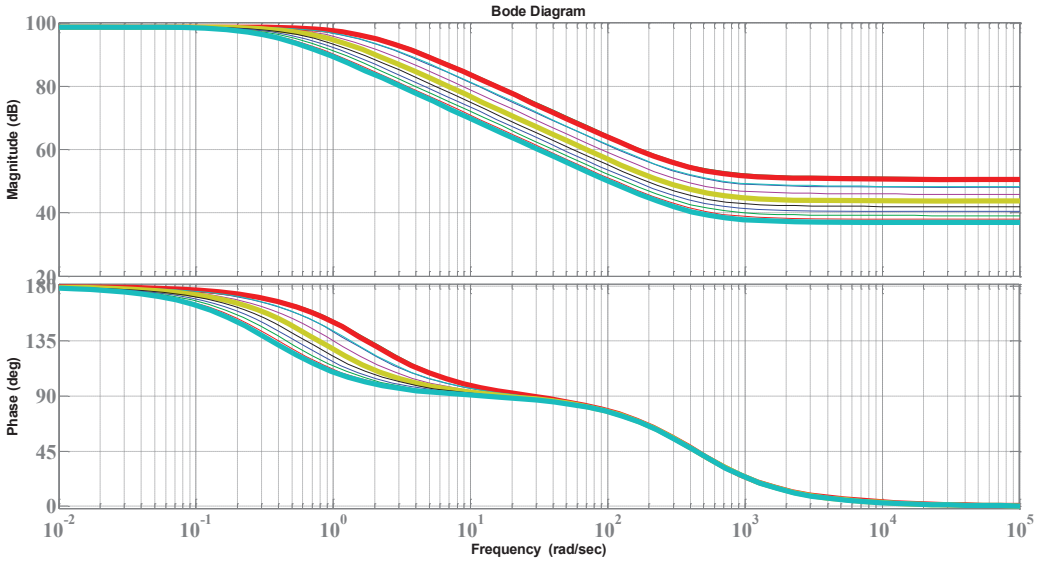

(b)

Fig. 3.5. (a) The bode diagram of transfer function (3-26) for changes in the value of $L_{DC\text{-}eq}$ from 0 µH to 1500 µH. (b) The bode diagram of transfer function (3-26) for changes in the value of C_{eq} from 6.250 mF to 22.509 mF.

TABLE 3.3: POLES OF TRANSFER FUNCTION (3-26)

	$P_{DC\text{-}0}$ (MW)	$L_{DC\text{-}eq}$ (µH)	Pole #1	Pole #2
0.903251706142112	-2.50	150	6248.29630188654	-174.641173585950
1.00401606425703	-2.25	150	6925.33808528244	-157.527846120342
1.13008538422903	-2.00	150	7776.50736518159	-140.288238252926
1.29236071223435	-1.75	150	8877.89954990001	-122.933786589689
1.50905432595573	-1.50	150	10357.4575580875	-105.476793054246
1.81305398871878	-1.25	150	12448.2032213613	-87.9303604408540
2.27043390514632	-1.00	150	15623.9996880719	-70.3083124084502
3.03643724696356	-0.75	150	21019.1452880359	-52.6250986934129
4.58248472505092	-0.5	150	32194.3125296580	-34.8956868500401
9.33609958506224	-0.25	150	69082.4346351711	-17.1354423429469
250	0	150	-461346.775394900	-0.640002491534809

TABLE 3.4: POLES OF TRANSFER FUNCTION (3-26)

R_L	C_{eq} (F)	$P_{DC\text{-}0}$ (MW)	$L_{DC\text{-}eq}$ (μH)	Pole #1	Pole #2
250	0.006250	-2.5	150	5988.39503135594	-1.31672958462074
250	0.004375	-2.5	150	5914.77404884766	-1.90445552999090
250	0.004688	-2.5	150	5931.13300665639	-1.77258923791523
250	0.006093	-2.5	150	5983.98995055213	-1.35148603872352
250	0.008047	-2.5	150	6026.75987293148	-1.01619232184741
250	0.010273	-2.5	150	6055.68348062651	-0.792151231508317
250	0.012637	-2.5	150	6075.23375036078	-0.641933056016771
250	0.015068	-2.5	150	6088.94903348342	-0.537129176871885
250	0.017534	-2.5	150	6098.97274582884	-0.460834417232739
250	0.020017	-2.5	150	6106.57080625886	-0.403170471554247
250	0.022509	-2.5	150	6112.51017283585	-0.358195426671133

In fact, changes in R_L and C_{eq} change the slow dynamics of the nominal plant; however, $L_{DC\text{-}eq}$ creates one unstable fast pole, provided that either (3-31) or (3-33) is satisfied for the criteria of instability in each mode of operation. An increase in $L_{DC\text{-}eq}$ (i.e., due to unmodeled uncertainty) places the unstable pole close to the $j\omega$-axis from the RHP and makes it more dominant.

Owing to the fact that the open loop plant is unstable either in rectification mode or in inversion mode according to practical values of $L_{DC\text{-}eq}$, the validity of modeling is tested when the controller is synthesized for the linearized system, equation (3-26), and both nonlinear dynamics and linearized system are employed in the closed loop system. Then, the results of nonlinear plant and linearized model with the same applied controller in the closed-loop system are compared to validate the credential of the mathematical modeling of the original nonlinear system; it will be provided in Section 3.4.2.

The results in Fig. 3.2-Fig. 3.5 show that there are dramatic degradations in both the stability and the performance of the dc-side dynamics in a grid-connected VSC owing to the fact that all mentioned parameters can change the location of the poles and zeroes in a significant way. Consequently, not only operating point variation but also the parameters of the energy storage components within the converter system are able to degrade stability and performance. The situation becomes worse when parametric uncertainty is combined with operating point variation.

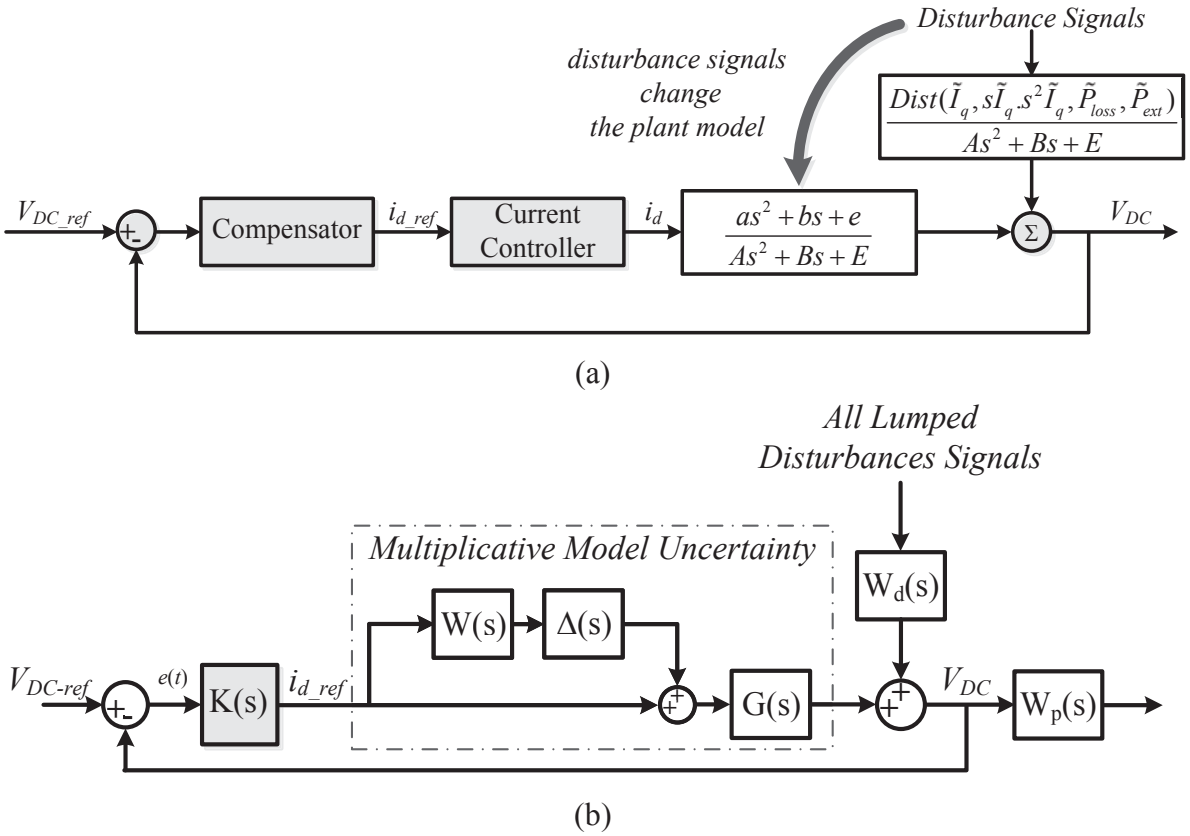

Fig. 3.6. (a) Proposed control scheme for grid-connected VSC in hybrid ac/dc micro-grid with uncertain dc LC-filter (b) Structure used to synthesize the feedback controller.

3.4 Synthesizing Controller for Grid-connected VSC

According to the preceding analysis, because the non-minimum phase situation occurs along with unstable modes in the small-signal dynamics of (3-26), it is not possible to benefit from the robust control structure with two degrees of freedom proposed in [63] and [80], which requires a plant with stable poles. Furthermore, a switching adaptive controller [69] is not a suitable control candidate owing to the fact that both the operating point and the system parameters are changing, which yields a wide range of plant parameters and complicates the desing of a stable switching controller. Therefore, in this chapter, an optimal robust controller that makes the closed-loop system robust against the aforementioned parametric uncertainties and operating point variation is proposed. A robust control approach is selected owing to the systematic design approach, fixed-order controller, and suitability for industrial applications.

3.4.1 Controller Synthesis

The employed structure is a controller with one degree of freedom, and both reference tracking and disturbance rejection are simultaneously guaranteed. Thus, the controller is synthesized based on the internal model principle to guarantee both reference tracking and disturbance rejection of step signals at the input and output, respectively [80]. The applied structure has been depicted on Fig. 3.6.

One of the best ways to optimally reject the disturbance signal affecting the output is minimizing the H_∞ norm from the filtered disturbance signals to the filtered output in the presence of weighted uncertainty using structured singular values μ-synthesise by applying *DK*-iteration method. Therefore, μ-synthesis controller using *DK*-iteration is employed to optimally synthesize the controller [81]-[84].

It is worth to point out that although polynomial method can also be employed as it has been employed in [63], it is not applicable in the scenario and problem sketched in this chapter. It is owing to the fact that the range of variation of vertices of the polytopic system proposed in [86] is such vast that linear matrix inequality (LMI) condition is not feasible [63], [86]-[88].

In order to have one structure that models changeable variables discussed in Section 3.3, all possible transfer functions have been randomly generated by MATLAB. The uncertain plant model given by (3-26) contains six uncertain elements—*A*, *B*, *E*, *a*, *b*, and *e*—that are affected by $I_{d\text{-}0}$, $I_{q\text{-}0}$, $L_{DC\text{-}eq}$, and C_{eq}. It is often appropriate to simplify the uncertainty model while approximately retaining its overall variability for optimal feedback design purposes. One hundred twenty random samples of all possible transfer functions have been generated, and the nominal transfer function and its related unmodeled dynamics have been extracted using the MATLAB Robust Control Toolbox [82]-[83]. Referring to Fig. 3.6 and using the nominal system parameters, the transfer functions $G(s)$ and $W(s)$ are given by (3-36) and (3-37), respectively.

$$G(s)=\frac{-649.5s^2-5.641\times10^{-8}s-1.748\times10^{+9}}{s^3+353.8s^2+1.785\times10^{+5}s+2.956\times10^{+7}} \tag{3-36}$$

$$W(s)=\frac{1.732s^2+1224s+3.062\times10^{+4}}{s^2+347.5s+1.552\times10^{+4}} \tag{3-37}$$

Also, $W_d(s)$ and $W_p(s)$ have been written in equation (3-38) and equation (3-39), respectively.

$$W_d(s) = \frac{1}{s + 10^{-4}} \tag{3-38}$$

$$W_p(s) = \frac{1}{s + 10^{-3}} \tag{3-39}$$

By choosing $G(s)$—the nominal plant dynamics—using (3-37), the controller guarantees robust performance and stability with varying A, B, E, a, b, and e. $W_d(s)$ is selected using (3-38) to reject P_{ext} as much as possible by minimizing the H_∞ norm from disturbance to the output in Fig. 3.6. $W_p(s)$ is selected using (3-39) to induce internal model dynamics and hence facilitates simple controller design with appropriate performance [80] and [81]-[84].

The controller $K(s)$ given by (3-40) has been synthesized using the robust controller design approach via the μ-synthesis and model order reduction tools in the Robust Control Toolbox of MATLAB.

$$K(s) = \frac{-0.0007032s^7 - 0.07585s^6 - 0.08029s^5 - 0.0163s^4 - 0.0009548s^3 \ldots}{\mathrm{s}^7 + 0.284s^6 + 0.01924s^5 + 3.708\times10^{-5}s^4 + 2.433\times10^{-8}s^3 \ldots} \\ \frac{\ldots - 9.625\times10^{-7}\mathrm{s}^2 - 2.879\times10^{-10}\mathrm{s} - 2.098\times10^{-14}}{\ldots + 6.286\times10^{-12}\mathrm{s}^2 + 5.087\times10^{-16}\mathrm{s} + 3.159\times10^{-21}} \tag{3-40}$$

As shown in Fig. 3.6, the synthesized controller is a single transfer function employed in the one-degree-of-freedom structure, which simplifies the implementation. In spite of the somewhat high controller order, it is relatively easy to implement using commercial-grade signal processors.

3.4.2 Model Validation

The robust controller designed in Section 3.4.1 is employed for two different transfer functions generated by (3-26) for two modes of rectification and inversion operating close to maximum VSC capacity. The same controller is then employed with the total nonlinear system, and the results are obtained at the same operating points used for linearization. Six scenarios have been considered—three for the inversion mode and three for the rectification mode. For the inversion mode, the VSC works at +2.25/0.00 MW/Mvar; an additional 0.25 MW is then loaded on the converter. The corresponding transfer function is extracted from (3-26) for the operating point +2.25/0.00 MW/Mvar. The reference dc-link voltage $V_{DC\text{-}ref}$ is then set to increase to 1700 V while the VSC works at 2.5/0.00 MW/Mvar for both cases. For the rectification mode, the VSC

works at –2.25/0.00 MW/Mvar; an additional 0.25 MW is then loaded on the converter. The corresponding transfer function is extracted from (3-26) for the operating point –2.25/0.00 MW/Mvar. $V_{DC\text{-}ref}$ is then set to increase to 1700 V while the VSC works at –2.5/0.00 MW/Mvar for both cases. The obtained results are compared and demonstrated in Fig. 3.7 and Fig. 3.8.

Fig. 3.7 and Fig. 3.8 demonstrate acceptable compatibility between the closed-loop response of the nonlinear plant and the linearized model extracted from the nonlinear plant working at the appropriate operating point. In fact, the number and instant of occurrence of the oscillations are very well matched and consistent for both responses of the nonlinear and linearized plants. The results reveal the validity of the linearized model for which the LTI robust controller was designed. Close matching is observed at different values of operating points and nominal dc-link voltages.

3.5 Simulation Results

A typical multiterminal dc grid with four terminals, presented in Fig. 3.9, was considered for the simulation study to test the performance of the proposed control system under typical and practical disturbances imposed under multi-converter operation in modern dc grids. The system was simulated in the MATLAB/Simulink environment. The system was composed of four zones. Zone I was a 580 V, 60 Hz ac grid that can inject or absorb power to or from the point of common coupling (PCC-1). Zone I mimicked the grid-connected VSC. Zone II was a 580 V, 60 Hz grid interfaced to the dc side of Zone I via a VSC to control the power flow from or to PCC-2. The VSC in Zone II, VSC-PQ, was controlled in the PQ mode. Zone III was composed of a 1.0 MW renewable energy source that could produce dc power (e.g., full-scale wind turbine system). A VSC, VSC-W, was used to interface the variable-frequency wind turbine system to the dc grid. Zone IV modeled a 1.0 MW, 500 V-dc dc micro-grid with energy storage system (ESS) interfaced to the dc grid via a bidirectional dc/dc converter. The controllers employed in different zones are shown in Fig. 2. In Zone I, the VSC worked as a dc voltage power port to control the dc-link voltage. Zone II employed a standard voltage-oriented PQ control structure with inner PI current control loops in the synchronous *dq*-frame [36]. Zone III employed a synchronous-frame PI controller applied in *dq*-frame. Zone IV employed a standard PI controller for the bidirectional dc/dc converter.

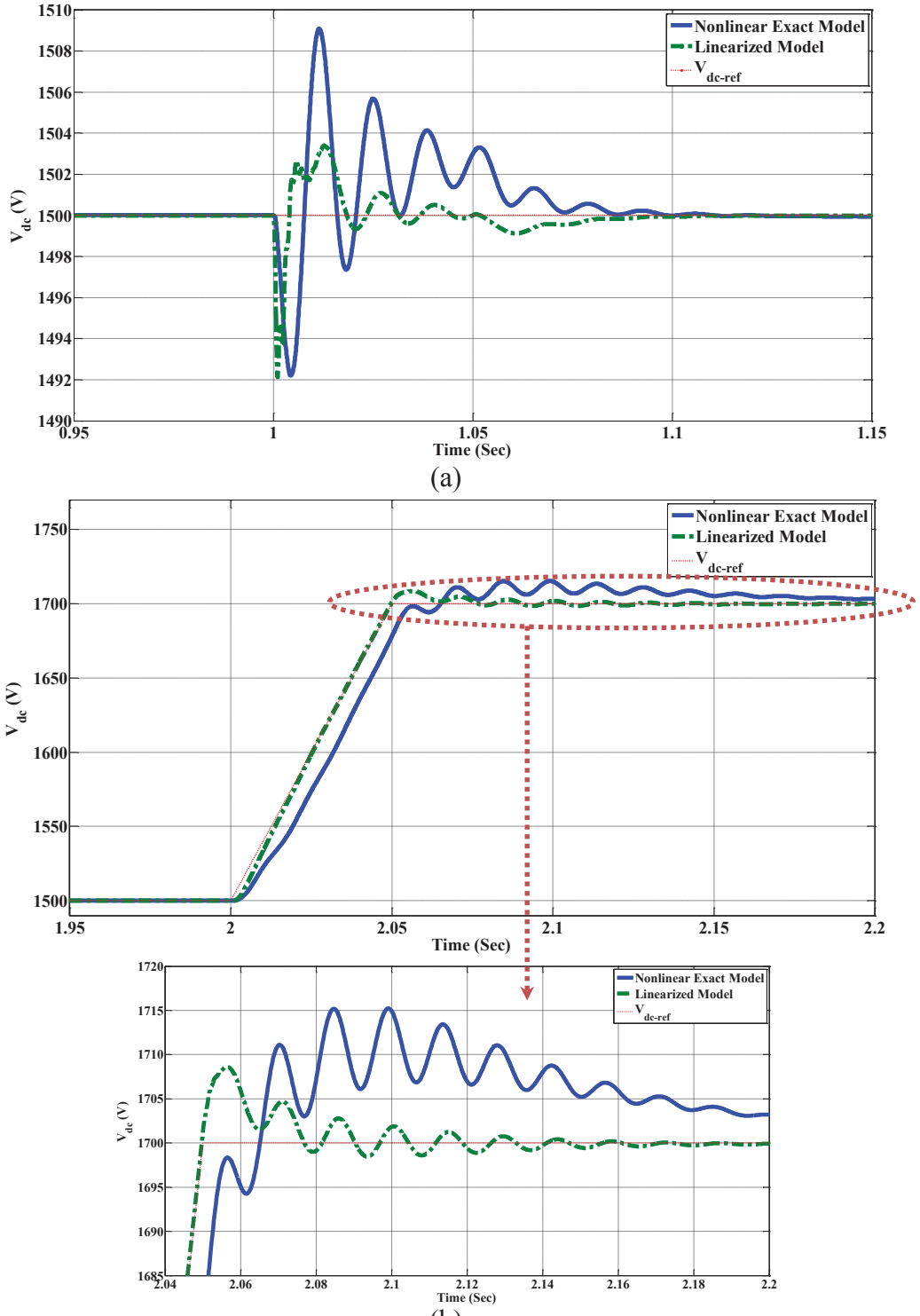

Fig. 3.7. Results of model validation for inversion mode (a) V_{dc} for the nonlinear and linearized model when 0.25 MW is loaded on the converter working at +2.25/0.00 MW/Mvar along with $V_{dc\text{-}ref}$. (b) V_{dc} and $V_{dc\text{-}ref}$ for the nonlinear and linearized model when $V_{dc\text{-}ref}$ is changed from 1,500 V to the new set 1,700 V.

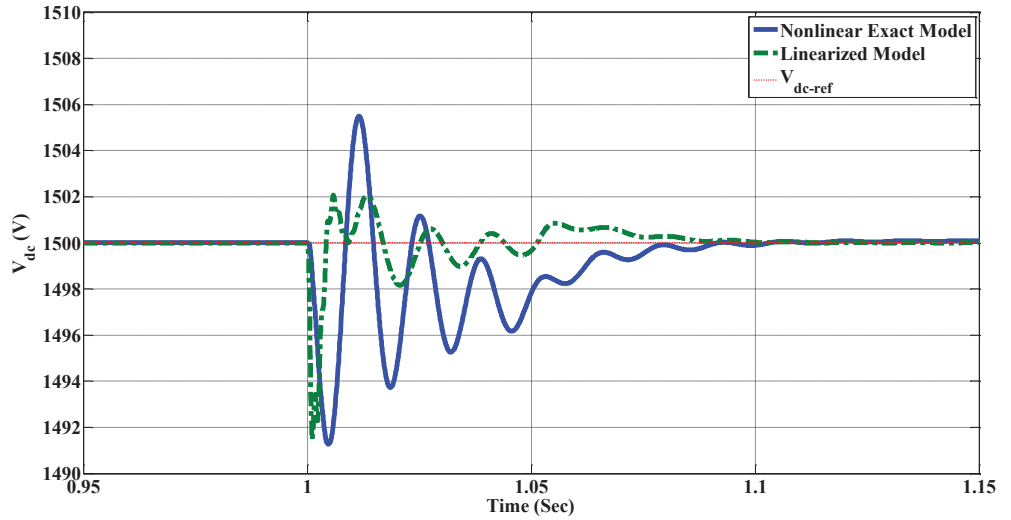

(a)

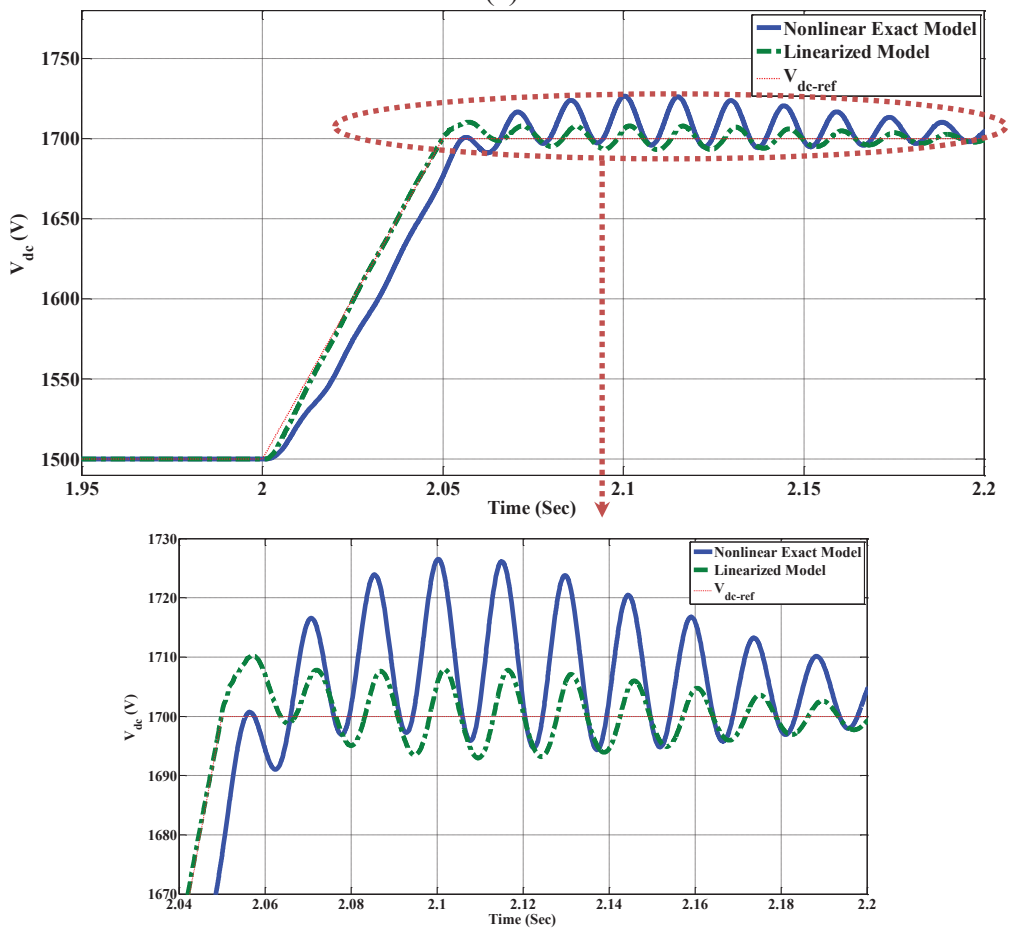

(b)

Fig. 3.8. Results of model validation for rectification mode (a) V_{dc} for the nonlinear and linearized model when 0.25 MW is loaded on the converter working at -2.25/0.00 MW/Mvar along with $V_{dc\text{-}ref}$. (b) V_{dc} and $V_{dc\text{-}ref}$ for the nonlinear and linearized model when $V_{dc\text{-}ref}$ is changed from 1,500 V to the new set 1,700 V.

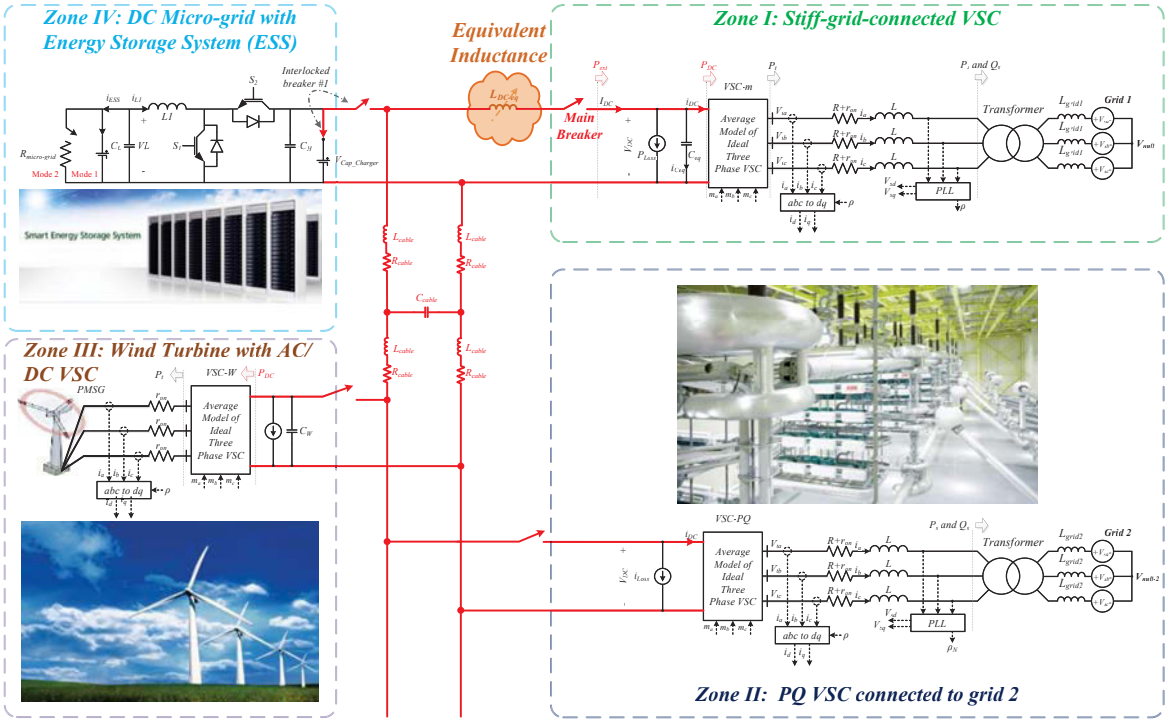

Fig. 3.9. The complete detailed structure of the simulated network.

The complete system parameters are given in Section 3.7. The proposed controller was applied to the VSC in Zone I using the system parameters given in Section 3.7. The average model of VSCs in Zones I, II, and III is used to reduce the computational burden without loss of accuracy. A switching model of the bidirectional dc/dc converter system (Zone IV) was implemented to test the control performance under typical high-frequency disturbances associated with converter switching. To evaluate and demonstrate the performance of the proposed voltage control scheme, the proposed controller was tested as follows; key results are reported accordingly.

First, the dc-side capacitor was energized from its initial zero state by a ramp function that started from zero at $t = 0$ and increased to its final value, 1500 V, at $t = 0.05$ s. Zone II was then connected to the dc grid at $t = 0.10$ s with zero active and reactive power. At $t = 1.00$ s, Zone II was set to absorb 2.25 MW/2.0 Mvar from the dc grid and inject to its ac grid; the reactive power command of Zone II was kept constant within the rest of the simulation. Thus, the grid-connected VSC worked as a rectifier, and it injected 2.25 MW/0.00 Mvar active/reactive power to its ac grid. At t =2.00 s, Zone II was set to inject 2.0 MW to the dc grid, so it absorbed 2.0 MW from its ac grid; meanwhile, it still injected 2.0 Mvar to its ac grid. Thus, the grid-connected

VSC worked as an inverter, and it absorbed 2.0 MW from the dc grid. Also, Zone I was set to inject 1.00 Mvar to its ac grid at t = 2.5 s; the reactive power command of Zone I was kept constant within the rest of the simulation. Zone II was again set to absorb 2.0 MW from the dc grid and inject to its ac grid at t = 3.00 s; again, within this period, it still injected 2.0 Mvar to its ac grid. This situation was kept for Zone II during the rest of the simulation.

Afterward, Zone III, which mimicked a wind farm directly connected to the dc grid via a single VSC, was connected to the dc grid at t = 4.00 s. It injected 2.0 MW into the dc grid at unity power factor, and it reduced its power from 2.0 MW to 0.0 MW during the period from t = 4.50 s to t = 4.55 s.

Finally, Zone IV was connected to the dc grid at t = 5.00 s using interlocked breaker #1. Initially, the dc micro-grid load was disconnected, and the ESS was controlled in the boost mode to inject 0.75 MW to the dc grid by controlling the inductor current i_{L1} in Fig. 1 via a simple PI controller. The dc micro-grid load was connected to the bidirectional dc/dc converter, and the battery was disconnected to model a contingency event and test the performance of the proposed controller under overload conditions. Accordingly, the dc/dc converter was set to suddenly change its control mode from boost to buck in order to transfer 0.90 MW from the dc grid to the dc micro-grid load. The power reversal instant was at 5.50 s, and it lasted approximately 0.70 s.

To assess the system performance under a static load connection to the dc grid, a 1.00 MW dc static load, which is equivalent to 2.25 Ω at 1500 V, was directly connected to the dc grid without any interface at t = 4.2 s, and then it was directly disconnected from the dc grid at t = 4.7 s.

The control performance of the proposed controller under various simulation scenarios is shown in Fig. 3.10-Fig. 3.11. The figures show the performance of the stiff-grid-connected VSC (connected to Grid1) under several scenarios of injecting and absorbing power into and from the dc network. Despite the large power disturbance and the uncertainty in the equivalent dc-link capacitor as “seen” by the VSC owing to the connection of VSC-PQ and the wind-turbine VSC with local dc-link capacitor of 3000 μF, robust voltage control performance was yielded with over-/undershoot voltage that was less than 30 V (2.00%) and recovery time of approximately 0.2 s.

Furthermore, the controller performance when connecting/disconnecting the dc static load is shown in Fig. 10; the maximum over-/undershoot voltage (for average dc voltage) is 115/103 V

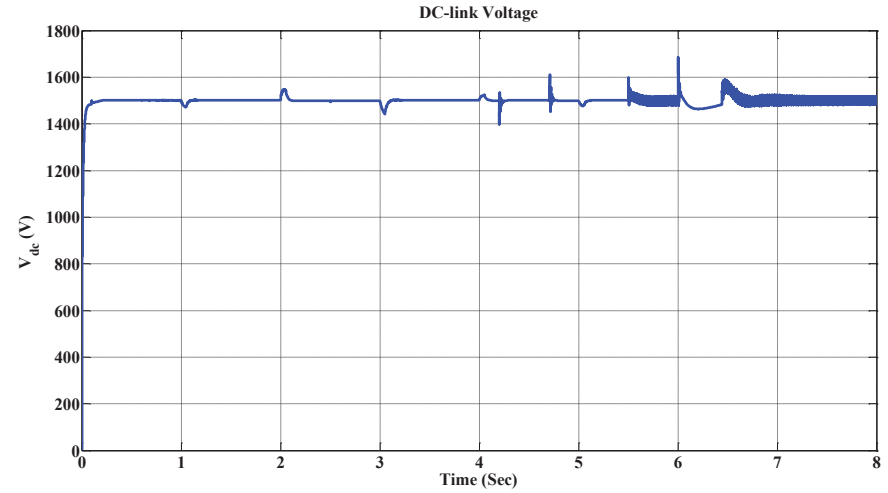

(a)

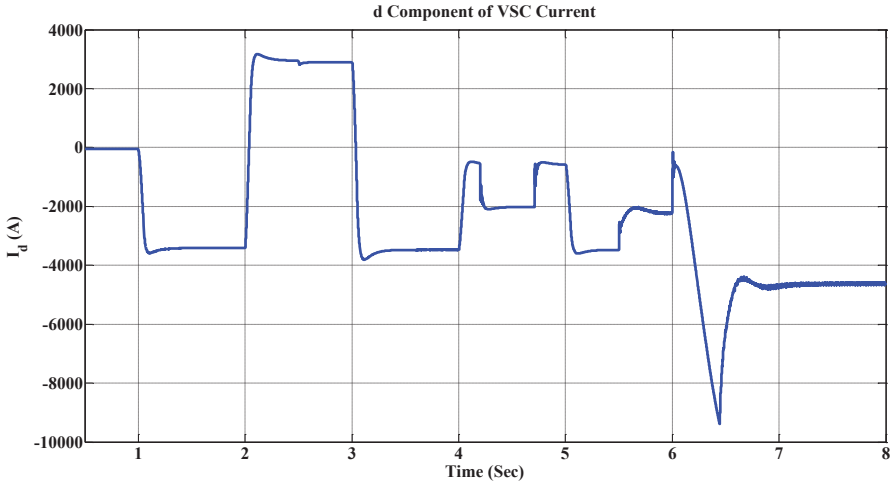

(b)

Fig. 3.10. The simulation of the Fig. 3.9. (a) DC-link voltage of grid-connected VSC, (b) *d* component of the current of grid-connected VSC.

(7.67%/6.87%) with a recovery time of 0.05 s. In addition, Fig. 3.10 shows the controller performance when the ESS was connected via a bidirectional dc/dc converter. Again, in spite of the harsh transient conditions—i.e., I_d changes from approximately 0 A to approximately –9000 A, which drifts the operating point outside the rated power range (approximately 2.57 P.U. where the nominal value of I_d is approximately ±3524 A) to challenge the controller's performance, the maximum over-/undershoot voltage (for average dc, not switching, voltage) is 150/40 V (10%/2.66%) with a recovery time of 0.1 s; the proposed controller successfully ensures robust voltage control performance in the presence of dynamic interactions between the dc/dc converter and the dc grid and in operating points outside the range used for the controller design.

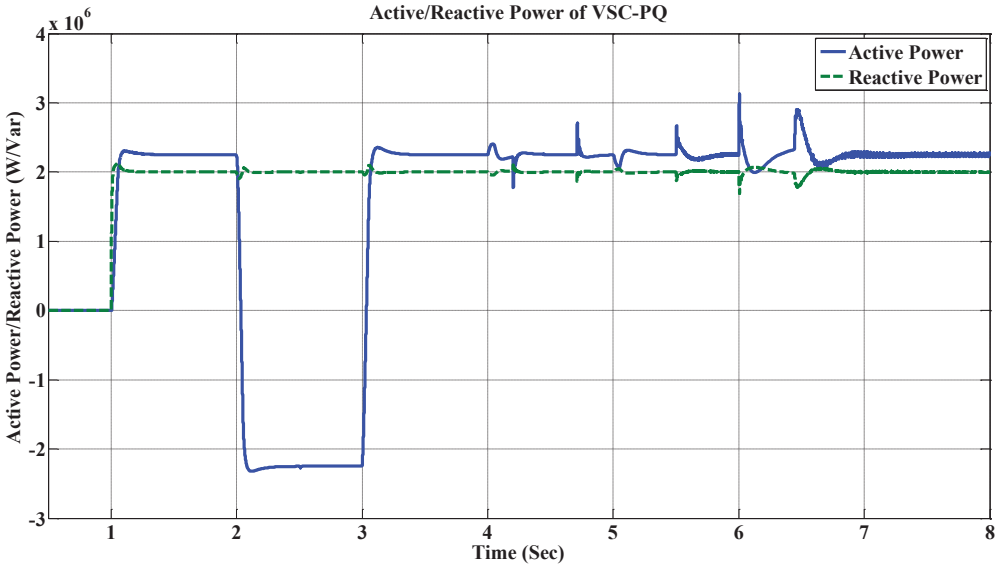
Active/Reactive Power of VSC-PQ
x 10^6
Active Power
Reactive Power
Active Power/Reactive Power (W/Var)
Time (Sec)

(a)

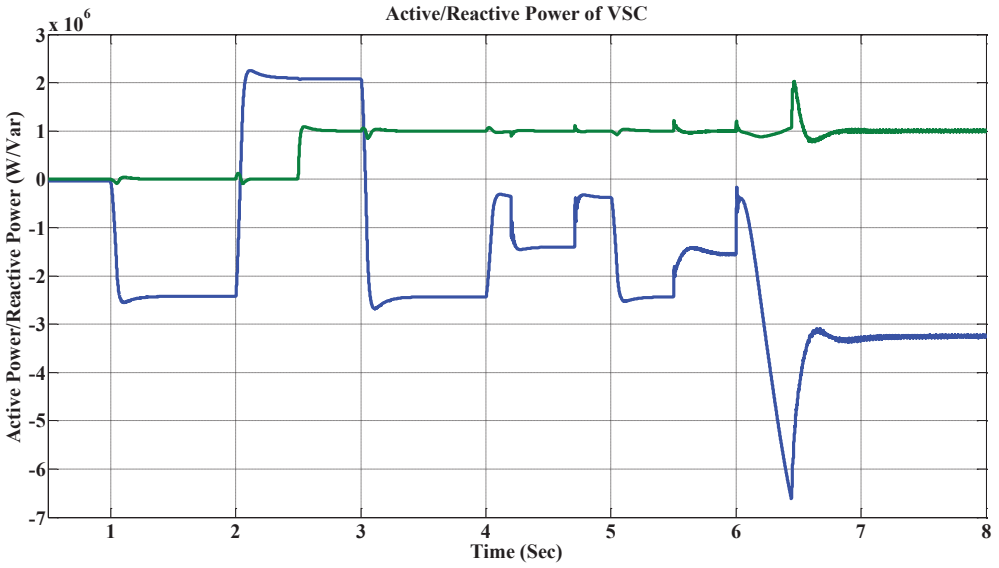
Active/Reactive Power of VSC
x 10^6
Active Power/Reactive Power (W/Var)
Time (Sec)

(b)

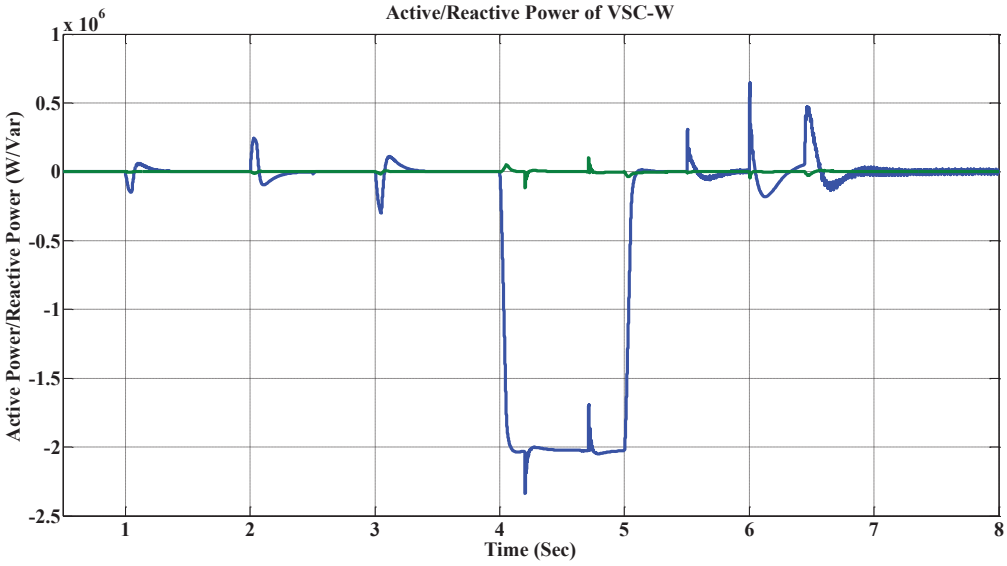

(c)

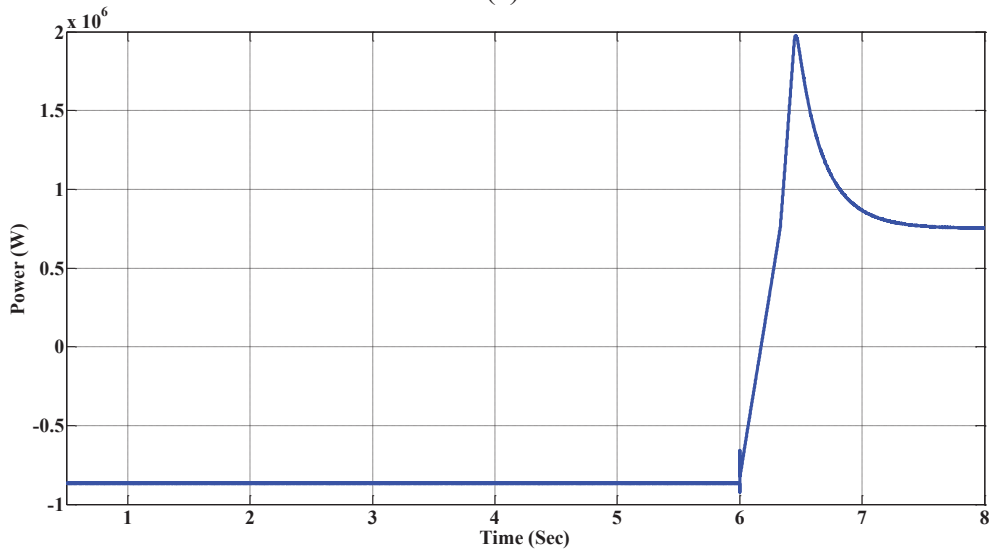

(d)

Fig. 3.11. Active and reactive power responses in different zones of Fig. 3.9, (a) Active-reactive power of VSC-PQ, (b) Active-reactive power of the grid-connected VSC, (c) Active-reactive power of VSC-W, (d) Active power of the ESS.

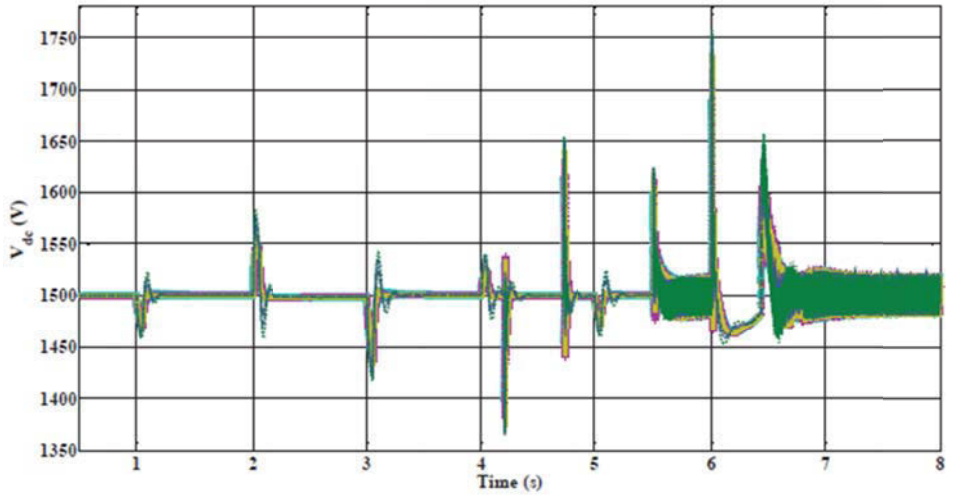

(a)

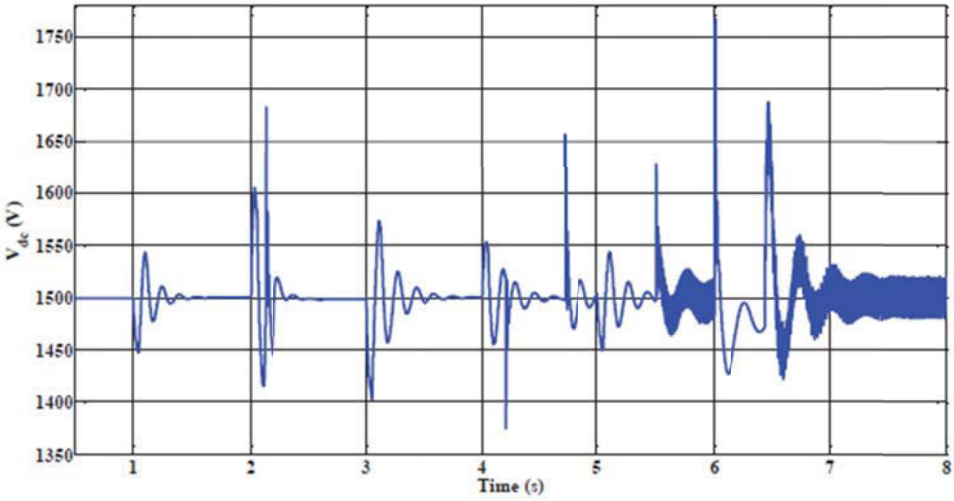

(b)

Fig. 3.12. Performance of the proposed controller under changes in the value of $L_{DC\text{-}eq}$. (a) $L_{DC\text{-}eq}$ = 3000 µH, i.e., within a specific range for which the controller synthesized, 0 < $L_{DC\text{-}eq}$ < 4500 µH, (b) out of the specific range for which the controller synthesized, $L_{DC\text{-}eq}$= 7500 µH.

This section has been allocated to compare the performance of the proposed controller with another recently developed robust dc-link voltage controller [9]; the suggested controller in [63] has been employed in the comparative study because it improves the dc-link voltage performance compared to that of the PI-lead controller [30]. Furthermore, it was designed considering the instantaneous power of the ac-side inductor; therefore, it is a good candidate to verify the unique impact of the instantaneous power of the dc inductor. Consequently, the proposed controller and the controller reported in [63] were simulated for different values of the dc inductor. The simulation results are shown in Fig. 3.12 and Fig. 3.13. Both controllers were tested under the simulation parameters described previously.

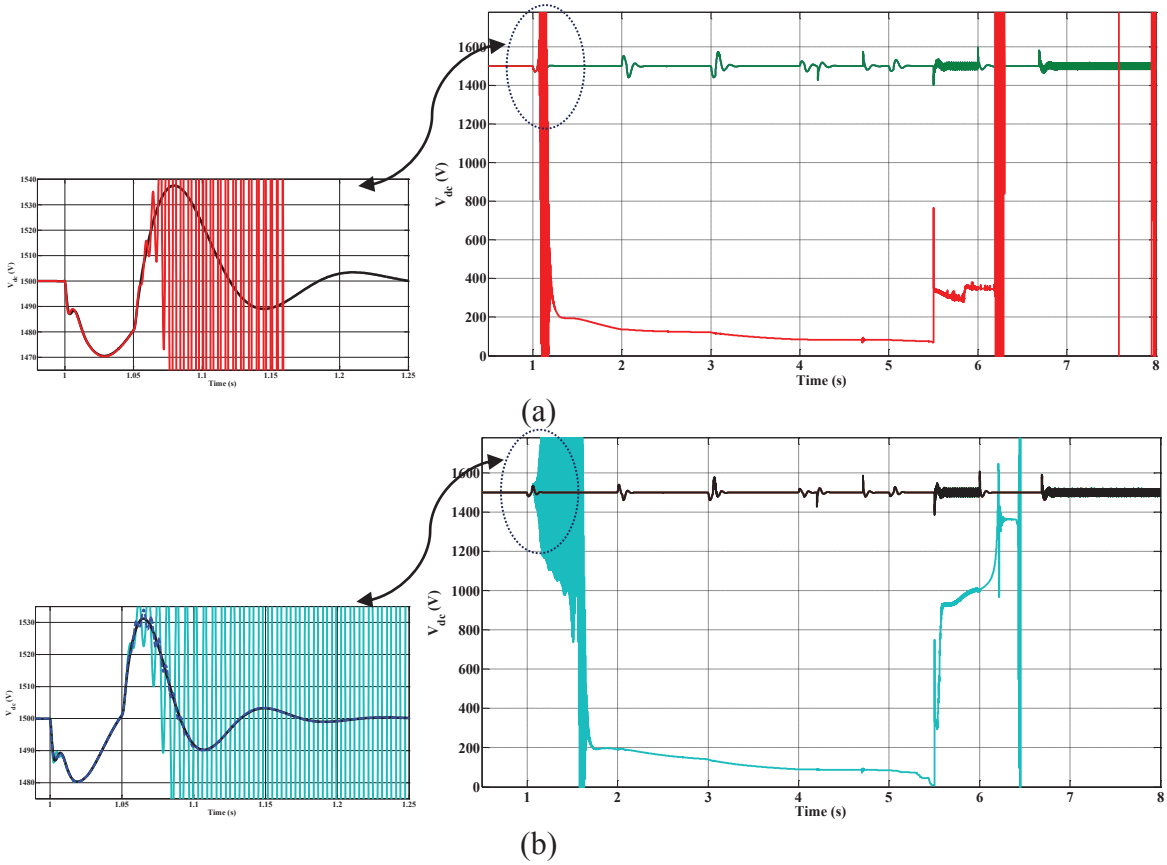

Fig. 3.13. Performance of the controller in [63] under uncertainty in L_{DC}., $L_{DC\text{-}eq}$ = 300 μH: (a) with the full controller synthesized in [63], (b) with the controller synthesized by means of the first step in [63].

As predicted by the theoretical analysis, the proposed controller demonstrated sufficient robustness against changes in the value of L_{DC} within a specific range. One simulation was conducted for $L_{DC\text{-}eq}$ = 7500 μH, which is out of the specific range ($0 < L_{DC\text{-}eq} < 4500$ μH) used to design the robust controller to further challenge the proposed controller. The dc-link voltage remains stable as shown in Fig. 12. However, the closed-loop system was not stable, even with the nominal value of L_{DC}, when the controller synthesized by the method suggested in [63] was employed to stabilize the dc-link voltage. It is worth noting that the controller proposed in [63] contained two steps for the purpose of synthesizing a robust dc-link voltage controller. In the first step, the controller was robust only against operating point variations induced by the instantaneous power changes of the three-phase ac-side inductor L. In the second step, the controller was altered to ensure robustness against C_{eq} variation and have all closed-loop poles within a prespecified region in the s-plane.

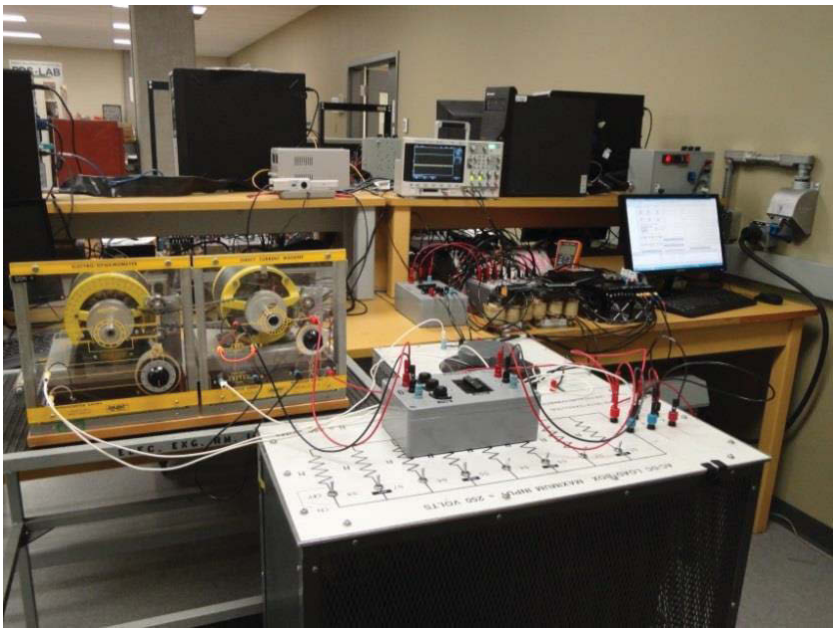

Fig. 3.14. A view of the experimental setup.

Although C_{eq} was fixed to its nominal value to nullify the effect of C_{eq} changes in the simulation results demonstrated in Fig. 3.13, both controllers failed to stabilize the dc-link voltage dynamics when the nominal value of L_{DC} was employed.

3.6 Experimental Results

The experimental setup described in Chapter 2, depicted in Fig. 3.14, is used. A dc side inductor with rated inductance 1.7 mH is added to form an LC dc filter with uncertainty in the dc side inductance.

The proposed controller was tested under the rectification mode when connecting/disconnecting different types of dc loads to/from the dc grid. The impact of both a static load and a dynamic load on dc grid dynamics was considered in the experimental test. Also, the effective dc-link capacitance was doubled to assess the robustness of the proposed controller against variation in the effective dc-link capacitance.

Fig. 3.15 shows the performance of the proposed dc-link voltage control under parametric uncertainty and operating point variation. The actual dc-link capacitance was doubled whereas the nominal value was used in the controller design. Further, the dc-side inductance was doubled,

and the static load was suddenly connected to generate variation in the operating point (from no load to full load) and excite the system dynamics. Fig. 3.16 shows the system performance under the same conditions with load disconnection. The first trace in Fig. 3.15 and Fig. 3.16 show the control level and the direct-axis current, the second trace shows the dc-link voltage, and the third trace shows the corresponding modulation index for phase A.

Additionally, Fig. 3.17 and Fig. 3.18 depict the performance of the proposed controller under connection/disconnection of the active load (dc-motor) to/from the dc grid. The dynamic load generated continuous variation in the operating point along with the added parametric uncertainties. The proposed controller maintained robust performance under operating point variation and parametric uncertainties. Furthermore, the voltage over-/undershoot and recovery times were very small, which ensured perfect regulation performance.

Fig. 3.19 shows the performance of the robust controller in [63] when the dc-link inductor was added and removed. Because the controller was designed without considering any uncertainty in the dc-link inductance, the system became unstable when the physical dc-link inductance was added. Stability was regained when the dc-link inductance was bypassed. Therefore, even with a robust dc-link voltage controller, the effect of the dc-side inductance could destabilize the system. Therefore, accurate modeling is needed to design an effective robust controller.

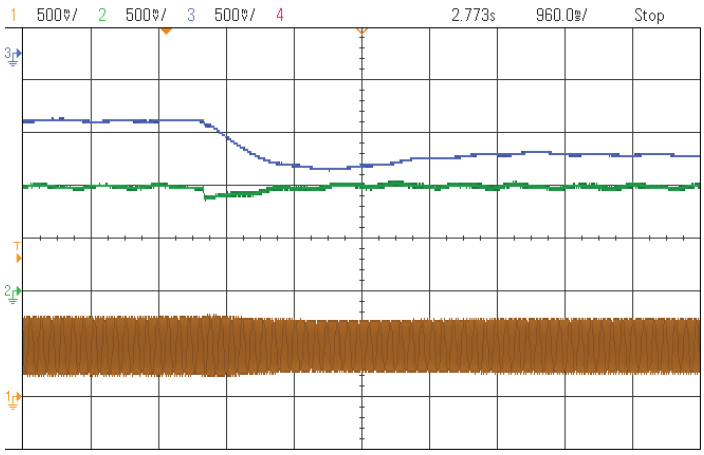

Fig. 3.15. Experimental results of the proposed controller performance under connected static dc load and existing uncertainty in the components of dc-link filter, dc side capacitor and inductor, as well as operating point variations; Channel 3 (top line): control lever, i_d, the positive value is considered when the power is flowing from the dc side to the ac side 10 A/Div; Channel 2 (middle line): V_{dc} in per-unit, 0.5 V/Div; Channel 1 (bottom line): modulation index of phase A (bounded between 0 and 1 based on dSPACE1104 requirements), 0.5 V/Div; horizontal axis: 960 ms/Div.

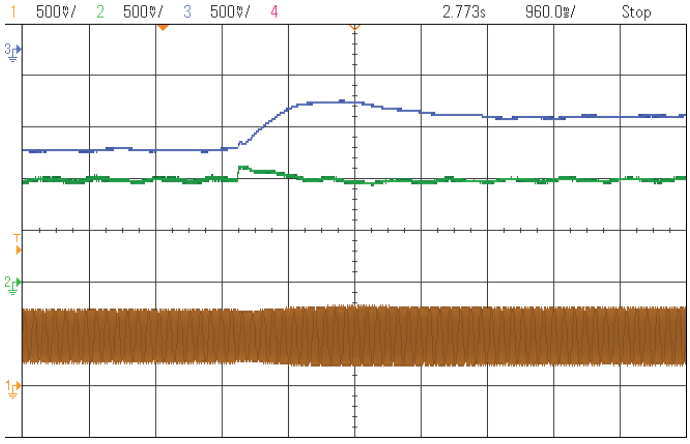

Fig. 3.16. Experimental results of the proposed controller performance during connecting static dc load and existing uncertainty in the components of dc-link filter, dc side's capacitor and inductor, as well as operating point variations; Channel 3 (top line): control lever, i_d, the positive value is considered when the power is flowing from dc side to the ac side 10 A/Div; Channel 2 (middle line): V_{dc} in per-unit, 0.5 V/Div; Channel 1 (bottom line): modulation index of phase-a (bounded between 0 to 1 based on dSPACE1104 requirement). 0.5 V/Div; Horizontal Axis: 960 ms/Div.

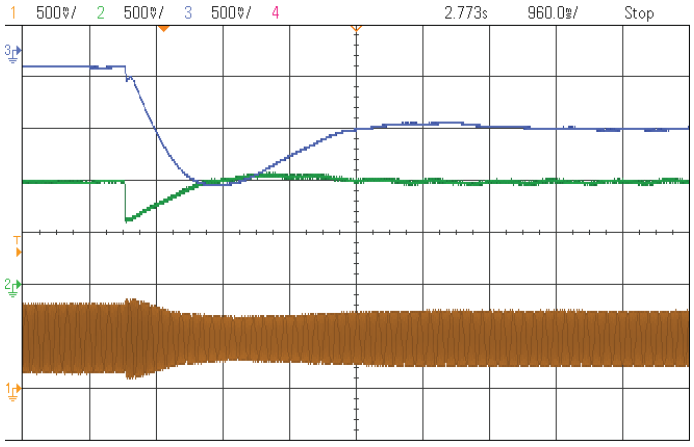

Fig. 3.17. Experimental results of the proposed controller performance during connecting active dc machine load and existing uncertainty in the components of dc-link filter, dc side's capacitor and inductor, as well as operating point variations; Channel 3 (top line): control lever, i_d, the positive value is considered when the power is flowing from dc side to the ac side 10 A/Div; Channel 2 (middle line): V_{dc} in per-unit, 0.5 V/Div; Channel 1 (bottom line): modulation index of phase-a (bounded between 0 to 1 based on dSPACE1104 requirement). 0.5 V/Div; Horizontal Axis: 960 ms/Div.

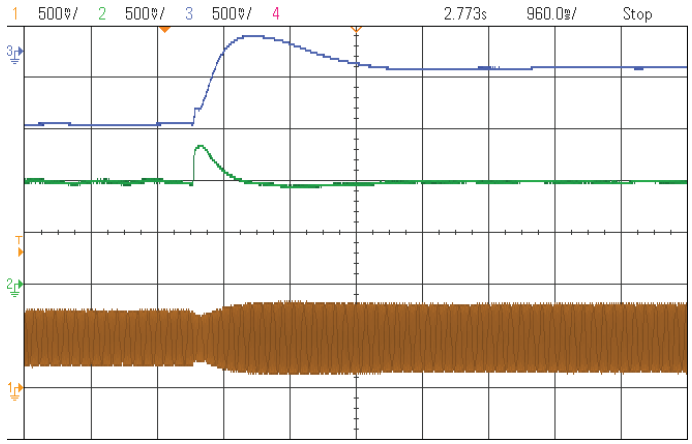

Fig. 3.18. Experimental results of the proposed controller performance during connecting active dc machine load and existing uncertainty in the components of dc-link filter, dc side's capacitor and inductor, as well as operating point variations; Channel 3 (top line): control lever, i_d, the positive value is considered when the power is flowing from dc side to the ac side 10 A/Div; Channel 2 (middle line): V_{dc} in per-unit, 0.5 V/Div; Channel 1 (bottom line): modulation lindex of phase-a (bounded between 0 to 1 based on dSPACE1104 requirement). 0.5 V/Div; Horizontal Axis: 960 ms/Div.

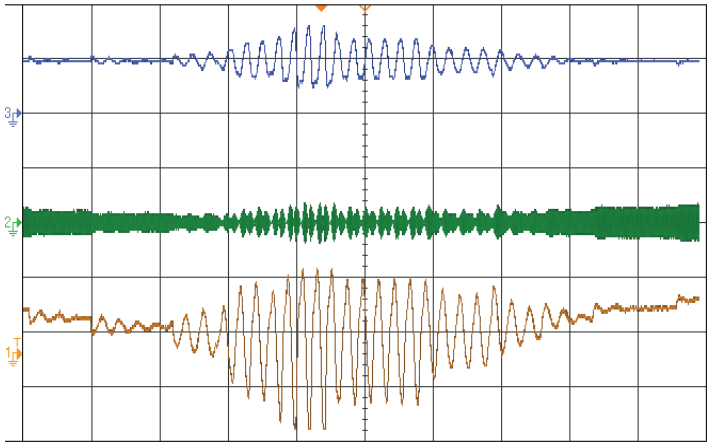

Fig. 3.19. Experimental results of the controller in [63] under connection/disconnection of dc-side inductor uncertainty. Channel 3 (top line): V_{dc} in per-unit, 1.0 V/Div. Channel 2 (modulation index of phase A [bounded between 0 and 1 based on dSPACE1104 requirements]. 0.5 V/Div), Channel 1 (third line) control lever, i_d.

3.7 Parameters of Simulated System, Fig. 3.9

DC grid: rated voltage = 1500 V, dc cable length = 50 km, R_{cable} = 0.82 mΩ/km, C_{cable} = 0.014 μF/km, L_{cable} = 0.98 μH/km

DC Filter: C_f = 3000 μF, $L_{DC\text{-}eq}$ = 300 μH, R_{res} = 1 Ω;

Zone I: grid-connected VSC: VSC-PQ: rated power = 2.5 MVA, grid 2 voltage = 580 V at 60 Hz; P_{Loss} = 5000 W; R = 0.06 mΩ; L = 300 μH; switch resistance = 1.0 mΩ; diode resistance = 1.0 mΩ; K_p = 0.06 Ω; K_i = 0.7 Ω/s

Zone II: VSC-PQ: rated power = 2.5 MVA, grid 2 voltage = 580 V at 60 Hz; P_{Loss} = 5000 W; R = 0.06 mΩ; L = 300 μH; C = 3000 μF, switch resistance = 1.0 mΩ; diode resistance = 1.0 mΩ; K_p = 0.06 Ω; K_i = 0.7 Ω/s

Zone III VSC-W: rated power = 2.5 MVA, grid 2 voltage = 580 V at 60 Hz; P_{Loss} = 5000 W; R = 0.06 mΩ; L = 300 μH; C = 3000 μF, switch resistance = 1.0 mΩ; diode resistance = 1.0 mΩ; K_p = 0.06 Ω; K_i = 0.7 Ω/s

Zone IV: power rating = 0.9 MW, ESS and load voltage 500 V_{dc}, C_L = 1000 μF, C_H = 6000 μF, L_1 = 100 mH, R_{DC} = 1 Ω, K_p (mode1) = 0.4, K_i (mode1) = 4 × 10^{-4}, K_p (mode2) = 0.0133, K_i (mode2) = 0.0533, V_{L_Ref} = 500 V, i_{L_Ref} = 1800 A.

3.8 Conclusion

Dynamics and control of VSCs considering the instantaneous power of both the ac-side filter and uncertain dc-side inductor have been addressed in this chapter. Uncertainty in the dc-side component parameters, including filter capacitance and dc-side inductance, affects the stability and performance of the converter owing to connecting/disconnecting electric devices to/from the dc grid. Furthermore, small-signal dynamic analysis has shown that the dc-link voltage dynamics are highly dependent on the converter operating point. When operating point variation is combined with possible parametric uncertainties, unstable open-loop dynamics along with non-minimum phase behavior can be easily generated in grid-connected converters. To overcome those difficulties, this chapter has presented a detailed small-signal model of the dc-link dynamics in grid-connected VSCs while the instantaneous power of both ac- and dc-side energy storage components are considered, and then a robust optimal dc-link voltage controller is designed. The proposed controller has yielded excellent tracking performance, robust disturbance rejection, and robust performance against operating point and parameter variation with a simple fixed-parameter controller. Comparative simulation studies and experimental results have validated the theoretical results and demonstrated the effectiveness of the proposed control structure.

Chapter 4

Variable-Structure-Based Nonlinear Control for the Master VSC in MTDC Grids

4.1 Introduction

This chapter proposes a variable-structure-based nonlinear controller, which regulates the dc-link voltage of the master VSC using a sigma-delta modulation scheme, to overcome the difficulties mentioned in Section 1.3.3. Also, this chapter shows that improved control performance and stability can be achieved in dc-energy-pool applications when the master VSC is controlled to regulate the dc-link voltage with global stability characteristics using a nonlinear controller with a sigma-delta modulation scheme. Using the proposed controller, dc energy pool dynamics can benefit from an equilibrium-to-equilibrium (EtoE) maneuver feature which is very important in controlling non-minimum phase output by indirect use of variables and employing the flatness concept [93]; this is exactly the case in a the dc-link voltage dynamics from the global stability point of view when the master VSC regulates the dc-link voltage [6], [12]-[30]. To synthesize the controller, a passivity-based design approach has been employed to shape the total energy of the closed-loop system [94]-[96]. The proposed controller yields the following features. 1) Easy implementation on digital hardware devices as well as very good performance in typical and harsh scenarios, such as start-up during dc-link charging. 2) Global stabilization of all system's states, simultaneously, which is not considered in previous work. Hence, it guarantees the large-signal stability of master VSC. 3) Robust performance under parametric uncertainties due to the inherent robustness of the variable-structure controller. 4) Excellent control performance, in terms of tracking and disturbance rejection, that does not depend on the converter operating point. 5) Effective rejection of the second harmonic component induced on the dc-link voltage under unsymmetrical ac-grid conditions without dedicated 2^{nd} harmonic controller. 6) Effective fault-ride-through performance against dc-side faults as the dc-energy pool voltage is controlled,

independently of any internal current control strategy which requires regulated dc-link voltage. Simulation and experimental results are presented to show the effectiveness of the proposed regulator structure.

4.2 Discussion on Controlling DC-Energy Pool-Based Grids Using Current Controlled PWM-based VSC

A typical MTDC grid with has been shown in Fig. 2.7. Zone I employs a bidirectional VSC connected to a strong grid, and it controls the dc-energy pool voltage (master VSC). Zone II employs a VSC connected to grid 2 and works as an active-reactive power (PQ) controller. Zone III employs a bi-directional dc/dc converter as an interface to an energy storage system (ESS) and dc loads. Conventional PI current and voltage controllers are used in Zone II as well as Zone III, whereas the proposed control structure for the master VSC is used in Zone I. System parameters are given in Section 4.7 too.

Referring to Section 2.2, a small-signal dynamic model of the dc-link voltage around an operating point considering the instantaneous power of the ac-side filter and system's disturbances can be given by (4-1).

$$\begin{aligned}\tilde{V}_{DC}^2(s) = &\frac{R_P}{\frac{R_P C_{eq}}{2}s+1}\tilde{P}_{ext}(s) - \frac{3}{2}R_P(V_{sd0}+2RI_{d0})\frac{\frac{LI_{d0}}{V_{sd0}+2RI_{d0}}s+1}{0.5R_P C_{eq}s+1}\tilde{I}_d(s)\\ &-\frac{3}{2}\frac{R_P I_{d0}}{0.5R_P C_{eq}s+1}V_{sd0} - 3RR_P I_{q0}\frac{Ls/2R+1}{0.5R_P C_{eq}s+1}\tilde{I}_q(s)\end{aligned} \tag{4-1}$$

where (I_d, I_q), (V_{sd}, V_{sq}), and (m_d, m_q) are dq components of the VSC's output current, grid voltages, and converter's modulation index; R_p is a resistance representing the equivalent converter losses; R is the filter resistance plus equivalent average conduction resistance of the VSC, L is filter inductance, P_{ext} is the external dc-link power imposed on the VSC, and C_{eq} is the equivalent dc-link capacitance at the master VSC terminals [63] and [30]; "~" denotes small-signal variable; and subscript "0" denotes an operating point. Besides, the current dynamics is governed by (4-2.a) and (4-2.b).

$$L\frac{dI_d}{dt} = L\omega I_q - RI_d + 0.5V_{DC}m_d - V_{sd} \tag{4-2.a}$$

$$L\frac{dI_q}{dt} = -L\omega I_d - RI_q + 0.5V_{DC}m_q - V_{sq} \tag{4-2.b}$$

Considering (4-1), I_d is considered as the control lever in PWM-based VSCs applied in previous studies. Therefore, the second transfer function of (4-1) is the plant model, and other terms of (4-1) are considered as disturbances affecting the output. It can be noted that the second-term of (4-1) has a non-minimum phase zero when I_{do} is negative and it changes at different operating points. Indeed, the zero of the second term of (4-1) is located at $-(V_{sd0}+2RI_{d0})/(LI_{d0}) \approx -V_{sd0}/LI_{d0}$. The zero is a positive value when I_{d0} is negative which happens when VSC operates as a rectifier; accordingly, the zero appears in the right-half-plane (RHP).

A large-signal dynamic model for the master VSC with the instantaneous power of the ac side filter can be given by (4-3).

$$\begin{aligned}
&\frac{d(0.5C_{eq}V_{DC}^2)}{dt} = P_{ext} - \frac{V_{DC}^2}{R_P} - \frac{3L}{4}\left(\frac{d(I_d^2)}{dt} + \frac{d(I_q^2)}{dt}\right) - \frac{3R}{2}(I_d^2 + I_q^2) - \frac{3}{2}V_{sd}I_d \\
&L\frac{dI_d}{dt} = L\omega I_q - (R + r_{on})I_d + 0.5V_{DC}m_d - V_{sd} \\
&L\frac{dI_q}{dt} = -L\omega I_d - (R + r_{on})I_q + 0.5V_{DC}m_q - V_{sq}
\end{aligned} \tag{4-3}$$

Equation (4-3) shows that V_{dc} and I_d are very highly coupled via nonlinear dynamics. As a result, a cascaded control structure, i.e., controlling V_{dc} via an outer loop including inner current control loop, yields unmodeled dynamics that affects both stability and performance. In other words, when a current-controlled PWM-based VSC is employed as an actuator for the dc energy pool, a comprehensive dynamic model is not used in synthesizing controller.

This situation worsens if other VSCs (say the *k*-th VSC) connected to dc energy pool are controlled by current-controlled PWM-based strategy. In this case, any deterioration of the performance of V_{dc}, which is originally induced by the controller of *VSC-m*, is completely reflected to the ac side of other converters connected to the dc link, and vice-versa. To show this dynamic coupling, one can write (4-4) as the dynamic model of the complete multi-converter MTDC system as it has been shown in Fig. 1.1; all parameters with index *k* are related to the connected current-controlled PWM-based VSC-*k*. Equation (4-4) shows the importance of VSC-*m* in stabilizing the dynamics of the entire system via effective dc-link voltage control, and it shows that the dynamics of the current controller of VSC-*m* completely affects the dynamics of V_{dc} as well as dynamics of other VSCs.

$$
\left.\begin{aligned}
&\frac{d(0.5C_{eq}V_{DC}^2)}{dt} = \\
&P_{ext} - \frac{V_{DC}^2}{R_P} - \frac{3L}{4}\left(\frac{d(I_d^2)}{dt} + \frac{d(I_q^2)}{dt}\right) - \frac{3R}{2}(I_d^2 + I_q^2) - \frac{3}{2}V_{sd}I_d \\
&L\frac{dI_d}{dt} = L\omega I_q - (R + r_{on})I_d + 0.5V_{DC}m_d - V_{sd} \\
&L\frac{dI_q}{dt} = -L\omega I_d - (R + r_{on})I_q + 0.5V_{DC}m_q - V_{sq}
\end{aligned}\right\} dynamics\ of\ VSC - m
$$

$$
\left.\begin{aligned}
&L_1\frac{dI_{d_1}}{dt} = L_1\omega_1 I_{q_1} - (R_1 + r_{on_1})I_{d_1} + 0.5V_{DC}m_{d_1} - V_{sd_1} \\
&L_1\frac{dI_{q_1}}{dt} = -L_1\omega_1 I_{d_1} - (R_1 + r_{on_1})I_{q_1} + 0.5V_{DC}m_{q_1} - V_{sq_1}
\end{aligned}\right\} dynamics\ of\ VSC_1
$$

$$
\vdots
$$

$$
\left.\begin{aligned}
&L_k\frac{dI_{d_k}}{dt} = L_k\omega_k I_{q_k} - (R_1 + r_{on_1})I_{d_k} + 0.5V_{DC}m_{d_k} - V_{sd_k} \\
&L_k\frac{dI_{q_k}}{dt} = -L_k\omega_k I_{d_k} - (R_1 + r_{on_1})I_{q_k} + 0.5V_{DC}m_{q_k} - V_{sq_k}
\end{aligned}\right\} dynamics\ of\ VSC_k
\tag{4-4}
$$

Therefore, in such demanding configurations, VSC-*m* should be controlled with a different strategy that eliminates the conventional cascaded control structure. Hence, this chapter presents a nonlinear control strategy for the master VSC. It should be noted that other VSCs connected to the dc-energy-pool can be controlled by the usual current-controlled PWM-based controllers since V_{dc} is independently regulated by another nonlinear regulator.

4.3 Switching Modeling of the Master VSC

In order to model a VSC for synthesizing the class of variable-structure-based controllers, the switching function of different switches is considered. In other words, the control lever is the switching function which takes its values from the discrete set {-1, 0, +1}. In general, for a two-level VSC, the switching function takes its values from {-1, 1}. In previous studies, the switching function for PWM-based converters is usually modeled considering the fact that a VSC is switched with PWM strategy [97]-[98]; i.e., the switching function is not considered as the general set {-1, 0, +1} without existing PWM strategy.

Unlike the conventional power-balance-based model, resulted in equation (4-1) [63]-[64], the complete switching model of the master VSC can be given by

$$\begin{cases} L_s \dfrac{di_a}{dt} = -u_a V_{dc} - (R_s + r_{on}) i_a + V_m \cos(\omega t) \\ L_s \dfrac{di_b}{dt} = -u_b V_{dc} - (R_s + r_{on}) i_b + V_m \cos(\omega t - \dfrac{2\pi}{3}) \\ L_s \dfrac{di_c}{dt} = -u_c V_{dc} - (R_s + r_{on}) i_c + V_m \cos(\omega t + \dfrac{2\pi}{3}) \\ \dfrac{dV_{dc}}{dt} = \dfrac{u_a}{C_{eq}} i_a + \dfrac{u_b}{C_{eq}} i_b + \dfrac{u_c}{C_{eq}} i_c - i_{external} \end{cases} \tag{4-5}$$

where i_a, i_b, and i_c are ac currents of the inductive output filter, L_s is the inductance of the filter, R_s is the resistance of the filter, r_{on} is the equivalent resistance associated with IGBTs and their related diodes, and u_a, u_b and u_c are switching signals to VSC-*m* which take value from set {-1, 1}; V_m is the peak of the ac-side voltage, and $i_{external}$ is the dc-current injected or absorbed from the dc-link. In (4-5), it is supposed that the reference phase angle and magnitude of three phase ac voltage are feeding from the phase-locked loop and grid-voltage measurements. Besides, by replacing $u_{a,b,c}$ with the average signal, $u_{ave\_a,b,c}$, one can reach average model of VSC-m using its switched model. In this case, u_{a_ave}, u_{b_ave}, and u_{c_ave} are bounded within the interval [-1 +1].

After applying normalization of (4-5) using method in [99]-[100], (4-6) can be reached.

$$\begin{cases} \dfrac{di_{n\_a}}{dt_n} = -u_{a\_ave} V_{n\_dc} - (R_s + r_{on}) i_{n\_a} + \cos(\omega_n t_n) \\ \dfrac{di_{n\_b}}{dt_n} = -u_{b\_ave} V_{n\_dc} - (R_s + r_{on}) i_{n\_b} + \cos(\omega_n t_n - \dfrac{2\pi}{3}) \\ \dfrac{di_{n\_c}}{dt_n} = -u_{c\_ave} V_{n\_dc} - (R_s + r_{on}) i_{n\_c} + \cos(\omega_n t_n + \dfrac{2\pi}{3}) \\ \dfrac{dV_{n\_dc}}{dt_n} = \dfrac{u_{a\_ave}}{C_{eq}} i_{n\_a} + \dfrac{u_{b\_ave}}{C_{eq}} i_{n\_b} + \dfrac{u_{c\_ave}}{C_{eq}} i_{n\_c} - i_{n\_external} \end{cases} \tag{4-6}$$

where

$$\begin{cases} i_{n\_a,b,c} = (\dfrac{1}{V_m} \sqrt{L_s / (R_s + r_{on})}) i_{a,b,c} \\ V_{n\_dc} = V_{dc} / V_m \\ t_n = t / \sqrt{L_s C_{eq}} \end{cases} \qquad \begin{cases} q = (R_s + r_{on}) \sqrt{C_{eq} / L_s} \\ V_{n\_dc} = V_{dc} / V_m \\ \omega_n = \omega \sqrt{L_s C_{eq}} \Rightarrow \omega t = \omega_n t_n \end{cases}$$

and subscript "*n*" indicated normalized variable.

To overcome the impact of the external current $i_{external}$, it can be modeled as a state-dependent variable via a variable effective resistor R_{Load} representing the change of the effective load resistance at the dc-side of VSC-*m* in different loading conditions. In other words, the

effective resistor R_{Load} is the equivalent resistance of the total load viewed by the dc port of the master VSC. It should be noted that this modeling approach fits both static (resistive loads) and active (PQ controlled power converter) loads in both rectification and inversion modes by simple estimation of the equivalent load resistance as shown by (4-7).

$$i_{external} = \frac{V_{dc}}{R_{Load}}, \quad i_{n\_external} = \frac{V_{n\_dc}}{q_{Load}}$$
$$q_{Load} = R_{Load}\sqrt{C_{eq}/L_s} \tag{4-7}$$

where .

Finally, the state-space model of the overall nonlinear system can be given by (4-8) using the methodology followed in [101]-[101].

$$\frac{dx_n}{dt_n} = (A_c + A_d)x_n + bu_{ave} + V_n \tag{4-8}$$

where

$$x_n = \begin{bmatrix} i_{n\_a} \\ i_{n\_b} \\ i_{n\_c} \\ V_{n\_dc} \end{bmatrix}, A_c = \begin{bmatrix} 0 & 0 & 0 & -u_{a\_ave} \\ 0 & 0 & 0 & -u_{b\_ave} \\ 0 & 0 & 0 & -u_{c\_ave} \\ u_{a\_ave} & u_{b\_ave} & u_{c\_ave} & 0 \end{bmatrix}, A_d = -\begin{bmatrix} q & 0 & 0 & 0 \\ 0 & q & 0 & 0 \\ 0 & 0 & q & 0 \\ 0 & 0 & 0 & \frac{1}{q_{Load}} \end{bmatrix},$$

$$b = 0, \qquad V_n = \begin{bmatrix} cos(\omega_n t_n) \\ cos(\omega_n t_n - \frac{2\pi}{3}) \\ cos(\omega_n t_n + \frac{2\pi}{3}) \\ 0 \end{bmatrix} = \begin{bmatrix} cos(\omega t) \\ cos(\omega t - \frac{2\pi}{3}) \\ cos(\omega t + \frac{2\pi}{3}) \\ 0 \end{bmatrix}$$

The matrix A_d is associated with the total losses of the system whereas A_c is associated with the total stored energy of the system.

Considering above configuration, a passivity-based controller is one of the best options to stabilize the closed-loop system due to the fact that it can dissipate the total energy of the controlled system in a stable manner [94]-[96].

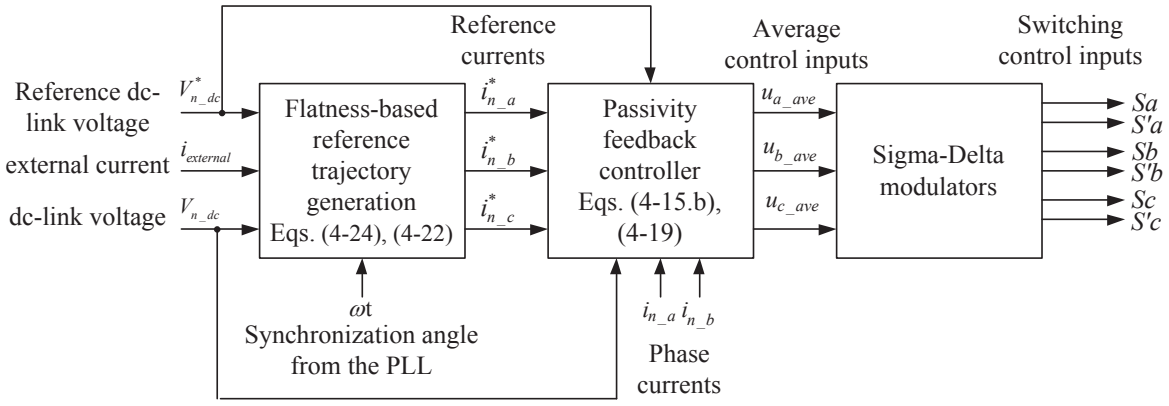

Fig. 4.1. Proposed control structure.

4.4 Proposed Control Strategy of the Master VSC

The complete structure of the proposed controller of the master VSC is shown in Fig. 4.1. The switching control signals are generated as follows. First, the measured dc-link voltage, dc-link external current, and reference dc-link voltage are processed by a flatness-based function to generate the reference state trajectories of the VSC (i.e., reference currents). Second, the reference currents, measured currents, and measured dc-link voltage are processed by a passivity-based controller to generate the reference average control signals required to globally stabilize the master VSC and to force all states (currents and dc-link voltage) through their reference trajectories. Third, three sigma-delta modulators are employed to transfer the average control signals into switching ones and to yield a sliding mode characteristics required to globally stabilize the states under the variable structure nature of VSCs. Detailed control system development is explaining in the following subsections. The essence of a passivity-based controller is presented in Subsection 4.4.2. Subsection 4.4.2 presents the design procedure of the proposed passivity-based controller for the trajectory tracking problem of VSC-*m*. Afterward, to generate the reference trajectory signals, which have to be tracked by the passivity controller, the flatness concept of nonlinear systems is employed, as shown in Subsection 4.4.3, to benefit from its properties associated with non-minimum phase nonlinear systems, which is the case in the master VSC. Finally, Subsection 4.4.4 and Subsection 4.4.5 present, respectively, the sigma-delta modulation process and the essence of implementing switching signals using sigma-delta modulation to have sliding mode regiment.

4.4.1 Nonlinear Controller Synthesis Using Passivity Strategy – A General Framework

If the output of the system is considered as in equation (4-9), where B is the input matrix in the general states space represenstion of dynamic system, then the output is a passive one [94]-[96].

$$y_{passive\_output} = B^T x_n \tag{4-9}$$

Hence, one of the candidates of Lyapunov function is the total stored energy of the system which is equivalent to $V(x_n)=0.5x_n^T x_n$. In this case, the system is Hamiltonian as well [94]-[96]. Consequently, one has the following time derivative of $H(x_n)=V(x_n)$ in (4-10).

$$\frac{dH(x_n)}{dt_n} = -x_n^T(A_d)x_n + yu_{ave} \tag{4-10}$$

then

$$H(x_n(t_n))\text{-}H(x_n(t_0)) \le \int_{t_0}^{t_n} y(\tau)u_{ave}(\tau)d\tau$$

In all trajectory tracking problems, the control objective is to regulate the state x_n to zero since x_n is chosen to be the tracking error of the original plant's trajectories with respect to the desired ones. The passivity criterion requires that, along the trajectories of the system, (4-11) is satisfied [94]-[96].

$$\frac{dH(x_n)}{dt_n} \le yu_{ave} = -x_n^T(A_d)x_n + x_n B u_{ave} \tag{4-11}$$

Accordingly, the control input can be chosen as

$$u_{ave} = -Ky_{passive\_output} = -KB^T x_n \tag{4-12}$$

where K is a positive definite diagonal matrix. Employing (4-12), (4-10) is converted to (4-13).

$$\frac{dH(x_n)}{dt_n} = -x_n^T(A_d + BKB^T)x_n \tag{4-13}$$

Consequently, the stability condition for the closed-loop system, using the mentioned passivity output, can be given by (4-14).

$$\begin{cases} u_{ave} = -KB^T x_n^T \\ A_d + BKB^T > 0 \end{cases} \tag{4-14}$$

4.4.2 Passivity-Based Controller Synthesis for Average Model of VSC-m

Equation (4-8) represents the average model of the VSC-*m* considering the control lever as the average switching signals. If the reference state trajectories x_n^* are available, the state-space model (4-8) can be converted to the tracking error dynamics which requires the control effort error $e_u=u_{ave}-u^*_{ave}$; where the reference control effort u^*_{ave} can be obtained according to (4-15.a), where superscript "*" denotes reference values. As shown in Fig. 4.3, the passivity-based controller needs the reference state trajectories as an input. Subsection 4.4.3 explains how to obtain the reference state trajectories via the flatness concept. Now, it is supposed the reference state trajectories are available, so they satisfy equation (4-15-a).

$$\frac{dx_n^*}{dt_n}=(A_c^*+A_d)x_n^*+bu_{ave}^*+V_n \tag{4-15.a}$$

where

$$x_n^*=\begin{bmatrix} i_{n\_a}^* \\ i_{n\_b}^* \\ i_{n\_c}^* \\ V_{n\_dc}^* \end{bmatrix}, {}^*A_c=\begin{bmatrix} 0 & 0 & 0 & -u_{a\_ave}^* \\ 0 & 0 & 0 & -u_{b\_ave}^* \\ 0 & 0 & 0 & -u_{c\_ave}^* \\ u_{a\_ave}^* & u_{b\_ave}^* & u_{c\_ave}^* & 0 \end{bmatrix}, A_d=-\begin{bmatrix} q & 0 & 0 & 0 \\ 0 & q & 0 & 0 \\ 0 & 0 & q & 0 \\ 0 & 0 & 0 & \frac{1}{q_{Load}} \end{bmatrix},$$

$$b=0, \qquad V_n=\begin{bmatrix} cos(\omega_n t_n) \\ cos(\omega_n t_n-\frac{2\pi}{3}) \\ cos(\omega_n t_n+\frac{2\pi}{3}) \\ 0 \end{bmatrix}=\begin{bmatrix} cos(\omega t) \\ cos(\omega t-\frac{2\pi}{3}) \\ cos(\omega t+\frac{2\pi}{3}) \\ 0 \end{bmatrix}$$

$$\Rightarrow \begin{cases} u_{a\_ave}^*=\dfrac{-\frac{di_{n\_a}^*}{dt_n}-qi_{n\_a}^*+cos(\omega t)}{V_{n\_dc}^*} \\ u_{b\_ave}^*=\dfrac{-\frac{di_{n\_b}^*}{dt_n}-qi_{n\_b}^*+cos(\omega t-\frac{2\pi}{3})}{V_{n\_dc}^*} \\ u_{c\_ave}^*=\dfrac{-\frac{di_{n\_c}^*}{dt_n}-qi_{n\_c}^*+cos(\omega t+\frac{2\pi}{3})}{V_{n\_dc}^*} \end{cases} \tag{4-15.b}$$

Accordingly, the tracking error dynamics, $e=x_n-x^*_n$, can be given by

$$\frac{de}{dt_n}=(A_c+A_d)e+Bu_{ave}+(A_c-A_c^*)x_n^* \tag{4-16}$$

where $A_c=A_c(u_{ave})$ and $A^*_c=A^*_c(u^*_{ave})$. Since those matrices are analytic, one can employ their Taylor series to convert (4-16) to (4-17).

$$\frac{de}{dt_n}=(A_c+A_d)e+Bu_{ave}+(\frac{\partial A_c(u_{ave})}{\partial u_{ave}}|_{u_{ave}=u^*_{ave}})x^*_n(u_{ave}-u^*_{ave}) \tag{4-17}$$

Considering (4-10), (4-14), and (4-17), one can conclude the following passivity-based controller, for the trajectory tracking problem of the master VSC in multiterminal dc grids.

$$\begin{cases} e=x_n-x^*_n \\ e_{y_{passive\_output}}=y_{passive\_output}-y^*_{passive\_output}=(B+\dfrac{\partial A_c(u_{ave})}{\partial u_{ave}}x^*_n)^Te \\ u_{ave}-u^*_{ave}=e_u=-Ke_{y_{passive\_output}}=-K(B+\dfrac{\partial A_c(u_{ave})}{\partial u_{ave}}x^*_n)^Te \\ A_d+(B+\dfrac{\partial A_c(u_{ave})}{\partial u_{ave}}x^*_n)K(B+\dfrac{\partial A_c(u_{ave})}{\partial u_{ave}}x^*_n)^T>0 \end{cases} \tag{4-18}$$

where K is a positive definite diagonal matrix, K=diag(k,k,k).

After employing the abovementioned method to the nonlinear dynamics of VSC-m, (4-19) can be reached.

$$\begin{cases} u_{a\_ave}=u^*_{a\_ave}-k(-V^*_{n\_dc}i_{n\_a}+V_{n\_dc}i^*_{n\_a})) \\ u_{b\_ave}=u^*_{b\_ave}-k(-V^*_{n\_dc}i_{n\_b}+V_{n\_dc}i^*_{n\_b})) \\ u_{c\_ave}=u^*_{c\_ave}-k(-V^*_{n\_dc}i_{n\_a}+V_{n\_dc}i^*_{n\_c})) \end{cases} \tag{4-19}$$

where $i^*_{n\_a,\,b,\,c}$ can be found based on the method explained in Subsection 4.4.3. The simplicity of the controller is obvious from (4-19).

To ensure closed-loop stability, it is only required that k to be greater than zero, from one side. On the other side, k affects the value of controller efforts, $u_{a,\_ave}$, u_{b_ave}, and u_{c_ave}, as well as convergence rate. Based on Subsections 4.4.4 and 4.4.5 as well as average model (4-6), it is required that $u_{a,\_ave}$, u_{b_ave}, and u_{c_ave} to be limited within the interval [-1 +1] to have sliding mode regiment when it is applied to the sigma-delta modulation. Consequently, k is selected to ensure that $-1<u_{a,\_ave}<+1$, $-1<u_{b,\_ave}<+1$, and $-1<u_{c,\_ave}<+1$.

4.4.3 Finding the Reference State Trajectories, $i^*_{n\_a,\,b,\,c}$

To find the state trajectories, $i^*_{n\_a}$, $i^*_{n\_b}$, and $i^*_{n\_c}$, it is more convenient to use the flatness property of the nonlinear systems [93]. Briefly speaking, a nonlinear multi-input multi-output system is

called flat if there is a set of independent outputs, no matter physical or virtual ones, which differentially parameterize the system's states, control inputs, and real outputs; that set of independent outputs is called flat output. Based on the flatness property definition given in [93], a variable differentially parameterizes another one if the second variable can be written in terms of the first variable and a finite number of its time derivatives. Hence, all parameters of the system can be completely expressed by flat outputs as well as a finite number of their derivatives; this facilitates finding the nominal inputs and states to have desired trajectories. This concept is very applicable in non-minimum phase systems, such as VSC-*m*, to have EtoE maneuver control characteristics [93].

Considering (4-15.a) and considering a three-wire system employed in VSC-*m*, i.e., $i^*_{n\_a}+i^*_{n\_b}+i^*_{n\_c}=0$, results in $u^*_{a\_ave}+u^*_{b\_ave}+u^*_{c\_ave}=0$ and (4-20) can be written.

$$\begin{cases} \dfrac{di^*_{n\_a}}{dt_n} = -u^*_{a\_ave}V^*_{n\_dc} - qi^*_{n\_a} + V_{n\_a} \\ \dfrac{di^*_{n\_b}}{dt_n} = -u^*_{b\_ave}V^*_{n\_dc} - qi^*_{n\_b} + V_{n\_b} \\ \dfrac{dV^*_{n\_dc}}{dt_n} = u^*_{a\_ave}(2i^*_{n\_a}+i^*_{n\_b}) + u^*_{b\_ave}(i^*_{n\_a}+2i^*_{n\_b}) - \dfrac{V^*_{n\_dc}}{q_{Load}} \end{cases} \tag{4-20}$$

One of the possible sets of flat outputs is given in (4-21); $Flat\_Output_1$ has also, somehow, stored energy concept.

$$\begin{cases} Flat\_Output_1 = {i^*_{n\_a}}^2 + i^*_{n\_a}i^*_{n\_b} + {i^*_{n\_b}}^2 + 0.5{V^*_{n\_dc}}^2, \\ Flat\_Output_2 = V^*_{n\_dc} \end{cases} \tag{4-21}$$

If x^*_n is given by (4-22),

$$\begin{cases} i^*_{n\_a} = I\cos(\omega t+\varphi) \\ i^*_{n\_b} = I\cos(\omega t+\varphi-\dfrac{2\pi}{3}) \\ i^*_{n\_c} = I\cos(\omega t+\varphi+\dfrac{2\pi}{3}) \\ V^*_{n\_dc} = V_{dc\_energy\_pool} \end{cases} \tag{4-22}$$

then one can reach (4-23) from (4-21) and (4-22).

$$\left\{\begin{array}{c} Flat\_Output_1 = 0.75I^2 + 0.5V^*_{n\_dc}, \\ Flat\_Output_2 = V^*_{n\_dc} \end{array}\right\} \Rightarrow \left\{\begin{array}{c} \dfrac{dFlat\_Output_1}{dt_n} = 0, \\ \dfrac{dFlat\_Output_2}{dt_n} = 0 \end{array}\right\} \tag{4-23}$$

From $d(Flat\_Output_1)/dt_n=0$, the relation between I and $V_{dc\_energy\_pool}$, can be given by (4-24).

$$I = \frac{1}{2q} - \sqrt{0.25\frac{1}{q^2} - \frac{2V^*_{n\_dc}}{3qq_{Load}}} \tag{4-24}$$

Thus, equations (4-15.b), (4-19), (4-22), and (4-24) can be employed to synthesize the controller of the average nonlinear model of VSC-*m*. The average control signals are synthesized by the sigma-delta modulator as explained in Subsection 4.4.4 and 4.4.5.

4.4.4 Sigma-Delta Modulation Techni que as a Converter of Average Signal to Digital One

Sigma-delta modulation is employed in signal quantization as well as sliding mode control synthesis [99]-[100]. Fig. 4.2 shows the configuration of sigma-delta modulation. It is worthy to mention that sigma-delta modulation employed in [99]-[101] is completely different from the sigma-delta modulation employed in [103]-[107] or delta modulation discussed in [36]. Indeed, sigma-delta modulation, which is an improvement of delta modulation from the signal characteristic perspective, is the mechanism of synthesizing required average signals in variable-structure systems such as VSCs [99]-[100], but in [103]-[107], and similar researches, the VSC is directly embedded in the modulation process. In other words, the sigma-delta modulation can be employed in a way similar to the PWM employed in usual PWM-based VSCs [99]-[101], or it can be used as a translator of the average control signal to the switching one [103]-[107]. This chapter employs the latter implementation.

Considering Fig. 4.2, equation (4-25) expresses the action of the comparator.

$$u_q(t) = Q(e_i(t)) = \left\{\begin{array}{l} b \ when \ e_i > 0 \\ a \ when \ e_i \le 0 \end{array}\right. \tag{4-25}$$

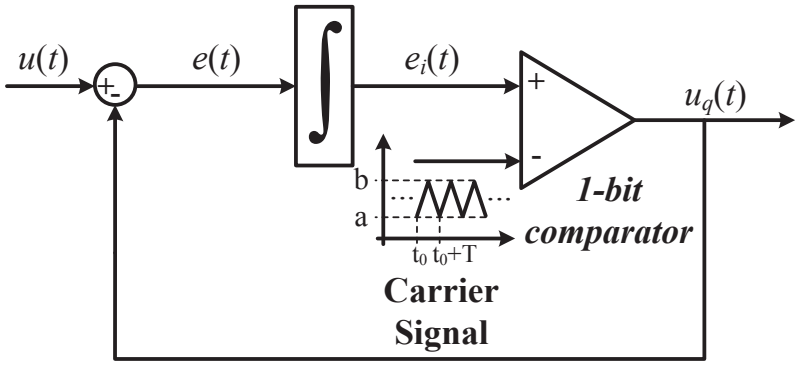

Fig. 4.2. Sigma-delta modulation with the capability of controlling maximum realizable output frequency.

First of all, it is assumed that T in Fig. 4.2, which is the time period of the carrier signal, reaches zero. Considering (4-25), if signal $u(t)$ is smooth, i.e., it is differentiable infinite number of time with respect to its arguments, and if it is bounded in the interval $[a, b]$, then $e(t)=u(t)-u_q(t)$ converges to zero. In other words, there is a sliding motion on the surface $e_i(t)=0$ for any arbitrary initial value $e_i(t_0)$, shown in Fig. 4.2, after hitting time, t_h. Besides, under ideal sliding conditions, i.e., $e_i(t)=0$ and $de_i/dt=e(t)=0$, the average value of the switched output signal, $u_q(t)$, is equal to $u(t)$ [99]-[100]. In reality, it is not possible to assume that T reaches zero due to induced infinity frequency which is not applicable in real physical systems. However, if it is considered that T is a finite number, there will be no ideal condition but there will be still sliding regiment on the surface $e_i(t)$ [99]-[100].

It should be pointed out that by controlling the carrier signal, shown in Fig. 4.2, it is possible to guarantee a finite switching frequency as well as the capability of starting and stopping the switching signal command to power switches as it may be required in some practical circumstances in the application of power electronic converters in power systems. Also, T can be used to dictate the maximum switching frequency in the controller schemes implemented by sigma-delta modulation. The modulation scheme depicted in Fig. 4.2 is known as PWM based sigma-delta modulation because of the existence of the carrier signal in addition to the comparator [103]-[107].

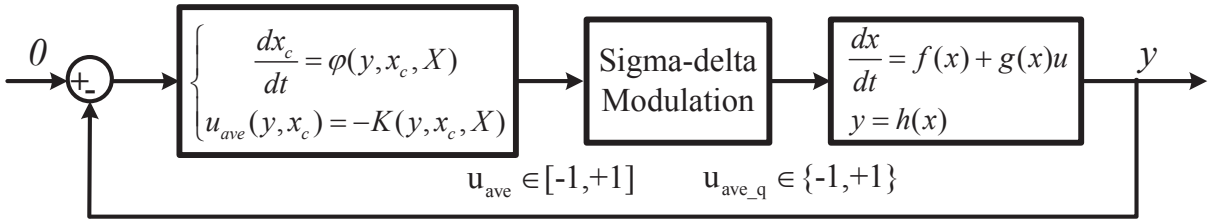

Fig. 4.3. Implementing sliding mode controller using average continuous output feedback via sigma-delta modulation.

4.4.5 Average Feedback and Implementing Sliding Mode Control Using Sigma-Delta Modulation

In this subsection, the implementation a switching-based controller for the switching variable structure plant using the controller designed for the average model of the original switching plant is discussed. In fact, the controller is designed for the average model of the switching variable-structure plant. Then, it is synthesized using sigma-delta modulation to generate switching signal so that the average dynamics of the original plant follows the average dynamics of the closed-loop which the controller was designed for the average plant dynamics.

Suppose that the following state-space model describes the average nonlinear dynamics of a plant which is originally switching system, i.e., (4-26) is describing the dynamics of a switching plant in the average sense.

$$\begin{aligned} \frac{dx}{dt} &= f(x) + g(x)u \\ y &= h(x) \end{aligned} \tag{4-26}$$

where, $x \epsilon R^n$, $u \epsilon \{-1,1\}^m$ and $y \epsilon R^p$. The function $f(x)$ is a smooth vector field defined over the space R^n and usually addressed as the drift vector field. $g(x)$, called input matrix, is an $n \times m$ matrix, whose entries are smooth functions of the state x of the system. The columns of $g(x)$, denoted by means of $g_i(x)$s, for $i = 1, 2, \ldots, m$, also represent smooth vector fields. The output function, $h(x)$, is a smooth map taking values in R^n.

In [99]-[100], it has been shown that if the smooth output feedback dynamic controller (4-27) locally (globally or semi-globally) asymptotically stabilizes the system (4-26) towards a desired constant equilibrium state, represented by X, then the closed-loop system presented by (4-28), shown in Fig. 4.3, exhibits an ideal sliding dynamics, which is locally (globally or semi-globally) asymptotically stable to the same constant state equilibrium point of the system, i.e.,

X [99]-[100], [108]. It should be noted that (4-27) is the controller synthesized for the average model of the original switching variable structure plant, and the control signal *u* is uniformly strictly bounded by the closed interval [-1, 1] due to physical limitations, such as the switching function of VSCs; it can be only on or off.

$$\begin{cases} \dfrac{dx_c}{dt} = \varphi(x_c, y) \\ u = -K(x_c, y) \end{cases}$$
$$x_c \in R^k \tag{4-27}$$

$$\begin{aligned} &\frac{dx}{dt} = f(x) + g(x)u \\ &y = h(x) \\ &\frac{dx_c}{dt} = \varphi(y, x_c, X) \\ &u_{ave}(y, x_c) = -K(y, x_c, X) \\ &\frac{de_i}{dt} = e = u_{ave} - u_{ave\_q} \\ &u_{ave\_q} = Q(u_{ave}) = \begin{cases} +1 \; when \; e_i > 0 \\ -1 \; when \; e_i \le 0 \end{cases} \end{aligned} \tag{4-28}$$

The implementation of the switching variable structure system is demonstrated in Fig. 4.3. It is worthy to note that, as it is clear from Fig. 4.3, the plant is not included in the sigma-delta modulation process, and sigma-delta modulation is applied only as a controller not as an analog-to-digital converter. Besides, it is important that the average controller produces the control inputs *u* within the interval [-1 +1] to have sliding mode regiment; it is the duty of the average dynamics smooth output feedback controller (4-27) to generate the control input *u* within this interval. The equilibrium point is considered as zero which is the case in trajectory tracking problem, or equilibrium point can be converted to zero in many other problems. Thus, there is no loss of generality.

The complete structure of the dc-energy pool including conventional PI controllers of Zone II and Zone III is depicted in Fig. 4.5. Also, the proposed controller of the master VSC in Zone I has been demonstrated in Fig. 4.1 and Fig. 4.4.

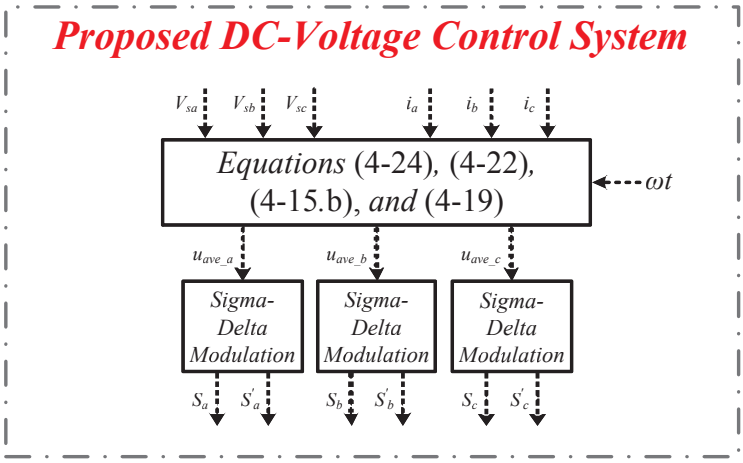

Fig. 4.4. Proposed Nonlinear DC Voltage Power Port Controller.

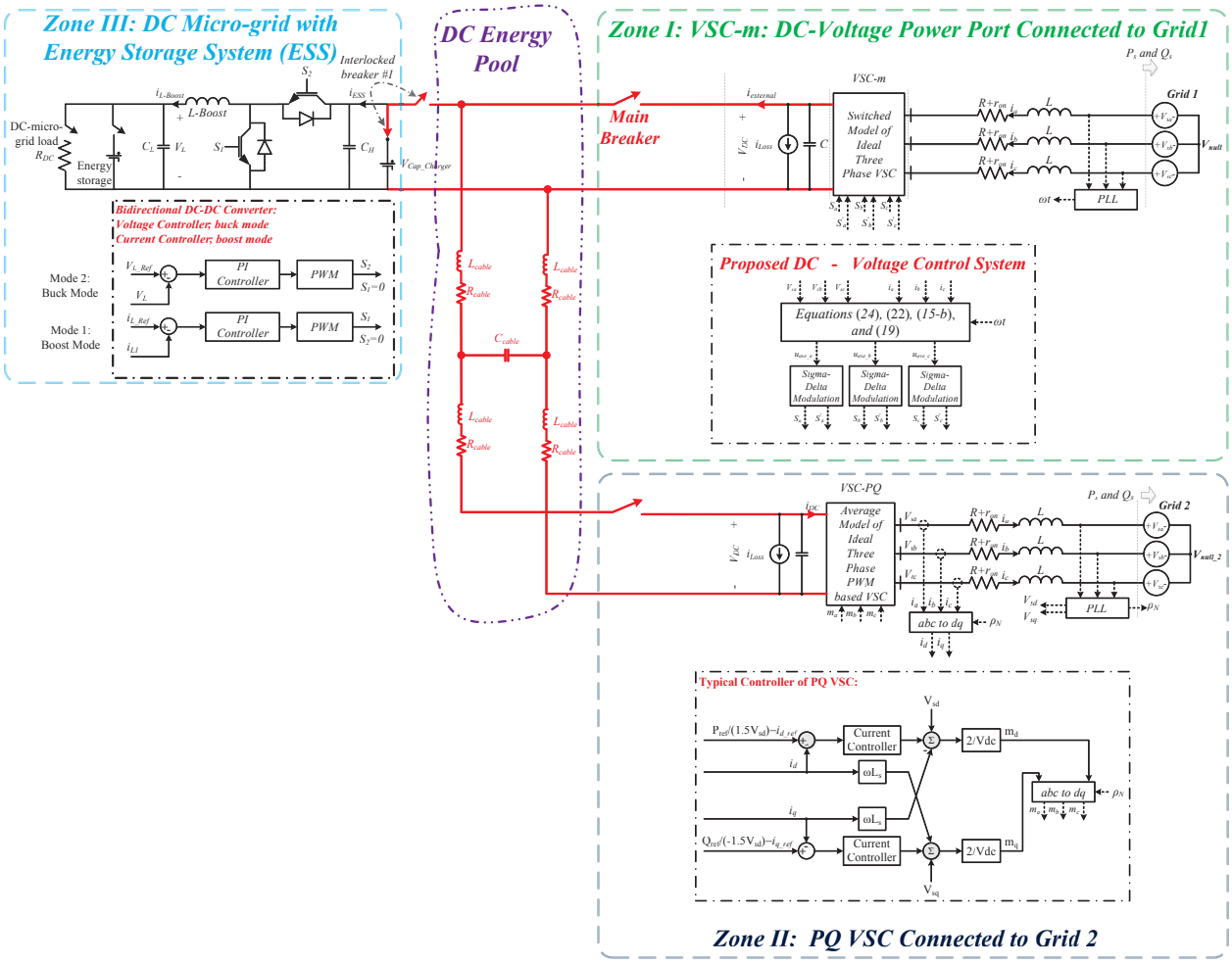

Fig. 4.5. Simulated dc-energy pool based hybrid multiterminal ac/dc configuration with controllers.

4.5 Simulation Results

The MTDC system, presented in Fig. 4.5, is simulated under the MATLAB/Simulink environment. The detailed switched models of VSC-*m*, Zone I, and dc/dc converter, Zone III, are used in simulation for better accuracy and to test the control performance of VSC-*m* under typical high-frequency disturbances associated with switching-based loads, such as dc/dc converters; however, the average model of the VSC in Zone II is used to reduce the computational burden without loss of accuracy. Also, Zone II is simply controlled by PWM-based voltage-oriented controllers [30], [36]. System parameters are given in Section 4.7. Based on Subsection 4.4.2 and theorem provided in Subsection 4.4.5, k is selected based on the plant's parameters to satisfy $-1<u_{a,\_ave}<+1$, $-1<u_{b,\_ave}<+1$, and $-1<u_{c,\_ave}<+1$; accordingly, k=0.01 satisfies the aforementioned limits, and provides fast convergence rate as verified by simulation results.

Several scenario and events have been considered and simulated to assess the performance of the proposed voltage control scheme. Key results are reported in the following. For the sake of performance comparison, the proposed controller is compared with two common controllers employed in the PWM-based VSC [30]; 1) The conventional PI-Lead controller without any feed-forward compensation implemented in PWM based VSCs, which is designed based on the complete dynamics of (4-1) evaluated at the rated power in rectification mode, (i.e., the worst case scenario). 2) The PI-Lead controller with feed-forward compensation of the external power P_{ext}. The lead part is synthesized and added to compensate for the phase reduction induced by RHP zero induced in the rectification mode at the worst operating point. The feed-forward compensation of P_{ext} is implemented to enhance the disturbance rejection performance of the controller, which demands measurement of P_{ext}. Both controllers yield a phase margin of 45^o for the dc-link voltage dynamics. Using nominal system parameters in Section 4.7, the designed PI-lead controller is given by equation (4-29).

$$K_{pi\text{-}lead}(s)=-(2.6329(s+19))/(s^2+2077s) \qquad (4\text{-}29)$$

The tested events are as followings:

1) Event I: This event shows the normal performance of the dc-energy pool employing the aforementioned PI-lead controllers. First, the dc energy pool is energized from its initial

zero states by a ramp function which starts from zero at t=0 s to its final value, 1500 V at t=0.5 s. Then, Zone II is connected to the dc-energy pool at t=1 s with zero active and reactive power. At t=2 s, Zone II is commanded to absorb 0.5 MW/0.0 var from its ac grid and to inject to the dc-energy-pool. Thus, VSC-*m* is working as an inverter, and it is injecting 0.5 MW active power to its ac grid. At t=3 s, Zone II is commanded to inject 0.5 MW/0.0 var to its ac grid and to absorb from the dc energy pool. Thus, VSC-*m* is working as a rectifier, and it is absorbing 0.5 MW from its ac grid. Zone II is again commanded to absorb 0.5 MW/0.0 var from its ac grid and to inject to the dc-energy-pool at t=4 s, and within this period, it is commanded to inject 0.5 var to its ac grid at t=4.5 s. Hence, after t=4.5 s, Zone II is absorbing 0.5 MW from its ac grid, and it is injecting 0.5 Mvar to its ac grid. The performance of the dc-link voltage of the VSC-*m* is shown in Fig. 4.6(a).

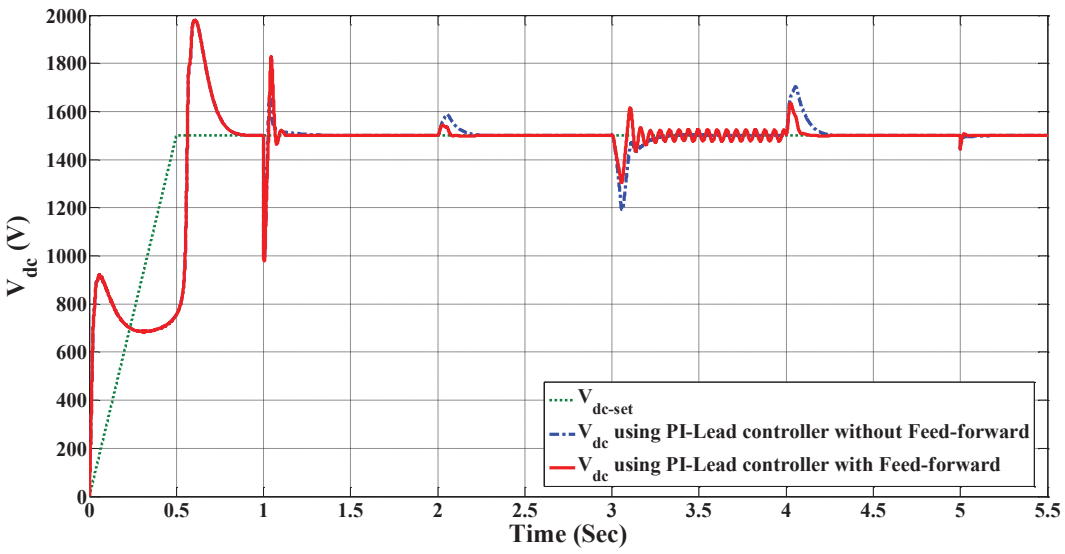

(a)

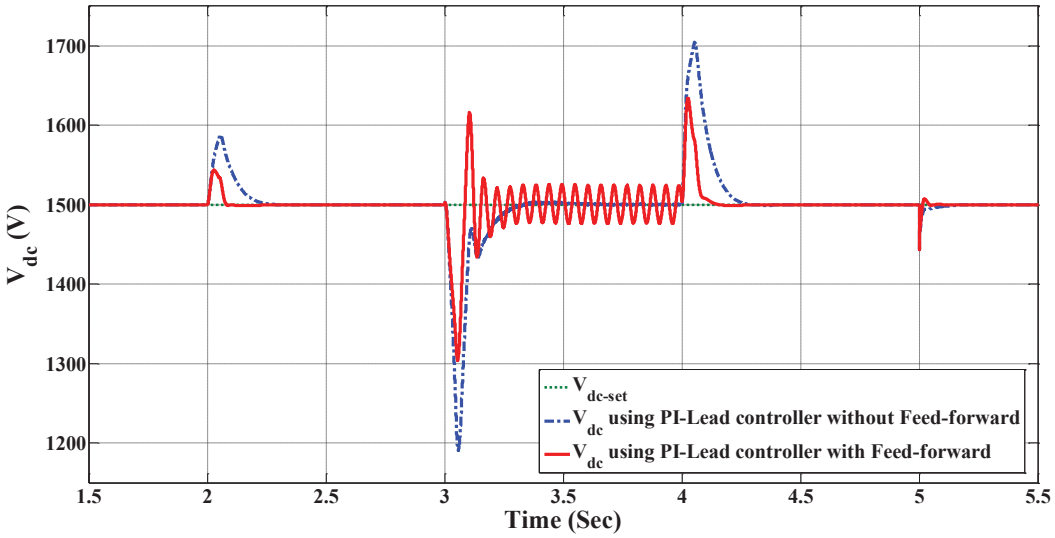

(b)

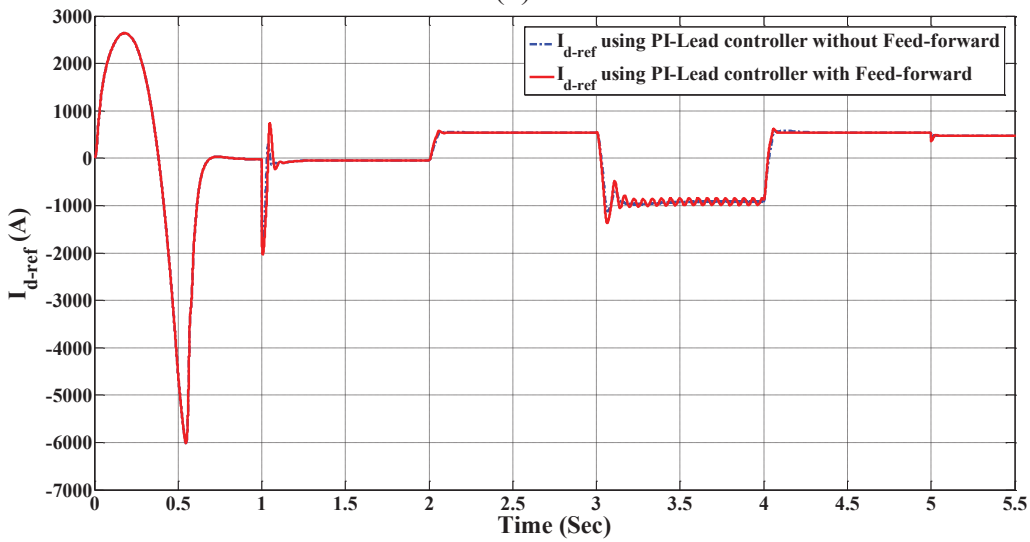

(c)

Fig. 4.6. Event I: response of the dc-energy pool using PI-Lead controller without feed-forward compensation and with feed-forward compensation (a) V_{dc}; dc-link voltage (b) the magnified view of Fig. 4.6(a) (c) I_d generated by PI-lead controller as the control lever.

2) Event II: This event is exactly the same as Event I. However, the master VSC is controlled by the proposed controller (shown in Fig. 4.4). The performance of the proposed controller under this event is shown in Fig. 4.7; comparison of the dc-link voltage of the VSC-*m*, shown in Fig. 4.7(a), with Fig. 4.6 shows excellent tracking and disturbance rejection performances of the proposed controller where the recovery time is around 0.2 s, and dc-link voltage quality during variations of the power direction is very good from overvoltage and under voltage perspectives. Fig. 4.7(b) shows the active and reactive power responses

of VSC-m, whereas Fig. 4.7(c) shows the average control effort of the proposed controller. Fig. 4.7(d) shows the converter output currents. Event II also includes the response of the dc-energy-pool to the connection of VSCs directly tied to the dc-energy-pool, which also affect the effective dc-link capacitance of VSC-m. However, the proposed controller shows enough robustness against this parametric uncertainty. Besides, comparing Fig. 4.7 with Fig. 4.6, it is clear that proposed controller outperforms the PI-lead controller in terms of reference tracking and disturbance rejection performances, even when the PI-lead controller is equipped with feed-forward control.

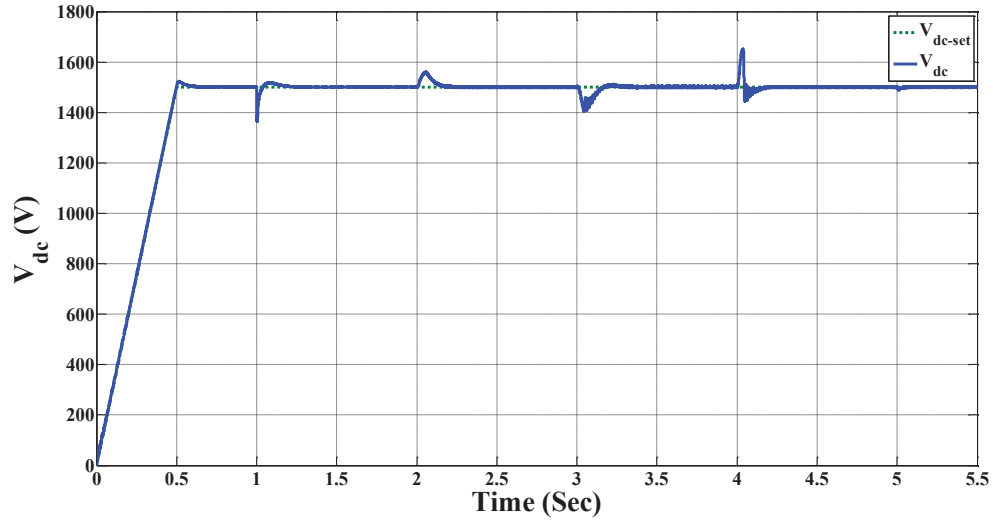

(a)

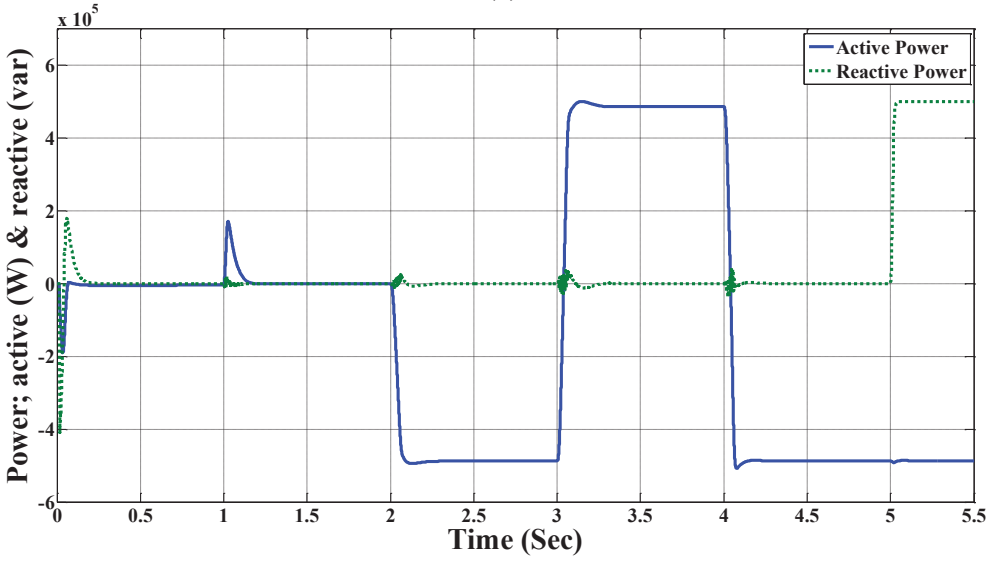

(b)

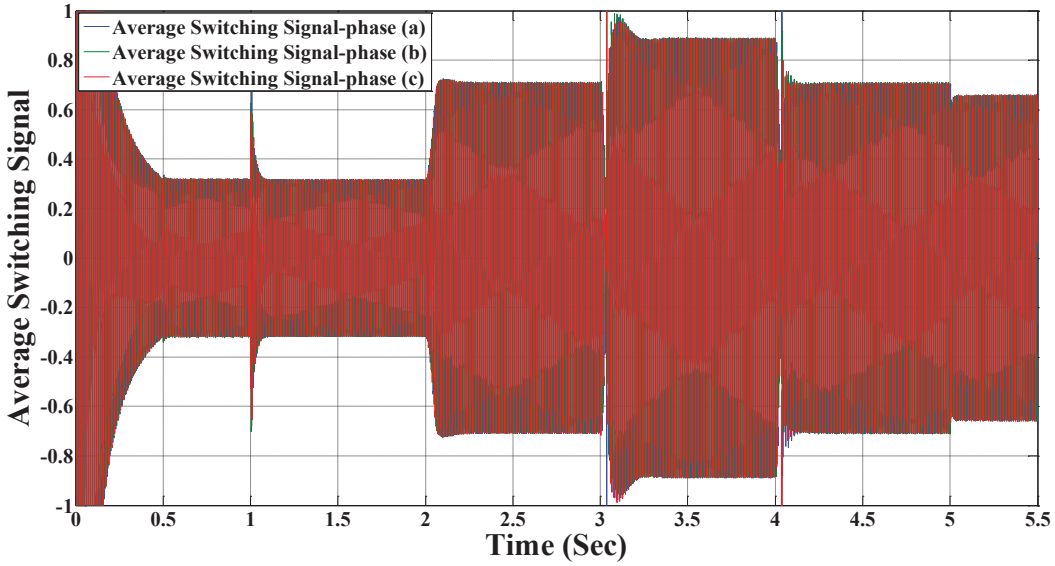

(c)

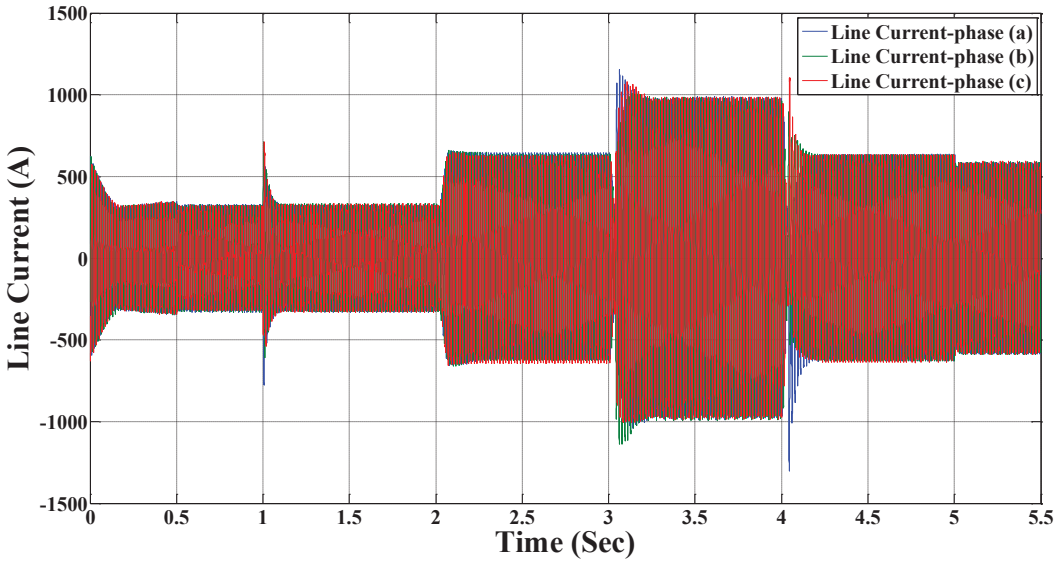

(d)

Fig. 4.7. Event II: Response of the switching model of VSC-m (a) output dc voltage and its reference signal. (b) variations of the active and reactive power when Zone II change its own demand. (c) control lever, average switching signal. (d) line current of VSC-m.

3) Event III: The dc-energy-pool is energized from its initial zero states by a ramp function which starts from zero at t=0.0 s to its final value, 1500 V at t=0.5 s. Then, Zone II is connected to the dc-energy-pool at t=1 s with zero active and reactive power. At t=2.0 s, Zone II is commanded to absorb 0.25 MW/0.00 var from the dc-energy-pool and to inject it to its ac grid. Thus, VSC-*m* is working as a rectifier, and it is absorbing 0.25 MW from its ac grid. At t=3 s, the interlocked switched shown in 0, changes its position, so Zone III

is commanded to absorb 0.3 MW from the dc energy pool. Thus, VSC-*m* is working as a rectifier in this period. After that, Zone III is commanded to inject 0.9 MW to the dc-energy-pool at *t*=4 s, and within this period, VSC-*m* changes its mode from rectifier to inverter. The performance of the proposed controller under this event is shown in Fig. 4.8. Fig. 4.8(a) shows the dc-link voltage; Fig. 4.8(b) shows the average switching signal; Fig. 4.8(c) shows the VSC-*m* output current. Also, Fig. 4.8(d) shows the boost current of the dc/dc converter of the ESS units. As it is obvious from Fig. 4.8, it takes time for ESS to change its power direction, so at instant around 4.472 s, the ESS starts to inject power to the dc-energy-pool and this situation continues until the whole rated power is completely reached at *t*=4.75 s. As it is clear from Fig. 4.8, the recovery time is again around 0.2 s, and dc-link voltage quality during variations of the power direction is very good from overvoltage and under voltage perspectives in spite of the harsh power reversal scenario in this case. Fig. 4.8(e) shows the performance of the PI-lead controller under the same conditions. The small-signal-based design approach associated with linear controllers, such as the PI-lead controller, yields several oscillations and large transients in the dc-link voltage.

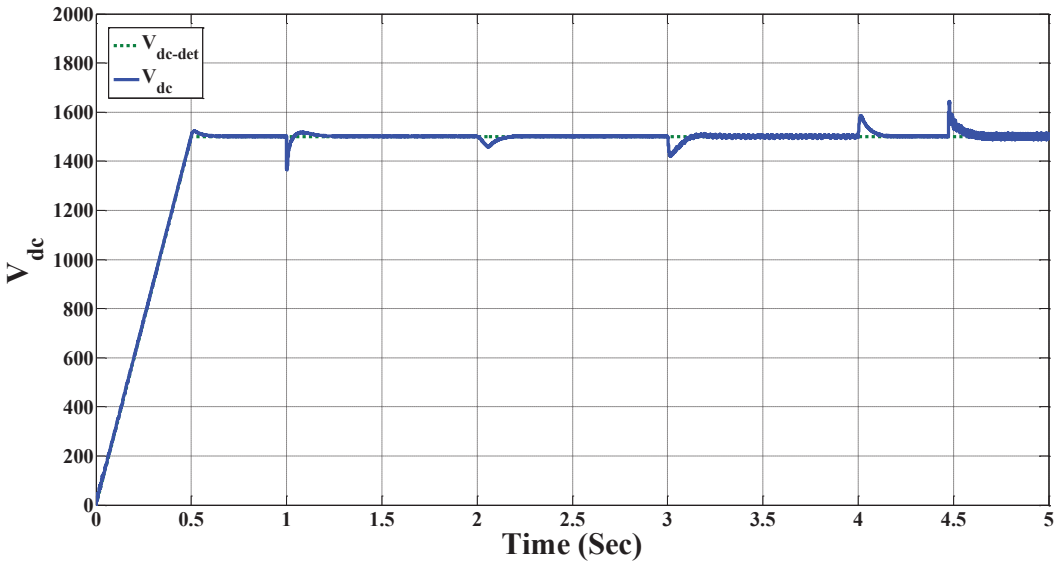

(a)

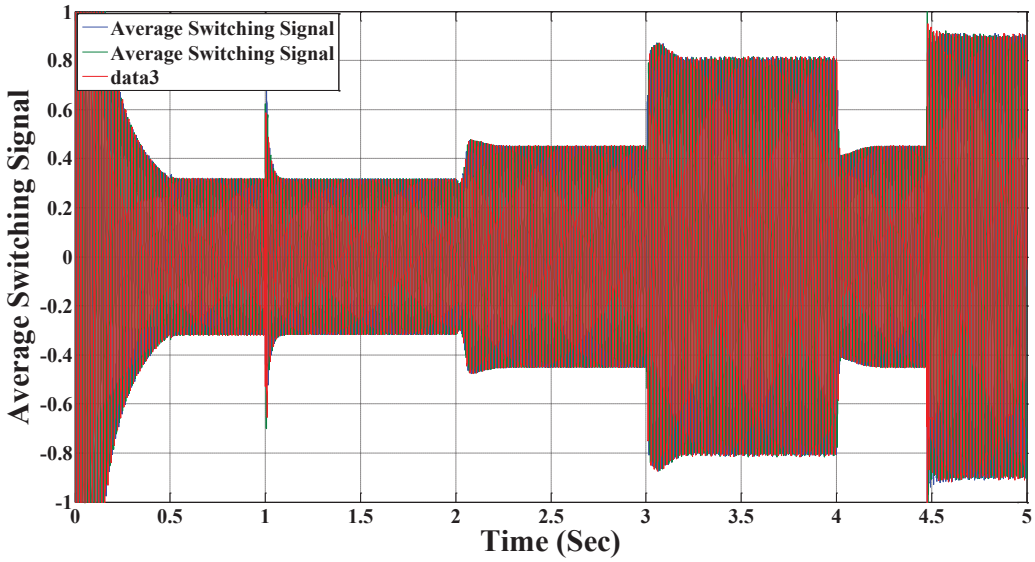
Average Switching Signal
Average Switching Signal
data3
Average Switching Signal
Time (Sec)

(b)

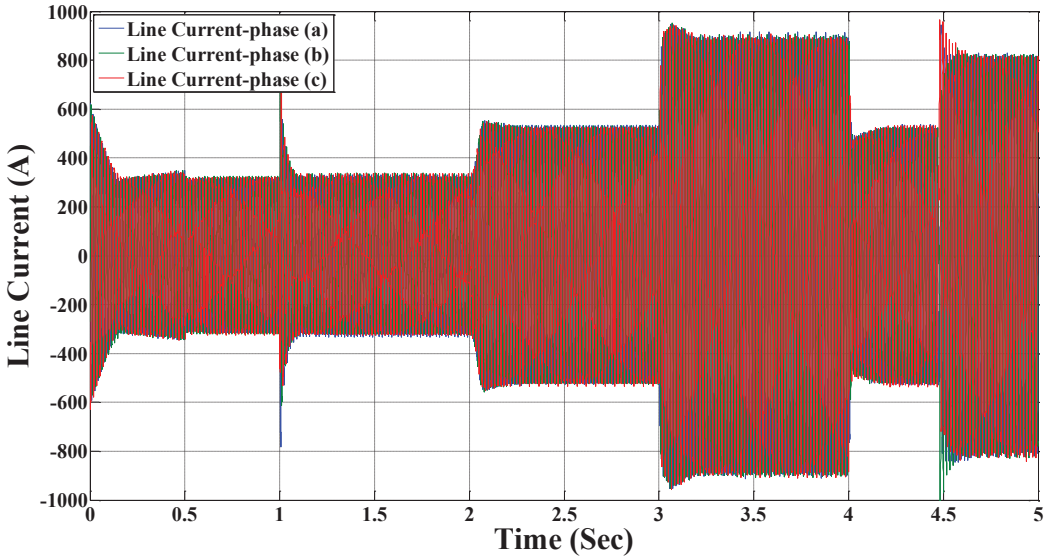
Line Current-phase (a)
Line Current-phase (b)
Line Current-phase (c)
Line Current (A)
Time (Sec)

(c)

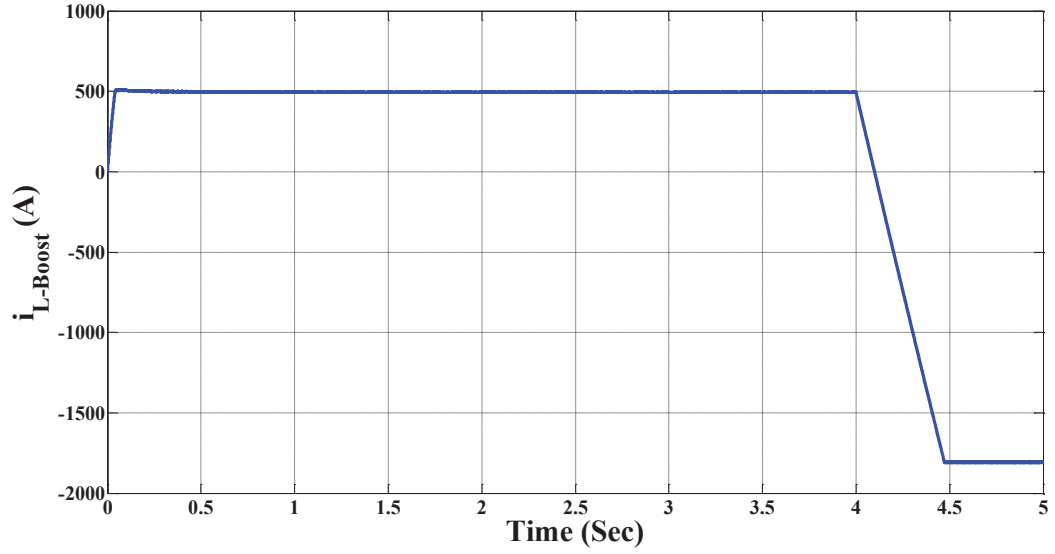

(d)

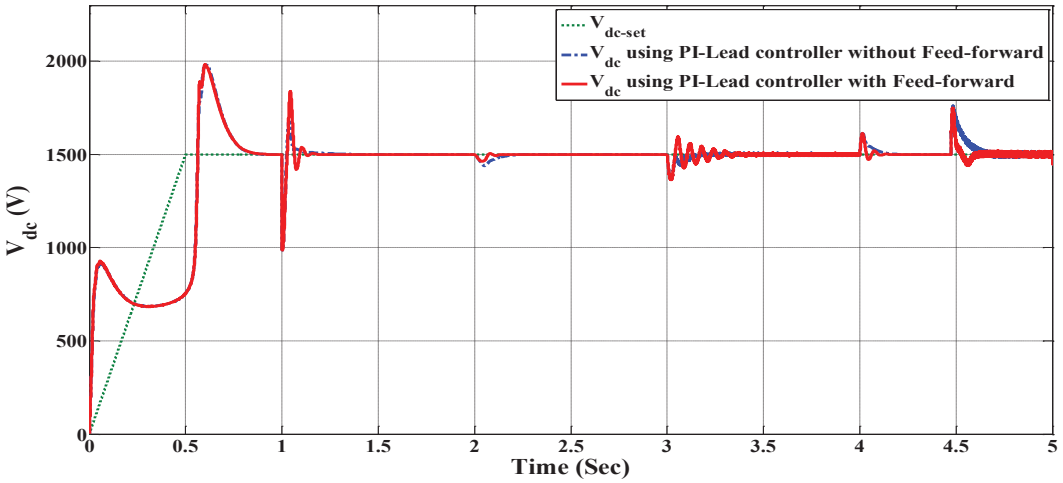

(e)

Fig. 4.8. Event III: Response of the switching model of VSC-m (a) Output dc voltage and its reference signal. (b) Control lever, average switching signal. (c) Line current of VSC-*m*. (d) $i_{L\text{-}Boost}$ of Fig. 6. (e) Response of V_{dc} using PI-Lead controller without and without feed-forward compensation.

4) Event IV: It is a mild asymmetric condition in the ac grid of Zone II; first, the dc energy pool is energized from its initial zero states by a ramp function which starts from zero at t=0s to its final value, 1500 V at t=0.5 s. Then, Zone II is connected to the dc energy pool at t=1 s with zero active and reactive power. At t=2 s, Zone II is commanded to absorb 0.4 MW from the dc-energy-pool and to inject to its ac grid. Thus, VSC-m is working as a rectifier, and it is absorbing 0.4 MW from its ac grid. At t=3 s, an asymmetric condition is induced in the ac grid of Zone II which results in 20% and 35% magnitude reduction of

two phase voltages; such voltage sag lasts till t=3.8 s. As it is clear from Fig. 4.9, the recovery time is around 0.38s, and dc-link voltage quality during such asymmetric condition in grid II is better than that of the robust controller developed in [17] and [63] from overvoltage and under voltage perspectives, and the presence of the 2nd harmonic on the dc-link voltage. Similar results are obtained under harsh asymmetric conditions with 75% magnitude reduction of one phase voltage from t=3 s to t=3.8 s. The dc-link voltage and the ac-grid voltages under this case are shown in Fig. 4.10(a), and Fig. 4.10(d), respectively. Fig. 4.9(e) and Fig. 4.10(e) show the performance of the PI-lead controller under the same conditions. However, both controllers fail to stabilize the system under such large-signal disturbance. Fast variation in the operating point inherently does not match the small-signal model that is used for linear controller design. Further, the assumption that the inner current control loop operates ideally is not valid under large-signal disturbances in the dc-link voltage, which generates un-modeled nonlinear dynamics, which makes the situation worse for PI-lead controller.

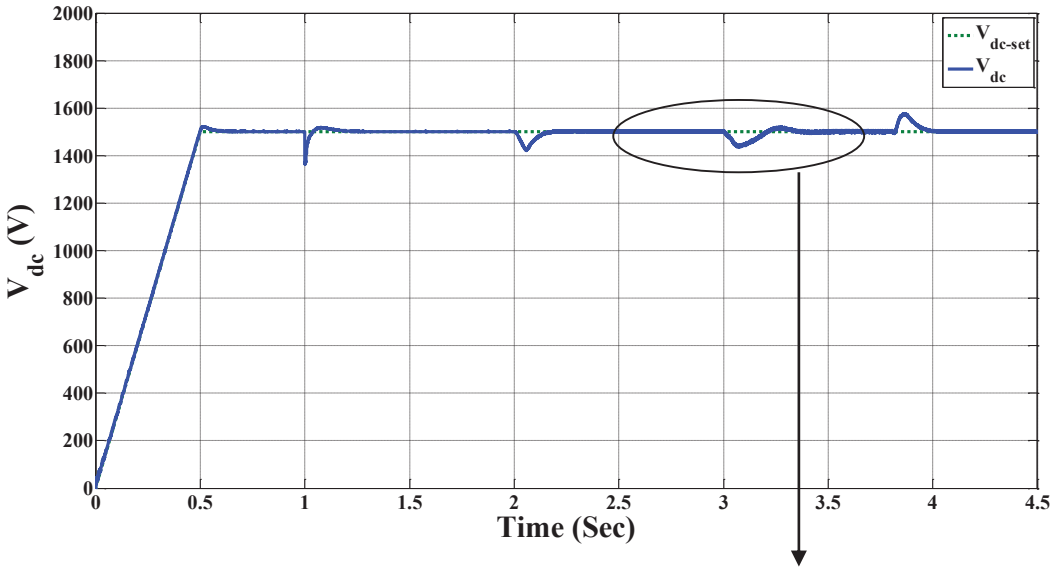

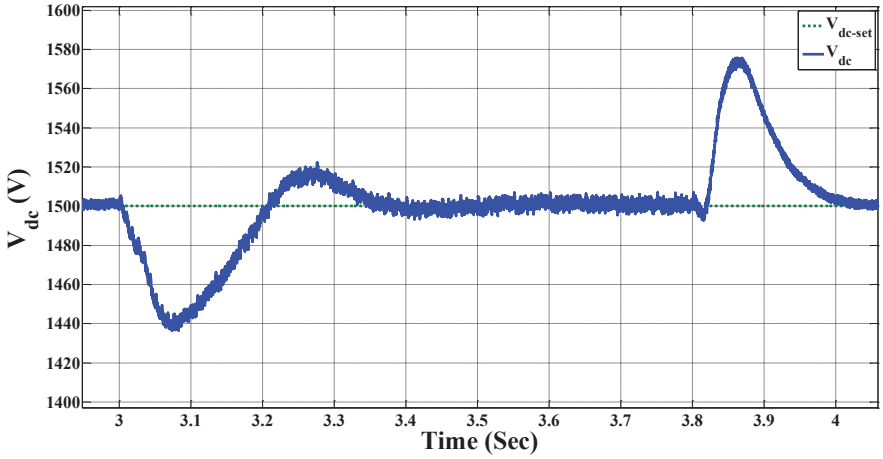
V dc-set
V dc
V dc (V)
Time (Sec)

(a)

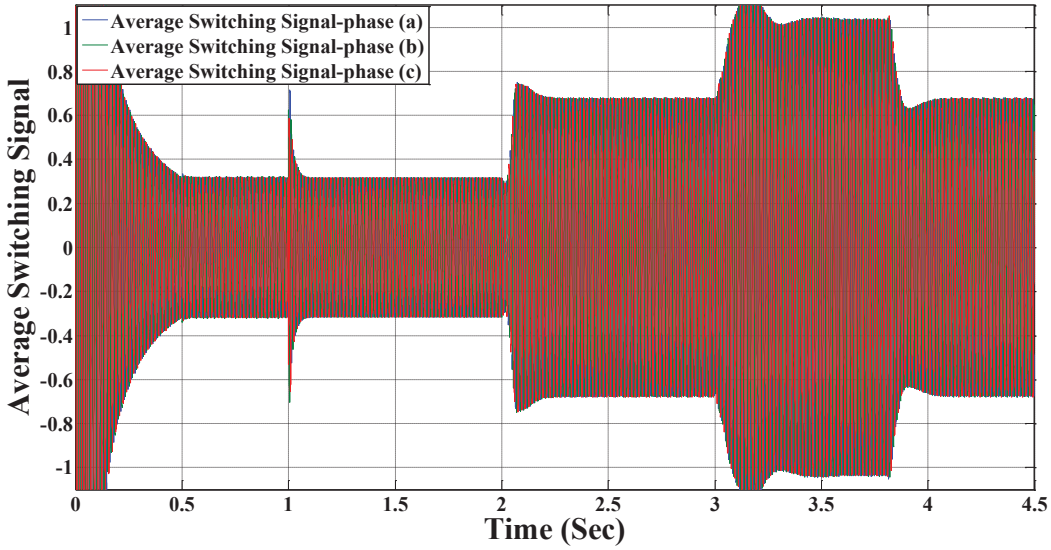
Average Switching Signal-phase (a)
Average Switching Signal-phase (b)
Average Switching Signal-phase (c)
Average Switching Signal
Time (Sec)

(b)

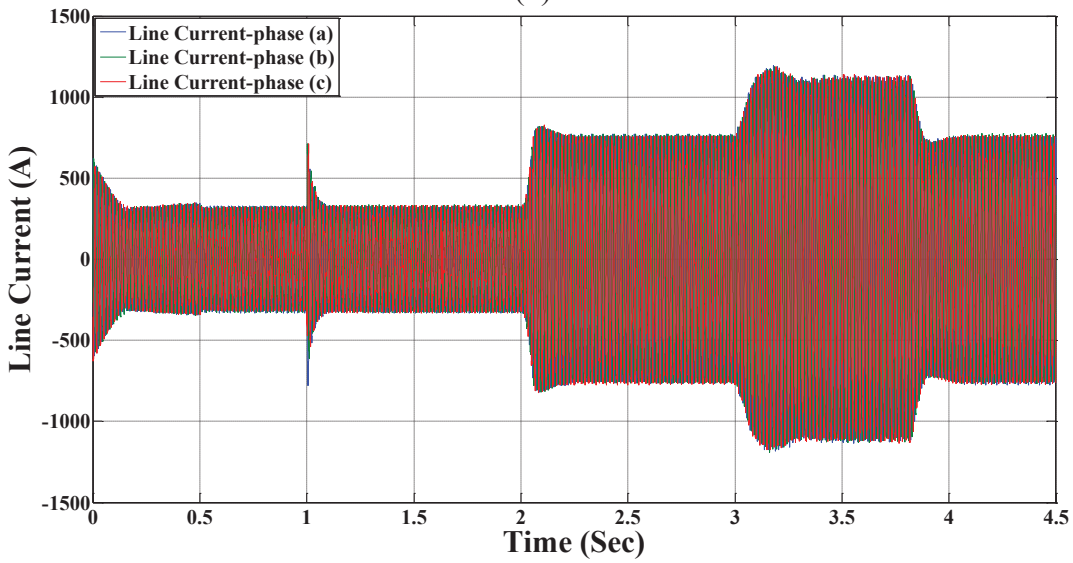
Line Current-phase (a)
Line Current-phase (b)
Line Current-phase (c)
Line Current (A)
Time (Sec)

(c)

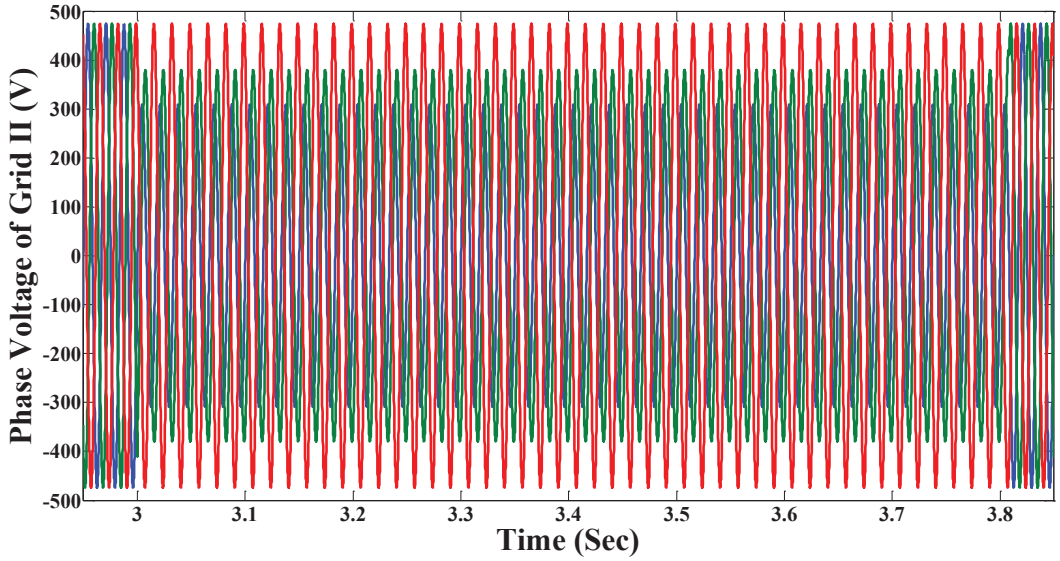

(d)

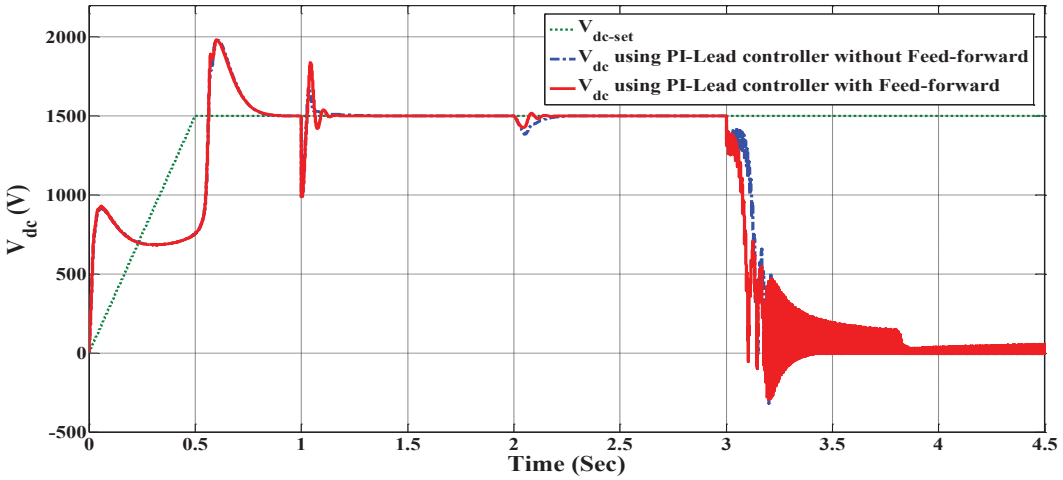

(e)

Fig. 4.9. Event IV: Response of the switching model of VSC-m under mild asymmetric conditions with 20% and 35% magnitude reduction of two phase voltages (a) Output dc voltage and its reference signal. (b) Control lever, average switching signal. (c) Line current of VSC-*m*. (d) Phase voltage of grid II of Zone II. (e) V_{dc} response using PI-Lead controller without feed-forward compensation and with feed-forward compensation.

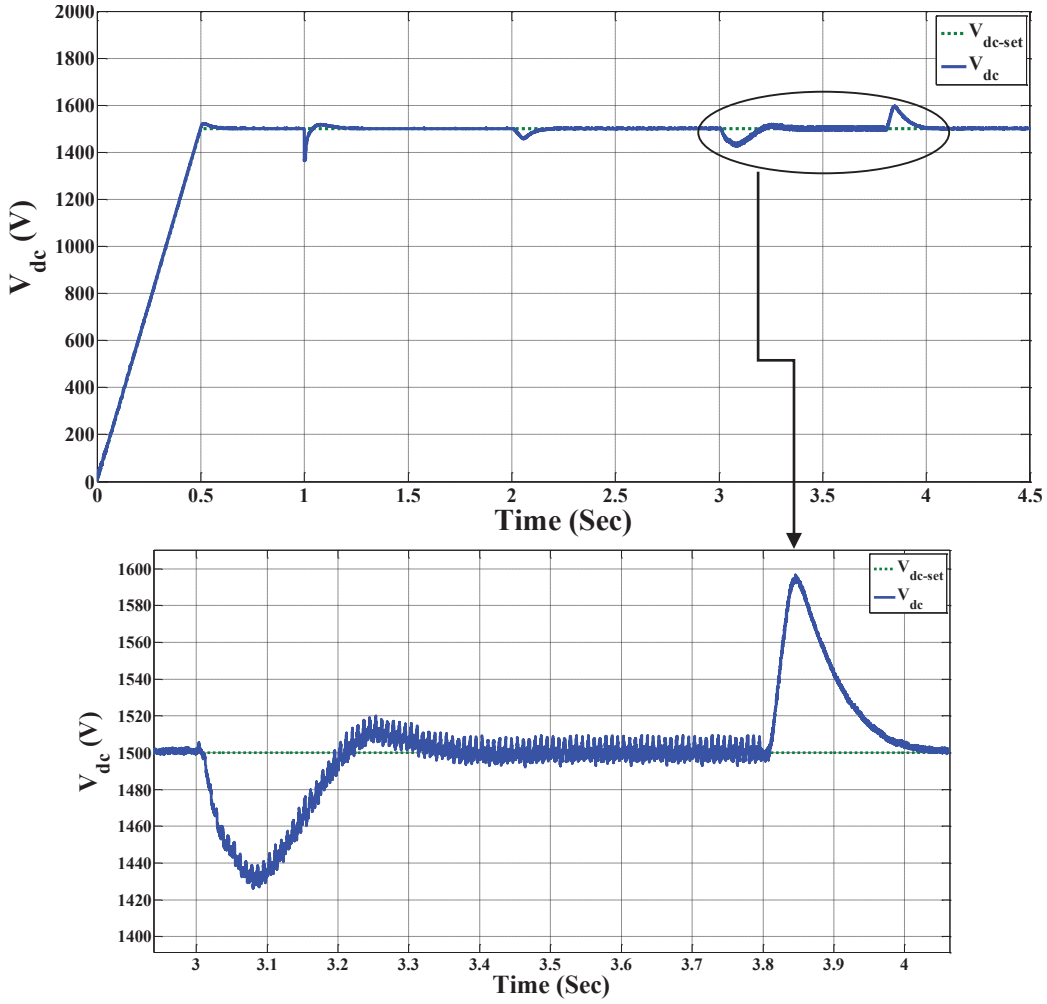
V_dc-set
V_dc
V_dc (V)
Time (Sec)
2000
1800
1600
1400
1200
1000
800
600
400
200
0
0.5
1
1.5
2
2.5
3
3.5
4
4.5
1600
1580
1560
1540
1520
1500
1480
1460
1440
1420
1400
3
3.1
3.2
3.3
3.4
3.5
3.6
3.7
3.8
3.9
4

(a)

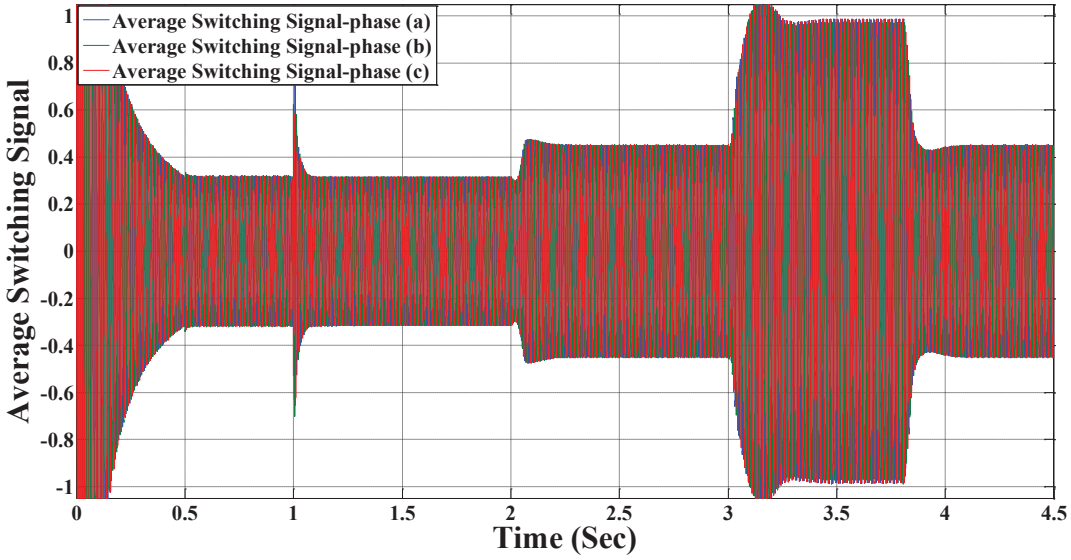
Average Switching Signal-phase (a)
Average Switching Signal-phase (b)
Average Switching Signal-phase (c)
Average Switching Signal
Time (Sec)
1
0.8
0.6
0.4
0.2
0
-0.2
-0.4
-0.6
-0.8
-1
0
0.5
1
1.5
2
2.5
3
3.5
4
4.5

(b)

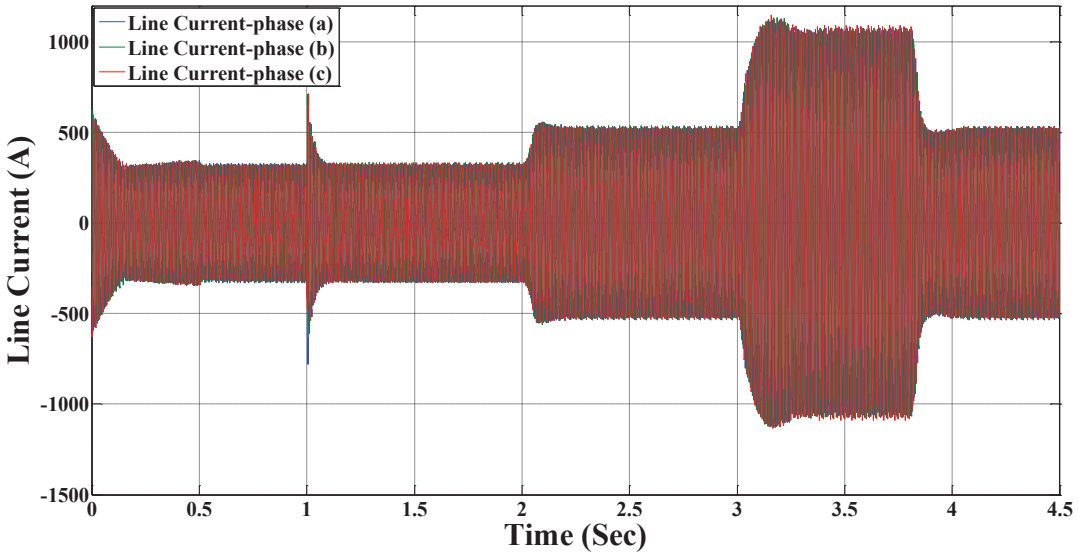
Line Current-phase (a)
Line Current-phase (b)
Line Current-phase (c)
Line Current (A)
Time (Sec)

(c)

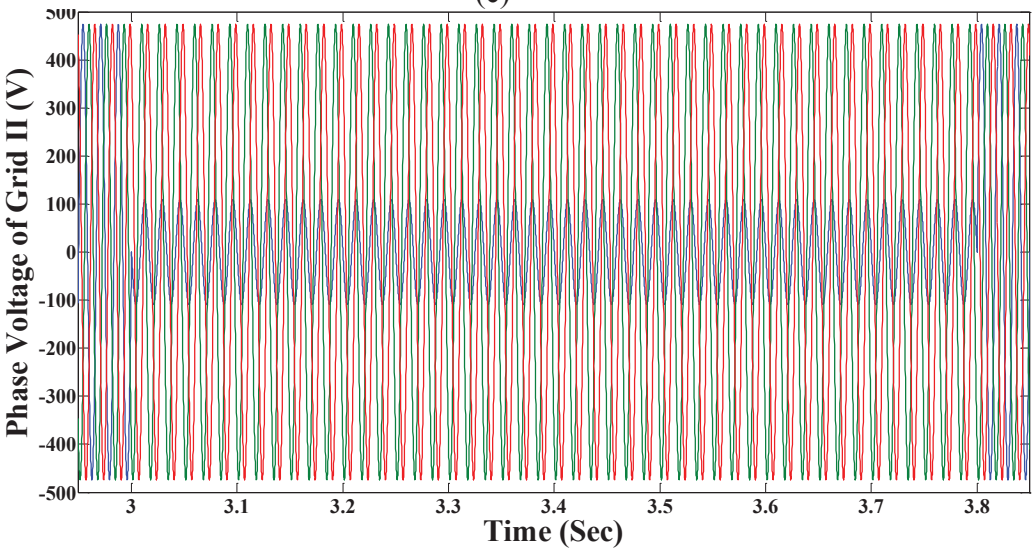
Phase Voltage of Grid II (V)
Time (Sec)

(d)

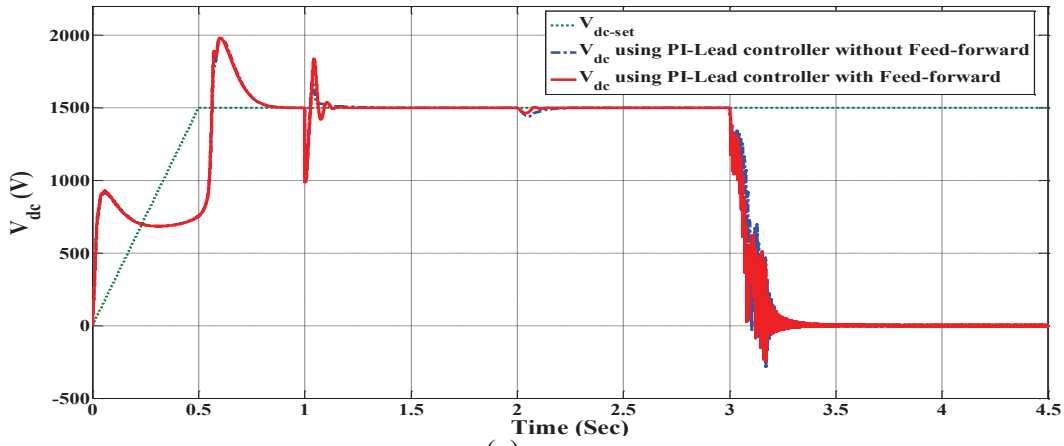

(e)

Fig. 4.10. Event IV: Response of the switching model of VSC-m under harsh asymmetric conditions with 75% magnitude reduction of one phase voltage (a) Output dc voltage and its reference signal. (b) Control lever, average switching signal. (c) Line current of VSC-m. (d) Phase voltage of grid II of Zone II. (e) V_{dc} performance using PI-Lead controller without and with feed-forward compensation.

5) Event V: It is a fault condition in the dc link. When VSC is operating at the rated power, a dc-side fault occurs at t=2.5 s and it cleared at t=2.6 s. The performance of the proposed controller under this event is shown in Fig. 4.11. Fig. 4.11(a) shows the dc-link voltage; Fig. 4.11(b) shows the average switching signal; Fig. 4.11(c) shows the VSC-*m* output current. As it is obvious from Fig. 4.11, it takes 0.4s for VSC-m to restore the dc-link voltage of the dc-energy pool. However, the performance of the dc-energy pool is completely unstable when PI-lead controller is applied. The reason is related to the fact that proposed controller guarantees global stability independent of current controller stability. Indeed, the current controller is unstable if the dc-link voltage is unstable in the conventional cascaded control structure; therefore the master VSC cannot restore itself under harsh disturbances in the dc-link voltage. The global stability of the proposed controller gives it a fault-ride-through feature, which can be an essential requirement in multiterminal dc grids to boost the service reliability under temporary fault conditions.

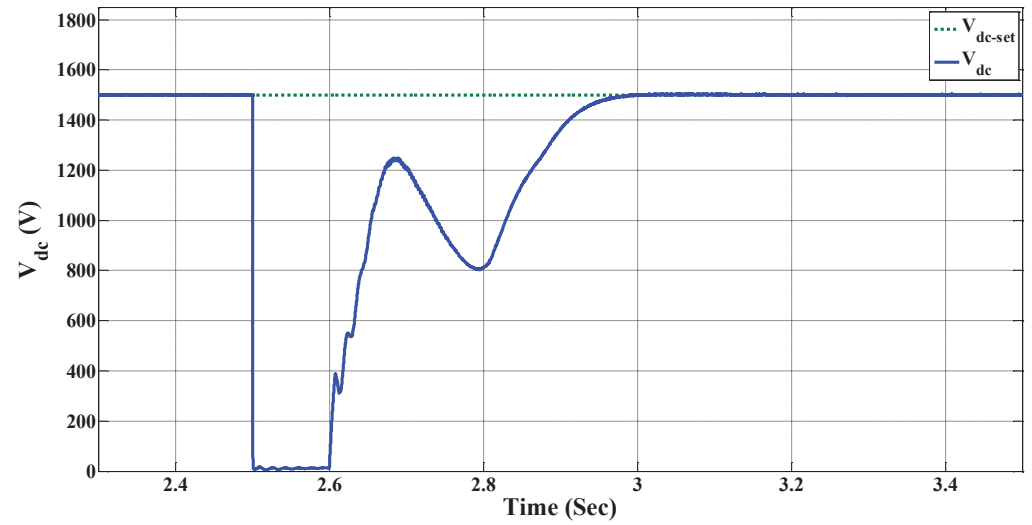
1800
1600
1400
1200
1000
800
600
400
200
0
V_{dc} (V)
2.4
2.6
2.8
3
3.2
3.4
Time (Sec)
V_{dc-set}
V_{dc}

(a)

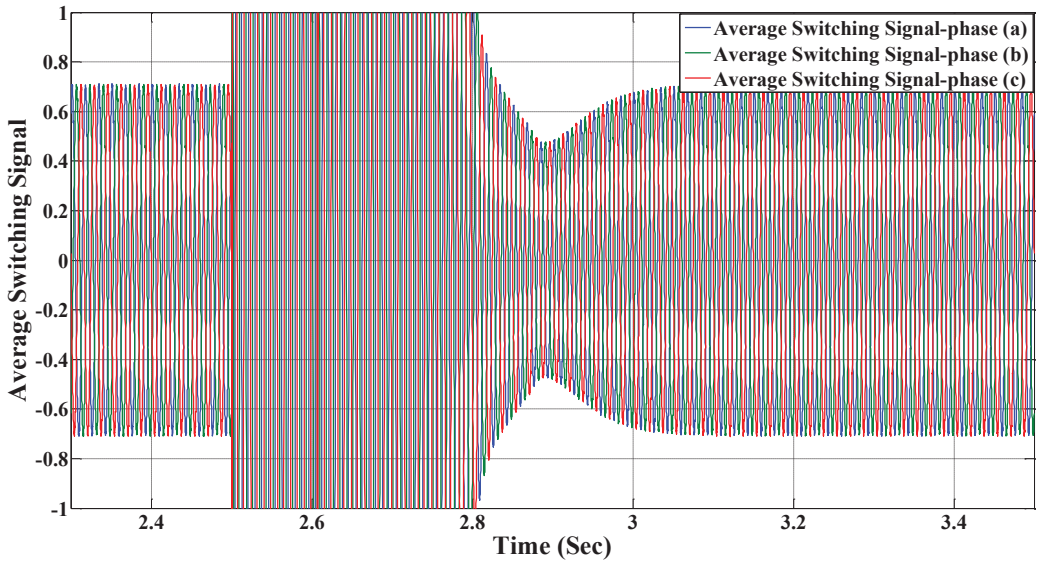
1
0.8
0.6
0.4
0.2
0
-0.2
-0.4
-0.6
-0.8
-1
Average Switching Signal
2.4
2.6
2.8
3
3.2
3.4
Time (Sec)
Average Switching Signal-phase (a)
Average Switching Signal-phase (b)
Average Switching Signal-phase (c)

(b)

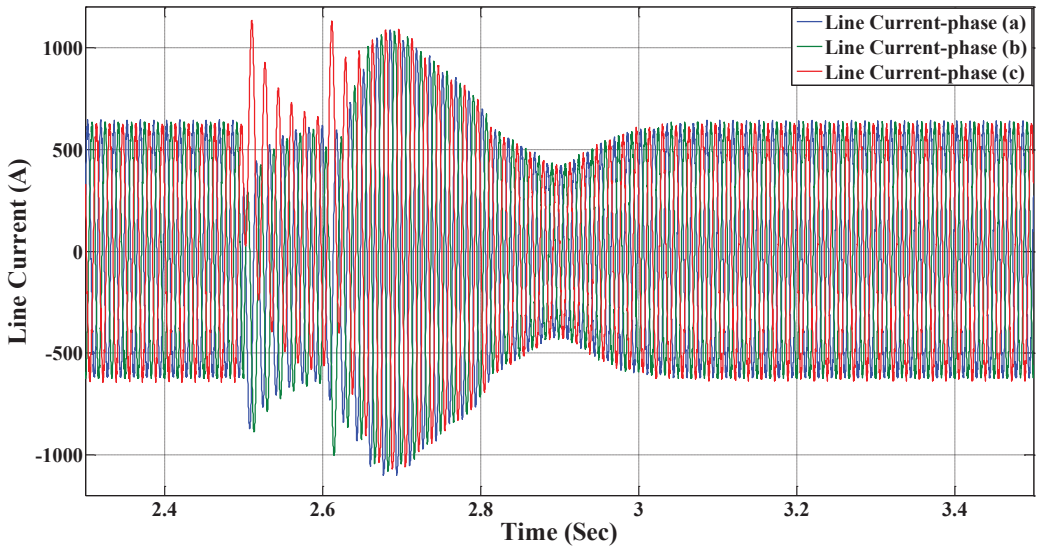

(c)

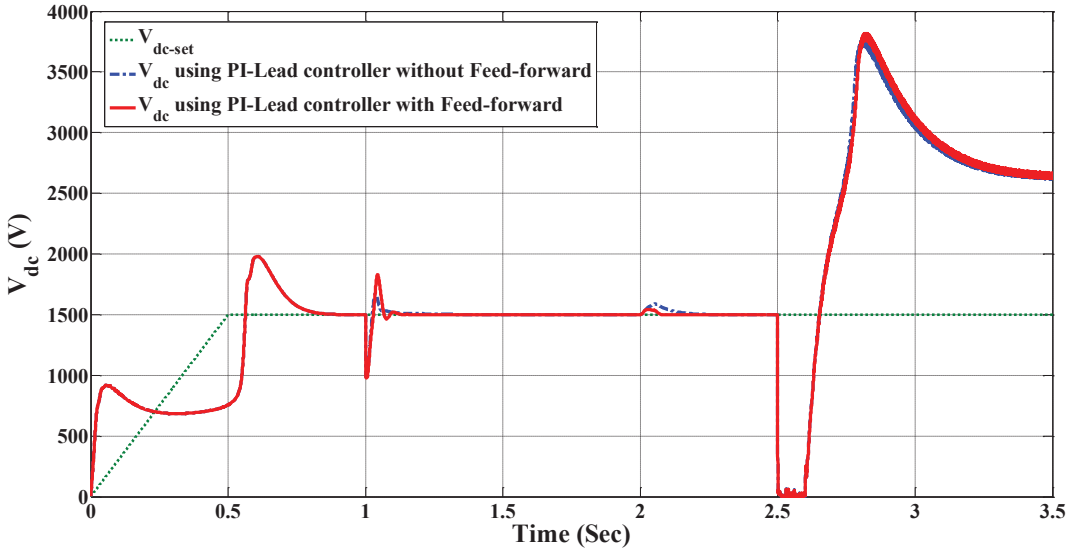

(d)

Fig. 4.11. Event V: Response of the switching model of VSC-m under dc fault condition (a) Output dc voltage and its reference signal. (b) Control lever, average switching signal. (c) Line current of VSC-m. (d) V_{dc} performance using PI-Lead controller without feed-forward compensation and with feed-forward compensation.

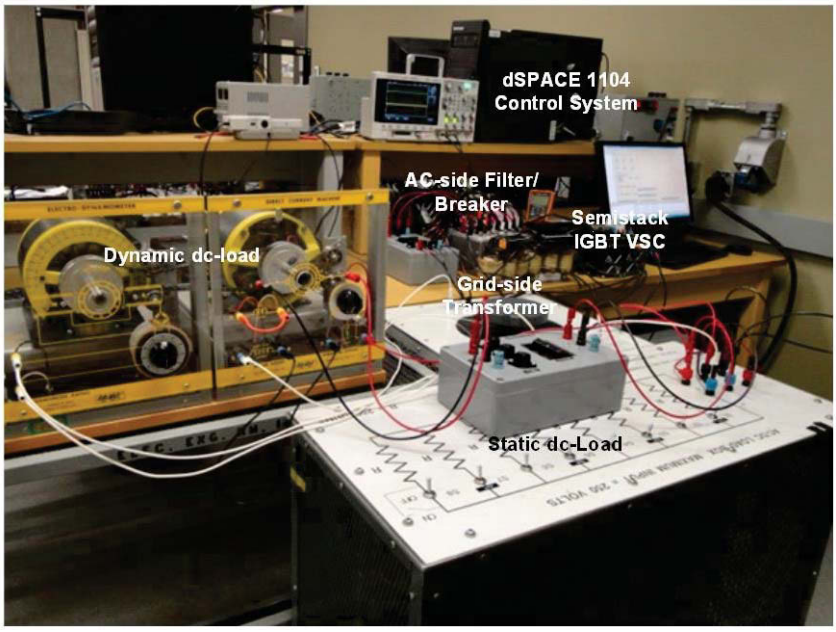

Fig. 4.12. A view of the experimental setup.

4.6 Experimental Results

The experimental setup described in Chapter 2, demonstrated in Fig. 4.12, is used.

The control performance of the proposed controller is compared with that of the conventional PI-lead controller with feed-forward control to enhance the disturbance rejection performance. The PI-lead controller is designed in the rectification mode and at the maximum converter current. i.e., 20 A. The proposed controller is designed following the detailed procedure presented in Section 4.4. Key results are reported as follows.

Fig. 4.13 shows the control performance of the master VSC with PI-lead dc-link voltage controller in the rectification mode during the start-up of the dc micro-grid. As can be seen, during large and dynamic variation of the operating point of the converter, instability is yielded due to the large and fast drift in the operating point induced by the starting of the dynamic load. It should be noted that instability occurs even when the converter current is less than the rated current. This indicates that system instability can be yielded under fast and large changes of the operating point even if the PI-lead controller is designed at the rated current. The phenomenon is attributed to the nonlinearity of the dc-link voltage dynamics, i.e., the system does not exhibit small-signal dynamics that can be stabilized by a simple PI-lead controller. The dc-link voltage collapses and the converter is tripped due to control system

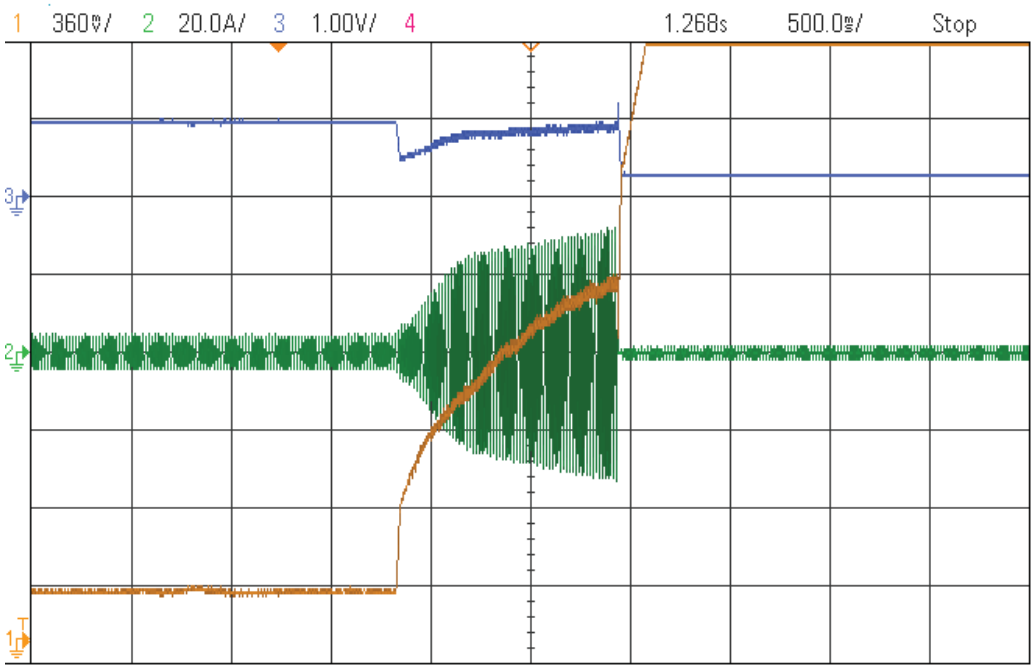

Fig. 4.13. Experimental results of the PI-lead controller during starting of the dc micro-grid load (dc motor load); Channel 3 (top): V_{dc} in per-unit Channel 2 (middle): one phase ac-line current; Channel 1 (bottom): I_d in per-unit generated by PI-lead controller.

instability. Fig. 4.14 shows the control performance with the PI-lead controller when the load current is changing moderately, in terms of magnitude and ramp rate by controlling the dynamometer load. As the PI-lead controller is designed with a lead-filter, stable control performance is yielded even at the rated load current and when the load is increasing gradually. However, the disturbance rejection performance in terms of the voltage dip and recovery time is weak. The proposed controller has been tested under the same event (i.e., in the rectification mode during the start-up of the dc energy pool and its dynamic load) and the corresponding results are shown in Fig. 4.14 and Fig. 4.16. In spite of the dynamic and large variation in the dc micro-grid load current (motor starting current), the proposed controller offers robust stability against operating point variation and preserves the stability of the dc-link voltage because of the property of the equilibrium to equilibrium manoeuvre of the passivity-based controller. As compared with the PI-lead controller, Fig. 4.13, the suggested controller significantly contributes to the network stability under the occurrence of dynamic and large changes in the equilibrium as well as start-up situation. To gauge the robustness of the proposed controller against parametric uncertainty in the equivalent dc-link capacitance, the effective dc-link capacitance is doubled.

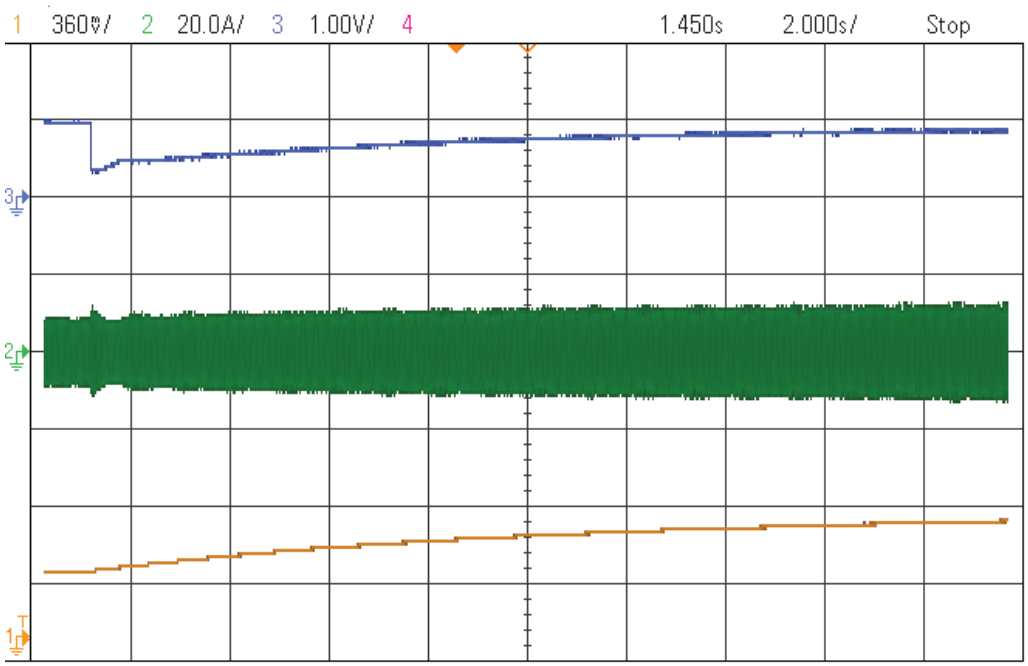

Fig. 4.14. Experimental results of the PI-lead controller with moderate changes of the dc micro-grid load (dc motor load); Channel 3 (top): V_{dc} in per-unit, Channel 2 (middle): one phase ac-line current; Channel 1(bottom): I_d in per-unit generated by PI-lead controller.

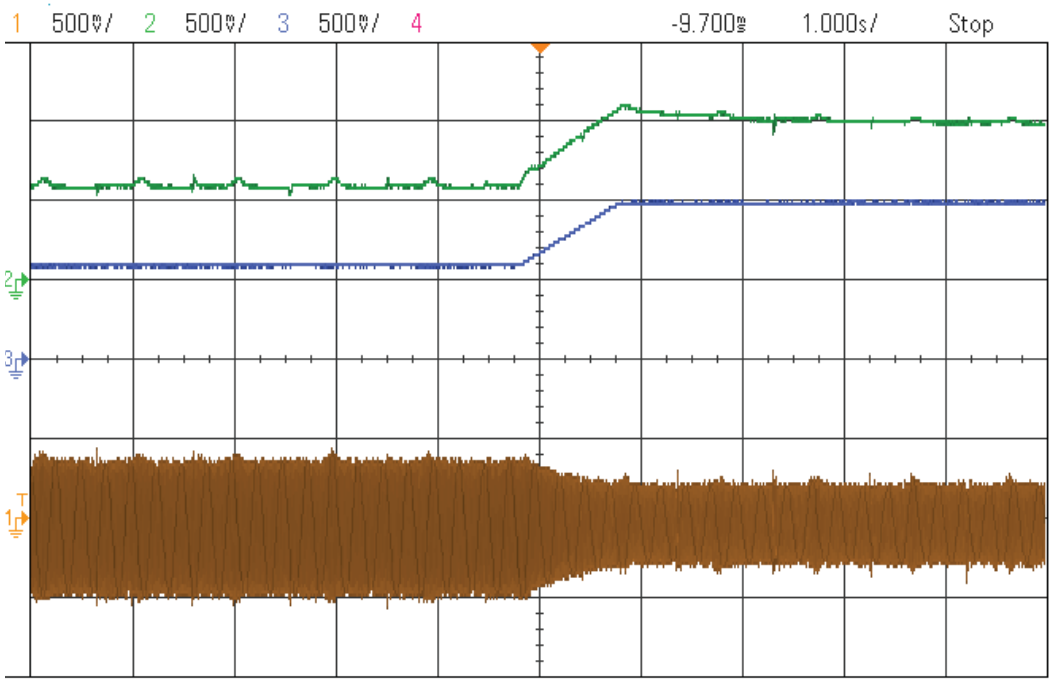

Fig. 4.15. Experimental results of the proposed controller during start-up the dc energy pool; Channel 2 (top): V_{dc} in per-unit, Channel 3 (middle): $V_{dc\text{-}set}$, Channel 1 (bottom): average switching signal.0.5 V/Div, 1.0 s/Div.

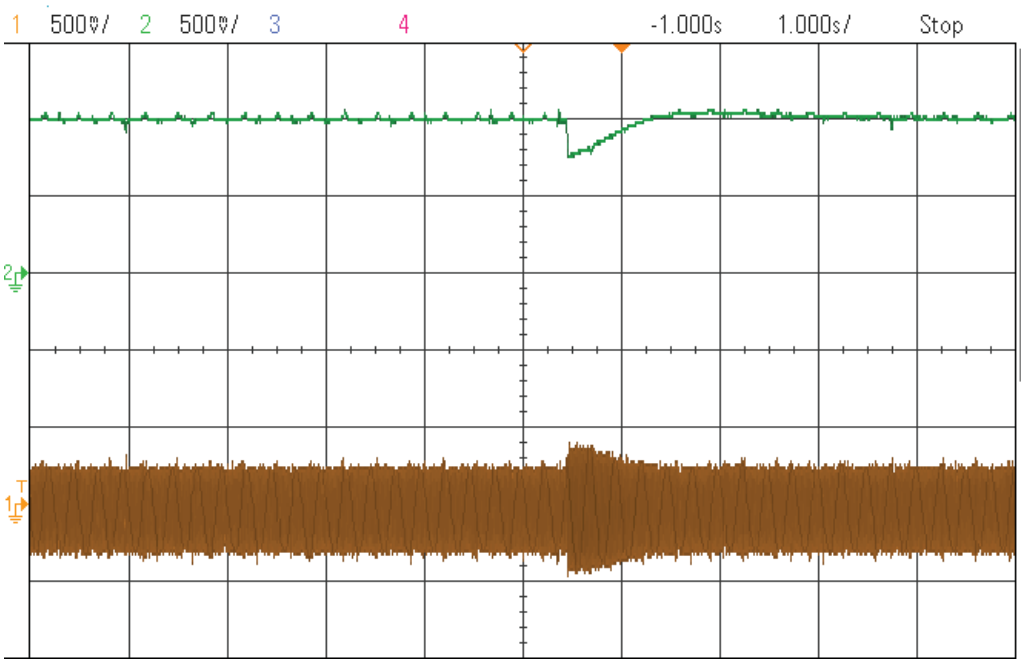

Fig. 4.16. Experimental results of the proposed controller during starting of the dc micro-grid load (dc motor load); Channel 2 (top): V_{dc} in per-unit, Channel 1 (bottom): average switching signal. 0.5 V/Div, 1.0 s/Div.

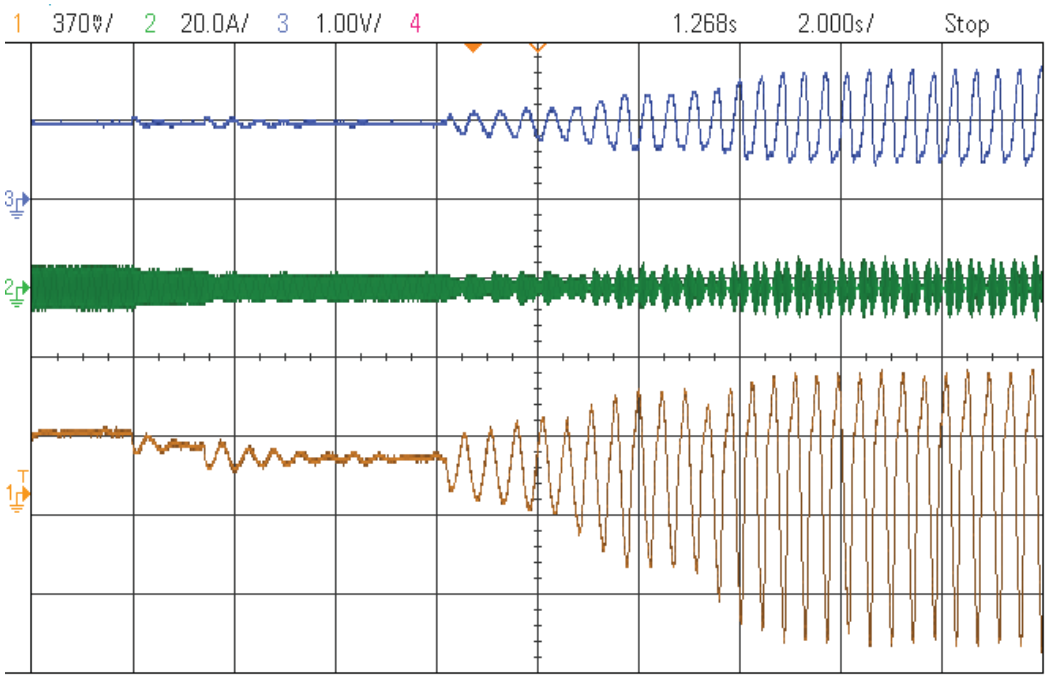

Fig. 4.17. Experimental results of the PI-lead controller with uncertainty in the dc-link capacitance; Channel 3 (top): V_{dc} in per-unit, Channel 2 (middle): one phase ac-line current; Channel 1(bottom): I_d in per-unit generated by PI-lead controller. (0.5 V/Div, 2.0 s/Div).

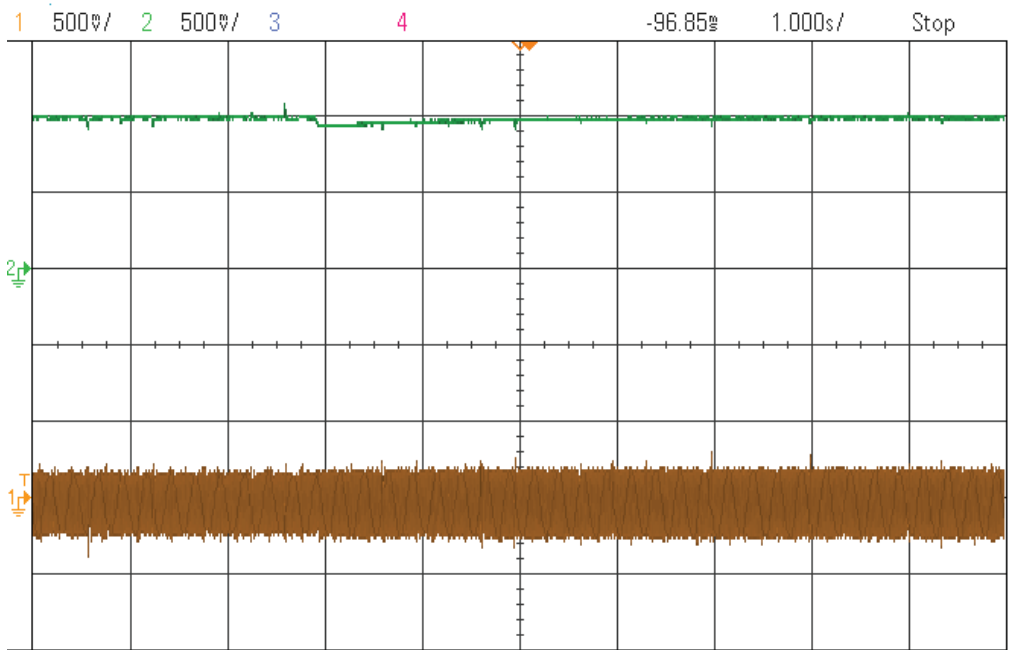

Fig. 4.18. Experimental results of the proposed controller during variations of static dc loads and existing of uncertainty in the dc-link capacitance as well as operating point variations; Channel 2 (top): V_{dc} in per-unit, Channel 1 (bottom): average switching signal. (0.5 V/Div, 1.0 s/Div).

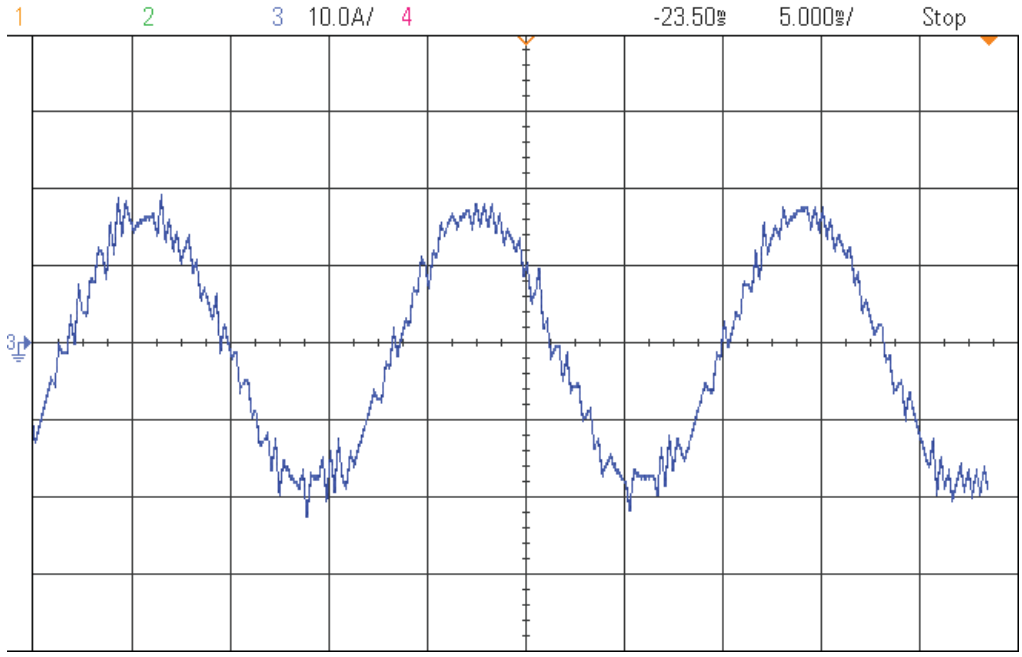

Fig. 4.19. The waveform of the line current of VSC-*m*; Channel 3 10 A/Div., Horizontal: 5 ms/Div.

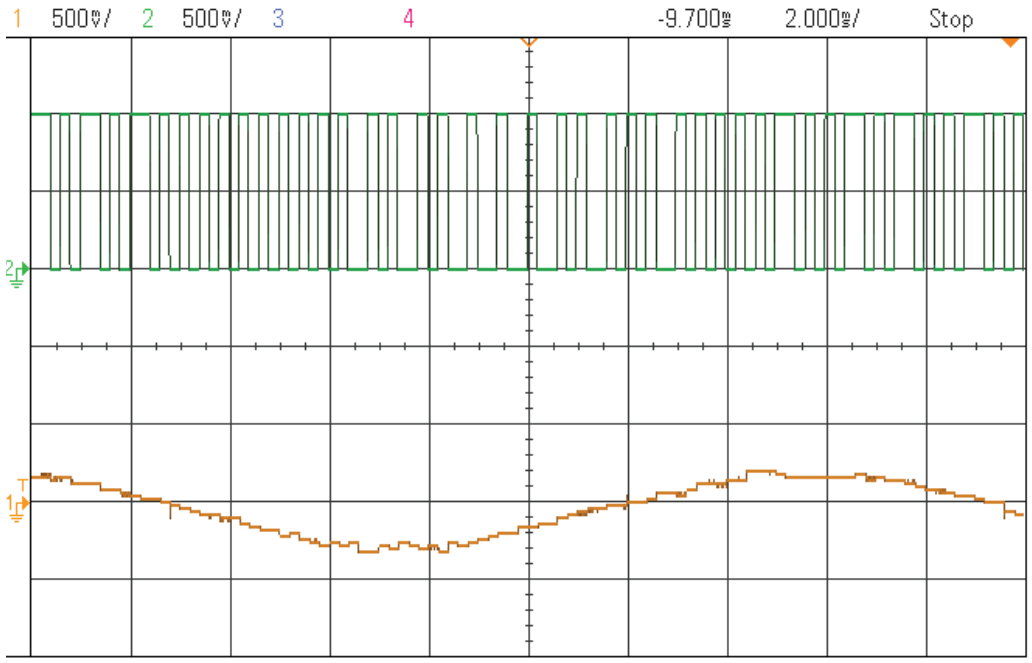

Fig. 4.20. The waveform the control signals under normal operation; Channel 2 (top): switching signal, Channel 1 (bottom): average switching signal.
Scale of Channel 1 and Channel 2 is 0.5 V/Div., Horizontal: 2 ms/Div.

To test the robustness of the PI-lead controller against variation in the effective dc-link capacitance, the effective dc-link capacitance is doubled. Fig. 4.17 shows the control performance under this parametric uncertainty condition and with the PI-lead controller. As predicted by the theoretical analysis, the conventional PI-lead controller can't preserve system stability under parametric uncertainty. The dc-link voltage oscillations are in the range of 40 rad/s, which is agree with the theoretical analysis. The simulation results in Fig. 4.9-Fig. 4.11 show that the conventional PI-lead controller cannot guarantee system stability under wide-range of operating point variation and parametric uncertainty in the effective dc-link capacitance. The proposed controller has been tested under the same event. Fig. 4.18 shows the control performance of the proposed controller under such parametric uncertainty. The system is excited by successive increase of the dc-side load. Due to the passivity-based design approach using complete nonlinear system dynamics as well as equilibrium to equilibrium manoeuvres property, the proposed controller shows robust control performance.

To test the power quality when sigma-delta modulator has been employed Fig. 20 and Fig. 21 are provided. Fig. 20 shows the typical line current of the VSC-*m*, which shows high-quality

current injected with total-harmonic distortion less than 5%. Fig. 21 shows both average and quantized typical switching signal employed in VSC-*m*.

4.7 Parameters of Simulated System, Fig. 4.5

Zone I and II: VSC-*m* and VSC-PQ: Rated Power=0.5 MVA, Grid 1, Grid 2 Voltage=580 V at 60 Hz; R_p=250 Ω; R=0.06 mΩ; L=200 μH; C_{eq}=12,500 μF, C_{new}=6000 μF, Switch resistance=1.0 mΩ; Diode resistance=1.0 mΩ; Switching Frequency=10 kHz*; k*, positive constant parameter of the proposed controller=0.01

Zone II Current Controller Parameters: K_p=0.06 Ω; K_i=0.7 Ω/s.;

Zone III: Power rating =0.9 MW, ESS and load voltage 500 V-dc, C_L=1000 μF, C_H=6000 μF, L_1=100 mH, R_{DC}=1 Ω, K_p(mode1)=0.4, K_i(mode1)=4×10^{-4}, K_p(mode2)=0.0133, K_i(mode2)=0.0533, V_{L_Ref}=500 V, i_{L_Ref}=1800 A.

DC-pool: Rated voltage=1,500 V, dc-cable length=50 km, R_{cable}=0.82 mΩ/km, C_{cable}= 0.014 μF/km, L_{cable}=0.98 μH/km

4.8 Conclusion

In this chapter, a dc-link voltage controller has been designed based on the average nonlinear dynamics of the master VSC employed in multiterminal dc grids, and the control efforts have been synthesized using general switching functions. Consequently, the synthesized controller has not suffered from small-signal control design issues, and the global stability has been guaranteed. Besides, the conventional power-balance and cascaded control-structure has been avoided; therefore, unmodeled nonlinear dynamics associated with a power balance framework and presence of inner loop current controller has inherently been mitigated. The controller has been synthesized using passivity-based criteria, and it has been implemented via sigma-delta modulation to induce sliding regiment required for the variable structure nature of the VSC. As a result, the existing EtoE maneuver of the proposed controller can handle the dependency of the controlled dynamics on the operating point variation. Finally, the global stability has been guaranteed using the simultaneous convergence of all states, including V_{dc}, to their equilibrium points. The performance of the proposed controller has also been compared with a PI-lead controller under the same test conditions. The proposed controller provides excellent tracking

and disturbance rejection performances, and it offers very effective fault-ride-thorough performance against ac- as well as dc-side faults. These features remarkably enhance the reliability of the dc-link voltage which is essential to stabilize the performance of MTDC grids. Besides, simulation and experimental results have been provided to verify the validity and effectiveness of the proposed controller.

Chapter 5

Dynamics and Robust Vector Control of a Very Weak Grid-Connected VSC Considering the Phase Locked Loop Dynamics

5.1 Introduction

To overcome the drawbacks associated with existing vector controllers under weak and very weak grid conditions (detailed in Chapter 1), a different approach is proposed in this chapter. Firstly, a detailed small-signal model for the ac-bus voltage dynamics, including the PLL dynamics, is developed in this chapter. Then, it is shown that the linearized dynamics strongly depends on the converter operating point due to the converter-grid coupling via the PLL. The dynamics can be unstable as well as non-minimum phase at different operating points and different values of the grid impedance. Therefore, synthesizing a robust ac-bus voltage controller against EtoE maneuvers and variation in the grid inductance is a must to ensure converter stability. Secondly, the augmented ac-bus voltage model, including the PLL dynamics, is used to design a robust ac-bus voltage controller. Because the developed model includes the PLL dynamics, the developed controller inherently stabilizes the negative impact of the PLL on the converter stability. The proposed controller is synthesized using the μ-synthesis approach [48] by minimizing the H_∞ norm from the exogenous disturbances to the output ac-bus voltage. The controller is synthesized to yield a robust control performance against operating point variation and uncertainty in the grid impedance. Therefore, the proposed controller facilities effective integration of VSCs under a wide range of grid impedances, and it yields excellent dynamic performance. By the proposed approach, the need to change the structure and/or the parameters of the standard vector controllers (e.g., current controller, PLL, and dc-link voltage controller) to

facilitate very weak grid integration is eliminated. A theoretical analysis and comparative simulation and experimental results are provided to show the effectiveness of the proposed controller.

5.2 Modeling of a Weak-grid-connected VSC

A typical 3.0 MVA, 580 V_{ac}, 1750 V_{dc}, 60 Hz weak grid-connected bidirectional VSC is shown in Fig. 5.1. The converter and system parameters are given in Section 5.7. An *L*-based ac filter with equivalent inductance *L* (representing the summation of filter and transformer leakage inductances) and equivalent resistance *R*, which is commonly used in high-power converters, is adopted. Furthermore, if high-order ac filters with appropriate filter resonance damping are adopted—e.g., *LC* or *LCL* filter—it has been found that their impact on the dominant converter dynamics is negligible owing to the frequency-scale separation between the *LCL* filter dynamics and the outer control loops (e.g., dc-link voltage and ac-bus voltage control loops). In other words, the bandwidths of the outer control loops are usually much less than the bandwidth of the inner current control loop; in this range, the ac-side filter behaves mainly as an *L* filter [92]. Therefore, the use of an *L* filter in this analysis is not a restricting assumption. The internal losses of the VSC are modeled by equivalent resistance r_{on} on the ac side, and a current source on the dc side to model the power loss P_{loss} due to the reverse recovery and tailing current processes of the power switches. As shown in Fig. 5.1, the external power on the dc side can be positive or negative for inversion and rectification operation, respectively. The ac system is modeled by its Thevenin's equivalent circuit composed of a grid inductance L_{grid}, and internal voltage V_s. It should be noted that it is extremely difficult and impractical to design the converter control system based on the overall exact system dynamics, which contain both the dc and ac grid dynamics. Therefore, the equivalent model of the ac grid, as viewed from the PCC is usually used during the analysis and control design stages [38]-[47]. The grid system is mainly inductive, which is the typical case in high power converters that are usually connected to highly inductive grids at the sub-transmission or transmission levels. A standard grid-oriented vector control scheme is adopted in this study owing to its widespread acceptance in the power converter industry. In this scheme, two proportional-integral (PI) current controllers (inner controllers), an outer dc-link voltage controller, and an outer ac-bus voltage controller are

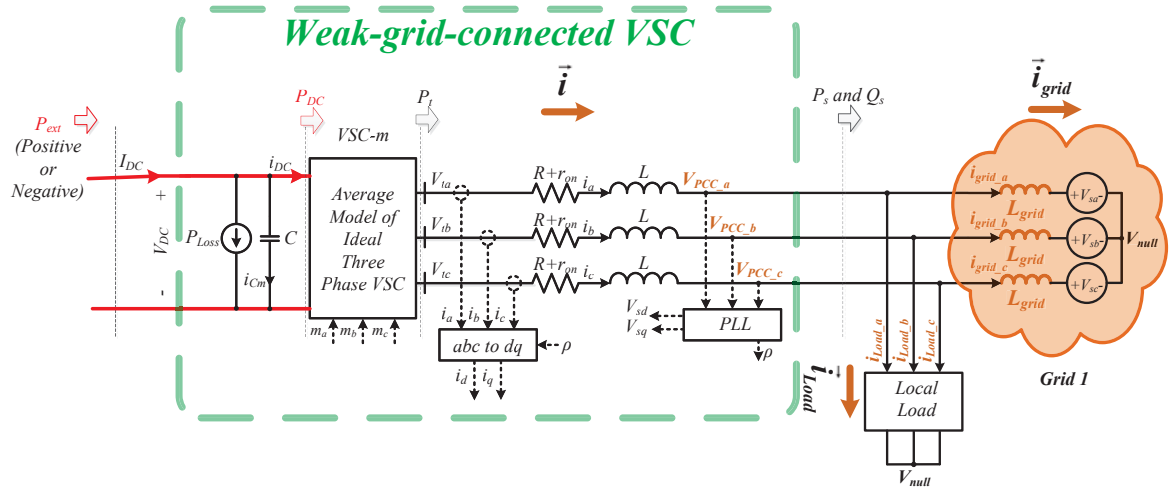

Fig. 5.1. VSC connected to a weak ac grid.

adopted. The dc-link voltage controller generates the *d*-axis reference current component, whereas the *q*-axis reference current component is generated by the ac-bus voltage controller for voltage regulation. A standard *dq*-based three-phase PLL [109] is adopted to extract the synchronization angle (ρ).

From the control perspective, the VSC can be controlled to 1) regulate the dc-link voltage and ac-bus voltage (V_{dc} and V_{ac} control), 2) inject or absorb preset values of active and reactive powers at a constant dc-link voltage (PQ-bus control), or 3) inject or absorb a preset value of active power and control the ac-bus voltage at a constant dc-link voltage (PV-bus control). In a weak grid connection, ac-bus voltage control yields higher stability margins are compared to the reactive power injection mode [46]. Furthermore, with dc-link voltage control under weak grid conditions, the coupling between the VSC and grid is higher than that in the case of preset active power control. This is because the dc-link voltage controller dynamically changes the active power to balance the power flow across the dc-link capacitor. Therefore, the more comprehensive case of V_{dc} and V_{ac} control is considered in this study.

5.2.1 AC Side Dynamics

In this section, the ac side dynamics in a weak-grid-connected VSC considering the PLL dynamics is modeled. Referring to Fig. 5.1, the relation between the grid voltages at the PCC, $V_{PCC\text{-}a}$, $V_{PCC\text{-}b}$, $V_{PCC\text{-}c}$, and the grid internal voltages, $V_{s\text{-}a}$, $V_{s\text{-}b}$, $V_{s\text{-}c}$,can be given by

$$\begin{cases} V_{PCC-a} = L_{grid}\dfrac{di_{grid-a}}{dt} + V_{s-a} \\ V_{PCC-b} = L_{grid}\dfrac{di_{grid-b}}{dt} + V_{s-b} \\ V_{PCC-c} = L_{grid}\dfrac{di_{grid-c}}{dt} + V_{s-c} \end{cases} \tag{5-1}$$

$$\begin{cases} i_{grid-a} = i_a - i_{Load-a} \\ i_{grid-b} = i_b - i_{Load-b} \\ i_{grid-c} = i_c - i_{Load-c} \end{cases} \tag{5-2}$$

where i_a, i_b, i_c are the converter currents, $i_{grid\text{-}a}$, $i_{grid\text{-}b}$, $i_{grid\text{-}c}$ are the grid side currents, and $i_{Load\text{-}a}$, $i_{Load\text{-}b}$, $i_{Load\text{-}c}$ are the local load currents. By employing the space vector representation, (5-3) and (5-4) can be written

$$\vec{V}_{PCC} = L_{grid}\frac{d\vec{i}_{grid}}{dt} + \vec{V}_s \tag{5-3}$$

$$\vec{i}_{grid} = \vec{i} - \vec{i}_{Load} \tag{5-4}$$

As an arbitrary operating point, $\vec{V}_s$ can be considered as

$$\vec{V}_s = V_{s\_\max} e^{j(\omega_0 t + \theta_0)} \tag{5-5}$$

where V_{s_max} is the amplitude of $\vec{V}_s$, θ_0 is the initial phase angle of $\vec{V}_s$, and ω_0 is the steady-state angular frequency of the ac system.

In the *dq*-frame that rotates with the synchronization angle generated by the PLL (ρ), (5-3) and (5-4) are transformed to (5-6) and (5-7)

$$V_{PCC\_dq} e^{j\rho} = L_{grid}\frac{d}{dt}(i_{grid\_dq} e^{j\rho}) + V_{s\_\max} e^{j(\omega_0 t + \theta_0)} \tag{5-6}$$

$$i_{grid\_dq} = i_{dq} - i_{Load\_dq} \tag{5-7}$$

It should be noted that under perfect synchronization, ρ converges to $\omega_0 t + \theta_0$. At this condition, the *q*-component of the grid voltage at the PCC $V_{s\_\max}\sin(\omega_0 t + \theta_0 - \rho)$ will be equal to zero. However, during transients, a perfect synchronization is not achieved, particularly in weak grid conditions, where the PLL is driven by the grid voltage at the PCC. Therefore, the PLL dynamics should be included in the ac-bus voltage dynamic model.

In a standard *dq*-based three-phase PLL, the rate of change of the synchronization angle, or

the estimated angular frequency $\omega(t)$, is generated by processing the *q*-component of the grid voltage at the PCC, $V_{PCC\_q}(t)$, by a PLL filter with a transfer function *H*(*s*) as shown in (5-8) [109],

$$\frac{d\rho}{dt} = \omega(t) = H(p)V_{PCC\_q}(t) \tag{5-8}$$

where *p* is the time-derivative operator. In industrial power converters, the PLL filter can be presented by a PID controller in the form $H(s) \triangleq \frac{K_D s^2 + K_P s + K_I}{s}$

After straightforward mathematical manipulation as well as considering the PLL dynamics in (5-8), the PCC voltage dynamics can be presented by:

$$\begin{cases} V_{PCC\_d} = L_{grid}\dfrac{di_{grid\_d}}{dt} - L_{grid}\omega_0 i_{grid\_q} + V_{s\_\max}\cos(\omega_0 t + \theta_0 - \rho) \\ V_{PCC\_q} = L_{grid}\dfrac{di_{grid\_q}}{dt} + L_{grid}\omega_0 i_{grid\_d} + V_{s\_\max}\sin(\omega_0 t + \theta_0 - \rho) \\ i_{grid\_d} = i_d - i_{Load\_d} \\ i_{grid\_q} = i_q - i_{Load\_q} \end{cases} \tag{5-9}$$

As shown in (5-8) and (5-9), the PCC voltage dynamics is nonlinear. To analyze the system dynamics and design a linear robust controller, which can be a very attractive controller in industrial applications due to its simplicity and fixed structure, the nonlinear dynamics in (5-8) and (5-9) can be linearized around an equilibrium point as shown in (5-10), where the subscript "0" indicates the steady-state operating point at linearization, and "~" indicates a small-signal perturbed variable around the operating point.

$$\begin{cases} V_{PCC\_d} = V_{PCC\_d0} + \tilde{V}_{PCC\_d} \\ V_{PCC\_q} = V_{PCC\_q0} + \tilde{V}_{PCC\_q} \\ i_{grid\_d} = I_{grid\_d0} + \tilde{I}_{grid\_d} \\ i_{grid\_q} = I_{grid\_q0} + \tilde{I}_{grid\_q} \\ \omega_0 t + \theta_0 - \rho = -(\rho_0 + \tilde{\rho}) \\ \dfrac{d\rho}{dt} = \omega_0 + \dfrac{d\tilde{\rho}}{dt} \Rightarrow \omega = \omega_0 + \tilde{\omega} \end{cases} \tag{5-10}$$

After mathematical manipulations, the linearized dynamics of (5-8) and (5-9) can be represented in the complex frequency domain as:

$$\tilde{V}_{PCC\_d}(s) = L_{grid} s\tilde{I}_{grid\_d}(s) - L_{grid}\omega_0\tilde{I}_{grid\_q}(s) - L_{grid}(I_{grid\_q0}s + \omega_0 I_{grid\_d0})\tilde{\rho}(s) \tag{5-11.a}$$

$$\begin{aligned}\tilde{V}_{PCC\_q}(s) = {} & L_{grid} s\tilde{I}_{grid\_q}(s) + L_{grid}\omega_0\tilde{I}_{grid\_d}(s) \\ & + [L_{grid} I_{grid\_q0}s - (V_{PCC\_d0} + L_{grid}\omega_0 I_{grid\_q0})]\tilde{\rho}(s)\end{aligned} \tag{5-11.b}$$

$$\tilde{\rho}(s) = \frac{H(s)}{s}\tilde{V}_{PCC\_q}(s) \tag{5-11.c}$$

where $\begin{cases}\tilde{I}_{grid\_d}(s) = \tilde{I}_d(s) - \tilde{I}_{Load\_d}(s) \\ \tilde{I}_{grid\_q}(s) = \tilde{I}_q(s) - \tilde{I}_{Load\_q}(s)\end{cases}$ & $\begin{cases}I_{grid\_d0} = I_{d0} - I_{Load\_d0} \\ I_{grid\_q0} = I_{q0} - I_{Load\_q0}\end{cases}$.

The synchronization angle dynamics can be obtained by combining (5-11.b) and (5-11.c) as follows:

$$\tilde{\rho}(s) = \frac{H(s)\left[L_{grid} s\tilde{I}_{grid\_q}(s) + L_{grid}\omega_0\tilde{I}_{grid\_d}(s)\right]}{\left[s - H(s)[L_{grid} I_{grid\_q0}s - (V_{PCC\_d0} + L_{grid}\omega_0 I_{grid\_q0})]\right]} \tag{5-12}$$

By substituting (5-12) in (5-11.a), the linearized PCC voltage dynamics can be given by

$$\begin{aligned}\tilde{V}_{PCC\_d}(s) = {} & \frac{Q(s)}{s - H(s)B(s)}\tilde{I}_d(s) - \frac{Q(s)}{s - H(s)B(s)}\tilde{I}_{Load\_d}(s) \\ & + \frac{M(s)}{s - H(s)B(s)}\tilde{I}_q(s) - \frac{M(s)}{s - H(s)B(s)}\tilde{I}_{Load\_q}(s)\end{aligned}$$

where

$$\begin{aligned}Q(s) &\triangleq L_{grid}\{s^2 - [sB(s) - \omega_0 C(s)]H(s)\} \\ M(s) &\triangleq L_{grid}\{-\omega_0 s + [\omega_0 B(s) - sC(s)]H(s)\} \\ C(s) &\triangleq L_{grid}(I_{grid\_q0}s + \omega_0 I_{grid\_d0}) \\ B(s) &\triangleq L_{grid} I_{grid\_q0}s - (V_{PCC\_d0} + L_{grid}\omega_0 I_{grid\_q0})\end{aligned} \tag{5-13}$$

Equation (5-13) represents the ac-bus voltage dynamics in a weak-grid-connected VSC. In (5-13), two signals, $\tilde{I}_d$ and, $\tilde{I}_q$ can be controlled by the VSC, whereas the other two signals, $\tilde{I}_{Load\_d}$ and $\tilde{I}_{Load\_q}$, are treated as disturbance signals. Owing to the fact that $\tilde{I}_d$ is used to regulate the dc-link voltage and the higher sensitivity of changes in V_{PCC_d} to changes in the reactive power $\tilde{I}_q$ in highly inductive grids, $\tilde{I}_q$ is selected as the control lever. Accordingly,$\tilde{I}_{Load\_d}$, $\tilde{I}_{Load\_q}$, and $\tilde{I}_d$ are treated as disturbances in (5-13), and the third transfer function in (5-13) represents the plant model.

It is worthy to mention that the relatively high switching frequency of modern VSCs facilitates the realization of fast current control dynamics so that the VSC can be considered as a

current amplifier within the closed-loop current control bandwidth (usually in the range of 15%-20% of the switching frequency). Therefore, from the outer ac-bus voltage control and dc-link voltage control perspectives, the inner current control loop dynamics can be modeled by a first-order low-pass-filter with a small time-constant τ_i [20]. Accordingly, the ac-bus voltage dynamics in response to the actual control level, the reference *q*-component of the converter current $\tilde{I}_q^*(s)$, can be given by

$$\begin{aligned}\tilde{V}_{PCC\_d}(s) = &\frac{Q(s)}{s-H(s)B(s)}\tilde{I}_d(s) - \frac{Q(s)}{s-H(s)B(s)}\tilde{I}_{Load\_d}(s) \\ &+ \frac{M(s)}{(\tau_i s+1)(s-H(s)B(s))}\tilde{I}_q^*(s) - \frac{M(s)}{s-H(s)B(s)}\tilde{I}_{Load\_q}(s)\end{aligned} \tag{5-14}$$

As shown in (5-14), in a stiff grid condition, i.e., L_{grid}=0, the PCC voltage is stiff and cannot be controlled by the converter currents. That is why a large converter rating is needed to control the grid voltage if the grid impedance is relatively small. Under weak grid conditions, the PLL couples the PCC voltage dynamics along with the converter dynamics. Such coupling increases as the grid impedance increases, and should be accounted for to stabilize the converter performance under very weak grid conditions. The SCC-R, which is defined as the grid short-circuit capacity at the PCC to the rated power of the VSC, is usually used to gauge the grid stiffness. Mathematically, the SCC-R can be defined as follows:

$$SCC\text{-}R = \frac{1.5\dfrac{V_{PCC-d}^2}{\omega_0 L_{grid}}}{VSC_{Capacity}} \tag{5-15}$$

The grid system is considered very weak when SCC-R = 1, and weak when $2 \leq$ SCC-R ≤ 3. The coupling between the converter and grid due to grid impedance significantly decreases for SCC-R > 3 [42].

5.2.2 DC Side Dynamics

The linearized dc-link voltage dynamics of a grid-connected VSC considering the instantaneous power of the ac filter can be given by [64]

$$\tilde{V}_{DC}^2(s) = -\frac{1.5R_P L I_{d0} s + 1.5R_P(V_{sd0} + 2RI_{d0})}{(\tau_i s + 1)(0.5R_P C s + 1)}\tilde{I}_d^*(s) - \frac{1.5R_P L I_{q0} s + 3RR_P I_{q0}}{0.5R_P C s + 1}\tilde{I}_q(s) + \frac{R_P}{0.5R_P C s + 1}\tilde{P}_{ext}(s) - \frac{1.5R_P I_{d0}}{0.5R_P C s + 1}\tilde{V}_{PCC\_d}(s) \quad (5\text{-}16)$$

where V_{DC} is the dc-link voltage, C is the dc-link capacitance, R_P is an equivalent resistance representing the converter losses, subscript "0" indicates the steady-state operating point at linearization, and "~" indicates a small-signal perturbed variable around the operating point.

Equation (5-16) relates the dynamics of V^2_{DC} to the control lever of the dc-link voltage $\tilde{I}_d^*$, as well as disturbance signals, $\tilde{I}_q$, $\tilde{P}_{ext}$, and $\tilde{V}_{PCC\_d}$. Therefore, the dynamics of the grid-voltage at the PCC affects the dc-link voltage dynamics, and can destabilize the converter; i.e., if $\tilde{V}_{PCC\_d}$ is unstably unbounded, then $\tilde{V}_{DC}$ is unstable too. Thus, a robust ac-bus voltage controller that yields close ac-bus voltage control characteristics enhances the dc-link voltage stability and overall converter system stability.

5.3 Dynamic Analysis of a Weak-grid-connected VSC

5.3.1 Model Validation

Before analyzing the dynamics characteristics of the ac-bus voltage dynamics in (5-14), model validation is essential. For this purpose, the model in (5-14) is evaluated at different critical operating points, and its response is compared to that of the detailed nonlinear time-domain simulation model. Both models have the same parameters (as given in Section 5.7) and are excited by the same disturbances. The models are tested under three values of the SCC-R; i.e., SCC-R = 1, 2 and 3. At each SCC-R level, the active power operating point is changed whereas the reference ac-bus voltage is set to 1.0 per-unit (pu). As will be shown by the eigenvalues analysis and frequency response, the dynamics in (5-14) can have unstable modes and non-minimum phase behavior at certain operating points and low SCC-R levels. Therefore, both the linearized and detailed models are tested with the feedback stabilizing controller described in Section 5.4.

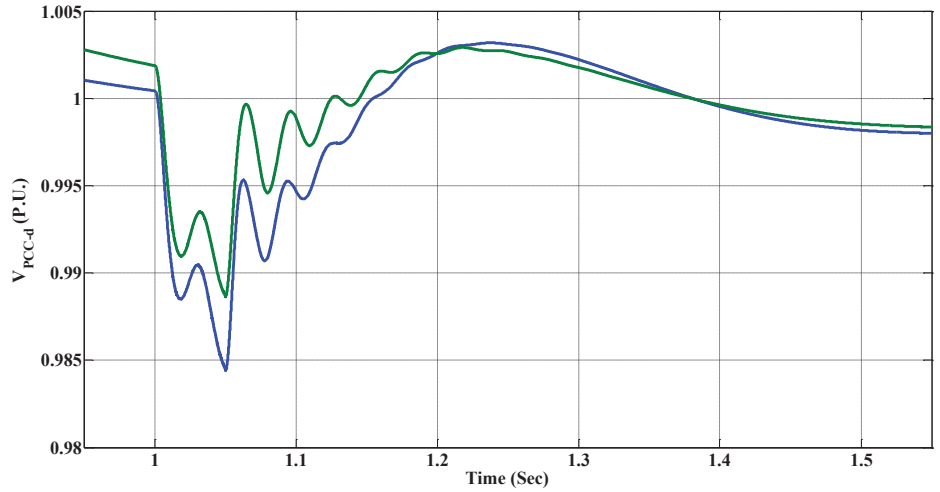

(a)

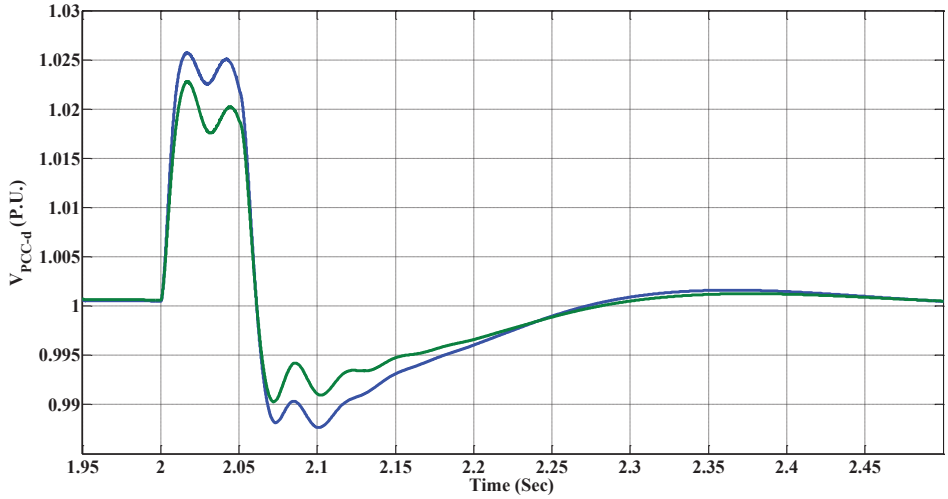

(b)

Fig. 5.2. Model validation results at SCC-R=3. (a) The converter operating point changes from 0 MW, 2.40 Mvar to -1.50 MW, +2.45 Mvar. (b) The converter operating point changes from -1.50 MW, +2.45 Mvar to +1.50 MW, +2.40 Mvar. Blue curves: small-signal model, green curves: detailed nonlinear time-domain simulation model.

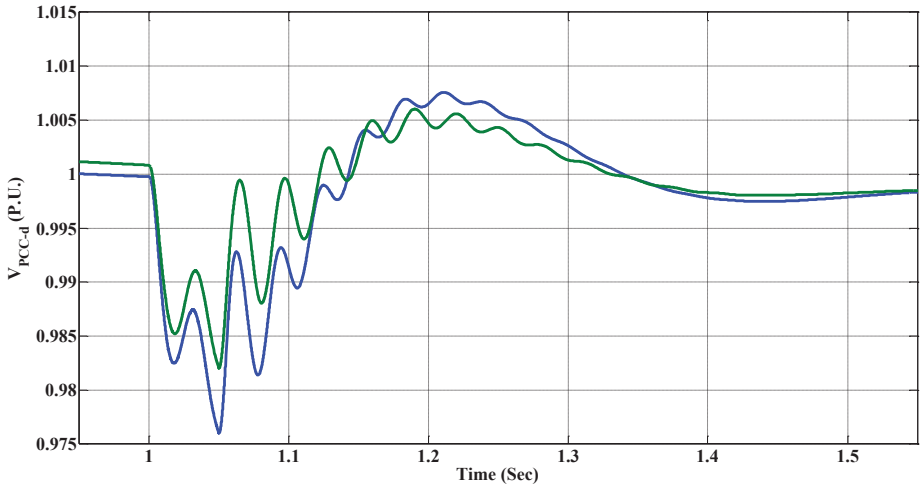

(a)

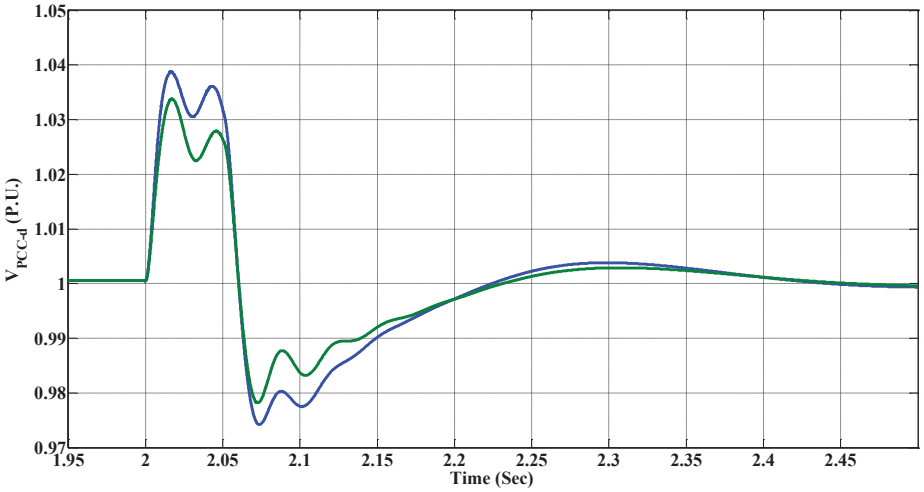

(b)

Fig. 5.3. Model validation results at SCC-R=2 (a) The converter operating point changes from 0 MW, +1.80 Mvar to -1.5 MW, +1.90 Mvar. (b) The converter operating point changes from -1.5 MW, +1.90 Mvar to +1.5 MW, +1.80 Mvar. Blue curves: small-signal model, green curves: detailed nonlinear time-domain simulation model.

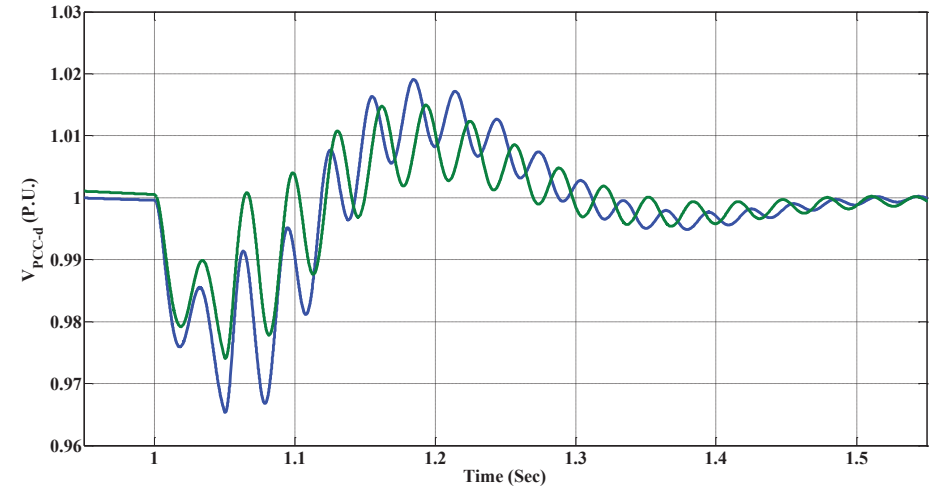

(a)

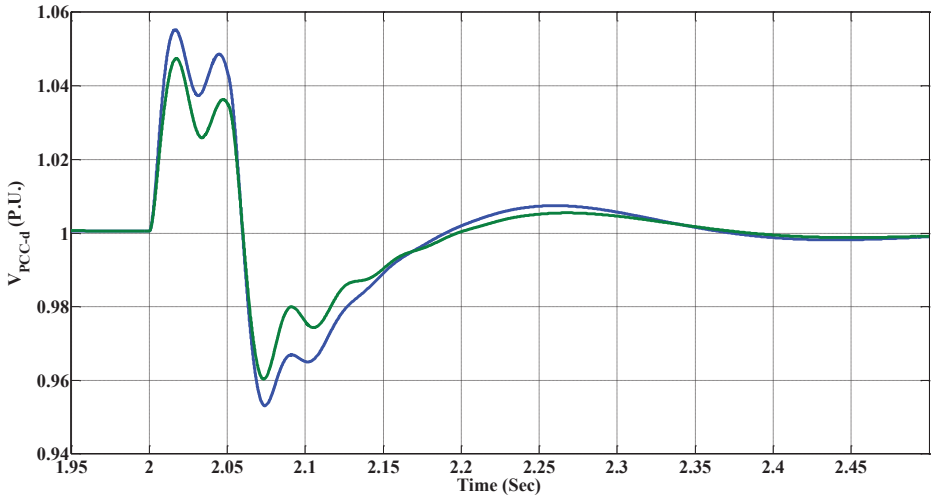

(b)

Fig. 5.4. Model validation results at SCC-R=1. (a) The converter operating point changes from 0 MW, +1.40 Mvar to -1.5 MW, +1.6 Mvar. (b) The converter operating point changes from -1.5 MW, +1.6 Mvar to +1.5 MW, +1.4 Mvar. Blue curves: small-signal model, green curves: detailed nonlinear time-domain simulation model.

Fig. 5.2 to Fig. 5.4 show the responses of both the small-signal model (blue curves) and the detailed nonlinear time-domain simulation model (green curves) at SCC-R = 3, 2, and 1, respectively. The figures show very good compatibility between the nonlinear plant and the linearized at different operating points and different SCC-R values. The number and instants of occurrence of the oscillations are very well matched and consistent in the responses of both models. Consequently, the results reveal the validity of the linearized model.

5.3.2 Eigenvalues and Sensitivity Analysis

From (5-14), the open-loop transfer function representing the ac-bus voltage dynamics can be given by

$$\frac{\tilde{V}_{PCC\_d}(s)}{\tilde{I}_q^*(s)} = \frac{L_{grid}\left\{-\omega_0 s + \omega_0\left(L_{grid}I_{grid\_q0}s - (V_{PCC\_d0} + L_{grid}\omega_0 I_{grid\_q0})\right)H(s)\right\}}{(\tau_i s+1)\left(s - H(s)\left(L_{grid}I_{grid\_q0}s - (V_{PCC\_d0} + L_{grid}\omega_0 I_{grid\_q0})\right)\right)} + \frac{-L_{grid}s\left(L_{grid}(I_{grid\_q0}s + \omega_0 I_{grid\_d0})\right)H(s)}{(\tau_i s+1)\left(s - H(s)\left(L_{grid}I_{grid\_q0}s - (V_{PCC\_d0} + L_{grid}\omega_0 I_{grid\_q0})\right)\right)} \quad (5\text{-}17)$$

As shown in (5-17), the plant dynamics depends on the converter operating point (represented by I_{grid_d0}, I_{grid_q0}, V_{PCC_d0}), the grid inductance L_{grid}, and the PLL filter $H(s)$. The impacts of the converter operating point and grid inductance on the dynamics in (5-17) are characterized using a numerical analysis of a typical converter with the parameters given in the Section 5.7. The PLL filter is usually designed according to the bandwidth criterion to ensure relatively fast tracking response and reasonable disturbance rejection under the occurrence of grid voltage unbalance and harmonics [109]. Therefore, the PLL filter is designed to meet the performance criteria; and the filter parameters, given in Section 5.7, are fixed in the numerical analysis. It should be noted that relying on retuning the PLL filter to enhance the ac-bus voltage dynamics is not a practical solution as it is limited by the performance trade-offs.

Firstly, the impact of operating point variation on the dynamics in (5-17) is analyzed. To respect the converter power rating, the converter active and reactive powers are assumed to change in the range of ±2.15 MW and ± 2.15 Mvar. It should be noted that in weak grid connections, a reasonable amount of the converter rating is allocated to the reactive power loading, which is essential to control the voltage at the PCC. Fig. 5.5 shows the poles and zeros of (5-17) when the converter reactive power, and consequently, $I_{grid\text{-}q0}$ changes from +2.15 Mvar to -2.15 Mvar, while the active power fixed at -2.15 MW (i.e., the converter operates in the rectification mode). As shown in Fig. 5.5(a), it can be seen that the system has an unstable pole that moves to the right side of the *s*-plane as the reactive power changes from the maximum positive value to the maximum negative one. The high sensitivity of the system poles to variation in the reactive power operating point is related to the fact that the voltage dynamics is highly affected by the reactive power in inductive grids. As shown in Fig. 5.5(b), the system does have non-minimum phase zeros. Fig. 5.6 shows the poles and zeros of (5-16) when the converter

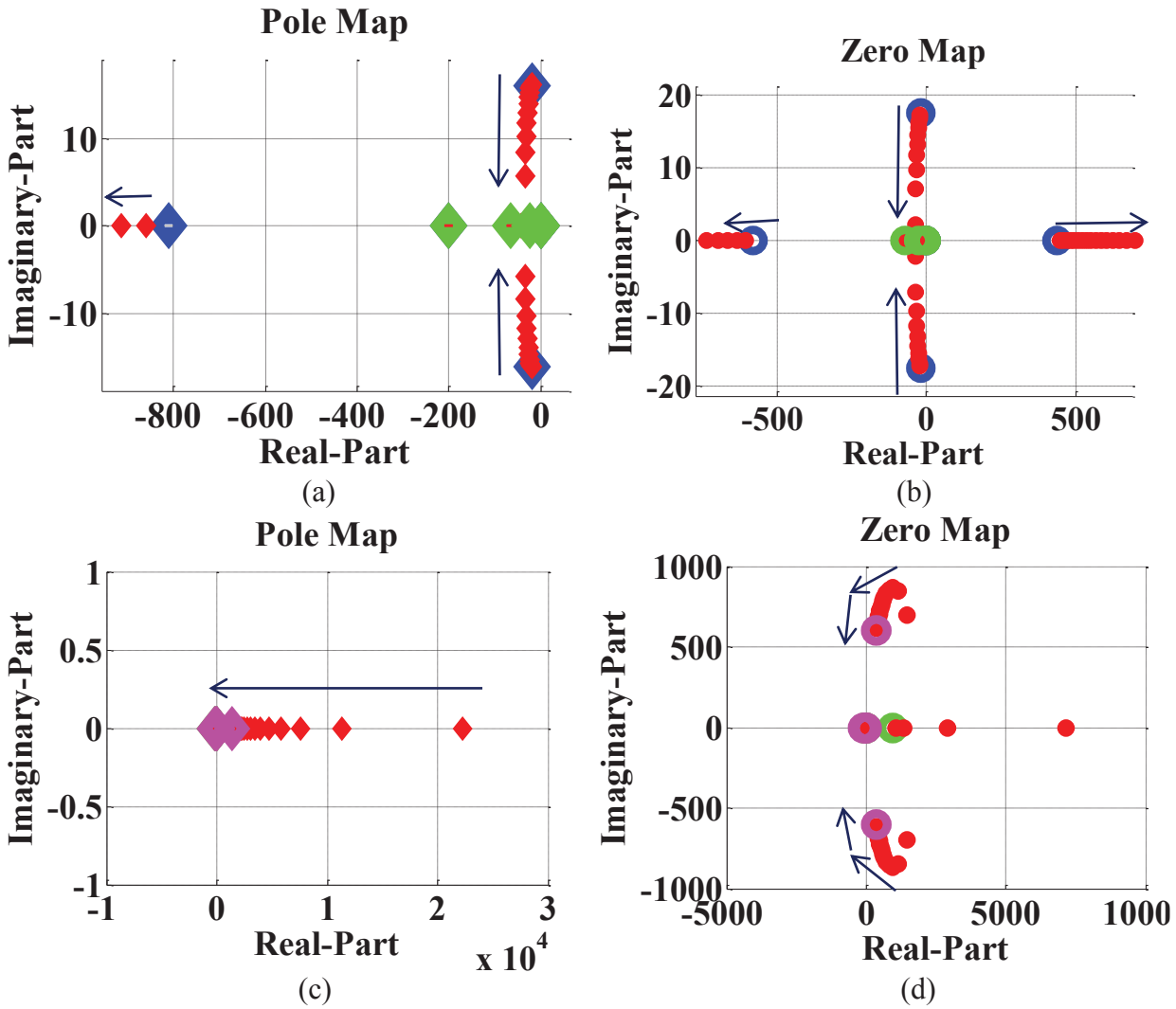

Fig. 5.5. Analysis of (5-16) when the converter reactive power, and consequently, $I_{grid\text{-}q0}$ changes from (a) Pole map; +2.15 Mvar to 0.00 Mvar (b) Zero map; +2.15 Mvar to 0.00 Mvar (c) Pole map; 0.00 Mvar to -2.15 Mvar, (d) Zero map; 0.00 Mvar to -2.15 Mvar, while the active power fixed at -2.15 MW.

reactive power, and consequently, $I_{grid\text{-}q0}$ changes from +2.15 Mvar to -2.15 Mvar, while the active power fixed at +2.15 MW (i.e., the converter operates in the inversion mode). Due to the high coupling between the voltage dynamics and reactive power operating points, the system has an unstable pole that moves to the right-hand side of the *s*-plane as the reactive power changes from the maximum positive value to the maximum negative one. Unlike the case in Fig. 5.5, the system does not have non-minimum phase behavior due to the presence of the dominant zeros in the left-hand side of the *s*-plane.

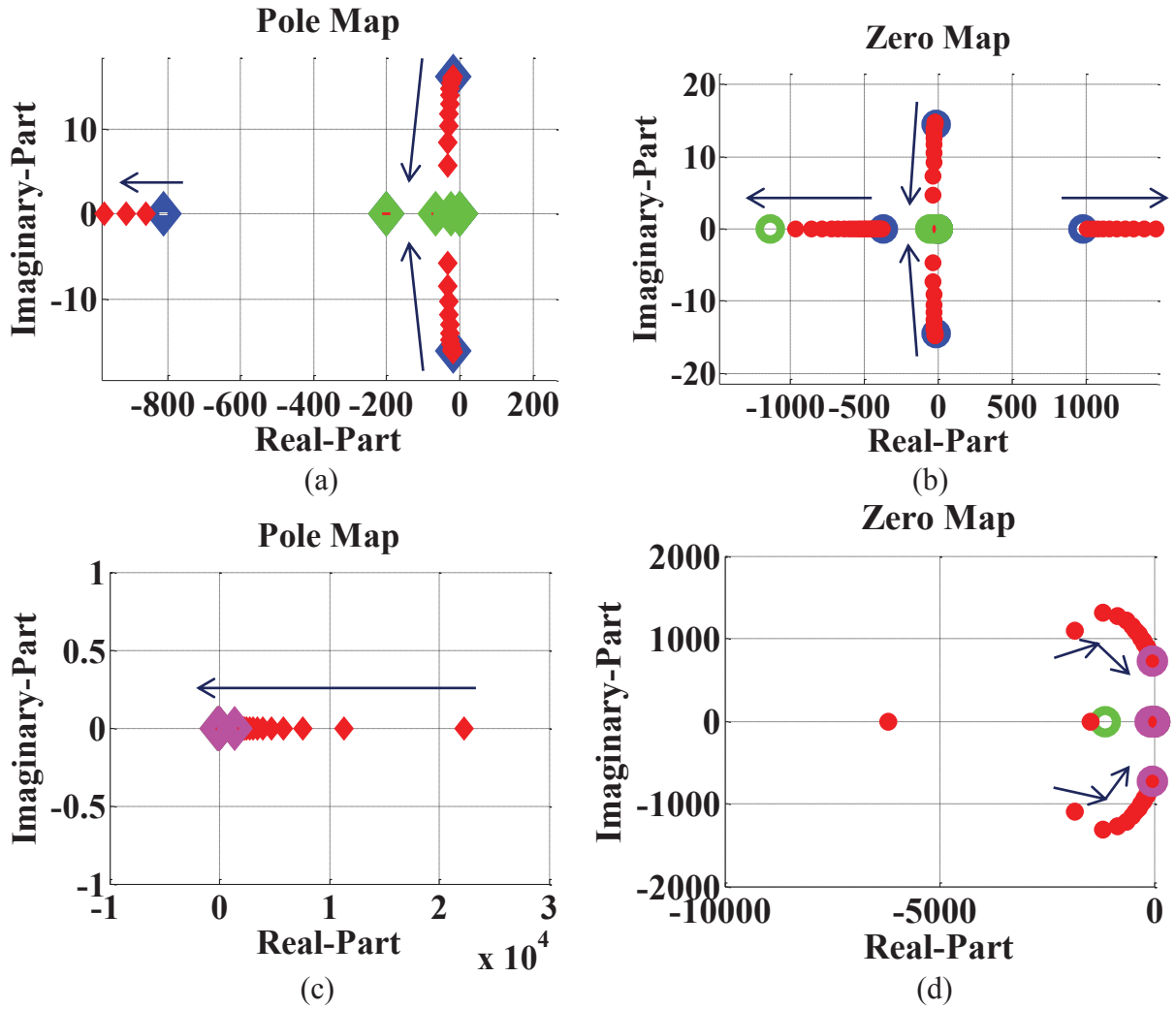

Fig. 5.6. Analysis of (5-16) when the converter reactive power, and consequently, $I_{grid\text{-}q0}$ changes from (a) Pole map; +2.15 Mvar to 0.00 Mvar (b) Zero map; +2.15 Mvar to 0.00 Mvar (c) Pole map; 0.00 Mvar to -2.15 Mvar, (d) Zero map; 0.00 Mvar to -2.15 Mvar, while the active power fixed at +2.15 MW.

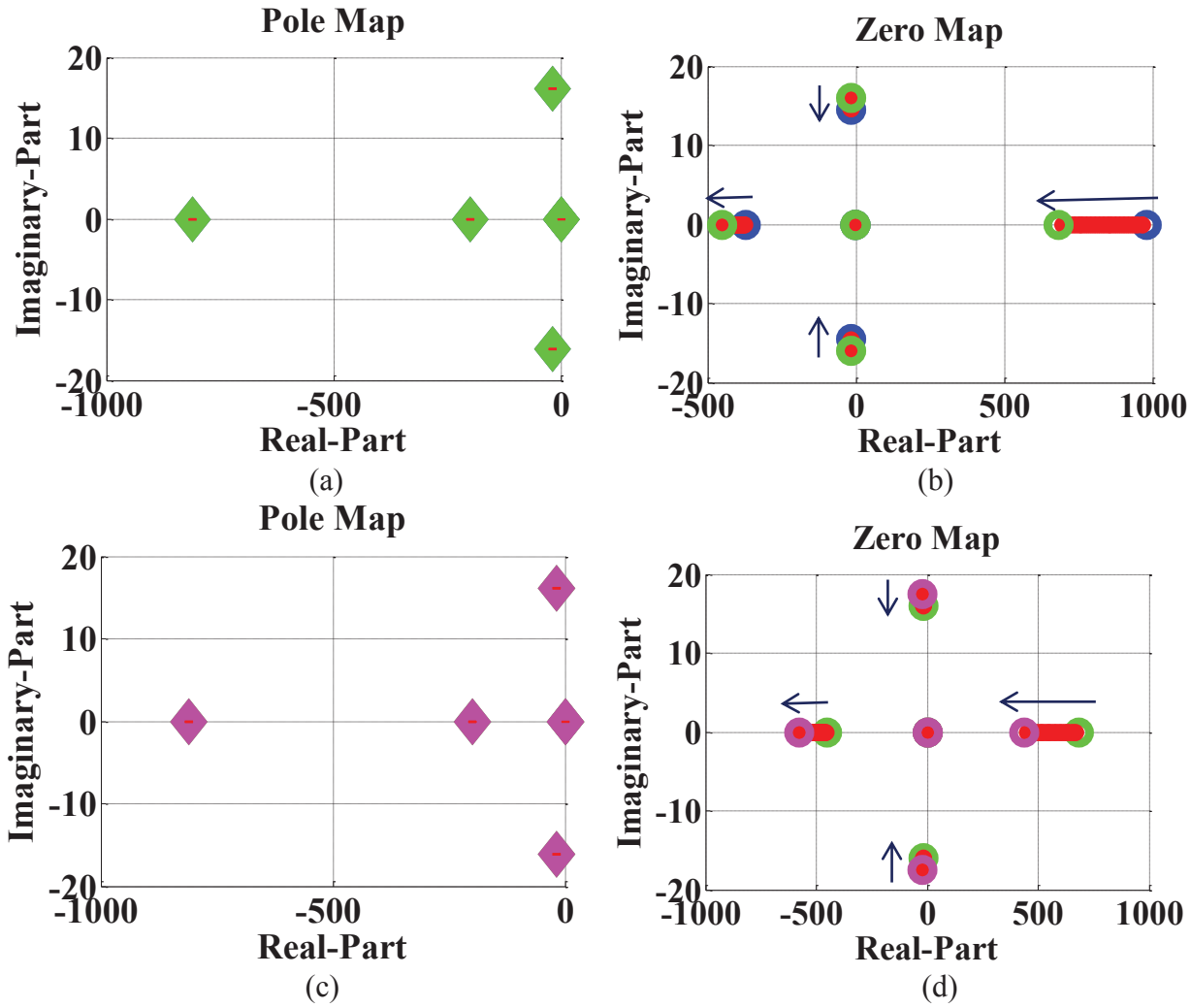

Fig. 5.7. Analysis of (5-16) when the converter active power, and consequently, $I_{grid\text{-}d0}$ changes from (a) Pole map; +2.15 MW to 0.00 MW (b) Zero map; +2.15 MW to 0.00 MW (c) Pole map; 0.00 MW to -2.15 MW, (d) Zero map; 0.00 MW to -2.15 MW, while the reactive power fixed at +2.15 Mvar.

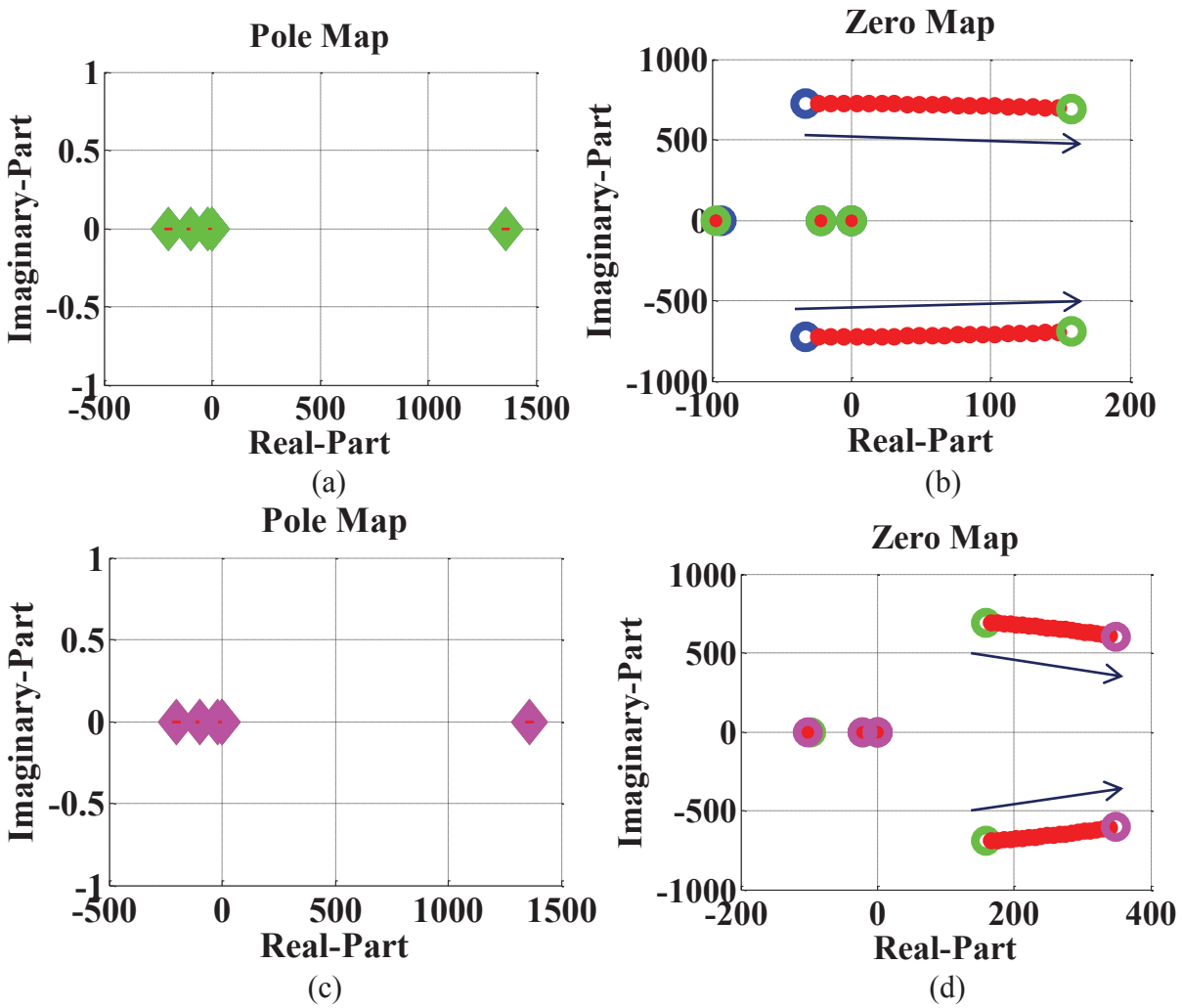

Fig. 5.8. Analysis of (5-16) when the converter active power, and consequently, $I_{grid\text{-}d0}$ changes from (a) Pole map; +2.15 MW to 0.00 MW (b) Zero map; +2.15 MW to 0.00 MW (c) Pole map; 0.00 MW to -2.15 MW, (d) Zero map; 0.00 MW to -2.15 MW, while the reactive power fixed at -2.15 Mvar.

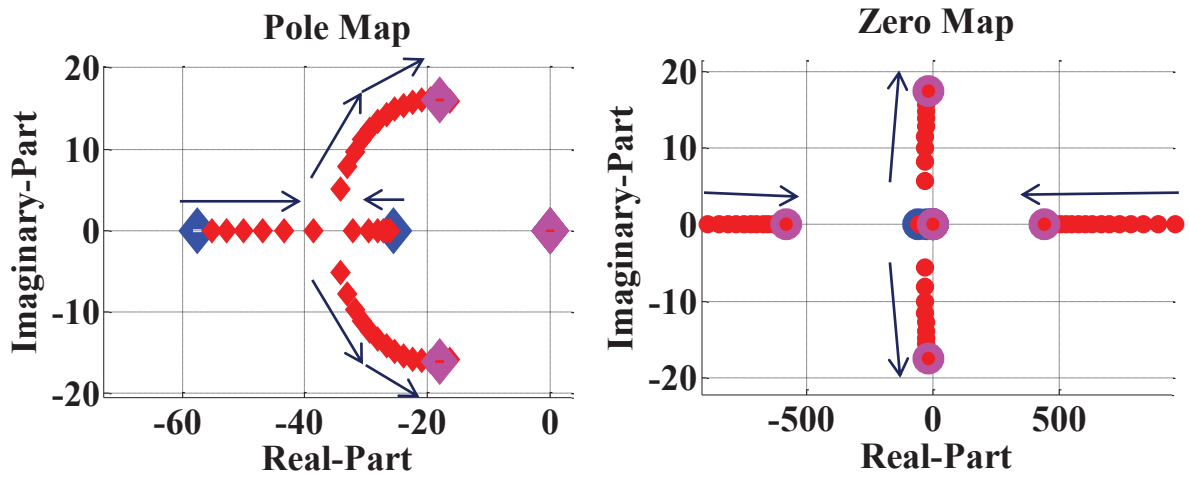

(a) (b)

Fig. 5.9. Analysis of (5-16) when the grid inductance changes from 50.00 μH to 297.44 μH while the converter active and reactive powers are fixed at -2.15 MW and +2.15 Mvar. (a) Pole map. (b) Zero map.

The impact of variation in the active power on the poles and zeros of (5-17) is shown in Fig. 5.7 and Fig. 5.8. The converter active power, and consequently, $I_{grid\text{-}d0}$ changes from +2.15 MW to -2.15 MW, while the reactive power fixed at +2.15 Mvar and -2.15 Mvar in in Fig. 5.7 and Fig. 5.8, respectively. As expected, changes in the active power does not impact the location of the system poles due to the decoupling between active power and ac-bus voltage in highly inductive ac grids. The system has an unstable pole when the reactive power is -2.15 Mvar, and all the poles are stable when the reactive power is +2.15 Mvar. However, the location of the non-minimum phase zero is affected by the active power operating point. As the active power increases in the rectification mode, the zero moves toward the imaginary axis in the complex-frequency plane.

The SCC-R, or equivalently, the grid impedance, is another important parameter that affects the ac-bus voltage dynamics in (5-17). Fig. 5.9 shows poles and zeros of (5-17) when the grid inductance increases from 59.48 μH to 297.44 μH while the active and reactive power operating point is -2.15 MW and +2.15 Mvar, respectively. As the grid inductance increases, the converter-grid coupling dynamics increases, and the pole of the small-signal dynamics moves toward the right-hand side of the *s*-plane. Also, the system zero moves to the right-hand side of the *s*-plane, leading to a non-minimum phase behavior. The non-minimum phase zero is relatively close to the imaginary axis, which yields a negative impact on the system dynamics, and limits the bandwidth of the closed-loop ac-bus voltage control dynamics.

5.4 Synthesizing AC-Bus Voltage Controller for a Weak-Grid Connected VSC

5.4.1 Control Objectives

The analysis of the ac-bus voltage dynamics in weak grid-connected VSCs showed the following.

1) The PLL couples the converter and grid dynamics; the coupling increases as the grid stiffness decreases and makes the ac-bus voltage dynamics dependent on the converter operating point and SCC-R.
2) The ac-bus voltage dynamics is highly dependent on the converter operating point in weak and very weak grids. The dynamics can be unstable and with non-minimum phase behavior at some operating points, which affects both the performance and stability of the VSC system. In bidirectional VSCs, where the operating point can swiftly change in a wide range of positive and negative values of the active power, the ac-bus voltage controller should be able to stabilize the plant dynamics under wide range of variation in the operating point.

   Although a simple linear ac-bus voltage controller (e.g., a PI controller) can be designed to yield an acceptable performance at the worst-case plant dynamics, the stability and robustness against operating point variation cannot be guaranteed. This is due to the fact the plant dynamics will change during operating point variation in a way that could not be stabilized by a controller designed to locally stabilize the linearized dynamics at a given operating point. Such controllers lack robustness against the dynamics associated with the operating point to operating point maneuvers. Therefore, the stability margins of VSCs when SCC-R=1 with conventional controllers are limited, and the active power operating point needs to be remarkably reduced, i.e., to 0.5-0.6 pu to ensure stability [7].
3) The ac-bus voltage dynamics is highly dependent on the SCC-R. Variation in the ac system impedance (e.g., due to grid reconfiguration and line tripping in faults and maintenance) can lead to considerable uncertainty in the SCC-R.

   In weak grid connections, the overall converter system stability is dependent on the ac-bus voltage stability at the PCC. In fact, with an effective ac-bus voltage control, the

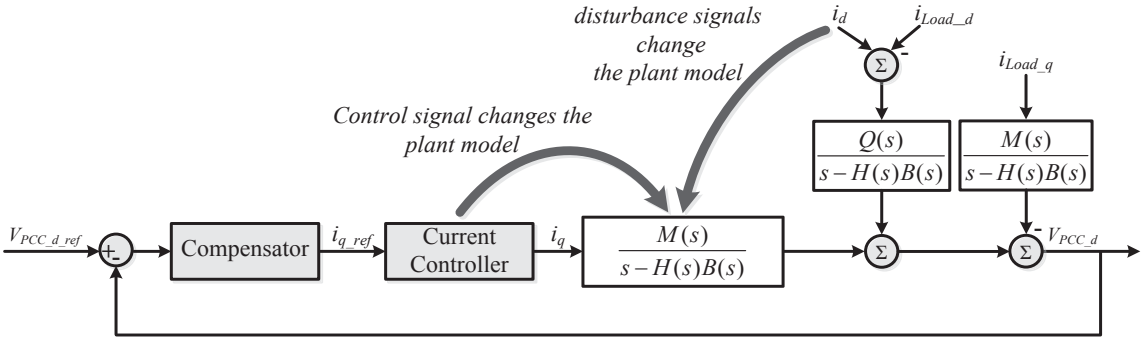

Fig. 5.10. Block diagram of the ac-bus voltage dynamics and feedback control structure.

converter transforms the weak grid into a virtual stiff grid where the PCC voltage will be close to 1.0 pu at different operating points; which in turns enables the dc-link v oltage controller to effectively regulate the dc-link voltage via bidirectional power transfer with the host ac grid.

To overcome these challenges, the ac-bus voltage controller should be robust against operating point variation, and uncertainty in the grid inductance. Furthermore, the controller should be designed using the complete dynamics, including the PLL filter, to enhance the controller robustness under weak grid conditions. To meet these design objectives, a robust ac-bus voltage controller is developed in this study.

5.4.2 Controller Design

The small-signal ac-bus voltage dynamics in (5-13), and the feedback control structure can be represented by the block diagram in Fig. 5.10. The ac-bus voltage controller generates the reference converter reactive current; the latter is processed by the inner current control loop. The actual converter is the control lever. The *d*-component of the converter current, as well as the *dq* components of the local load currents, act as output disturbances. Due to the nonlinear nature of the plant under control, both the control signal and disturbance signals change the small-signal plant dynamics as the latter depends on the converter operating point. Furthermore, the plant dynamics is subjected to uncertainties associated with the grid inductance.

Several robust control methods are available in the literature. To synthesize a simple robust controller against operating point variation and parametric uncertainties, the polynomial method [86] can be used. However, the method yields an unfeasible solution for the present

problem. This is due to the large range of possible operating points and grid parameters in a practical VSC. Under these practical conditions, the range of variation of the vertices of the polytopic system generated by the polynomial method is very large so that the linear matrix inequality condition is not satisfied [86] and [88]. In addition, because of the non-minimum phase situation occurs along with unstable modes in the small-signal dynamics of (5-13), it is not possible to benefit from the robust two degree-of-freedom (DOF) control structures that require a plant with stable poles and/or zeros [80]. Furthermore, a switching adaptive controller [69] is not a suitable control candidate owing to the fact that both the operating point and the system parameters are changing, which yields a wide range of plant parameters, and complicates the design of a stable switching controller. Therefore, in this chapter, an optimal robust controller that makes the closed-loop system robust against the aforementioned parametric uncertainties and operating point variation is proposed. The robust optimal control approach is selected owing to the ability to stabilize and maintain robust control performance under wide range of operating points and parameter variation, systematic design approach, fixed-order controller, and suitability for industrial applications.

One of the best ways to optimally reject the disturbances imposed on the output is minimizing the H_∞ norm from the filtered disturbance signals to the filtered output in the presence of weighted uncertainty using the structured singular values μ-method [48], [81], [82]. Therefore, a μ-synthesis controller using the *DK*-iteration method is employed to optimally synthesize the ac-bus voltage controller.

The employed structure is a controller with one DOF, and both reference tracking and disturbance rejection are simultaneously achieved. Thus, the controller is synthesized based on the internal model principle to guarantee both reference tracking and disturbance rejection of step signals at the input and output, respectively [80]. In order to account for unmodelled dynamics and nonlinear effects due to operating point variation and parametric uncertainties, the uncertainties in the ac-bus voltage control model are approximated by input multiplicative uncertainties. The applied control structure is shown in Fig. 5.11, where the nominal plant transfer function is $G(s)$ the uncertainties weight is $W(s)$, and disturbance and output weights are $W_d(s)$ and $W_p(s)$, respectively.

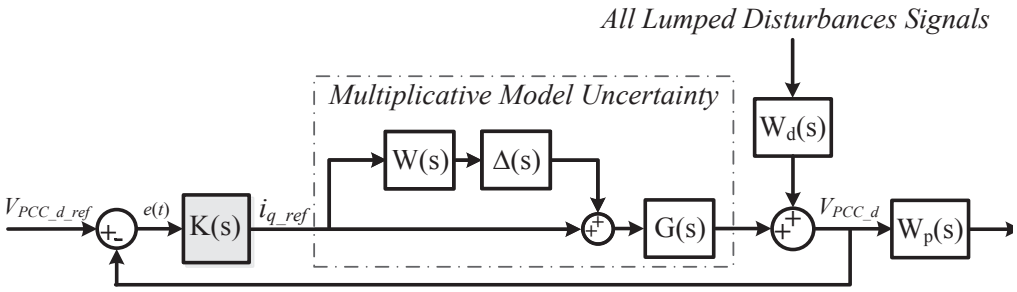

Fig. 5.11. Robust control structure used to synthesize the ac-bus voltage controller.

To have one control structure that models variable operating points and grid inductance, all possible transfer functions have been randomly generated by the Robust Control Toolbox in MATLAB [82]. The uncertain plant model, in (5-13), contains two uncertain transfer functions, $M(s)$ and $B(s)$, which are affected by (I_{d0}, I_{q0}), V_{PCC_d0}, and L_{grid}. It is often appropriate to simplify the uncertainty model while approximately retaining its overall variability for optimal feedback design purposes. One hundred and twenty random samples of all possible transfer functions have been generated, and the nominal transfer function and its related unmodeled dynamics have been extracted. Referring to Fig. 5.11, and using the nominal transfer function parameters, given in Section 5.7, the transfer functions $G(s)$ and $W(s)$ are given by

$$G(s)=\frac{3.076\times10^{+4}s^4+5.227\times10^{+6}s^3-2.548\times10^{+10}s^2-1.908\times10^{+12}s-3.393\times10^{+13}}{s^5+9.097\times10^5s^4+2.294\times10^9s^3+5.71\times10^{+11}s^2+3.23\times10^{+13}s+5.18\times10^{+14}} \quad (5\text{-}18)$$

$$W(s)=\frac{21.23\,s^2+4731s+4.998\times10^4}{s^2+625.9\,s+6.92\times10^4} \quad (5\text{-}19)$$

Also, the designed transfer functions $W_d(s)$ and $W_p(s)$ are given by

$$W_d(s)=\frac{10}{s+10^{-3}} \quad (5\text{-}20)$$

$$W_p(s)=\frac{1}{s+10^{-3}} \quad (5\text{-}21)$$

By choosing $G(s)$ as the nominal plant dynamics, the controller guarantees robust performance and stability with varying I_{d0}, I_{q0}, V_{PCC_d0}, and L_{grid}. The weights $W_d(s)$ and $W_p(s)$ are designed to ensure effective disturbance rejection and good transient response at nominal parameters [17], [27].

The controller $K(s)$ given by (5-22), has been synthesized using the robust controller design approach via the μ-synthesis and model order reduction tools in the Robust Control Toolbox of

MATLAB. As shown in Fig. 5.11, the synthesized controller is a single transfer function employed in the one DOF structure, which simplifies the implementation. In spite of the somewhat high controller order, it is relatively easy to implement using commercial-grade signal processors.

$$K(s)=\frac{\begin{array}{l}-1322\,s^6-1.548\times10^{+6}\,s^5-1.482\times10^{+8}\,s^4-6.648\times10^{+8}\,s^3\ \ldots\\ \ldots-7.791\times10^{+8}\,s^2-6.167\times10^{+7}\,\mathrm{s}-7.005\times10^{+4}\end{array}}{\begin{array}{l}s^7+3.984\times10^{+4}\,s^6+6.538\times10^{+5}\,s^5+1.245\times10^{+6}\,s^4+1.096\times10^{+5}\,s^3\ \ldots\\ \ldots+312.5\,s^2+0.2968\,\mathrm{s}+9.262\times10^{-5}\end{array}} \tag{5-22}$$

5.5 Simulation Results

A typical multiterminal dc grid with four terminals, presented in Fig. 5.12, is considered for the simulation study to test the performance of the proposed control system under typical and practical disturbances imposed under multi-converter operation in modern grids. The system is simulated in the MATLAB/Simulink environment. The system is composed of four zones as shown in Fig. 5.12. Zone I is composed of a 580 V, 60 Hz ac weak grid interfaced to the dc grid via a bidirectional VSC. The VSC in Zone I regulates the dc-link voltage of the dc grid and regulates the ac-voltage at the PCC (PCC-1). The converter in Zone I is synchronized to its ac grid by a standard three-phase *dq* PLL. Zone II is a 580 V, 60 Hz grid interfaced to the dc grid via a bidirectional VSC to control the power flow from or to PCC-2. The VSC in Zone II, VSC-PQ, is controlled in the PQ mode. Zone III is composed of a 2.5 MW renewable energy source that can produce dc power (e.g., a full-scale wind turbine system). A VSC, VSC-W, is used to interface the variable-frequency wind turbine system to the dc grid. Zone IV models a 1.0 MW, 500 V_{dc} dc-micro-grid with energy storage system (ESS) interfaced to the dc grid via a bi-directional dc/dc converter. In Zone I, the proposed ac-bus voltage controller is implemented, whereas a standard PI-lead dc-bus voltage controller [21] is used. The converter in Zone II employs a standard voltage-oriented PQ control structure with inner PI current control loops in the synchronous *dq*-frame [20][36]. The converter in Zone III employs a standard field-oriented controller synchronized with the rotor position of the permanent-magnet synchronous generator of the wind turbine. Standard three-phase *dq* PLLs are used in Zones I and II. Zone IV employs a standard PI controller for the bi-directional dc/dc converter. The average model of VSCs in Zones I, II, and III is used to reduce the computational burden without loss of accuracy.

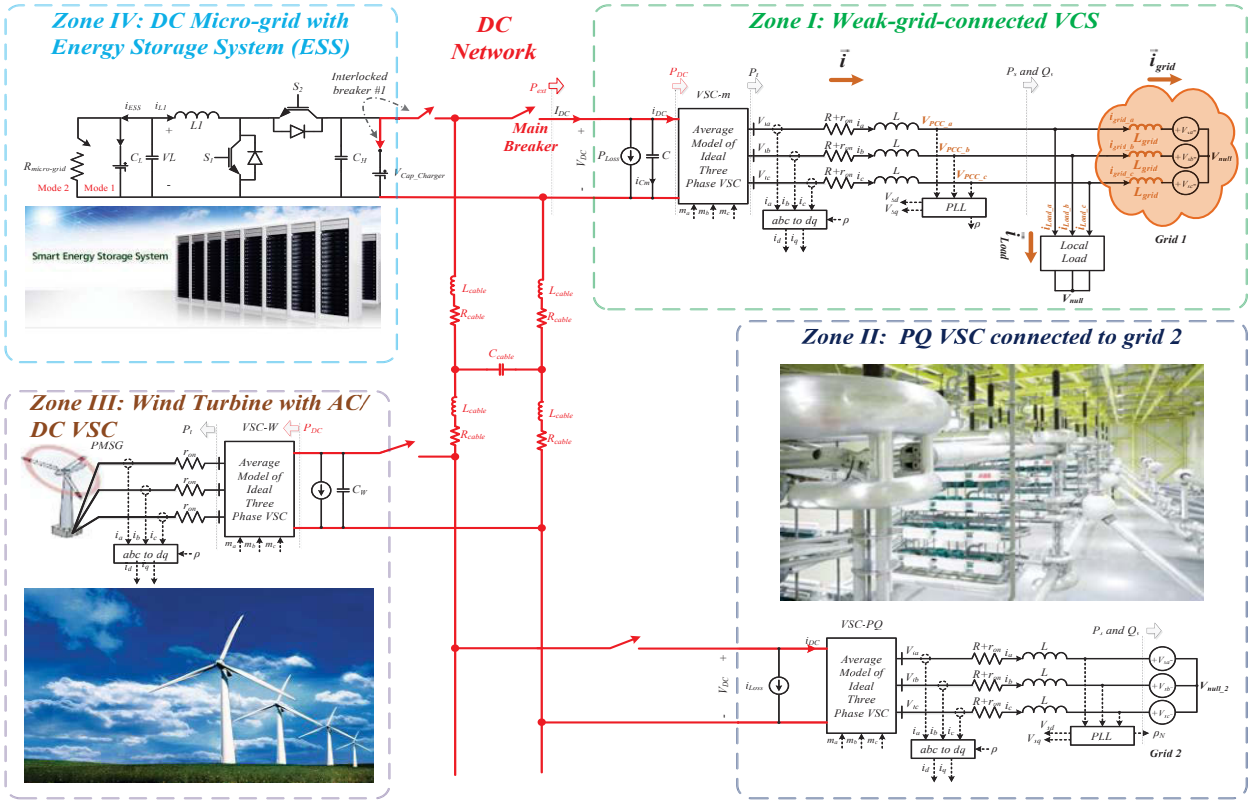

Fig. 5.12. Detailed structure of the simulated network.

A switching model of the bi-directional dc/dc converter system in Zone IV is implemented to test the control performance under typical high-frequency disturbances associated with converter switching. The system and controller parameters are given in Section 5.8.

First, the dc side capacitor in Zone I is energized from its initial zero state by a ramp function that starts from zero at t=0 to its final value, 1750V at t=0.05 s. Then, Zone II is connected to the dc grid at t=0.10 s with zero active and reactive power references. At t=1.0 s, Zone II is set to absorb 2.0 MW and 0 Mvar from the dc grid and to inject to its ac grid (VSC-PQ operates as an inverter). Thus, the weak-grid- connected VSC operates as a rectifier injecting 2.0 MW to its ac grid. At t=2.0 s, Zone II is set to inject 2.0 MW to the dc grid, so it absorbs 2.0 MW from its ac grid. Thus, the weak-grid-connected VSC operates as an inverter absorbing 2.0 MW from the dc grid. Zone II is again set to absorb 2.0 MW from the dc grid, at t=3.0 s. Finally, Zone II is commanded to reduce its active power to zero at t=4.0 s.

Afterward, Zone III, which mimics a wind turbine directly connected to the dc grid via a

single VSC, is connected to the dc grid at t=4.0 s while injecting 2.36 MW. The weak-grid connected VSC tracks this disturbance by changing its operating point from zero to 2.36 MW (about 0.944 pu active power) in the inversion mode. At t=4.2 s, a 1.36 MW dc static load, which is equivalent to 2.25 Ω at 1750 V, is directly connected to the dc grid without any interface to assess the system performance at sudden static load connection to the dc grid. The static load is disconnected form the dc grid at t=4.7 s. Zone III is disconnected from the dc grid at t=5.0 s. Finally, Zone IV is connected to the dc grid at t=5.0 s using interlocked breaker #1 (in Fig. 5.12). Initially, the dc-micro-grid load is disconnected, and the ESS is controlled in the buck mode to absorb 0.50 MW power from the dc grid by controlling the inductor current I_L via a simple PI controller. The dc micro-grid load is connected to the bi-directional dc/dc converter, and the battery is disconnected from the dc microgrid load to model a contingency event and test the performance of the proposed controller under such transient conditions. Accordingly, the dc/dc converter is commanded to suddenly change its control mode from buck to boost to transfer 0.86 MW power from the ESS to the dc grid. The power reversal instant is at 5.50 s, and it lasts around 0.70 s. All previous events are repeated for five different values of SCC-R; i.e., SCC-R=1, 2, 3, 4 and 5, via changing the values of L_{grid}, in each case. For the sake of performance comparison, the proposed controller is compared to 1) a PI controller, and 2) a robust controller designed for the plant dynamics without the PLL dynamics. Key results are reported as follows.

5.5.1 Performance of the Proposed Controller

The performance of the weak-grid connected VSC, with the proposed ac-bus voltage controller, under the aforementioned disturbances and at different values of the SCC-R is shown in Fig. 5.13. Fig. 5.13(a) shows the d-component of the converter voltage at the PCC of grid 1 (PCC-1), whereas Fig. 5.13(b) shows the q-component of the same variable. In spite of the large and fast disturbances that force the converter operating point to swiftly change in a wide positive and negative range, the presence of the PLL even at very weak grid condition (SCC-R=1), and uncertainty in the grid impedance, robust and stable ac-bus voltage control performance is yielded at all SCC-R levels. For the worst-case scenario, i.e., when the converter operates the rated power and SCC-R=1, the maximum over/under-shot voltages in the ac-bus voltage are less than 0.19 pu with recovery time around 0.2 s to one. For higher SCC-R levels, the disturbances in the ac-bus voltage are less than 0.07 pu. As shown in Fig. 5.13(b), the q-component of the

converter voltage is well regulated to zero where voltage disturbances are swiftly rejected. Fig. 5.13(c) shows the control effort of the proposed ac-bus voltage controller. Fig. 5.13(d) shows the dc-link voltage and Fig. 5.13(e) shows the control effort of the dc-link voltage controller. The maximum over/under-shot voltages in the dc-link voltage are less than 60/50 V with a recovery time around 0.2 s. The robust ac-bus voltage control performance helps the PLL to generate stable and robust output, and transforms the weak ac-bus voltage into a strong one so that the dc-link voltage controller can effectively exchange power with the host grid. These characteristics directly contribute the stability of the overall converter system.

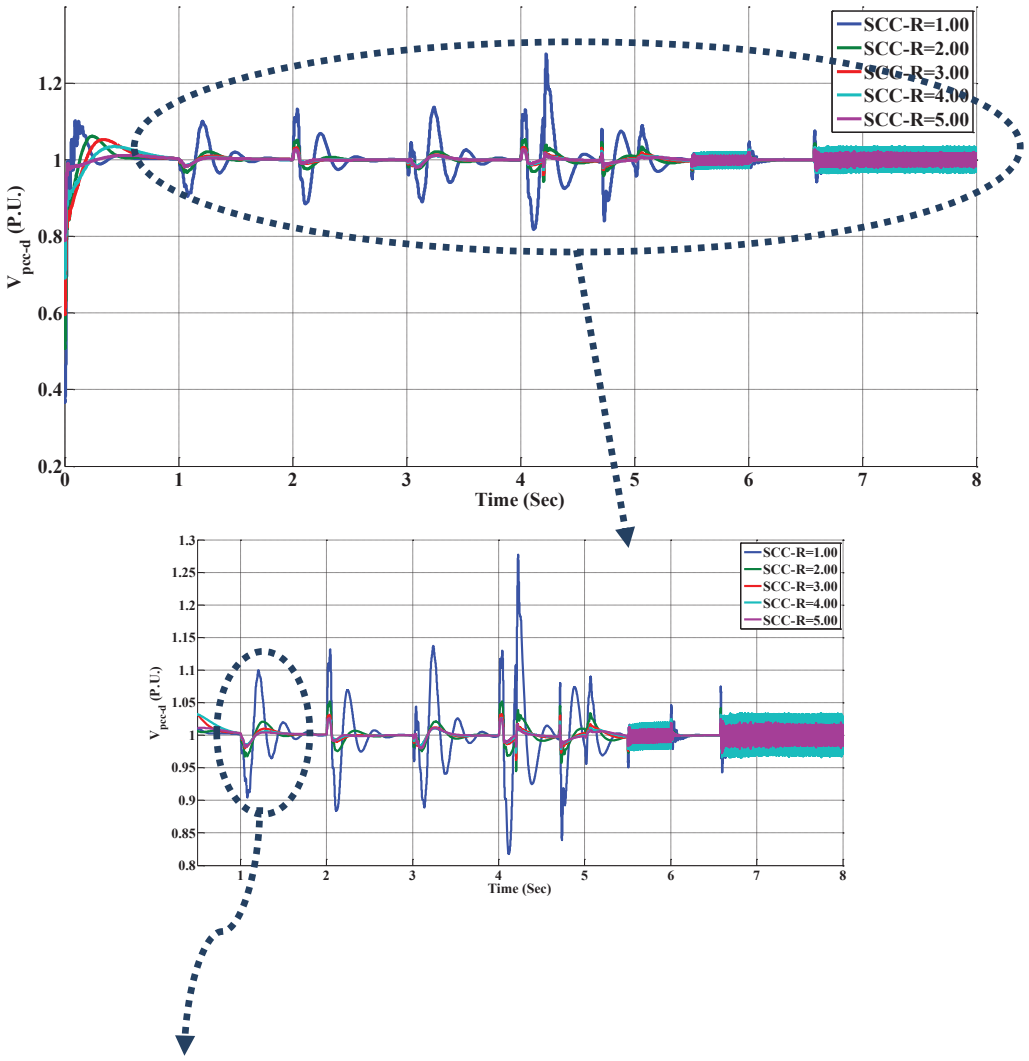

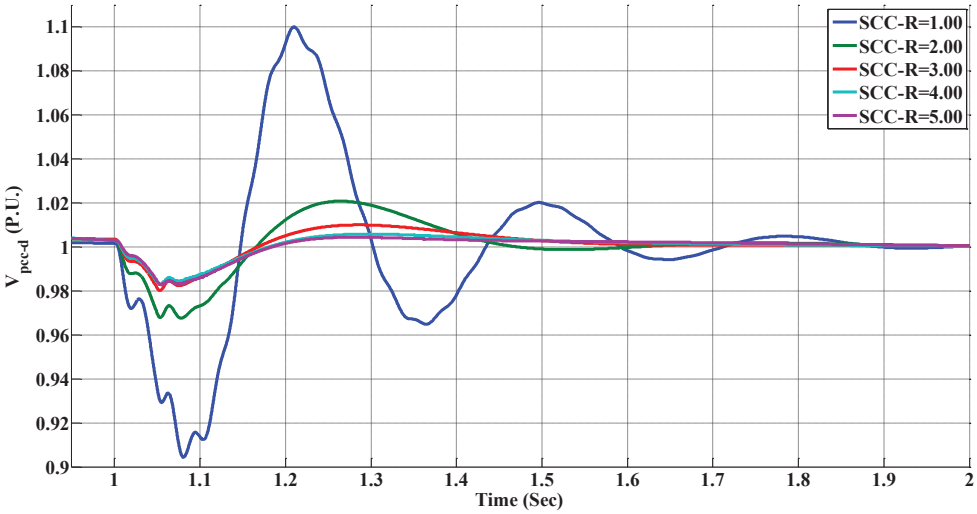
SCC-R=1.00
SCC-R=2.00
SCC-R=3.00
SCC-R=4.00
SCC-R=5.00
V pcc-d (P.U.)
Time (Sec)

(a)

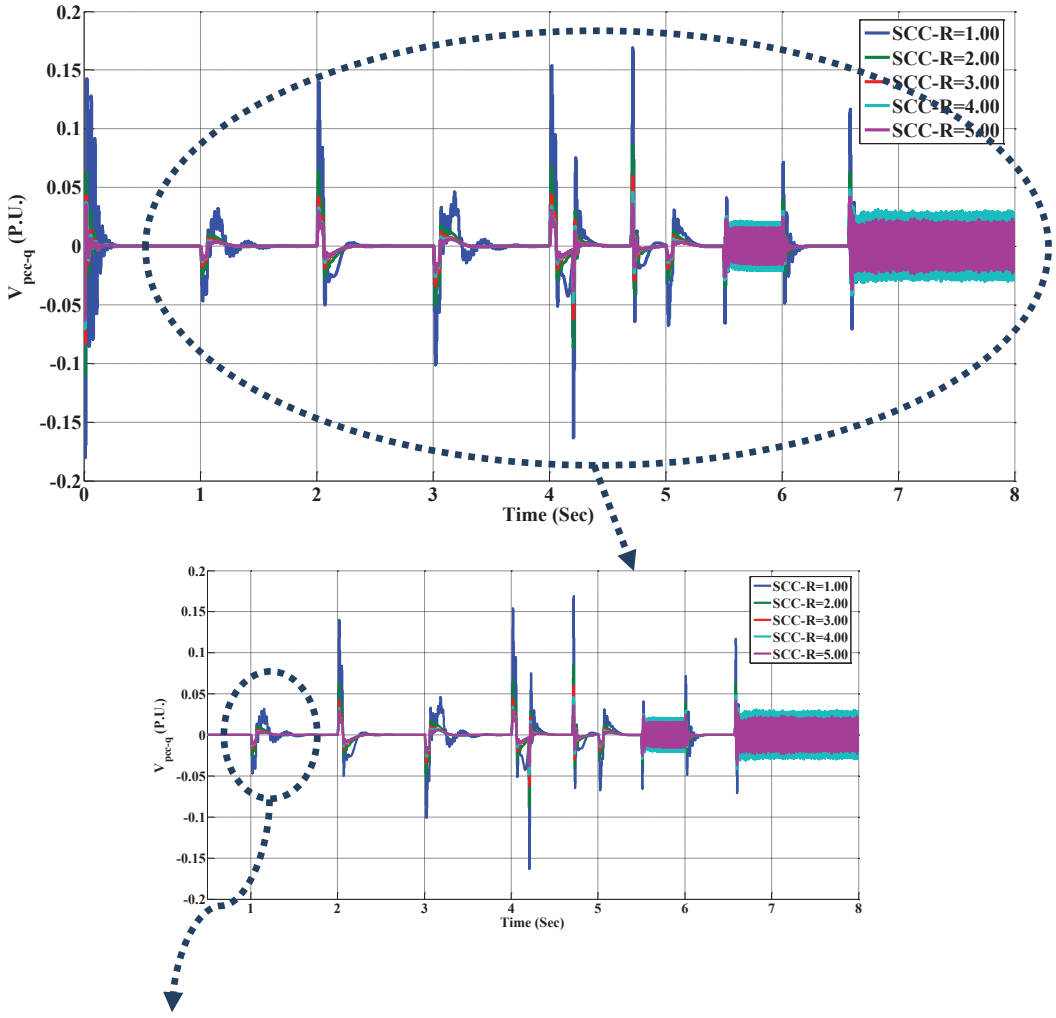
SCC-R=1.00
SCC-R=2.00
SCC-R=3.00
SCC-R=4.00
SCC-R=5.00
V pcc-q (P.U.)
Time (Sec)

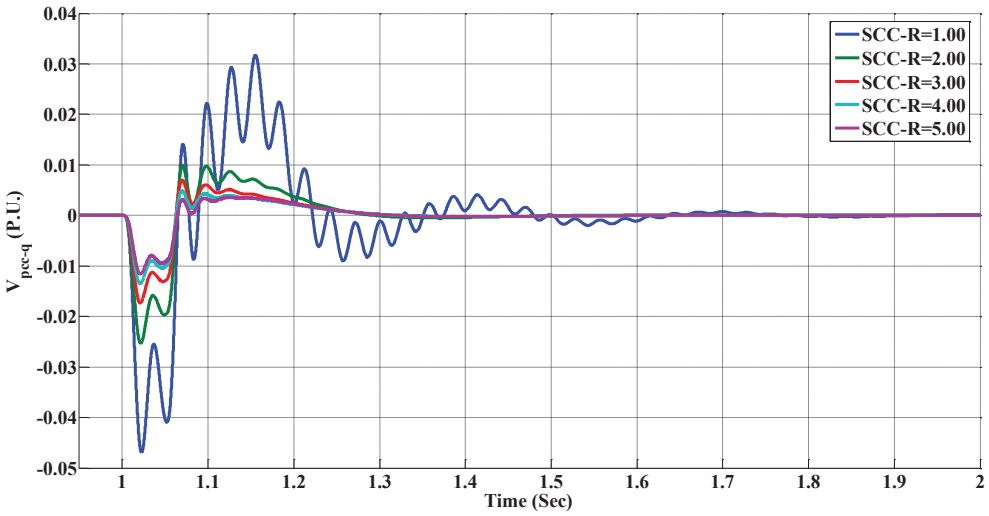
SCC-R=1.00
SCC-R=2.00
SCC-R=3.00
SCC-R=4.00
SCC-R=5.00
V_{pcc-q} (P.U.)
Time (Sec)

(b)

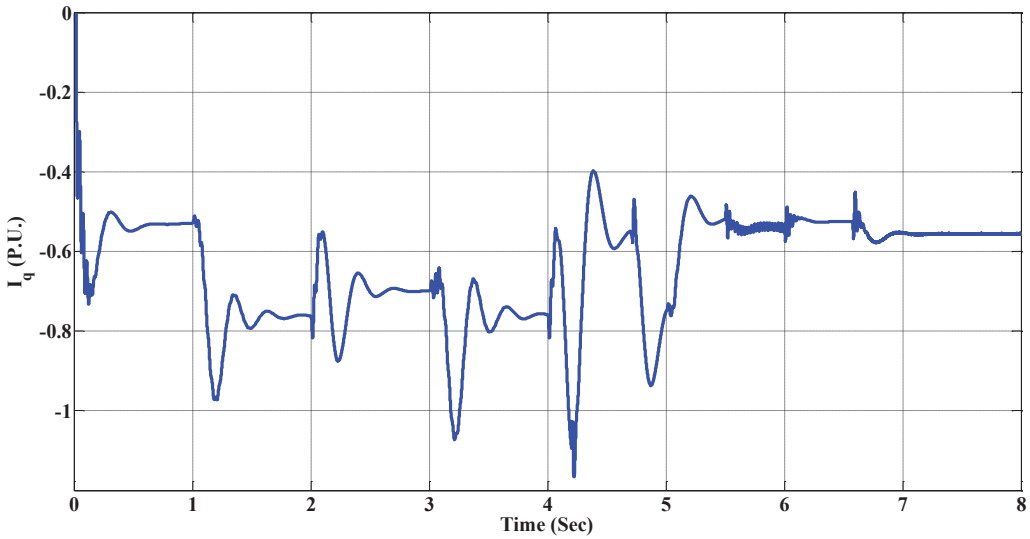
I_q (P.U.)
Time (Sec)

(c)

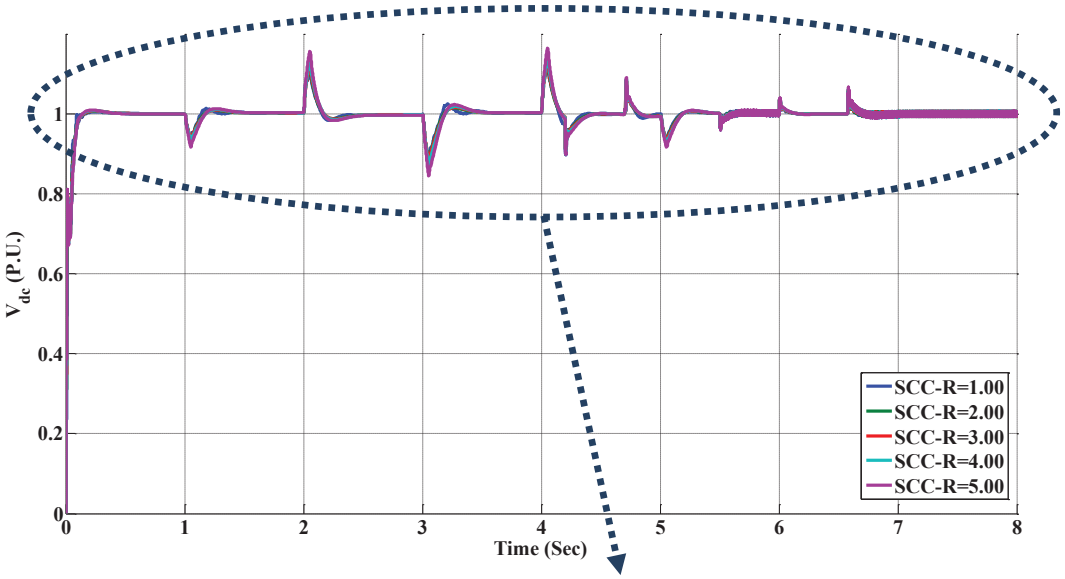

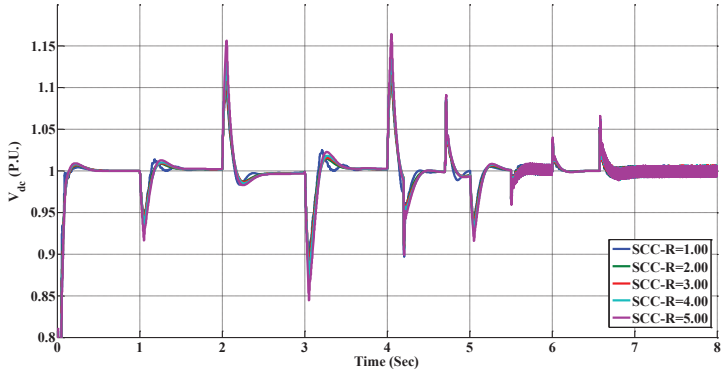

(d)

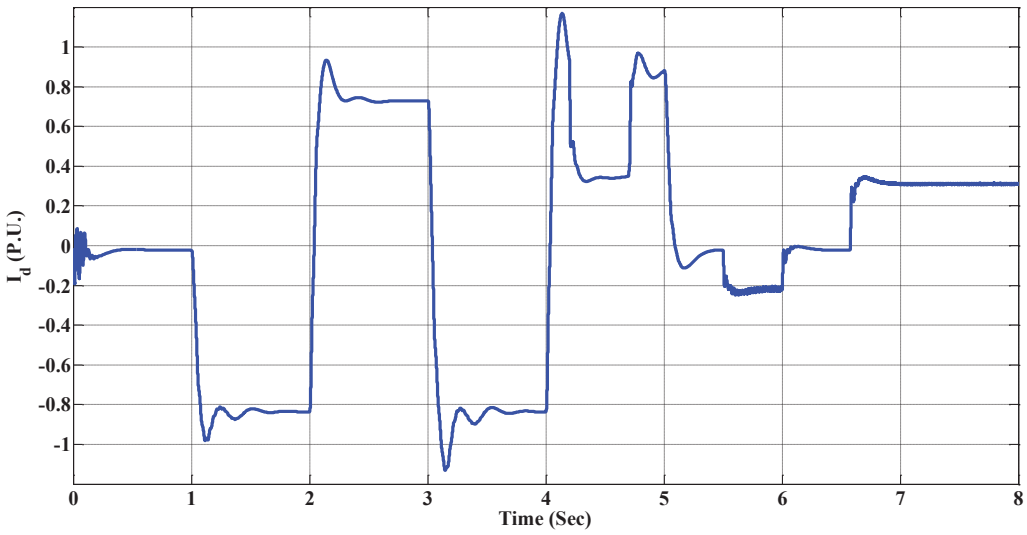

(e)

Fig. 5.13. Performance of the weak-grid connected VSC with the proposed ac-bus voltage controller; (a) $V_{PCC\text{-}d}$. (b) $V_{PCC\text{-}q}$. (c) I_q. (d) DC-link voltage. (e) I_d.

Table 5.1
BANDWIDTH AND PHASE MARGIN WITH PI CONTROLLER
BANDWIDTH [RAD/S]

SCC-R / Active Power (MW) /Reactive Power (Mvar) Operating Point	1.0	2.0	3.0	4.0	5.0
+2.15/-2.15	39.5740	47.2250	48.5350	49.1295	49.4253
+2.15/+2.15	53.0145	52.0571	51.6122	51.3570	51.1919
-2.15/-2.15	47.1867	48.3448	48.8927	49.2121	49.4211
-2.15/+2.15	70.5967	55.1386	53.0295	52.2213	51.7954

PHASE MARGIN

SCC-R / Active Power MW) /Reactive Power (Mvar) Operating Point	1.0	2.0	3.0	4.0	5.0
+2.15/-2.15	90.6780°	81.6751°	80.3796°	79.8632°	79.5857°
+2.15/+2.15	76.2987°	77.1799°	77.5828°	77.8137°	77.9634°
-2.15/-2.15	81.1453°	80.2166°	79.7936°	79.5517°	79.3952°
-2.15/+2.15	66.6546°	75.5623°	76.8891°	77.4213°	77.7079°

5.5.2 Performance of the PI Controller

Based on the dynamic model in (5-17), a simple PI controller is designed. To account for the impact of operating point variation, the plant transfer function in (5-17) is evaluated at four critical operating points (i.e., when the converter operates at maximum possible positive and negative active and reactive powers) as well as all possible values of SCC-R.

Using the frequency shaping method, a PI controller is designed to stabilize the aforementioned linearized transfer functions with an acceptable phase margin and bandwidth. The worst-case phase margin is around 66^{o}, whereas the lowest close-loop bandwidth is around

40 rad/s, which is suitable for ac-bus voltage regulation using high power converters [30]. The values of the bandwidths, as well as the phase margins of all transfer functions considered in the design process, are given in Table 5.1.

The performance of the weak grid-connected VSC, with the PI ac-bus voltage controller, under the aforementioned disturbances and at different values of the SCC-R is shown in Fig. 5.14. Fig. 5.14(a) shows the *d*-component of the converter voltage at the PCC of grid 1 (PCC-1), whereas Fig. 5.14(b) shows the *q*-component of the same variable.

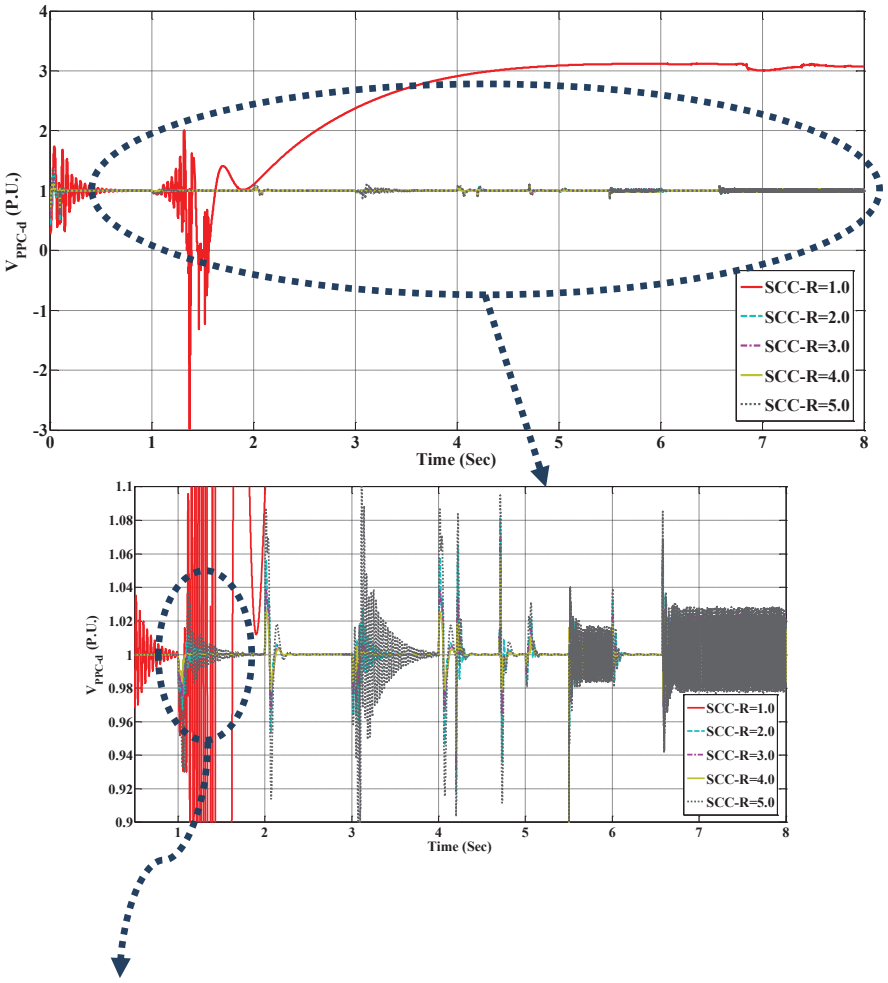

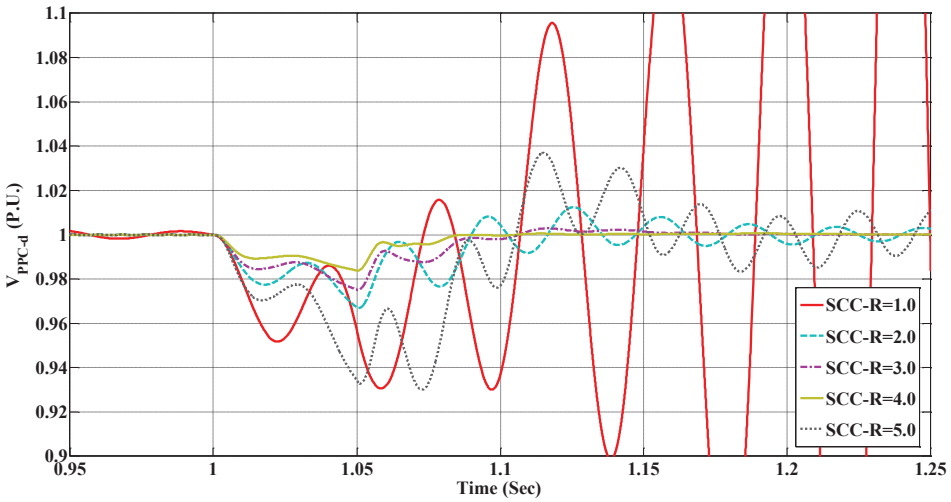
V_{PPC-d} (P.U.)
Time (Sec)
SCC-R=1.0
SCC-R=2.0
SCC-R=3.0
SCC-R=4.0
SCC-R=5.0

(a)

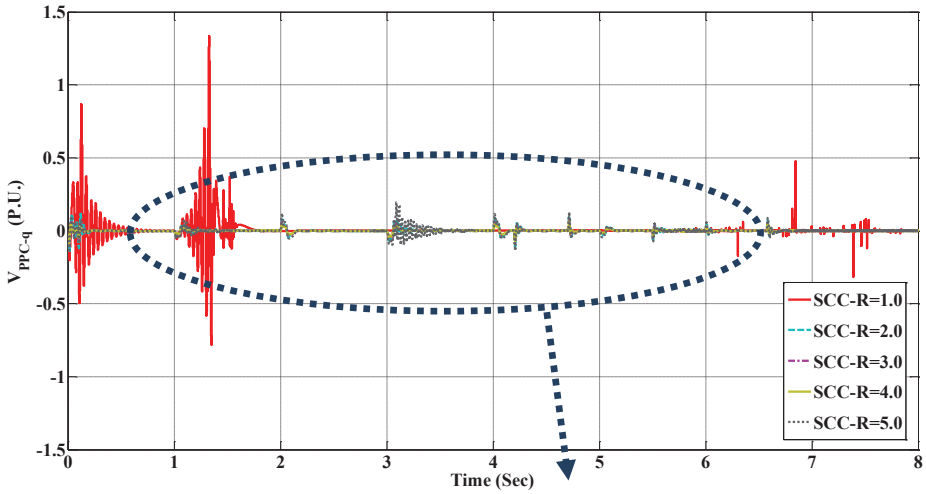
V_{PPC-q} (P.U.)
Time (Sec)
SCC-R=1.0
SCC-R=2.0
SCC-R=3.0
SCC-R=4.0
SCC-R=5.0

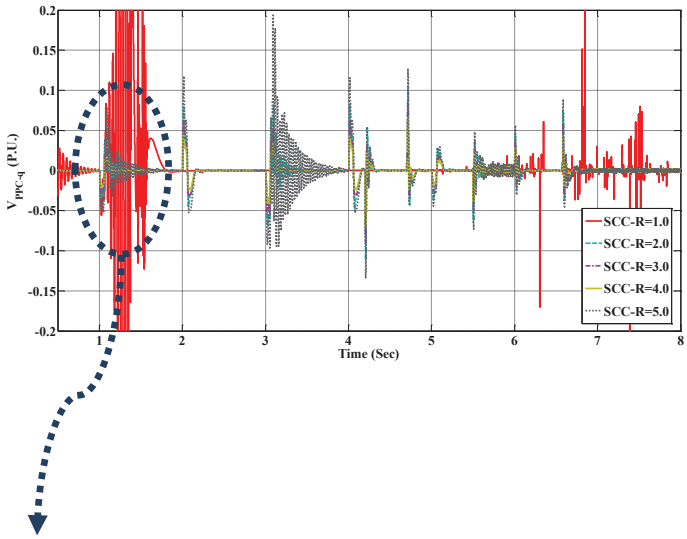
V_{PPC-q} (P.U.)
Time (Sec)
SCC-R=1.0
SCC-R=2.0
SCC-R=3.0
SCC-R=4.0
SCC-R=5.0

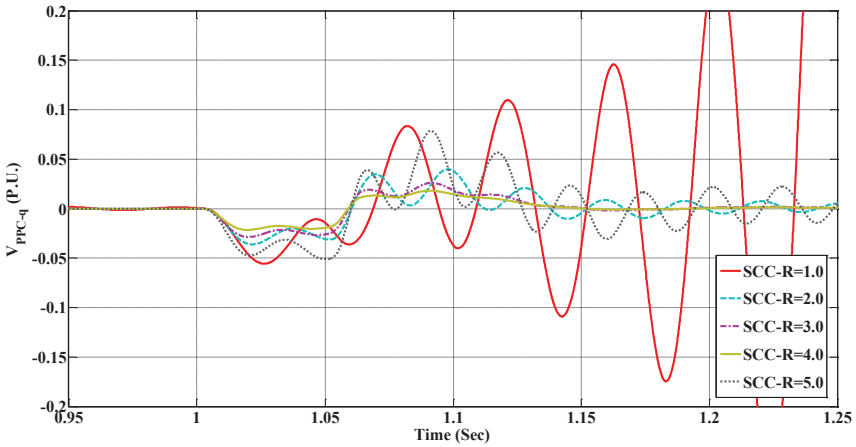

(b)

Fig. 5.14. Performance of the weak-grid connected VSC with a PI proposed ac-bus voltage controller; (a) $V_{PCC\text{-}d}$. (b) $V_{PCC\text{-}q}$.

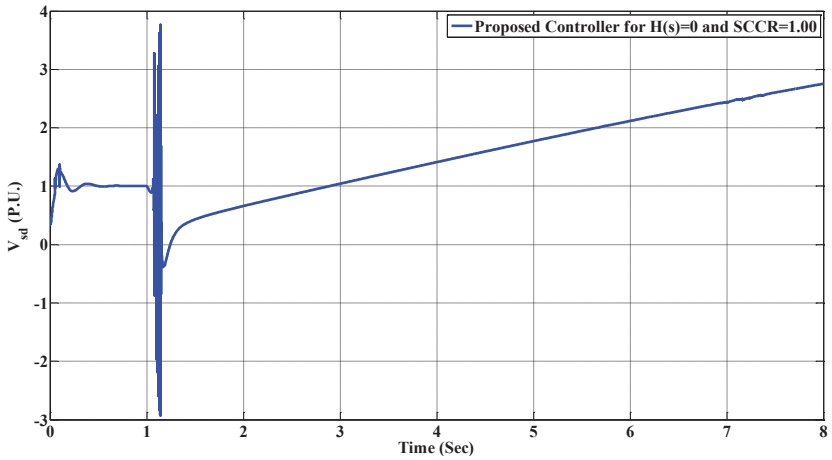

Fig. 5.15. Performance of the weak-grid connected VSC with a robust controller designed without the PLL dynamics (i.e., $H(s)$=0).

As shown in Fig. 5.14, the closed-loop system becomes unstable at SCC-R=1. Furthermore, the response is very oscillatory at higher values of SCC-R. In spite of the fact that the PI controller is synthesized such that the phase margin is acceptable at worst-case operating points and SCC-R, as shown in Table 5.1, the PI, as a local controller, individually stabilizes each of the linearized transfer functions. However, it fails to stabilize the system under operating point variation, which generates unmodelled dynamics associated with operating-point to operating-point maneuvers.

5.5.3 Performance of a Robust Controller Designed for the Linearized Plant without the PLL Dynamics

To show the importance of including the PLL dynamics in the ac-bus voltage dynamics, the dynamics in (5-14) is considered without the PLL dynamics by setting $H(s)$=0. In this case, (5-14) converges to

$$\tilde{V}_{PCC\_d}(s) = L_{grid} s\tilde{I}_d(s) - L_{grid} s\tilde{I}_{Load\_d}(s) - \frac{\omega_0 L_{grid}}{\tau_i s + 1}\tilde{I}_q^*(s) + \omega_0 L_{grid}\tilde{I}_{Load\_q}(s) \tag{5-22}$$

As shown in (5-22), without the PLL dynamics, the ac-bus voltage control dynamics becomes independent of the converter operating point. Using the simplified dynamics in (5-22), and following the design process presented in Section 5.4, the ac-bus voltage controller is redesigned to yield robustness against disturbances and variation in the grid inductance. The resultant controller is given in (5-23).

$$K(s) = \frac{-1.214\times10^{8}s^{4} - 4.431\times10^{10}s^{3} - 1.468\times10^{12}\mathrm{s}^{2} - 7.09\times10^{12}\mathrm{s} - 1.851\times10^{12}}{s^{5} + 2.556\times10^{8}s^{4} + 7.658\times10^{9}s^{3} + 3.056\times10^{10}\mathrm{s}^{2} + 5.192\times10^{7}\mathrm{s} + 2.136\times10^{4}} \tag{5-23}$$

Fig. 5.15 shows the ac-bus voltage in Zone I, with the ac-bus voltage controller in (5-23), at SCC-R=1. Due to the coupling between the grid and converter dynamics, the actual plant model is remarkably different from the simplified model in (5-22), which is used to design the controller. Such unmodelled dynamics destabilizes the system at the very weak grid condition as shown in Fig. 5.15.

5.6 Experimental Results

For further evaluation of the proposed controller, an experimental test system, based on the schematic diagram shown in Fig. 5.1, is employed to test the performance of a weak-grid-connected VSC. A Semistack intelligent power module, which includes gate drives, six insulated gate bipolar transistors (IGBTs), and protection circuit, is used to implement the grid-connected VSC. The VSC is rated at 35 A, 380 V. The ac filter inductance and resistance are 1.20 mH and 0.06 Ω, respectively. The dc-link capacitance is 2.04 mF. The very weak grid is created by connecting a series inductor to the ac grid so that SCC-R=1 at the PCC. The converter is de-rated to 1 kVA at 35 V_{ac}. With this rating, a 3 mH series inductor is needed to create a weak grid with SCC-R=1. The dc side of the converter is connected to a dc dynamic load (dc-motor loaded

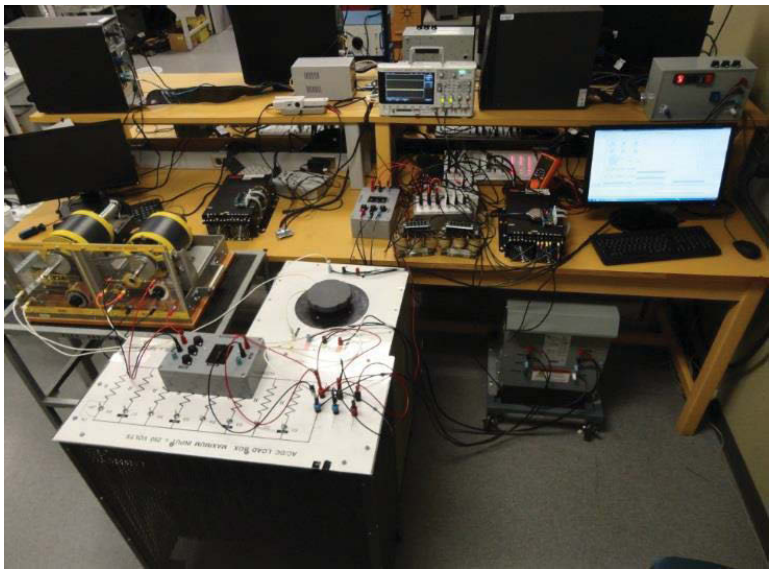

Fig. 5.16. A view of the experimental setup.

by a dynamometer), and static load (variable resistive load) representing a dc microgrid. The VSC is controlled in the rectification mode, which yields to the worst operating conditions with respect to the ac-bus voltage stability as shown by the analysis results in Section 5.3. The VSC inductor currents are measured by HASS-50-S current sensors whereas the voltages are measured by LEM-V-25-400 voltage sensors. The converter is interfaced to a dSPACE1104 control card using a CMOS/TTL interfacing circuit. The pulse-with modulation and the converter controllers are implemented on the dSPACE1104 control card supported with a TMS320F240-DSP coprocessor structure for switching signal generation. The dSPACE1104 interfacing board is equipped with eight digital-to-analogue channels and eight analogue-to-digital channels to interface the measured signals to/from the control system. The software code is generated by the Real-time-WorkShop under the MATLAB/Simulink environment. A view of the experimental setup is shown in Fig. 5.16.

The proposed controller is designed for SCC-R=2 whereas the actual SCC-R=1 to test the robustness of proposed controller under variable grid inductance and worst-case condition. Fig. 5.17 shows the performance of the proposed controller with SCC-R=1 while the converter operates at the rated power; the system is excited by a dynamics disturbance created by starting the loaded dc motor connected to the dc-link. The traces in Fig. 5.17 from top to bottom show the grid-voltage at the PCC, dc-link voltage, converter direct current, and converter reactive

current, respectively. In spite of the presence of parametric uncertainty and the very weak grid condition, the proposed controller successfully regulates the ac-bus voltage and shows excellent performance in terms of low voltage dip and fast recovery.

For the sake of performance comparison, the PI ac-bus voltage controller is tested under the same SCC-R and disturbances. The performance of the PI controller is shown in Fig. 5.18. At the very weak grid condition, the system becomes unstable as predicted by the simulation results. Due to the instability, the overcurrent protection of the converter is activated, and the converter pulses are blocked.

Fig. 5.19 shows the performance of the proposed controller when the system is excited by disconnecting and connecting the dc static load. The traces in Fig. 5.19 from top to bottom show the grid-voltage at the PCC, dc-link voltage, converter direct current, and phase-a modulation index, respectively. Again, the proposed controller yields excellent disturbance rejection performance under the very weak grid condition, and disturbances while operating at the rated power.

5.7 Parameters of Simulated System, Fig. 5.1

Rated Power=3.0 MVA, Grid Voltage=580 V at 60 Hz; L_{grid} range: 59.48 μH to 297.44 μH, which corresponds to SCC-R=5 to SCC-R=1, P_{Loss}=5000 W; R=0.06 mΩ; L=300 μH;, Switch resistance=1.0 mΩ; Diode resistance=1.0 mΩ; PI-current controller parameters: K_p=0.06 Ω; K_i=0.7 Ω/s; PID-PLL controller: K_p=180; K_i=3200; K_d=1.

The nominal plant transfer function $G(s)$ in (5-18) is generated with the following parameters: P_0= -1.075 MW and Q_0=+1.075 Mvar, L_{grid0} = 178.46 μH, which corresponds to SCC-R =1.667.

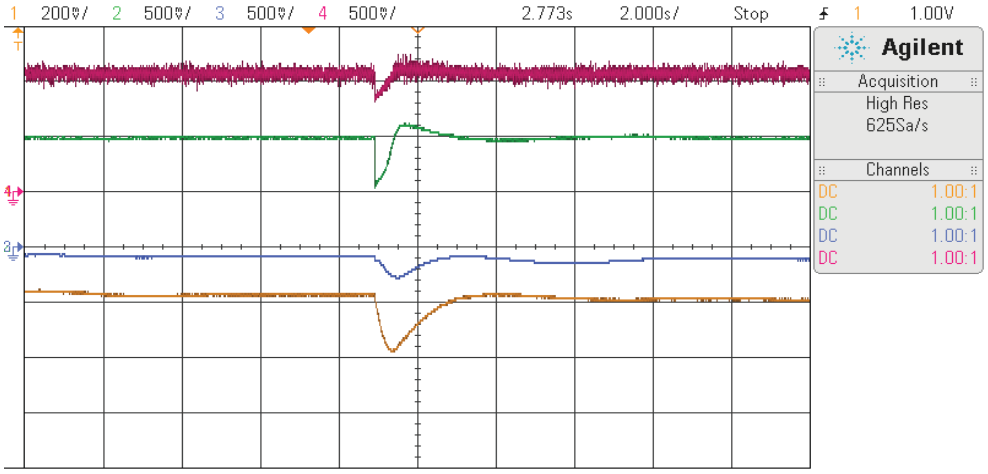

Fig. 5.17. Experimental results of the proposed controller performance during starting up the dynamic dc motor load and uncertainty in the grid inductance. Channel 4 (top line): $V_{PCC\text{-}d}$ in per-unit: 0.5 V/div, Channel 2 (the second line from top): V_{dc} in per-unit: 0.5 V/div, Channel 3 (the third line from top): control lever, i_d, 10 A/div, Channel 1 (bottom line): control lever, i_q 2 A/div. Horizontal Axis: 2 s/div.

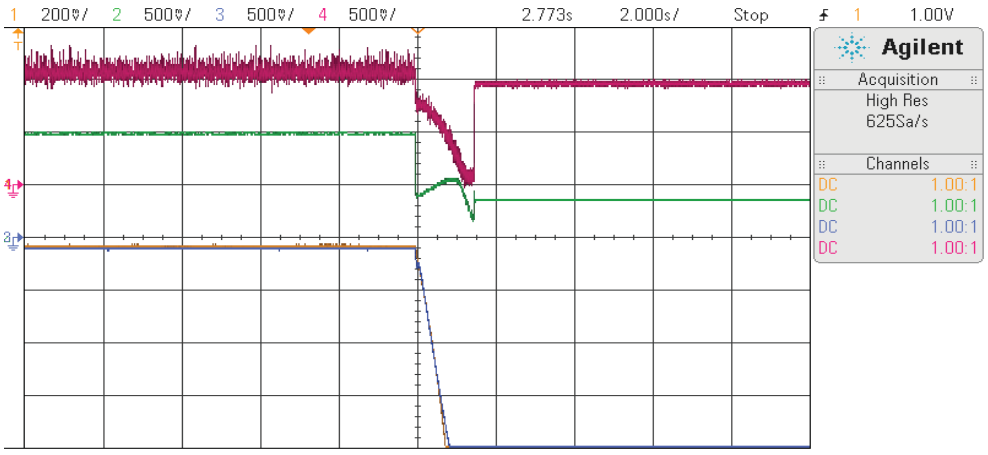

Fig. 5.18. Experimental results of the PI controller performance during starting up the dynamic dc motor load and uncertainty in the grid inductance. Channel 4 (top line): $V_{PCC\text{-}d}$ in per-unit: 0.5V/div, Channel 2 (the second line from top): V_{dc} in per-unit: 0.5 V/div, Channel 3 (the third line from top): control lever, i_d, 10 A/div, Channel 1 (bottom line): control lever, i_q 2 A/div. Horizontal Axis: 2 s/div.

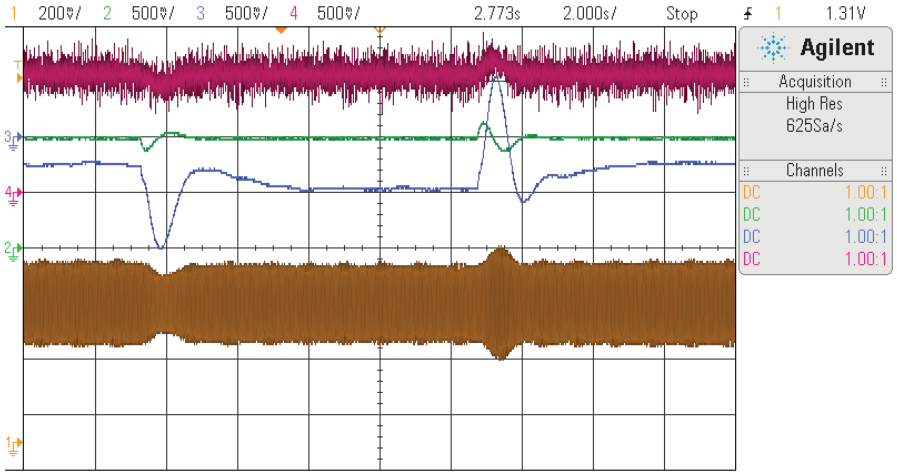

Fig. 5.19. Experimental results of the proposed controller performance disconnecting/connecting static loads and uncertainty in the grid inductance. Channel 4 (top line): $V_{PCC\text{-}d}$ in per-unit: 0.5 V/div, Channel 2 (the second line from top) V_{dc} in per-unit: 0.5 V/div, Channel 3 (the third line from top): control lever, i_d, 10 A/div, Channel 1 (bottom line): modulation index of phase-a (bounded between 0 to 1 based on dSPACE1104 requirement), Horizontal Axis: 2 s/div.

5.8 Parameters of Simulated System, Fig. 5.12

DC Grid: Rated voltage=1750 V, dc-cable length=20 km, R_{cable}=0.82 mΩ/km, C_{cable}= 0.014 μF/km, L_{cable}=0.98 μH/km

Zone I: Weak-grid-connected VSC: Rated Power=2.5 MVA, Grid Voltage=580 V at 60 Hz; L_{grid} range: 71.38 μH to 356.93 μH, which corresponds to SCC-R=5 to SCC-R=1, P_{Loss}=5000 W; R=0.06 mΩ; L=300 μH;, Switch resistance=1.0 mΩ; Diode resistance=1.0 mΩ; PI-current controller parameters: K_p=0.06 Ω; K_i=0.7 Ω/s; PID-PLL controller: K_p=180; K_i=3200; K_d=1.

Zone II: VSC-PQ: Rated Power=2.50 MVA, Grid 2 Voltage=580V at 60 Hz; P_{Loss}=5000 W; R=0.06 mΩ; L=300 μH; C=3000 μF, Switch resistance=1.0 mΩ; Diode resistance=1.0 mΩ; PI-current Controller Parameters: K_p=0.06 Ω; K_i=0.7 Ω/s; PID-PLL controller parameters: K_p=180; K_i=3200; K_d=1.

Zone III VSC-W: Rated Power=2.5 MVA, Grid 2 Voltage=580 V at 60 Hz; P_{Loss}=5000 W; R=0.06 mΩ; L=300 μH; C=3000 μF, Switch resistance=1.0 mΩ; Diode resistance=1.0 mΩ; PI-current Controller Parameters: K_p=0.06 Ω; K_i=0.7 Ω/s;

Zone IV: Power rating =0.9 MW, ESS and load voltage 500 V-dc, C_L=1000 μF, C_H=6000 μF, L_1=100 mH, R_{DC}=1 Ω, PI Controller: K_p(mode1)=0.4, K_i(mode1)=4×10^{-4}, K_p(mode2)=0.0114, K_i(mode2)=0.0457, V_{L_Ref}=500 V, i_{L_Ref}=1800 A.

5.9 Conclusion

A robust vector-controlled VSC that facilitates full converter power injection at weak and very weak grid conditions has been developed in this chapter. To realize the controller, firstly, a detailed dynamic model for the ac-bus voltage dynamics, including the PLL dynamics, has been developed and validated in this chapter. Secondly, the model has been used to optimally design a robust ac-bus voltage controller to stabilize the dynamics under operating point variation and grid impedance uncertainty. A theoretical analysis and comparative simulation and experimental results have shown the effectiveness of the proposed controller. The proposed controller has the following characteristics.

1) Because the developed model includes the PLL dynamics, the developed controller inherently stabilizes the negative impact of the PLL on the converter stability.
2) By the proposed approach, the need to change the structure and/or the parameters of the standard vector controllers (e.g., current controller, PLL, and dc-link voltage controller) to facilitate very weak grid integration is eliminated.
3) The controller gives a robust control performance against operation point variation and uncertainties in the grid inductance.
4) The controller has a systematic design approach and simple fixed-order structure; therefore, it can be easily implemented in commercial-grade digital signal processors.

Chapter 6

Robust DC-Link Voltage Control of a VSC Interfacing a Wind Turbine Into DC Grids

6.1 Introduction

Motivated by the difficulties mentioned in Section 1.3.5, this chapter presents a robust parallel distributed dc-bus voltage controller for a full-scale wind turbine connected to a dc grid. The turbine is directly used to control the dc-link voltage at the point of coupling to the dc grid at different operating points via a robust controller that offers a high robustness against large variation in the operating point, static and dynamic load variation, and parametric uncertainty. Firstly, a controllable model that is suitable for dc grid application is developed. Then, the modeled system is used for robust controller synthesis using the singular values μ-synthesis approach, to achieve robustness against wind turbine operation point variation as well as static and dynamic load variation. The H_∞ norm of the closed-loop system from the disturbance to the tracking error is minimized using the μ-synthesis approach considering uncertainties due to operating point variations as well as static load variations. To overcome a large variation of the operating points associated with the power characteristic curve of the wind turbine and the nonlinear system dynamics, the wind turbine is considered as a fuzzy model to develop a parallel distributed controller. For each fuzzy set, a robust controller is designed to cover all operating point variation, static/dynamic load variation, and parametric uncertainties. Then, all controllers are aggregated with the weight of the membership functions, which represent the fuzzy model of the dc-link voltage dynamics. A theoretical analysis and comparative simulation results are presented to show the validity and effectiveness of the proposed controller.

6.2 Model of DC-Energy Pool Controlled with Wind Turbine

A dc distribution system controlled with wind turbine has been shown in Fig. 6.1. A PMSG has been employed in this chapter because of its fast progress and widespread acceptance in present and future wind turbine applications [50]. The generator is interfaced to the dc grid via a VSC controlled in the *dq* synchronous frame that rotates with the machine rotor reference frame. The VSC is current-controlled to control the machine torque. An outer dc-link voltage control loop generates the speed reference for the variable speed PMSG turbine, whereas a speed controller generates the torque-producing current command for the current controller. As shown in Fig. 6.1(b), the dc grid can be connected to static (passive) loads) and dynamic (converter-based) loads (e.g., power converters interfacing the dc grid with other dc or ac grids, energy storage units, and loads). For example, a 1.0 MVA, 580 V grid-connected VSC is connected to the dc grid, and it is controlled to inject or absorb power from the dc grid. This converter can be modeled as a dynamic load with positive or negative generation connected to the dc grid.

According to Fig. 6.1(b), the power balance across the capacitor C_W can be described by:

$$\frac{d(0.5C_W V_{dc}^2)}{dt} = P_{dc} - P_{VSC\_loss} - P_{static\_load} - P_{dynamic\_load} \tag{6-1}$$

where P_{dc}, P_{VSC_loss}, P_{static_load}, and $P_{dynamic\_load}$ are dc power converted and processed by the VSC, power losses of the VSC, power absorbed by static loads modeled by a resistance, power absorbed by dynamic loads, respectively. Converter losses can be modeled as either static or dynamic element [111].

The dc-power is related to the turbine power by

$$P_{dc} = C_p P_{Wind} - P_{PMGS\_loss} - P_{acceleration} \tag{6-2}$$

where P_{Wind} is the total wind power that can be captured by a wind turbine if the power coefficient of the wind turbine is equal to one, C_p is the power coefficient of the wind turbine which is the main source of nonlinearity and uncertainty in this study, $P_{\text{PMSG\_loss}}$ is the power loss of the PMSG, and $P_{\text{accelaration}}$ is the accelerating power required to change the rotational speed of rotor of the PMSG.

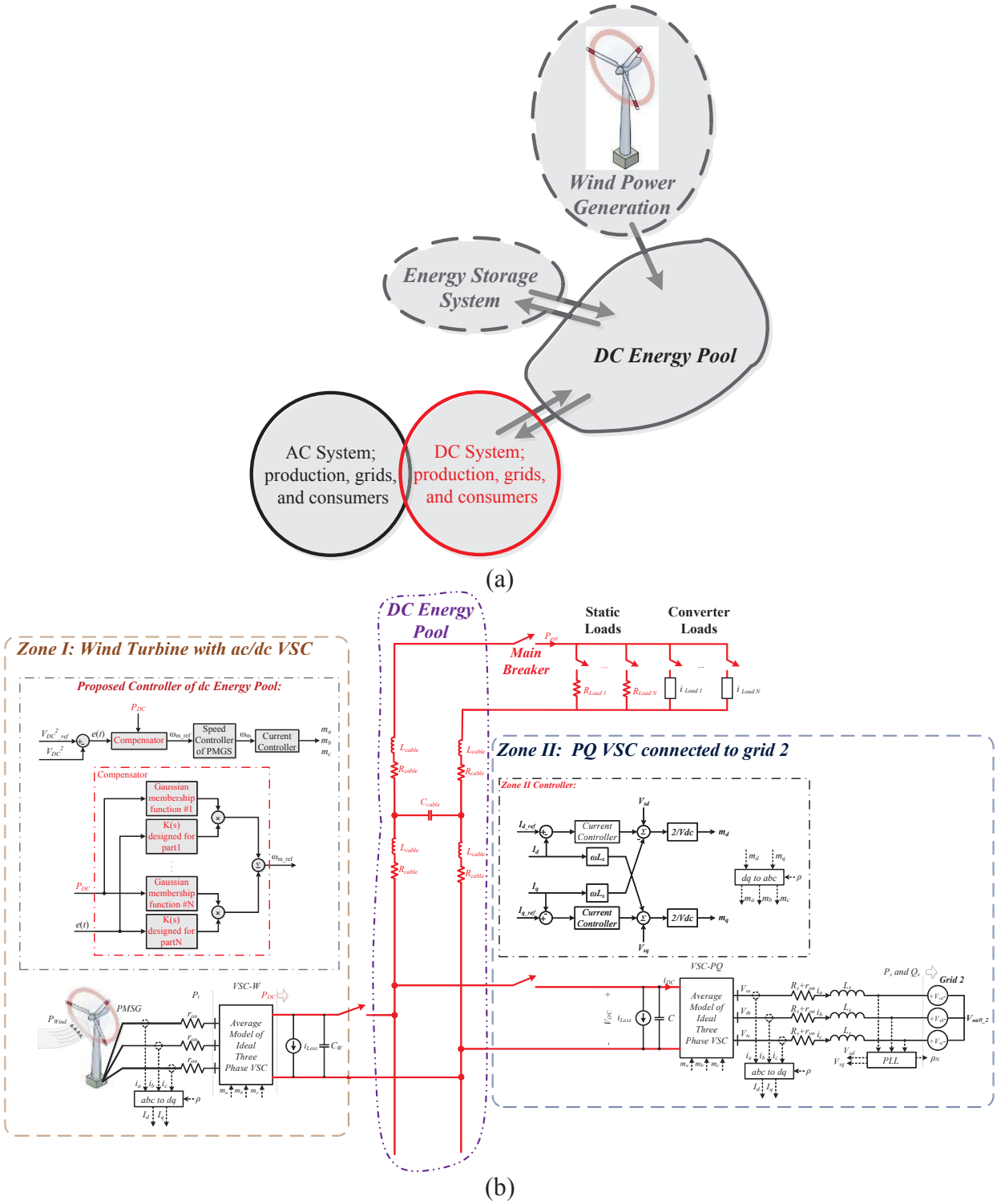

Fig. 6.1. DC grid with a full-scale wind turbine. a) General configuration b) Detailed configuration.

The dc-link voltage of the wind turbine is regulated by controlling P_{Wind} absorbed by the PMSG by controlling its rotational speed. In other words, the control lever of the dc-link voltage is the PMSG rotational speed. In this chapter, the controller is synthesized in a robust manner to be robust against C_p variation, static and dynamic load variation, and parametric uncertainties. To develop an appropriate model that captures all the information required for robust controller design (e.g., operating point variation and the presence of disturbances), there is a need to carefully model and linearize the plant dynamics [this point was not considered in previous works [51]-[52]].

The dc-link voltage dynamics can be written as

$$\frac{d(0.5C_W V_{dc}^2)}{dt} = C_p \times (0.5\rho A v^3) - P_{total\_loss} - J\omega_m\alpha - \frac{V_{dc}^2}{R_{load}} - P_{dynamic\_load} \tag{6-3}$$

where C_p is the power coefficient of the wind turbine that is a function of the rotational speed, ω_m, wind speed, v, and the pitch angle β; ρ is the air density; A is the area swept by turbine blades; P_{total_loss} is the total losses of the VSC and PMSG; J is the total system inertia reflected to the PMSG side; ω_m is the angular velocity of the PMSG; α is the angular acceleration; and $P_{dynamic\_load}$ is the power of the converter-based loads (e.g., power absorbed by the VSC in Zone II in Fig. 6.1b).

By considering V_{dc}^2 as an output, instead of V_{dc}, and using D as the derivative operator, (6-4) can be reached.

$$\begin{aligned}((0.5R_{load}C_W)D+1)V_{dc}^2 = {} & R_{load}(C_p(0.5\rho A v^3)) - R_{load}P_{total\_loss} \\ & - R_{load}J\omega_m\alpha - R_{load}P_{dynamic\_load}\end{aligned} \tag{6-4}$$

In (6-4), V_{dc}^2 and ω_m are the system output and input, respectively. Using the selected input and output signals yields a controllable control system from ω_m to V_{dc}^2. For simplicity, V_{dc}^2 is called V_{dc_s} hereafter. Equation (6-4) it is highly nonlinear because C_p is highly dependent on ω_m, v, and β; and more importantly, ω_m is the control lever. For robust control design, a linearization around an operating point is conducted. Equations (6-5.a) to (6-5.c) show the linearization process of (6-4).

$$((0.5R_{load}C_W)D+1)V_{dc}^2 = f(\omega_m, \alpha, v, P_{total\_loss}, P_{dynamic\_load}) \tag{6-5.a}$$

where

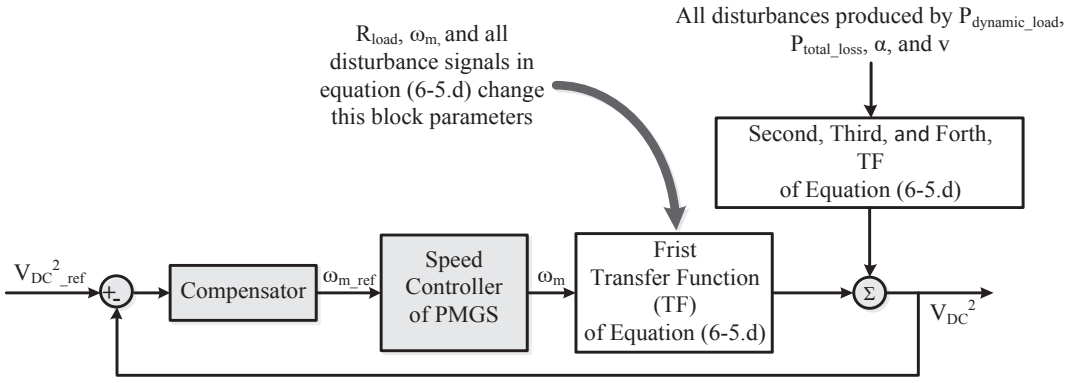

Fig. 6.2. Control system of a dc-voltage-controlled wind turbine.

$$
\begin{aligned}
&f(\omega_m, \alpha, v, P_{total\_loss}, P_{dynamic\_load}) = \\
&f(\omega_{m0}, \alpha_0, v_0, P_{total\_loss_0}, P_{dynamic\_load_0}) + \\
&\frac{\partial f}{\partial \omega_m}|_{\omega_m=\omega_{m0}}\ \omega_m(s) + \frac{\partial f}{\partial \alpha}|_{\alpha=\alpha_0}\ \alpha + \frac{\partial f}{\partial v}|_{v=v_0}\ \tilde{v}(s) + \\
&\frac{\partial f}{\partial P_{total\_loss}}|_{P_{total\_loss}=P_{total\_loss0}}\ P_{total\_loss} + \\
&\frac{\partial f}{\partial P_{dynamic\_load}}|_{P_{dynamic\_load}=P_{dynamic\_load0}}\ \widetilde{P_{dynamic\_load}} + \\
&(HOT)
\end{aligned}
\tag{6-5.b}
$$

where "~" denotes a perturbed signals around its operating point.

At an equilibrium point, one has

$$
f(\omega_{m0}, v_0, P_{total\_loss_0}, P_{dynamic\_load_0}, \alpha_0) = V_{dc}^2 \tag{6-5-c}
$$

Hence, the final linearized model of dc-link voltage dynamics can be given by (6-5.d).

$$
\begin{aligned}
V_{dc\_s}(s) &= \frac{-R_{load} J \omega_{m_0} s + R_{load} \frac{\partial P_{Wind}}{\partial \omega_m}|_{\omega_m=\omega_{m0}}}{(0.5R_{load}C_W)s+1}\omega_m(s) \\
&+ \frac{C_p(1.5\rho A v_0^2)}{(0.5R_{load}C_W)s+1}\tilde{v}(s) \\
&- \frac{R_{load}}{(0.5R_{load}C_W)s+1}P_{total\_loss}(s) - \frac{R_{load}}{(0.5R_{load}C_W)s+1}P_{dynamic\_load}(s)
\end{aligned}
\tag{6-5.d}
$$

$$k \triangleq R_{load}\frac{\partial P_{Wind}}{\partial \omega_m}|_{\omega_m=\omega_{m0}};\ DC\ Gain$$

$$\tau \triangleq 0.5R_{load}C_W;\ Time\ Constant$$

An important aspect of this modeling approach is that static loads in the dc grid (resistive

loads) affect the time-constant of the plant model, whereas dynamic loads (e.g., power converters) appear as a disturbance in the plant model. Besides, with a robust disturbance rejection controller, the disturbances induced by dynamic loads, angular acceleration, wind speed, and power losses can be rejected as well. Hence, all the second to the fifth terms in (6-5.d) are lumped into one disturbance as shown in Fig. 6.2. It is worthy to note that there is a non-minimum phase zero in the model in (6-5.d) because this chapter models the dynamics of the dc-link voltage using V^2_{dc}, not V_{dc}. Hence, (6-5.d) is also independent of V_{dc0}, the initial operating point of the dc voltage. Equation (6-5.e) represents the linearized model of the plant at the startup operating point (i.e., when ω_{m0} is close to zero). Equation (6-5.f) represents the plant model at a critical operating point, which is the operating point that yields the closest to the $j\omega$ axis non-minimum phase zero.

$$V_{dc\_s}(s) = \frac{+R_{load}\dfrac{\partial P_{Wind}}{\partial \omega_m}\Big|_{\omega_m=0}}{(0.5R_{load}C_W)s+1}\omega_m(s) \tag{6-5.e}$$

$$V_{dc\_s}(s) = \frac{-R_{load}J\omega_{m\_Critical}s + R_{load}\dfrac{\partial P_{Wind}}{\partial \omega_m}\Big|_{\omega_m=\omega_{m\_Critical}}}{(0.5R_{load}C_W)s+1}\omega_m(s) \tag{6-5.f}$$

To ensure robust performance and stability, the dc-link voltage controller should be also robust against variation in the equivalent dc-link capacitance C_W. In dc grid applications with several power converters connected/disconnected to/from the dc grid, the equivalent dc-link capacitance can be subjected to wide range of variation. In this chapter, the controller is designed with robustness against variation in the plant time-constant $C_W R_{load}$; therefore, both load and effective capacitance uncertainties can be rejected.

6.3 Proposed DC-Voltage Control Method

The controller adopted in this chapter is based on a nested controller structure. The inner controller is the current controller, the intermediate loop is the speed control loop of the PMSG, and the outermost loop is the dc-link voltage control loop. The fact that C_p changes with β and v yields a complicated nonlinear system dynamics. From the industrial application point of view, it is highly desirable to develop a robust and simple controller that offers robustness against operation point variation and disturbances.

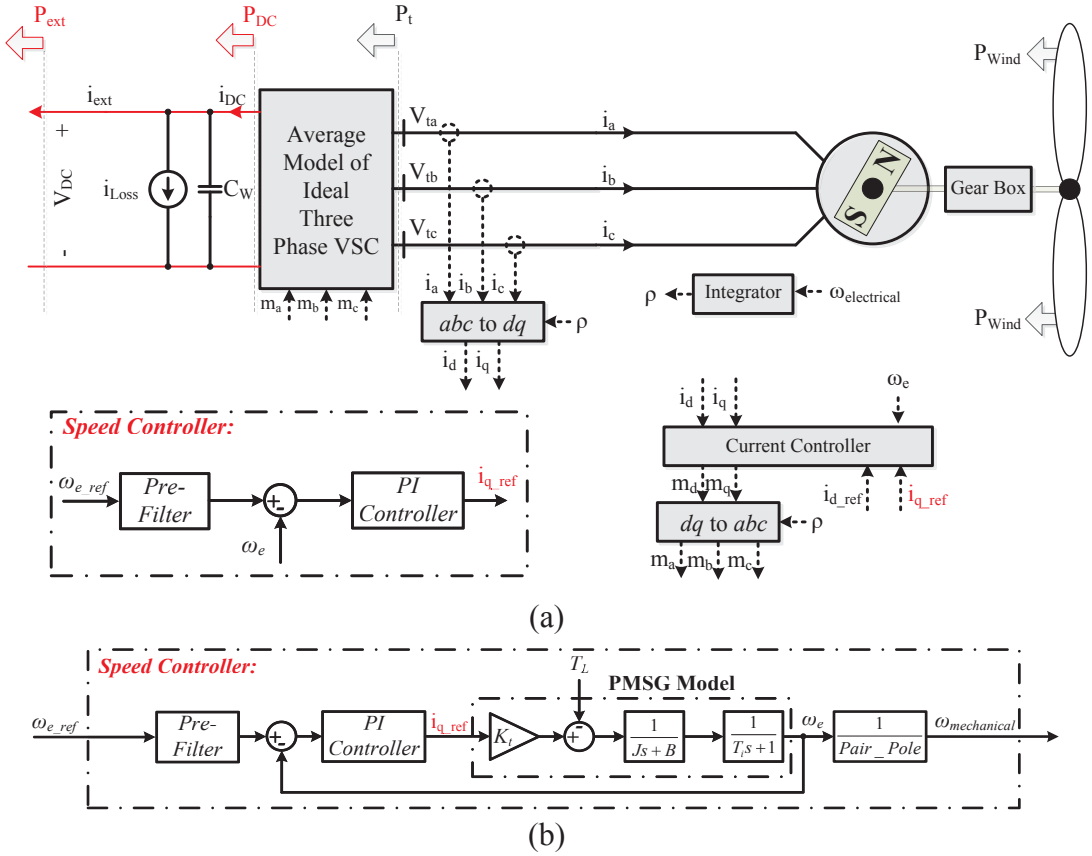

Fig. 6.3. DC-voltage controlled wind turbine. a) Complete system. b) Block diagram of the speed controller.

6.3.1 Inner Controller Loops

The current controller is simply a PI controller with feed-forward decoupling paths. In addition, a PI speed controller is used to generate the reference q-axis current for the current controller. The machine control structure follows the common field-oriented control (FOC) theory. The standard inner loop controllers are shown in Fig. 6.3 [50].

6.3.2 Outer Controller Loop

According to the first transfer function of (6-5.d), controller synthesis is highly dependent on the slope of C_p, which is highly variable due to many factors such as ω_m, v, and β. The expression of C_p is given by [50].

$$C_p(\lambda,\beta) = 0.5176\left(\frac{116}{\lambda_i} - 0.4\beta - 5\right)e^{\frac{-21}{\lambda_i}} + 0.0068\lambda$$
$$\frac{1}{\lambda_i} = \frac{1}{\lambda + 0.08\beta} - \frac{0.035}{\beta^3 + 1}$$
$$\lambda = \frac{R\omega_{Turbine}}{v} \tag{6-6}$$

where β is the pitch angle in degrees, ω_{Turbine} is the rotational speed of the wind turbine blades, and v is the wind speed. Fig. 6.4 shows the variation of P_{Wind} versus the PMSG speed in (rad/s) as well as variations of the slope of P_{Wind} versus the PMSG speed in (rad/s) at different values of the wind speed and the pitch angle β. All wind-turbine and system parameters are given in Section 6.5. It is worth mentioning that the impact of the pitch angle on the dc-link voltage dynamics is negligible due to the slow dynamics of the pitch angle controller [110].

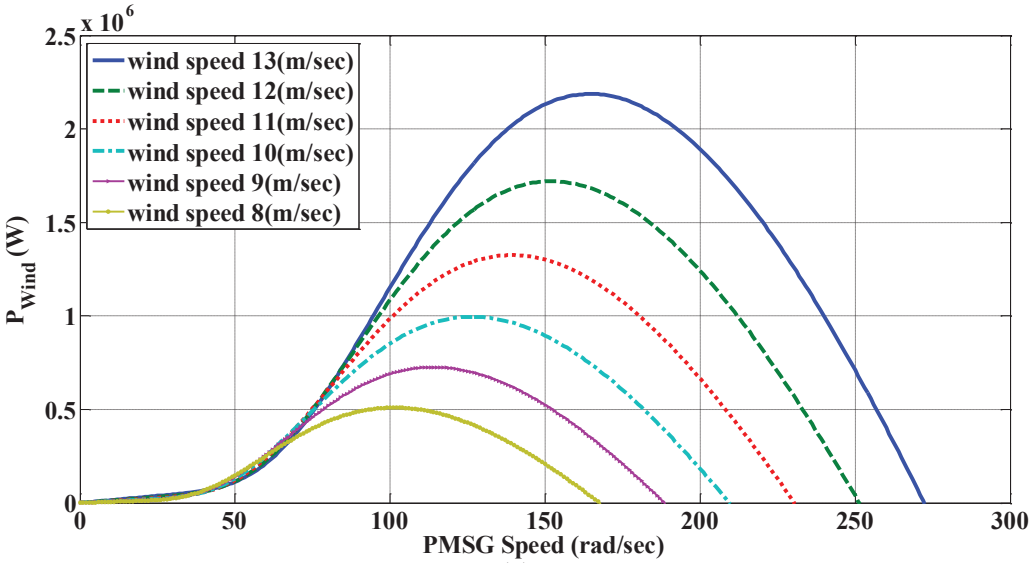

(a)

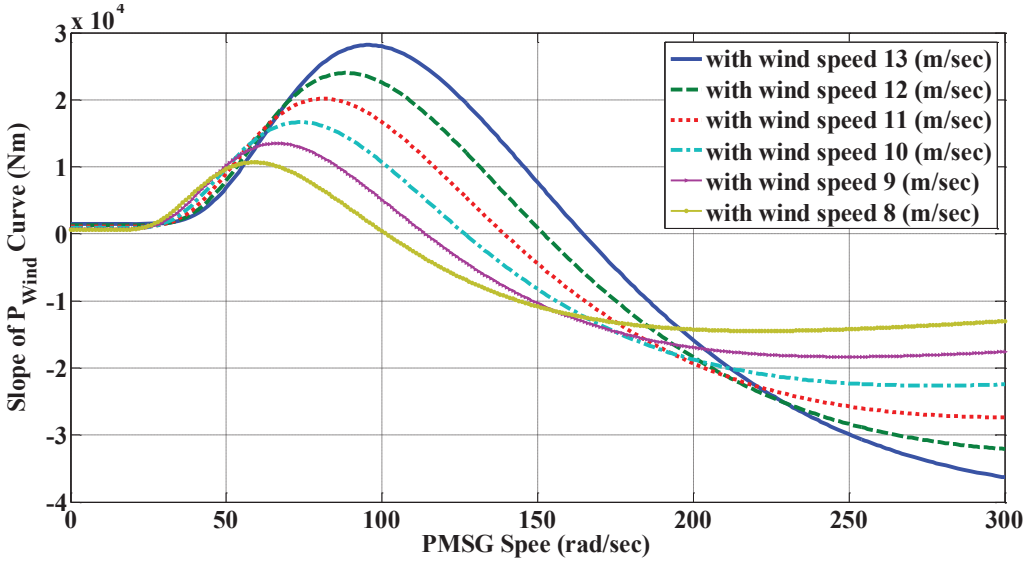
x 10^4
Slope of P_Wind Curve (Nm)
PMSG Spee (rad/sec)
with wind speed 13 (m/sec)
with wind speed 12 (m/sec)
with wind speed 11 (m/sec)
with wind speed 10 (m/sec)
with wind speed 9 (m/sec)
with wind speed 8 (m/sec)

(b)

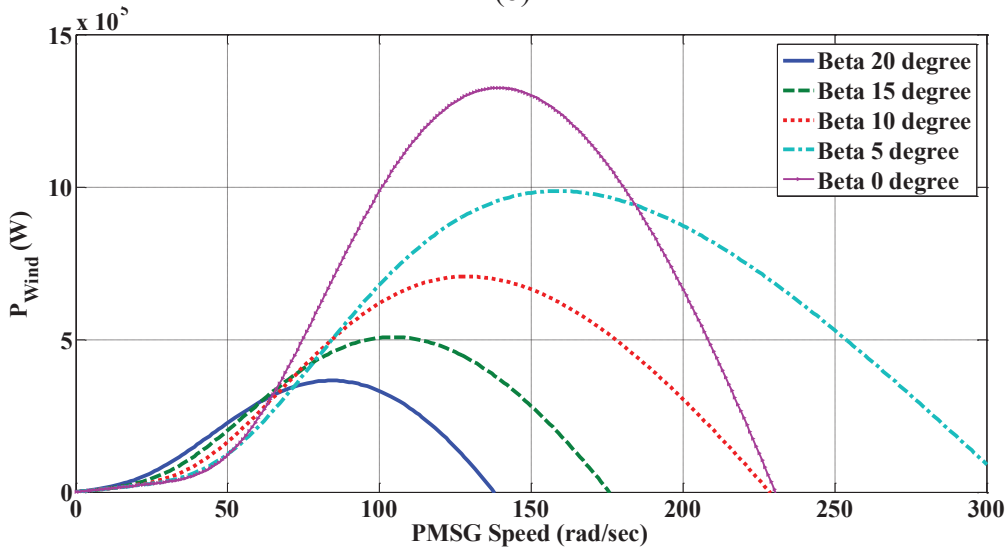
x 10^5
P_Wind (W)
PMSG Speed (rad/sec)
Beta 20 degree
Beta 15 degree
Beta 10 degree
Beta 5 degree
Beta 0 degree

(c)

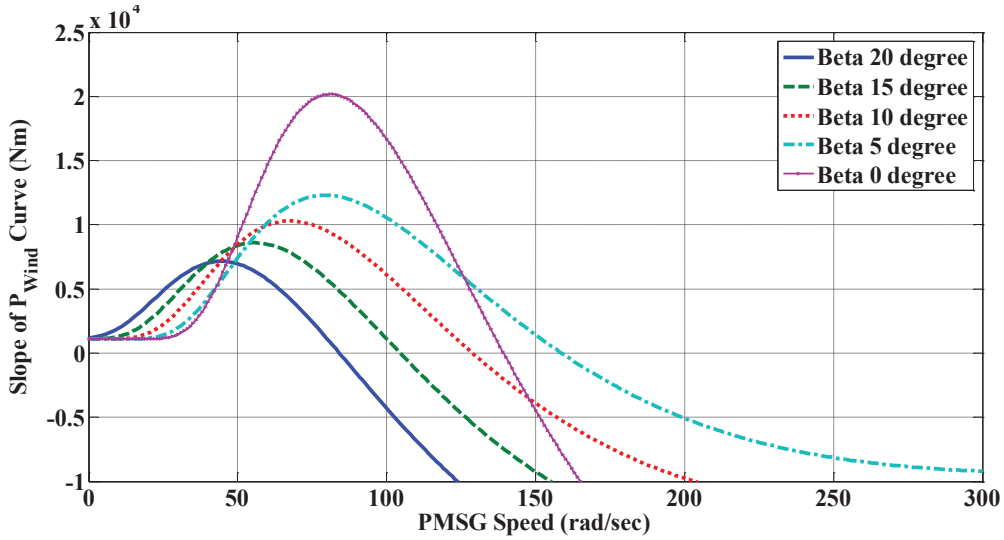

(d)

Fig. 6.4. Wind turbine characteristic curves. (a) P_{Wind} versus PMSG speed at different wind speeds. (b) $dP_{Wind}/d\omega_m$ versus PMSG speed at different wind speeds (c) P_{Wind} versus PMSG speed at different pitch angles β. (d) $dP_{Wind}/d\omega_m$ versus PMSG speed at different pitch angles β.

6.3.3 Robust Control Design

Fig. 6.4 and the first transfer function of (6-5.d) show the following. 1) The plant dynamics has a variable gain changing at different operating points induced by operating point variation. 2) Variations in the static load and CW affect the plant time constant. 3) Static and dynamic loads are affecting the plant dynamics in different ways as dynamic loads appear as a disturbance on the system. Furthermore, the plant model is subjected to significant unmodeled dynamics when the state of the system trajectories is changing from a stable equilibrium point, say V_{dc_s0}, to another one, say V_{dc_s1}, which is the natural result of nonlinear system dynamics. Therefore, robustness against dynamic operating point variation should be maintained. The performance of the system is also deteriorated by disturbances, the second term to the fifth term of (6-5.d). Thus, the controller synthesis objective is finding a controller that minimizes the effect of operating point variation, disturbances and variation in the plant parameters. For a limited range of variation in system parameters and operating points, it is possible to synthesize a single robust controller that ensures robust stability and robust performance with parameter variation and occurrence of disturbances. However, as indicated in Fig. 6.4, in dc-voltage-controlled wind turbines, the turbine characteristics yield a large range of variation in operating points. The range of uncertainty increases when the load parameter and equivalent capacitance variation is

considered. Therefore, several controllers can be designed at different operating points and used for controller-fusion, via a robust parallel distributed control approach, to ensure robust performance at wide range of operating conditions [113]-[114]. Each controller can be designed to ensure robust performance over a range of operating point variation whereas maintaining stability at all possible ranges. It has been found that based on a typical wind turbine characteristics, three robust controllers can be designed and augmented to ensure excellent robust performance with a relatively simple control structure. First, the design process of a robust controller at one range of operating points is described.

At this stage, there is a need to design a controller capable of rejecting the disturbances affecting the plant, parametric uncertainty and operating point variation in a range of wind turbine operating points. One of the best ways to reject the disturbance effect on the output is minimizing the H_∞ norm from a filtered disturbance signal to the filtered output in the presence of weighted uncertainty, or designing the controller based on the structured singular values μ-analysis [81]-[82]. The μ-synthesis controller leads to better robust performance as compared to the $H\infty$ controller. This feature allows the design of a disturbance rejection controller that preserves the robustness and stability under operating point variation, static loads, and dynamic loads. The block diagram of the proposed μ-analysis robust controller is shown in Fig. 5(a). Fig. 5(a) demonstrates perturbed plant with multiplicative uncertain linear system affected by disturbance and output noise. In fact, the variation of the plant model parameters in each part can be reflected as a perturbed plant with multiplicative uncertainty. Equation (6-7) and Theorem 1, given below, show the robust performance of the perturbed plant with multiplicative uncertainty. The perturbed model can be written as:

$$\tilde{G}(s) = (1 + W(s)\Delta(s))G_n(s) \tag{6-7.a}$$

where $W(s)$ is a fixed stable transfer function, $\Delta(s)$ is a variable transfer function satisfying $\|\Delta\|_\infty \leq 1$, and $G_n(s)$ is the nominal plant.

With a feedback controller $K(s)$, the sensitivity function is

$$\tilde{S}(s) = \frac{1}{1 + (1 + \Delta W)G_n K} = \frac{1/(1 + G_n K)}{(1 + G_n K + \Delta W G_n K)/(1 + G_n K)} \tag{6-7.b}$$

If $S(s) \triangleq \dfrac{1}{1 + G_n(s)K(s)}$ & $T(s) = 1 - S(s)$ then, $\tilde{S}(s) = \dfrac{S(s)}{1 + \Delta(s)W(s)T(s)}$.

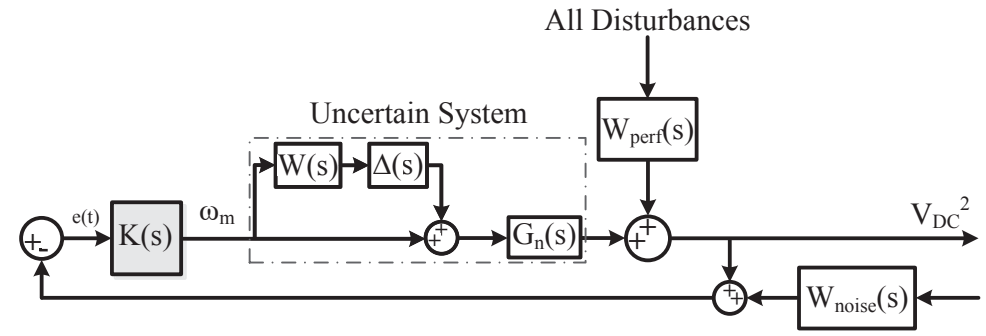

(a)

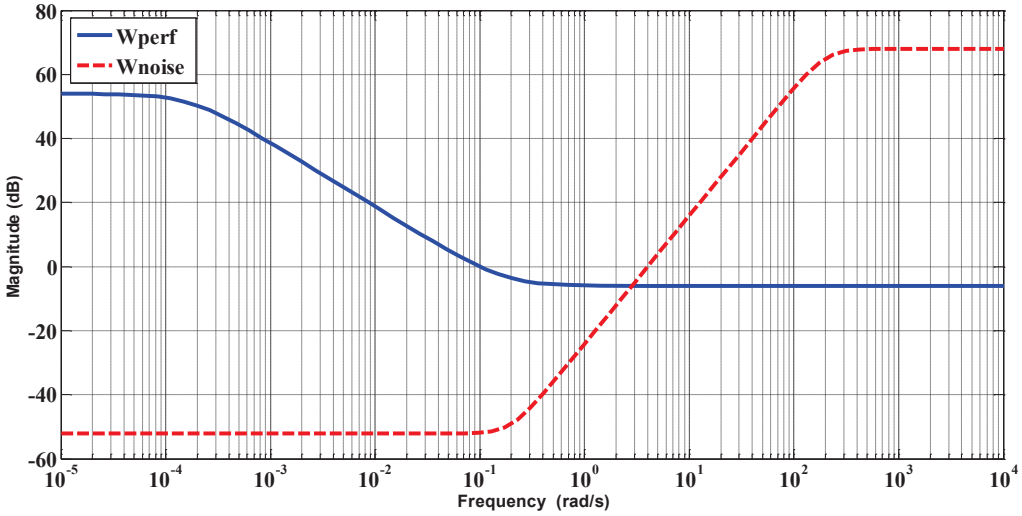

(b)

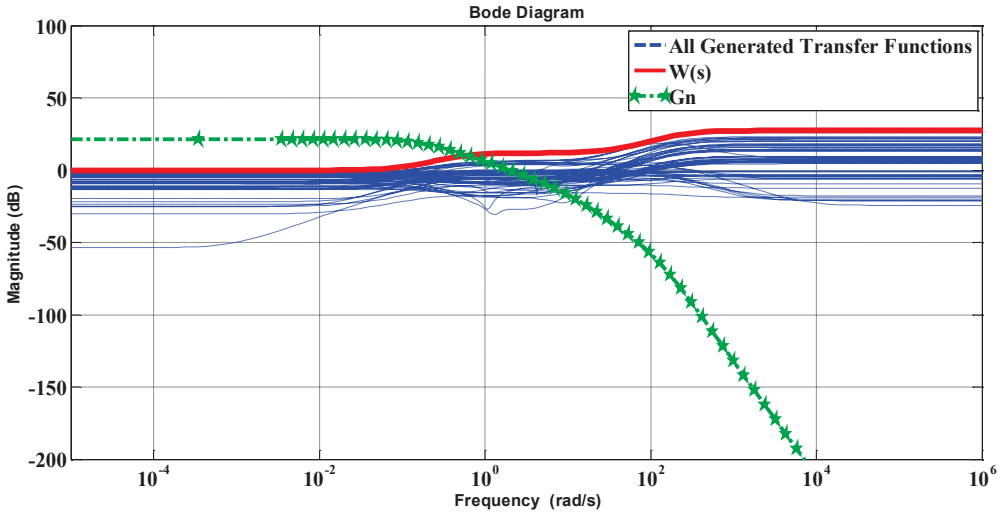

c)

Fig. 6.5. (a) The structure used for designing a robust controller for each specific part of the uncertain P_{Wind} curve. (b) Magnitude response of the performance and noise filter used to design $K(s)$. (c) Magnitude response of $W(s)$ and $G_n(s)$ employed in Fig. 6.5(a) as well as transfer functions generated by operating point variation in one part.

"Theorem 1: If K(s) provides nominal closed-loop stability for the nominal closed-loop system, which can be obtained using Fig. 5(a) when Δ(s)=0, then K(s) provides robust stability for the system of Fig. 6.5(a) if and only if $||WT||_\infty \leq 1$*. It also provides robust performance if and only if* $||W_{perf}S||_\infty + ||WT||_\infty \leq 1$ *[81]."*

Based on the proof of Theorem 1 [81], W_{Pref} is selected such that the tracking error is small at frequencies where $|W_{Pref}(j\omega)|$ is large, and the feedback controller is providing good tracking performance. It should be noted that the tracking error requirements are relaxed at frequencies where $|W_{Pref}(j\omega)|$ is small. Furthermore, W_{noise} is used to limit the controller bandwidth and to induce roll-off beyond the desired bandwidth requested by W_{Perf}. Thus, W_{noise} has magnitude larger than one at frequencies greater than ten times the desired bandwidth.

The frequency response of W_{Perf} and W_{noise} is shown in Fig. 6.5(b). All randomly generated transfer functions, $W(s)$, and the nominal plant $G_n(s)$, all for one range of operating points, are shown in Fig. 5(c). The numerical design of the μ-controller can be achieved with the aid of the MATLAB Robust Control Toolbox [15]. The main design steps can be summarized as follows.

1) To cover the range of variation in the plant gain and time constant, the "ureal" command can be used. Referring to the first term of (6-5.d), the gain varies with the variation of ω_m, v, α, and β, whereas the time constant varies with variations of R_{load} as well as C_W. Thus, with the separation of different parts of the characteristic wind turbine curves, a range of variation of each specific part can be used to find the bounds of the gain and time constant variation for distinct parts.
2) The "ultidyn" function has been employed to generate $\Delta(s)$ shown in Fig. 5(a).
3) To mimic the random behavior of the nonlinear system associated with changes in C_p and loads, the "usample" command has been used to sample some, in this study 60, possible uncertain transfer functions of the overall uncertain dynamic system. Each sample represents a potential transfer function of the system.
4) The "ucover" function has been used to find a simple uncertain model of the multiplicative structure out of the all possible generated transfer functions. Then, the bandwidth of the total closed-loop system has been fixed using loop shaping. Since the bandwidth of the speed controller, as the actuator of the dc voltage controller, is tuned at 30 rad/s, the bandwidth of the dc-link voltage controller is tuned at 0.5 rad/s. Thus, the performance weighting function, W_{perf}, has been selected based on 0.5 rad/s bandwidth. Besides, another

performance filter, W_{noise}, which has a magnitude greater than one at frequencies greater than time times of the selected bandwidth, 0.5 rad/s, has been employed in order to limit the controller bandwidth and induce a roll-off beyond the 0.5 rad/s. The designed transfer functions are given in the following section.

6.3.4 Parallel Distributed Robust Control Design

Considering the possibility of the large variation of the dc gain of the first transfer function of (6-5.d) as well as its time-constant, robust performance cannot be guaranteed due to the inherent trade-off between robust stability and robust performance in robust controllers. To ensure robust control performance at a wide range of operating conditions and system parameters, this chapter presents a parallel distributed compensation approach. To achieve robust performance for the entire system, the concept of fuzzy modeling from granular information point of view of the total nonlinear dynamics of the wind turbine and dc-link dynamics [113]-[114] is proposed. From this perspective, all possible characteristic curves of P_{Wind} versus the PMSG speed are granulated using membership functions that are differentiable and smooth. In each local region of the total nonlinear dynamic system, the controller is synthesized using the singular values μ-synthesis approach to have robust performance against operating point variation as well as load variation and disturbances. In fact, each controller guarantees the overall system stability, but not the overall system performance; i.e., the robust performance of each controller is not acceptable for the entire system due to the inherent trade-off between robust stability and robust performance. Hence, by employing the concept of fuzzy information granulation of the dc-link voltage dynamics, it becomes also possible to weight the controllers efforts in order to improve the robust performance at specific range of operating points [81]. Fig. 6.6 shows employed three typical parts when the wind speed is 12m/s.

The design of the local controllers is discussed in this section. For each part, appropriate design criteria are illustrated for further elaborations. All system parameters are given in Section 6.5. For the controller design, and unlike small-signal-based controllers designed at a certain operating point, it is assumed that wind speed is not fixed, and it contains uncertainty that is ±4 m/s around the nominal wind speed 12 m/s. This is an acceptable range for typical wind turbine operation. The range can be extended based on the designer preferences and given wind speed/turbine characteristics. The transfer functions W_{perf} and W_{noise} are the same in all local

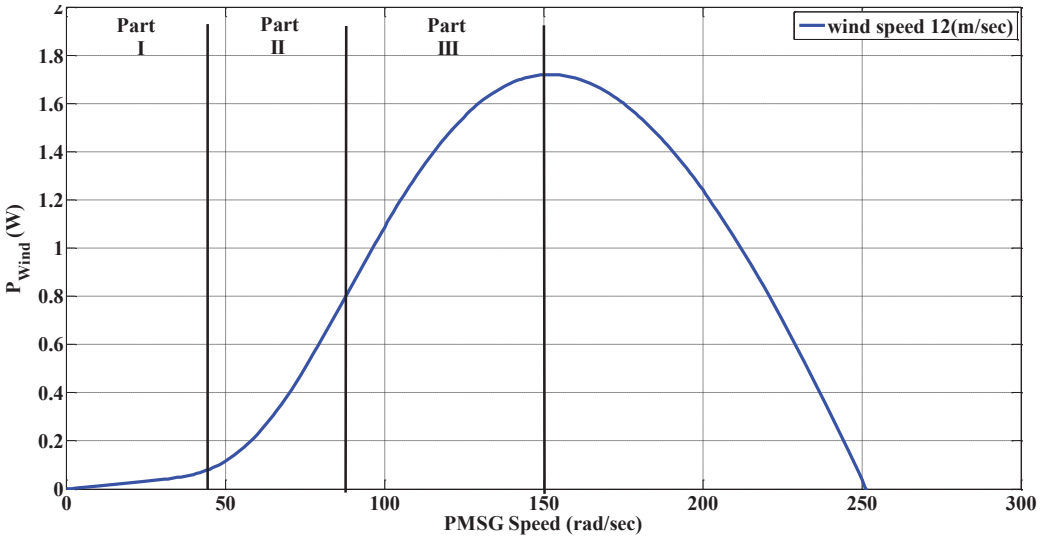

Fig. 6.6. Different typical parts of the characteristic curve of P_{Wind} versus PMSG rotational speed.

controllers. For parts 1 to 3 of the wind turbine power curves, the first term of (6-5.d) has significant frequency response variation as shown by the frequency response in Fig. 6.7. It should be noted that $G_n(s)$ employed in controller design, for each different part, is the combination of two transfer functions in series. They are the first term of (6-5.d), and the closed-loop transfer function of the speed controlled PMSG. The first transfer function is different for each part, whereas the second transfer function is the same for all parts and it is given by $TF_{CL\_speed\_controller}$ in (6-8.a). The central transfer function, $G_n(s)$ in Fig. 6.5, and its associated uncertainty shaping filter, $W(s)$, for each selected part, are given in (6-8.b).

$$TF_{CL\_speed\_controller} = \frac{9.8\times10^4}{0.784s^3+156.8s^2+11760s+9.8e4} \tag{6-8.a}$$

$$part1\begin{cases} G_n(s) = \dfrac{2.553\times10^5}{s^4+200.2s^3+1.503\times10^4 s^2+1.276\times10^5 s+2.172\times10^4} \\ W(s) = \dfrac{23.46s^2+893.9s+103.1}{s^2+227.5s+103.7} \end{cases}$$

$$part2\begin{cases} G_n(s) = \dfrac{3.519\times10^5}{s^4+200.2s^3+1.504\times10^4 s^2+1.278\times10^5 s+2.355\times10^4} \\ W(s) = \dfrac{32.15s^2+1374s+157.8}{s^2+210.5s+159.3} \end{cases} \tag{6-8.b}$$

$$part3\begin{cases} G_n(s) = \dfrac{5.303\times10^5}{s^4+200.6s^3+1.512\times10^4 s^2+1.343\times10^5 s+7.775\times10^4} \\ W(s) = \dfrac{19.6s^2+609.9s+271.9}{s^2+229.7s+296.4} \end{cases}$$

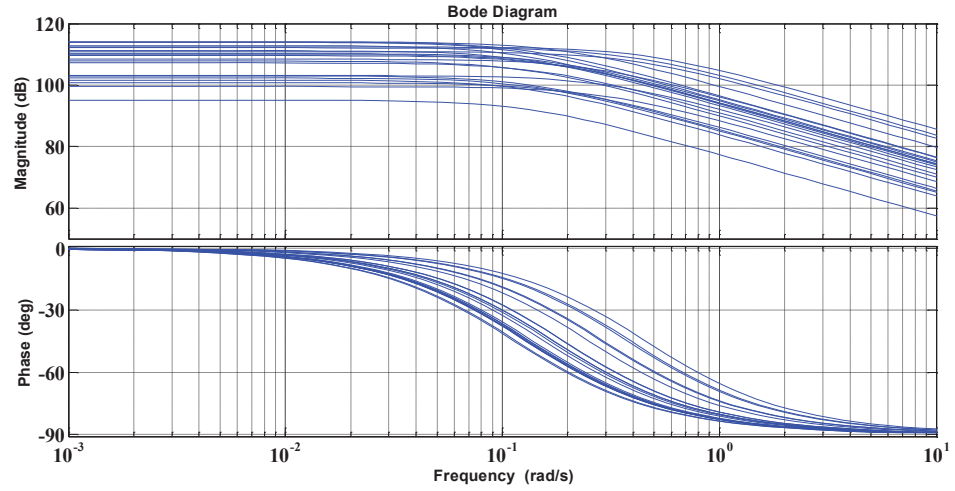

(a)

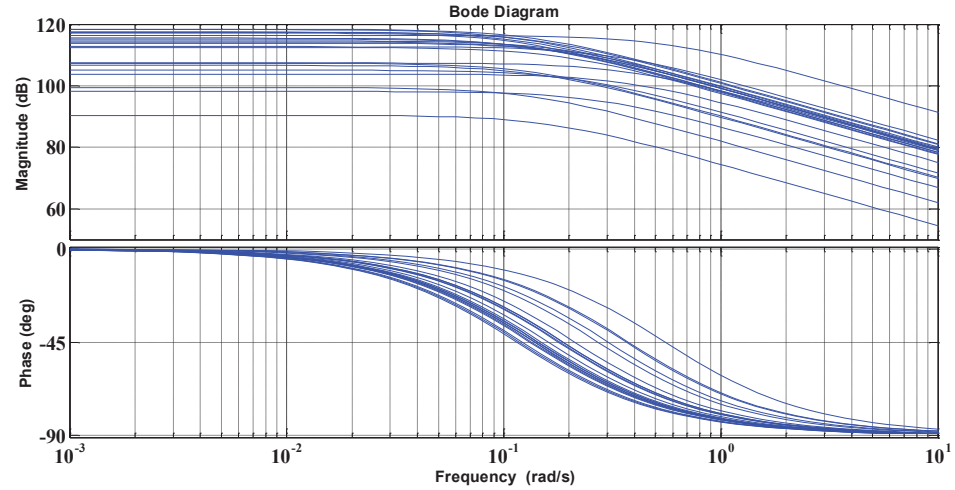

(b)

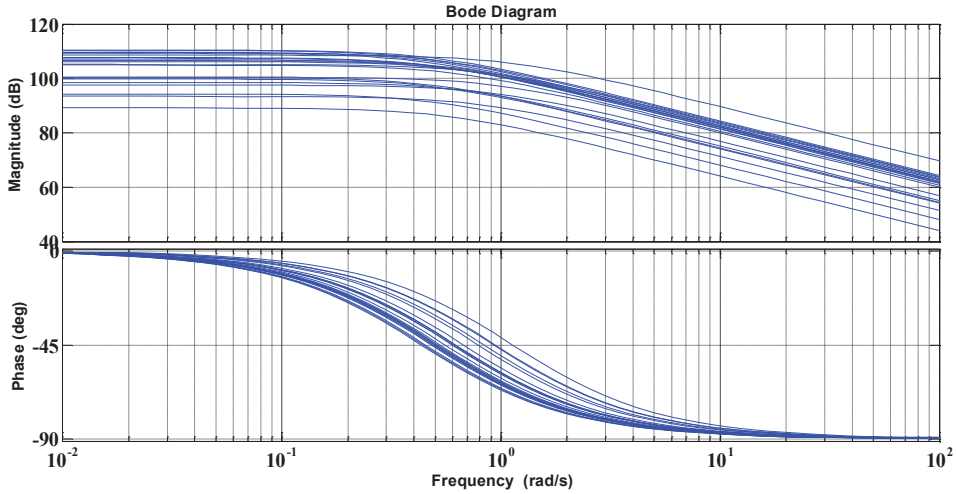

(c)

Fig. 6.7. Frequency response of different transfer functions of the first term of (6-5.d) at different uncertain P_{Wind} curves. (a) Part 1 (b) Part 2 (c) Part 3.

For different parts identified in (7-8), the synthesized controllers are given in (6-9). To improve the computational efficiency, the order of the synthesized controllers is reduced while preserving the same dynamic performance in the frequency range of interest.

$$\begin{aligned} part1:\ K(s) &= \frac{-0.04215s^4 + 1.252s^3 + 46.73s^2 + 16.9s + 0.002888}{s^4 + 6.87s^3 + 39.02s^2 + 0.01343s + 1.156\times10^{-6}} \\ part2:\ K(s) &= \frac{0.01695s^4 - 0.6711s^3 + 37.86s^2 + 23.61s + 1.336}{s^4 + 10.81s^3 + 57.68s^2 + 3.456s + 0.0005968} \\ part3:\ K(s) &= \frac{0.04643s^4 - 1.925s^3 + 41.16s^2 + 34.54s + 0.006908}{s^4 + 34.3s^3 + 121s^2 + 0.04484s + 4.03\times10^{-6}} \end{aligned} \tag{6-9}$$

The disturbance rejection transfer functions of each different part are calculated using the system block diagram Fig. 6.5, and they are shown in Fig. 6.8. Each graph shows the step response of the sensitivity function (i.e., due to external disturbances) of different parts at different operating points and parameters. The uncertain system, for each different part, is robustly stable to the modeled uncertainty as shown in Fig. 6.8. This fact is supported by the robust control indices, where the μ-index is bounded and less the unity for the designed controllers under the occurrence of disturbances, uncertainty and operating point variation.

A parallel distributed control structure can be realized using a fuzzy model of the total plant. The employed membership functions, to augment and activate the designed controllers in (6-9), are symmetric Gaussian membership function given by (6-10).

$$\begin{aligned} part1:\ & e^{\frac{-0.5(x-0)^2}{15000^2}} \\ part2:\ & e^{\frac{-0.5(x-35000)^2}{15000^2}} \\ part3:\ & e^{\frac{-0.5(x-70000)^2}{15000^2}} \end{aligned} \tag{6-10}$$

The input parameter to the proposed robust distributed controller is the output power that causes state traveling on the phase portrait of the dc-link voltage dynamics. To design the membership functions, the semantic soundness principle has been used to have a meaningful fuzzy model of the plant [13].

Fig. 6.9 shows a mathematical representation of the proposed controller with a fuzzy model of the complete plant model. Each individual controller guarantees the overall system stability at different operating points. However, the controller cannot guarantee robust performance at a wide range of operating points and parametric variation. Hence, if index i indicates the

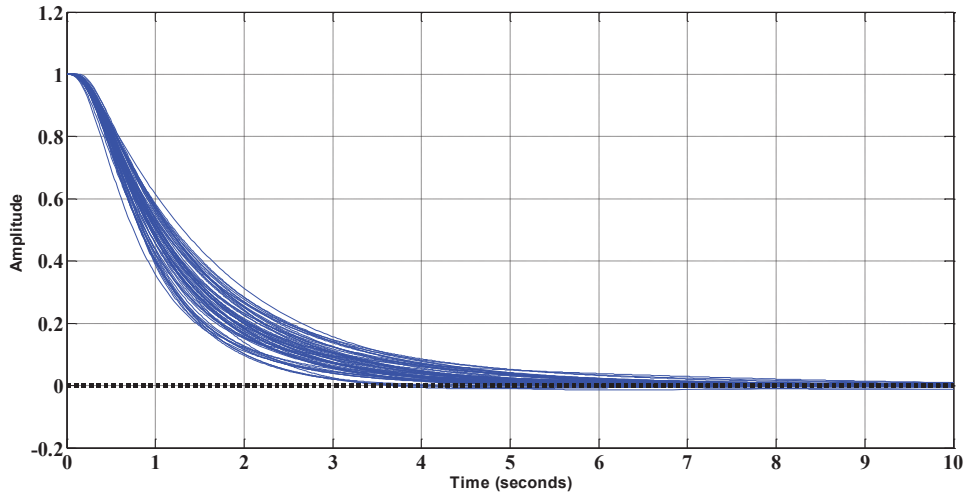

(a)

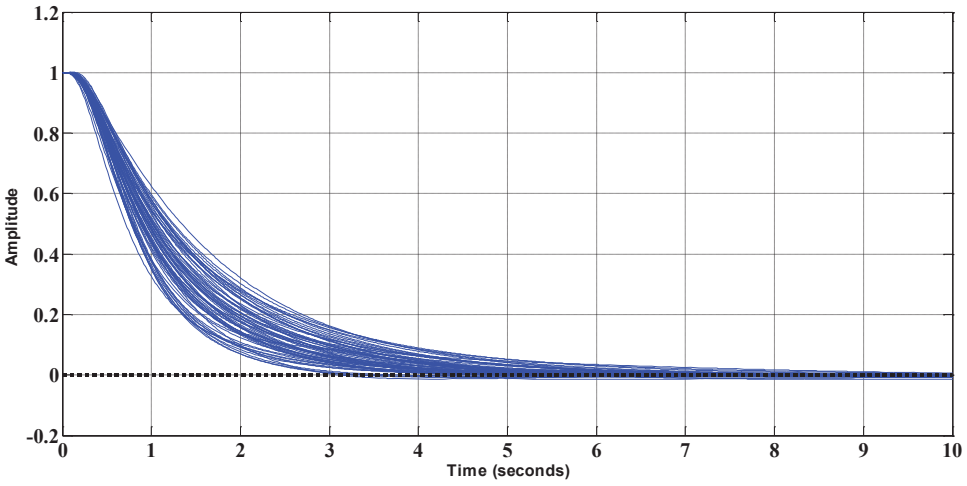

(b)

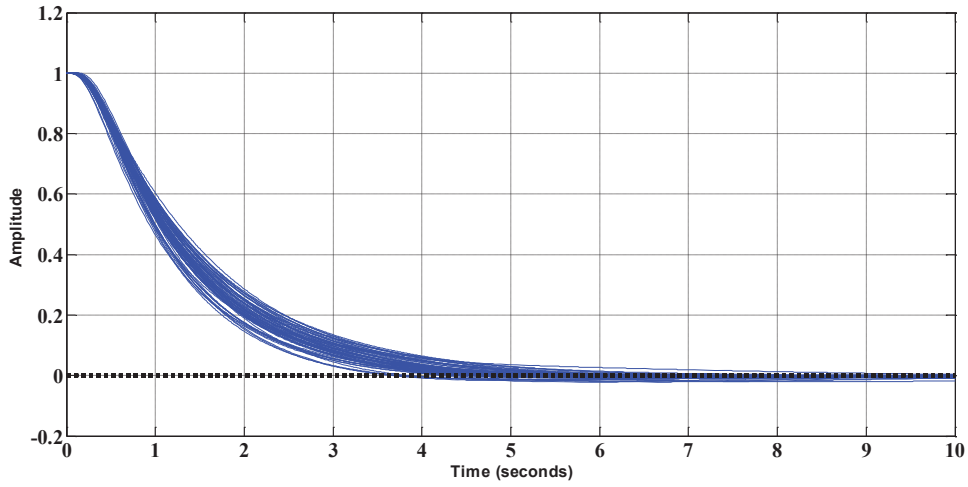

(c)

Fig. 6.8. Time response of the output disturbance rejection with the controller designed for (a) Part 1 (b) Part 2 (c) Part 3.

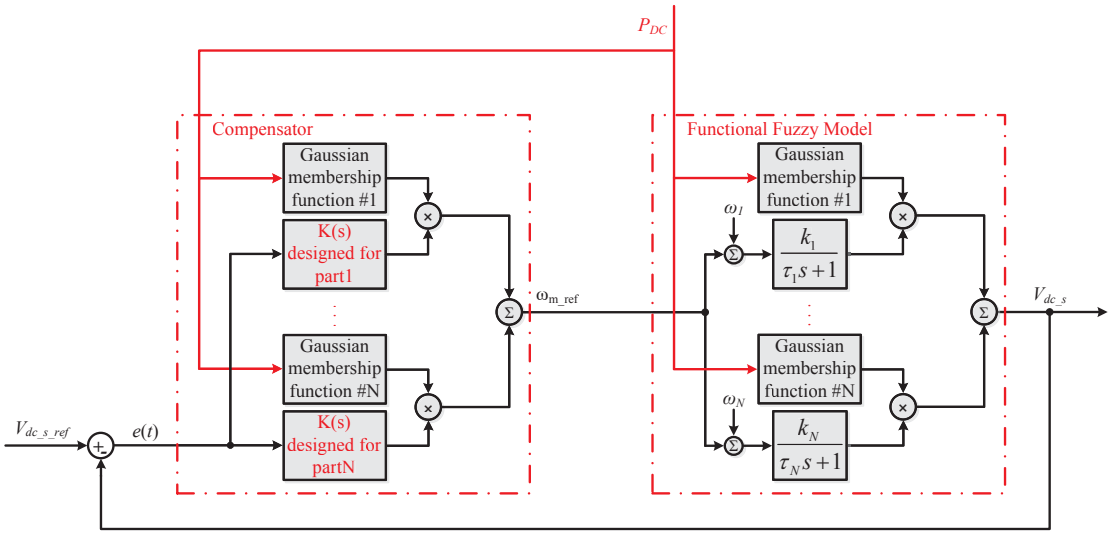

Fig. 6.9. Mathematical representation of the propose d controller considering functional fuzzy model.

parameters of the closed-loop system when the whole fuzzy functional model is controlled with a K_i controller, which is s ynthesized using the aforementioned steps to ensur e robust performance of part i, then (6-11.a) can be written

$$\frac{E_1(s)}{V_{dc\_s\_ref}} = \frac{1}{1+K_1\sum_{i=1}^{i=N} MF_i \frac{k_i}{\tau_i s+1}} \cdots\cdots \frac{E_N(s)}{V_{dc\_s\_ref}} = \frac{1}{1+K_N\sum_{i=1}^{i=N} MF_i \frac{k_i}{\tau_i s+1}} \qquad (6\text{-}11.a)$$

where E(s) is the feedback error, MF_i is the i^{th} membership function, $V_{dc\_s\_ref}$ is the reference dc-link voltage, and k_i and τ_i are the variable plant gain and time constant, respectively.

Because $V_{dc\_s\_ref}$ is typically a step function, $V_{dc\_s\_ref}(s)=1/s$; using final value theorem, (6-11.b) can be written

$$\begin{aligned} &stability\ and\ tracking\ of\ part1: \lim_{t\to\infty} e_1(t) = \lim_{s\to 0} sE_1(s) = 0 \\ &\vdots \\ &stability\ and\ tracking\ of\ partN: \lim_{t\to\infty} e_N(t) = \lim_{s\to 0} sE_N(s) = 0 \end{aligned} \qquad (6\text{-}11.b)$$

Thus

$$\lim_{s\to 0}(K_1\sum_{i=1}^{i=N} MF_i \frac{k_i}{\tau_i s+1}) = \infty \ldots \lim_{s\to 0}(K_N\sum_{i=1}^{i=N} MF_i \frac{k_i}{\tau_i s+1}) = \infty$$

and

$$\lim_{s\to 0}(\sum_{i=1}^{i=N} MF_i K_i \sum_{1\ i=1}^{i=N} MF_i \frac{k_i}{\tau_i s+1}) = \infty \Rightarrow \lim_{s\to 0} sE(s) = \lim_{t\to\infty} e(t) = 0 .$$

Consequently, the closed-loop system with parallel distributed controllers is stable.

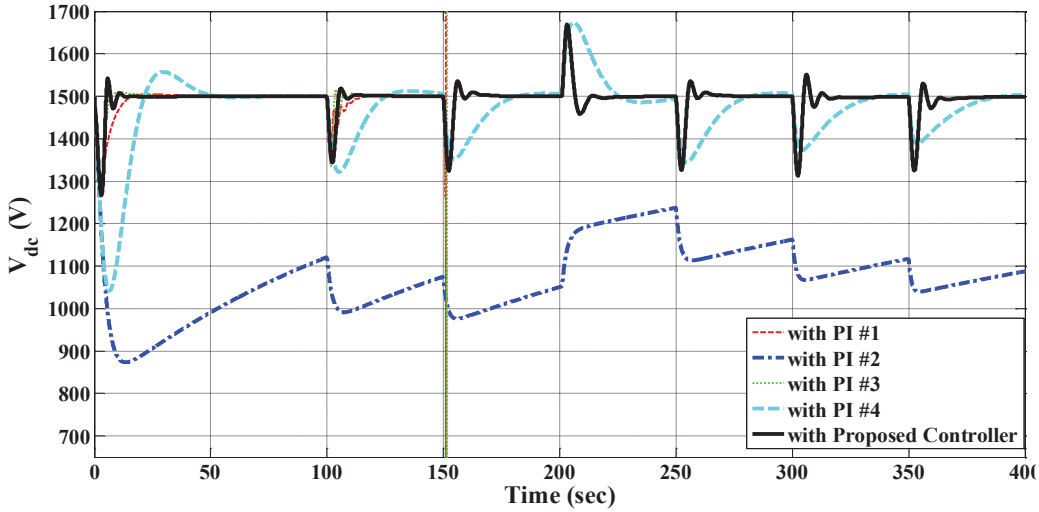

Fig. 6.10. Event I: Performance of the dc-link voltage under connecting/disconnecting of static loads; wind speed is constant at 13.5 m/s.

6.4 Simulation Results

The system under study, shown in Fig. 6.1, is simulated in the MATLAB/Simulink environment. Complete system parameters are shown in Section 6.5. For the sake of performance comparison, the proposed controller is compared to the following controller. A PI controller that is designed based on the method and structure reported in [10], i.e., using (6-5.e). Two PI controllers are designed. One at slow speed to mimic the start-up performance of the system, and one at the critical transfer function, i.e., equation (6-5.e) at the operating point that yields the lowest phase margin. For the start-up transfer function, (6-5.e) is generated with the slope of the $P_{Wind-PMSG\_speed}$ curve equals to 1300, and PMSG speed equals to 1 rad/s. In this case, the PI controller #1, $\frac{0.038736s+0.0081272}{s}$, is designed to yield 4.1 s response time, 2.41 s rise time, and 60 ° phase margin at 0.488 rad/s. The same procedure is applied to design a PI controller for the critical transfer function of (6-5.e), which is generated when the slope of $P_{Wind-PMSG\_speed}$ curve is 24000 Nm and the PMSG speed is 87.84 rad/s. Thus, the PI controller #2, $\frac{0.0040s+6.78\times10^{-5}}{s}$, is redesigned to have 2.06 s response time, 0.719 s rise time, and 53.2° phase margin at 0.97 rad/s. In this case, the settling time of the output disturbance rejection time response is 2.81s; which is a reasonable value for the critical plant from the phase margin stability perspective.

A PI controller that is designed based on the accurate small-signal model developed in (6-

5.d). Two PI controllers are designed at two operating points. For the first transfer function of (6-5.d) with the lowest gain, 71530, the PI controller #3, $\frac{1.3138\times10^{-5}s+5.2476\times10^{-6}}{s}$, has been designed to have a 4s response time, 2.61s rise time, and 60° phase margin at 0.5 rad/s. The second PI controller is designed for the first transfer function of (6-5.d) with the largest gain, 285800. In the case, the PI controller #4, $\frac{1.3857\times10^{-6}s+7.7503\times10^{-7}}{s}$, has been designed to have 2 s response time, 1.23 s rise time, and 60° phase margin at 0.99 (rad/s). All controllers are compared to the proposed controller under the same simulation scenarios.

Event I: In this scenario, the wind speed is fixed at 13.5 m/s, and static loads are connected to the dc link, sequentially with a step of 10 kW at t=1.0 s, 100 s, 150 s, 250 s, 300 s, and 350 s, then one static load is disconnected from the dc-link at t=200 s to check the control performance with load connection/disconnection. The dc-link voltage is shown in Fig. 6.10. As Fig. 6.10 shows, controllers #1 and #3 fail to maintain the stability of the dc grid (the dc-link response becomes unstable at t=150 s with the additional load increase, which causes drift in the operating point). However, controllers #2, #4, and the proposed controller successfully stabilize the dc-link voltage. The stable performance associated with controllers #1 and #3 is related to the conservative design approached adopted, as both controllers are designed based on the worst case scenario. However, their performance is not robust against disturbances and parametric uncertainties. The proposed controller benefits from both robust stability and robust performance criteria. Considering the results above, only controller #2 and controller #4 are considered in the following simulation events for performance comparison with the proposed controller.

Event II: In this event, a variation of the wind speed is studied, and its effect on the performance of dc-link voltage controller is investigated. For this purpose, the total load connected to the dc grid is kept constant at 30 kW to solely study the effect of wind speed variation. The wind speed has been changed as step functions generated by a random signal generator as shown in Fig. 6.11(a). It should be noted that harsh variation in the wind speed causes large variation in the operating point of the plant dynamics. The performance of controller #2, controller #4, and the proposed controller is shown in Fig. 6.11(b). Controller #2 shows sluggish performance due to the fact that this controller is designed based on the inaccurate plant model given by (6-5.d). Controller #4 shows better performance as it is designed based on the worst-case scenario of the accurate model developed in this chapter and given by (6-5.e).

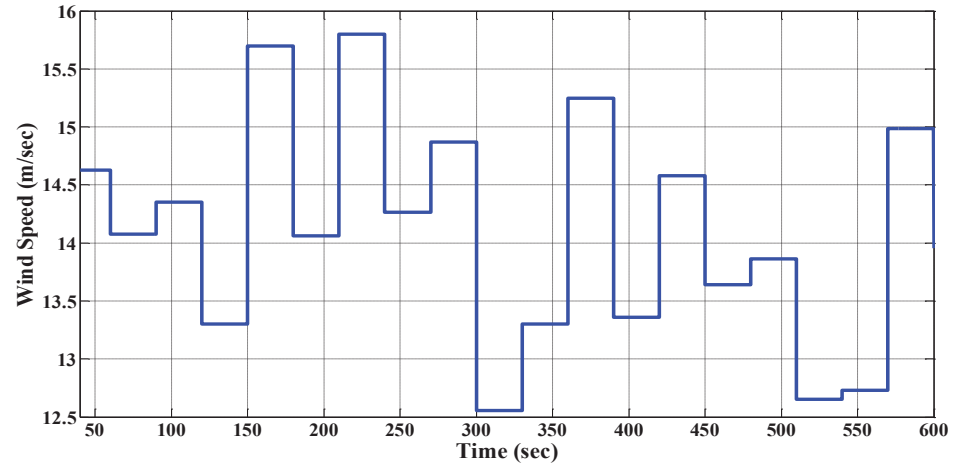

(a)

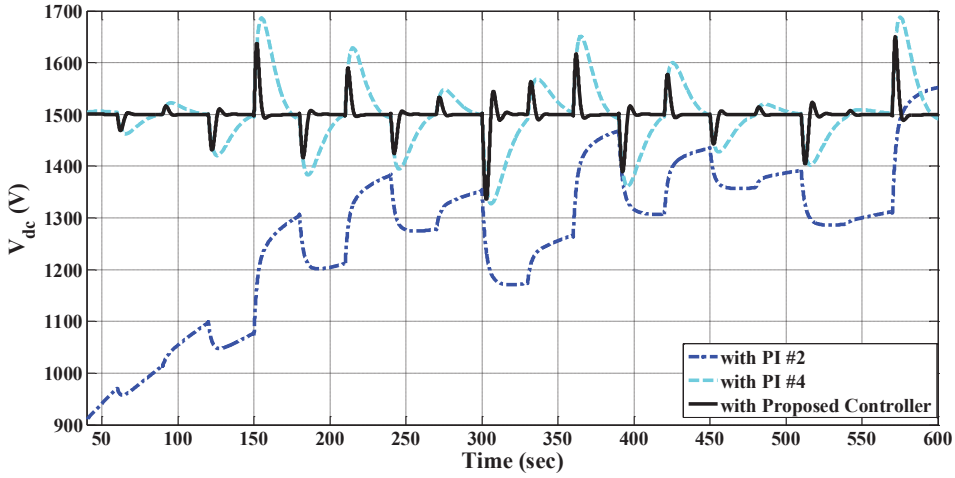

(b)

Fig. 6.11. Event II: Performance of the dc-link voltage under variable wind speed. (a) Wind speed. (b) DC-link voltage.

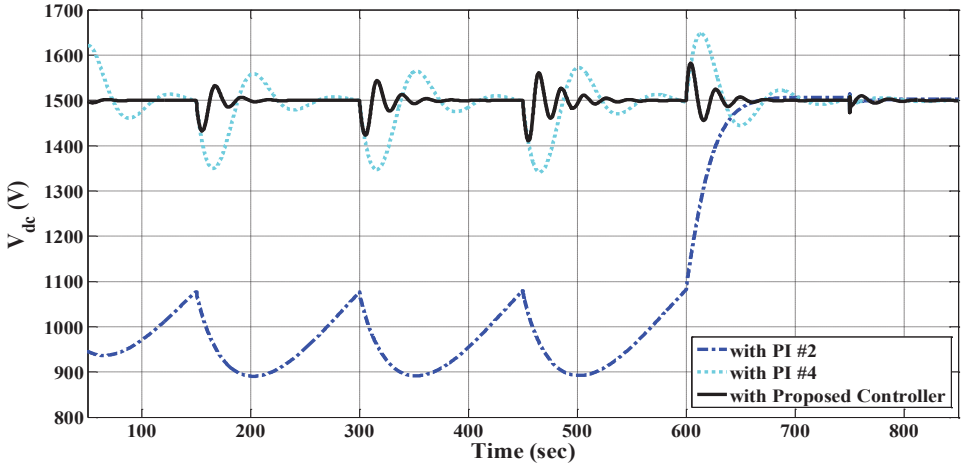

Fig. 6.12. Event III: Performance of the dc-link voltage under dynamic load changes, active and reactive power; wind speed is constant at 13.5 m/s.

However, the robust performance in terms of voltage dips and recovery times is not maintained with controller #4, where the over/undershoot in the dc-link voltage is around 15% with recovery times around 30 s. The proposed controller offers significant performance improvement where the over/undershoots in the dc-link voltage are reduced with recovery time less than 10 s.

Event III: In this event, a converter-based load (dynamic load) is considered to examine the impact of converter-based loads on the dc-link voltage stability. Zone II in the system under study is composed of a grid-connected VSC with inner current control loops and outer active/reactive power controller. Therefore, the tight regulation effect of a typical power converter can be examined. Zone II is commanded to absorb power from the dc grid and to inject it into the ac side of grid 2. At instants 150 s, 300 s, and 450 s, the dynamic load is increased by steps of 15 kW, whereas at instant 600 s, the dynamic load is reduced by 10 kW. Besides, at t=750 s, 100 kVAr reactive power is injected into the ac grid 2 in Zone II. The simulation results are reported in Fig. 6.12. Comparing Fig. 6.11 to Fig. 6.12, it is obvious that the dc-link voltage shows different dynamic performance when a converter-load is connected to the dc grid as compared to static loads. From the control performance point of view, the proposed controller maintains the dc-link voltage stability and robust performance with excellent disturbance rejection and fast recovery time as compared to controllers #2 and #4.

Event IV: In this event, the effect of a harsh asymmetric ac-side fault in the ac grid of Zone II (grid 2), on the performance of the controllers is investigated. The fault conditions yield a large-signal disturbance, which is a good scenario to test the robustness of the proposed controller against operating point variation and un-modeled dynamics. Initially, the dc grid is loaded with a 50 kW dynamic load at t=2 s, then, grid 2 is experiencing a bolted unbalanced double-line-to-ground fault at t=150 s. The voltage dip associated with the fault in grid 2 is shown in Fig. 13(a). The dc-link voltage dynamic response with controllers #2, 4 and proposed controller is shown in Fig. 6.13(b). The proposed controller swiftly mitigates the oscillatory response reflected to the dc-link voltage due to fault condition. Furthermore, the voltage recovery time is much faster than controller #4. It can be noted that controller #2 yields steady-state error due to the inaccurate plant dynamics used in the design process.

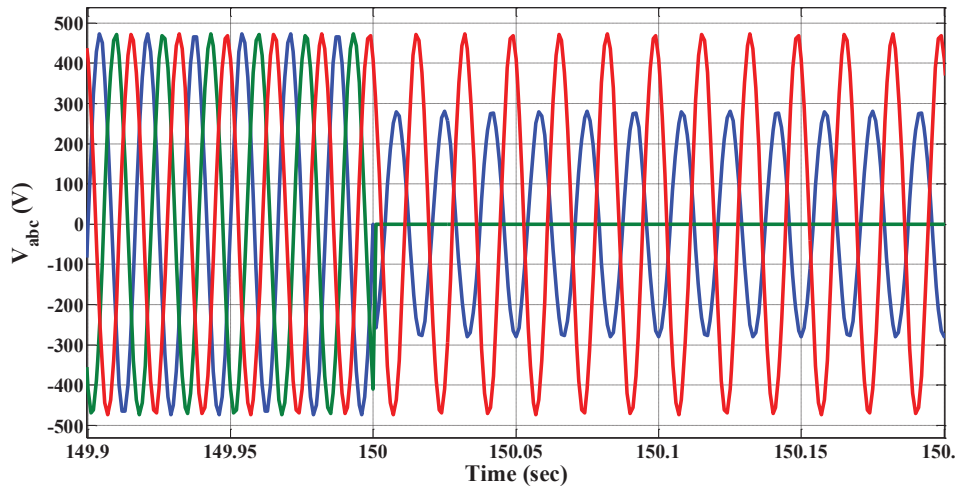

(a)

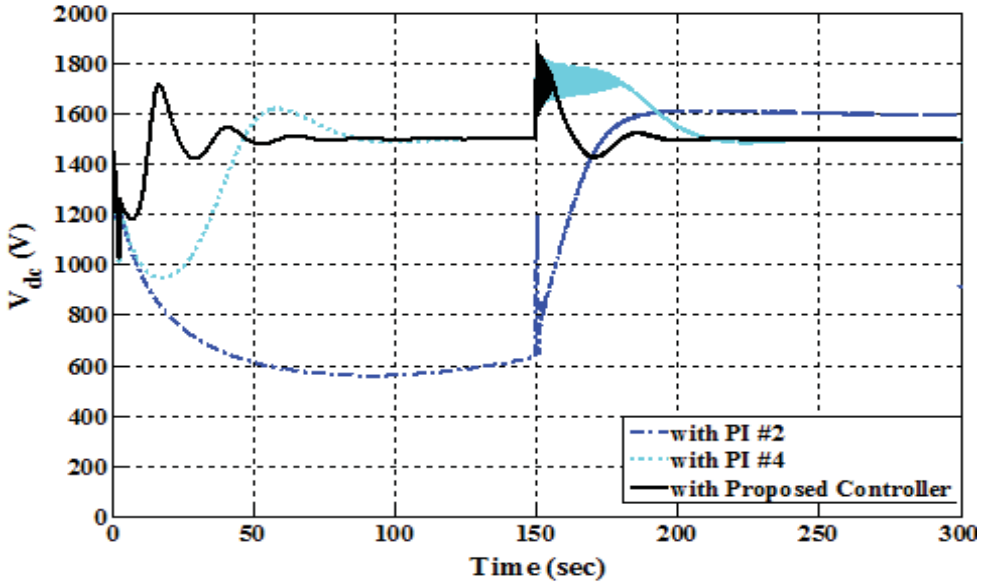

(b)

Fig. 6.13. Event IV: Performance of the dc-link voltage under asymmetric fault in the ac side grid 2. (a) Three-phase voltage of grid 2, (b) DC-link voltage.

6.5 Parameters of Simulated System, Fig. 6.1

Zone I: 2.5 MW wind turbine, PMSG number of pole pairs=4; L_d=0.514 mH; L_q=0.186 mH; R_{stator}=0.514 mΩ; Speed Controller: K_p =11760; K_i=98000. Wind Turbine and Wind Characteristics: Gear Box Ratio=1:50; J (wind turbine system inertia referred to the PMSG side)=156.8 kgm^2; v (rated wind speed;)=12 m/s; ρ (air density)=1.25 kg/m^3. VSC-W: C_W=75 mF, Switch resistance=1.0 mΩ; Diode Resistance=1.0 mΩ; Current Controller: K_p=0.4 Ω ; K_i=0.7 Ω/s.

Zone II: VSC-PQ: Rated Power=1.0 MVA, Grid 2 voltage=580 V at 60 Hz; R=3.5 mΩ; L=300 μH; C=37.5 mF, Switch Resistance=1.0 mΩ; Diode Resistance=1.0 mΩ; Current Controller K_p=0.06 Ω ; K_i=0.7 Ω/s.;
DC grid: Rated voltage=1,500 V, dc-cable length=20 km, R_{cable}=0.82 mΩ/km, C_{cable}= 0.014 μF/km, L_{cable}=0.98 μH/km.

6.6 Conclusion

A robust parallel distributed controller has been proposed for a dc-link-voltage controlled full-scale wind turbine in a dc grid. The controller offers the following characteristics. 1) Robust performance against large variation in the operating point associated with variation of the wind turbine characteristic curve which is affected by pitch angle, wind speed, and control lever itself (i.e., the rotational speed of the PMSG. 2) Robust performance against static as well as dynamic load variation (e.g., power converters or dc machines connected to the dc-link. 3) The effective rejection of disturbances associated with dynamic load variations as well as wind speed changes to enhance the performance of the closed-loop system. Furthermore, because the control lever is not affected by power changes in the ac sides of other VSCs connected to the dc grid, the dc voltage dynamics is not affected by the unsymmetrical condition (e.g., faults or unbalance) in the ac grids of other VSCs connected to the dc grid. Therefore, the controller enhances the reliability and performance of dc grids and provides excellent fault-ride-through performance.

Chapter 7

Robust DC-Link Voltage Regulation of Grid-Connected VSCs in DC Grids with Power Sharing Control

7.1 Introduction

Motivated by the difficulties mentioned in Section 1.3.6, this chapter presents a robust dc-bus voltage controller for VSCs in MTDC grids governed by droop dc-voltage control. Firstly, this chapter presents a detailed model of the dc-link voltage dynamics considering the impacts of the droop controller, instantaneous power of the ac inductor filter and dc side uncertainties. Secondly, a robust dc-link voltage controller is developed to ensure robust control performance under operating point variation, variable droop gain operation and dc side uncertainty and disturbances. A baseline robust dc-link controller is designed to minimize the H_∞ norm of the closed-loop system from the disturbance to the tracking error using the μ-synthesis approach considering uncertainties originated from operating point variations as well as external disturbances (i.e., power variation imposed by other converters in the dc grid). Then, the augmented dynamics that is composed of the dc-link voltage dynamics, baseline controller and droop feedback dynamics, is used to retune the controller parameters, via the polynomial method, to fix the poles of the characteristic equation of the augmented dynamics in a predetermined region under possible variation in the droop gain, equivalent dc-link capacitance and static loads in the dc grid. By this way, the controller ensures robust performance under a wide range of variation in the converter operating point and parametric uncertainties as well as the occurrence of disturbances. A theoretical analysis and simulation results are provided to show the validity and effectiveness of the proposed controller.

7.2 Dynamics of A Grid-Connected VSC Equipped with DC-Droop Control

7.2.1 System Structure

The conceptual design of a multiterminal dc grid is shown in Fig. 1(a). Several ac and dc systems can be connected to a common dc grid. Bidirectional VSCs are used to interface ac systems to the dc grid. The multiterminal dc grid architecture facilities effective and efficient integration of renewable energy resources and energy storage units with reduced number of power conversion stages. For autonomous dc-link voltage regulation, VSCs can be equipped with a dc droop function to share the power among different ac grids according to an economic power sharing criterion where the droop control function generates the dc-link voltage reference trajectory. In this way, dc-link voltage hunting is avoided. Other converters can be controlled in the active-reactive power control mode to inject or absorb power without contributing to the dc-link voltage regulation task (e.g., a wind or photovoltaic farm). Such converters impose a power disturbance (active load disturbance) on the dc-link voltage controlled VSCs. Furthermore, passive loads (mainly resistive) can be directly connected to the dc grid forming a passive load disturbance on the dc-link voltage controlled VSCs. Therefore, robust control of dc-droop-controlled grid-connected VSCs demands a special attention.

A typical 2.5 MW, 580 V_{ac}, 1500 V_{dc}, 60 Hz grid-connected VSC with a dc droop function for dc grid applications is shown in Fig. 7.1(b). The system parameters are given in Section 7.6. An L-based ac filter with equivalent inductance L (representing the summation of filter and transformer leakage) and equivalent resistance R, which is commonly used in high-power converters, is adopted. Furthermore, if high-order ac-side filters are adopted—e.g., LC or LCL filter—it has been found that their impact on the dc-link voltage dynamics is negligible owing to the frequency-scale separation between the LCL filter dynamics and dc-link voltage dynamics. In other words, the bandwidth of the dc-link voltage control loop is usually less than the fundamental frequency (in the range of 20 Hz to 50 Hz); in this range, the ac-side filter behaves mainly as an L filter [92]. Therefore, the use of an L filter in this analysis is not a restricting assumption. The internal losses of the VSC are modeled by equivalent resistance r_{on} on the ac side and a current source on the dc side to model the power loss P_{loss} due to the reverse recovery

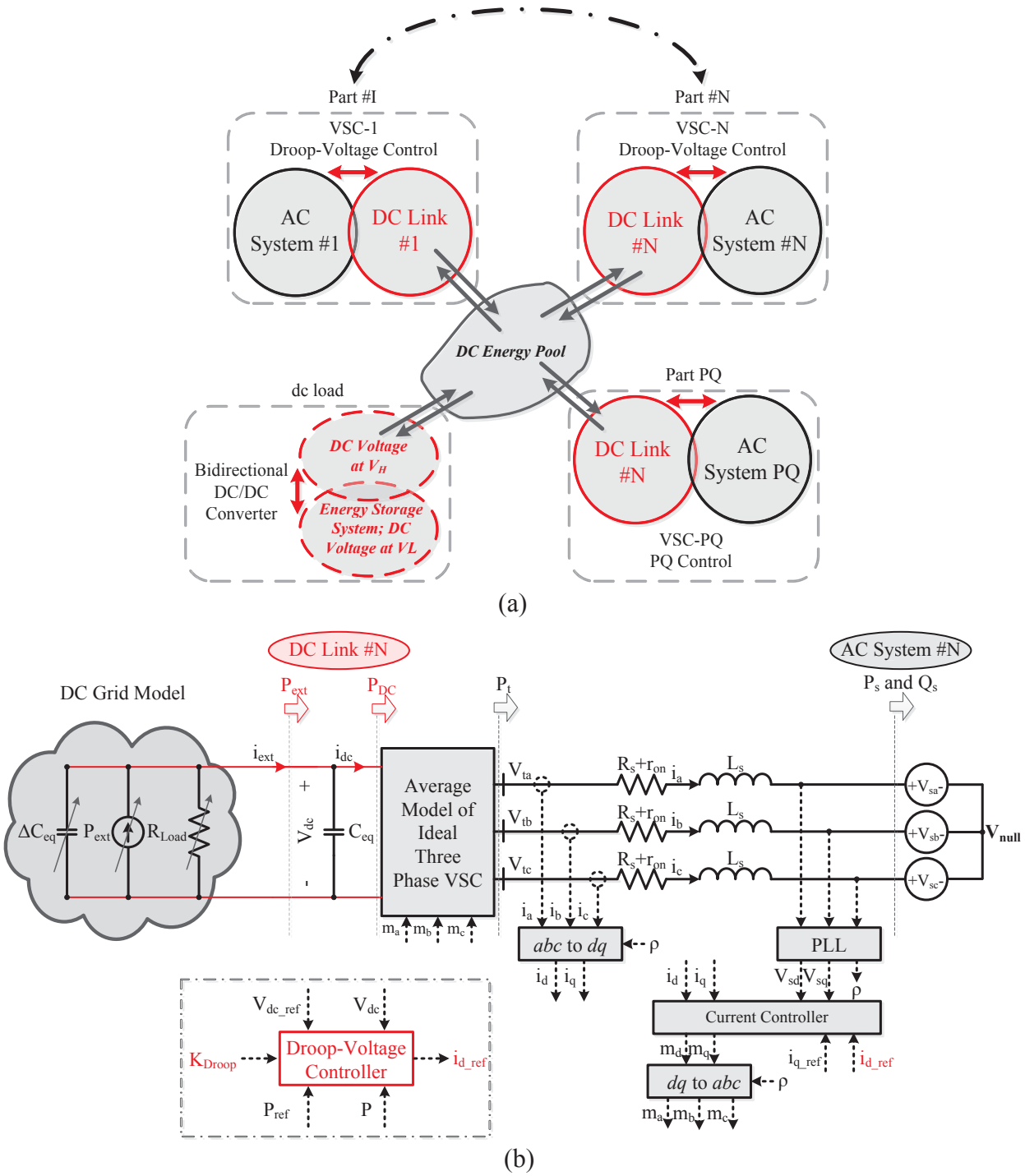

Fig. 7.1. (a) General configuration of a multiterminal dc system. (b) DC-droop-controlled grid-connected VSC.

and tailing current processes of the power switches. As shown in Fig. 7.1(a), the dc grid is modeled by 1) a variable current source representing external power P_{ext} that can be delivered or absorbed from the dc grid by dc generators and/or converter-based loads with regulated output

power (i.e., active load disturbance), and 2) an equivalent resistance R_{Load} representing equivalent passive loads in the dc grid.

It should be noted that it is extremely difficult and impractical to design the converter control system based on the overall exact system dynamics, which contain both the dc and ac grid dynamics. Therefore, the equivalent models of both grids (i.e., a Thevenin's equivalent circuit model of the ac grids and Norton's equivalent circuit of the dc grid) are usually assumed during the analysis and control design stages [30]. A standard grid-oriented vector control scheme is adopted in this study owing to its widespread acceptance in the power converter industry. In this scheme, two proportional-integral (PI) current controllers (inner controllers) and an outer dc-link voltage controller are adopted. The dc-link voltage controller generates the *d*-axis reference current component whereas the *q*-axis reference current component is set to zero to yield a unity power factor operation. A standard *dq*-based three-phase phase-locked loop (PLL) is adopted to extract the synchronization angle (ρ). The equivalent capacitance of the VSC, C_{eq}, can be subjected to uncertainty in its nominal value, which is a practical assumption owing to the uncertainty associated with the operation of the dc grid and the connection and disconnection of power converters on the dc grid; where the dc side equivalent model of a power converter can be modeled as a current source and a capacitor [115].

7.2.2 Modeling

To model the dc-link voltage dynamics, the power balance across the dc-link capacitor can be given by

$$\frac{d}{dt}(0.5C_{eq}V_{DC}^2) = P_{ext\_T} - P_{DC} - P_{loss} \tag{7-1}$$

where V_{DC} is the dc-link voltage; P_{ext_T} is the total external power at the dc grid; and P_{DC} is the power at the dc side of the VSC. The instantaneous power at the ac side of the VSC $P_t = P_{DC}$.

On the ac side, in the *dq* reference frame, the instantaneous power at the converter terminal can be given by

$$P_t = 1.5(V_{td}I_d + V_{tq}I_q) \tag{7-2}$$

where (V_{td}, V_{tq}) and (I_d, I_q) are the *d*- and *q*-axis components of the converter terminal voltage and current, respectively.

In medium- and high-power converters, the switching frequency is limited to reduce the switching losses. Therefore, the ac inductor filter is relatively large to ensure high power quality grid connection. In this case, the instantaneous power of the inductor filter cannot be ignored as it yields non-minimum phase behaviour in dc-link controlled VSCs [30]. Furthermore, the instantaneous power of the inductor filter yields operating-point-dependent small-signal dc-link voltage dynamics, which necessities robust control performance against fast variation in the operating point to ensure converter stability.

When the instantaneous power of the inductor filter is considered, the following equation can be written:

$$1.5(V_{td}I_d + V_{tq}I_q) = \frac{d}{dt}W_L + 1.5R|I|^2 + 1.5V_{sd}I_d \tag{7-3}$$

where $|I|$ is the amplitude of the line current going through R and L; W_L is the energy stored in the three-phase inductor filter; and V_{sd} is the d-component of the grid voltage at the point of common coupling (PCC). It should be noted that under the voltage-oriented vector control operation of VSC, the q-component of the grid voltage is zero at steady-state condition; therefore, the grid side power is given by the last term in (7-3). Furthermore, $|I|$ and W_L can be given by

$$|I| = \sqrt{I_d^2 + I_q^2} \tag{7-4}$$

$$W_L = 0.75L(I_d^2 + I_q^2) \tag{7-5}$$

Consequently, the differential equation relating the dc-link voltage to the ac current components can be given by

$$\frac{d(0.5C_{eq}V_{DC}^2)}{dt} = P_{ext} - \frac{V_{DC}^2}{R_{Load}} - \frac{3L}{4}\left(\frac{dI_d^2}{dt} + \frac{dI_q^2}{dt}\right) - \frac{3R}{2}(I_d^2 + I_q^2) - \frac{3}{2}V_{sd}I_d \tag{7-6}$$

Equation (7-6) can be linearized around an operating point, (I_{d0}, I_{q0}), as shown in (7-7) where V^2_{dc} is considered as the output. For simplicity, V_{dc_s}=V^2_{DC} will be used hereinafter

$$\begin{aligned}\tilde{V}_{dc\_s}(s) = & \underbrace{-\frac{1.5R_{Load}LI_{d0}s + 1.5R_{Load}(V_{sd0} + 2RI_{d0})}{0.5R_{Load}C_{eq}s + 1}\tilde{I}_d(s)}_{G(s)} \\ & \underbrace{+\frac{R_{Load}}{0.5R_{Load}C_{eq}s + 1}\tilde{P}_{ext}(s) - \frac{1.5R_{Load}I_{d0}}{0.5R_{Load}C_{eq}s + 1}V_{sd0} - 3RR_{Load}I_{q0}\frac{0.5Ls/R + 1}{0.5R_{Load}C_{eq}s + 1}\tilde{I}_q(s)}_{D(s)}\end{aligned} \tag{7-7}$$

where "~" denotes a small-signal variable and subscript "0" denotes an operating point.

The first term in (7-7), $G(s)$, is the plant transfer function that relates the dc-link voltage small-signal dynamics to the *d*-axis current component; the latter is the control lever in a current-controlled VSC.

To facilitate the power sharing function using local measurements, a dc droop function should be implemented in the VSC. In medium- and high-power applications, power versus dc-link voltage droop is usually adopted as follows [58], [61]:

$$\begin{aligned} V_{DC}^{2\,*} &= V_{DC\_ref}^2 + K_{droop}(P_{ref} - G_f(s)P_{DC}) \\ &= V_{DC\_ref}^2 + K_{droop}(P_{ref} - G_f(s)\frac{V_{DC}^2}{R_{Load}} - G_f(s)P_{ext}) \end{aligned} \tag{7-8}$$

where $V_{DC\_ref}^2$ is the square of the global reference dc-link voltage which acts as a global virtual communication link among droop-controlled VSCs in the dc grid; K_{droop} is the droop gain; P_{ref} is the reference power of the droop curve; $V_{DC}^{2\,*}$ is the local reference dc-link voltage of the VSC; and G_f(s) is a first-order low-pass filter used to smooth out the power signal fed to the droop controller and to induce time-scale separation between the droop controller (the most outer loop) and the next loop (dc-link voltage controller) in the cascaded control system. The square of the dc-link voltage is used in the droop equation because using the square of the dc-link voltage in the feedback control loop reduces the nonlinearity of the plant as shown in (7-1).

As shown in (7-8), the droop mechanism acts as a feedback control system to steer the reference dc-link voltage according to changes in the dc-link power. The droop gain K_{droop} is usually chosen according to the rating of the VSC and permissible dc-link voltage deviation. However, the predefined values of the droop gain can be changed in real-time operation due to uncertainty in the actual loading conditions, variable economic condition, and contingency situations [58], [61]-[62]. Furthermore, converter outage in the dc grid demands an adaptation in the droop gain. The values of the droop gains affect the converter and dc grid stability and determine the power sharing characteristics among the converters. Higher droop gains yield more power contributions, whereas smaller gains yield lesser deviation in dc-link voltages.

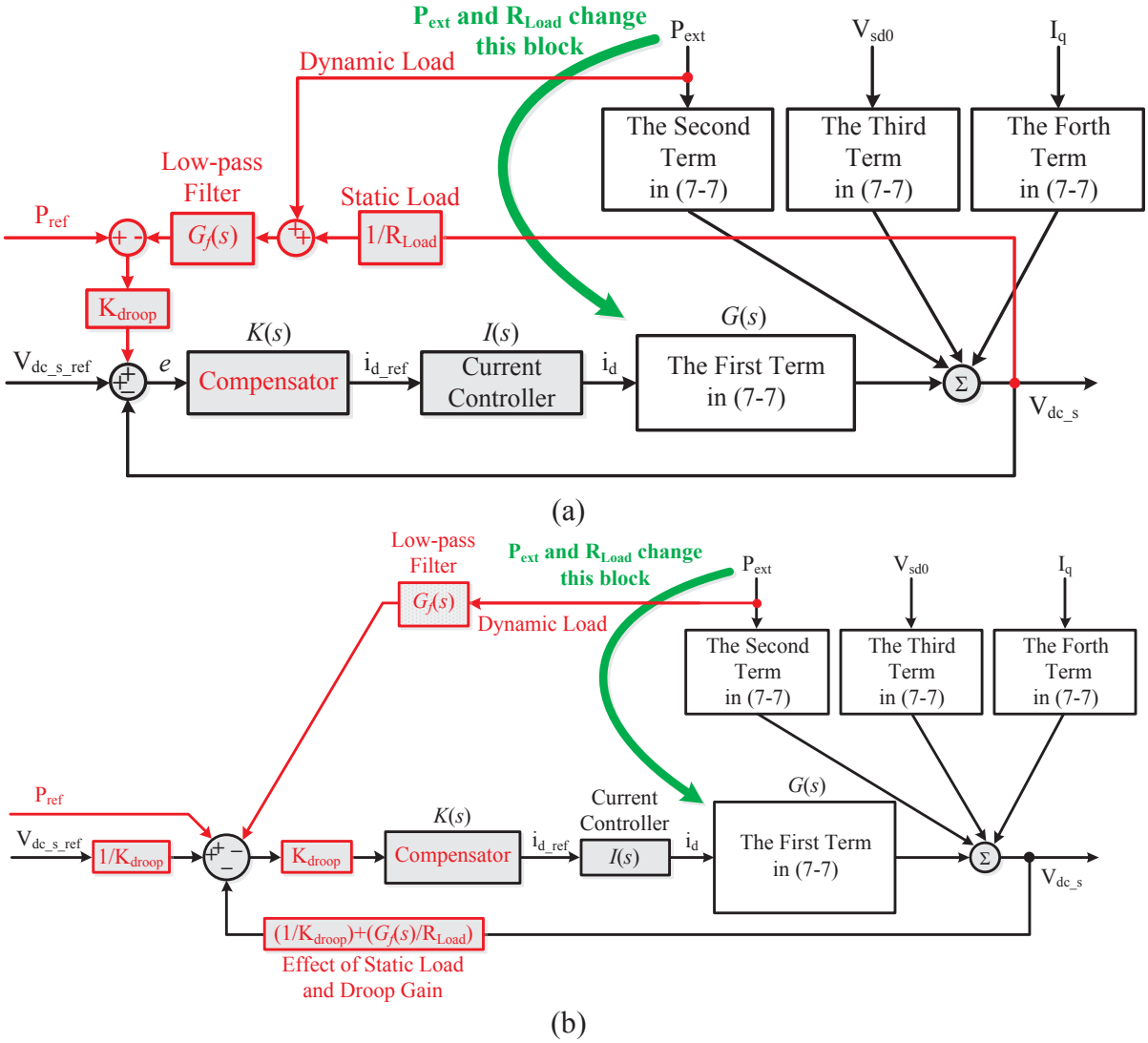

Fig. 7.2. (a) Small-signal dc-link voltage dynamics of a grid-connected VSC with dc droop feedback. (b) Equivalent model.

With the droop feedback mechanism, the dynamics in (7-7) can be combined with the droop function in (7-8). The block diagram of the combined system small-signal dynamics is shown in Fig. 7.2(a), where $K(s)$ is the dc-link voltage compensator; and $V_{DC\_s\_ref} = V^2_{DC\_ref}$. The current control dynamics is significantly faster than the dc-link voltage dynamics; therefore, the current control loop dynamics can be represented by a first order low-pass filter with a time constant τ_i. Accordingly, in Fig. 7.2 (a), $I(s) = 1/(\tau_i s + 1)$. The augmented dynamics in Fig. 2(a) can be given by

$$\begin{aligned}\tilde{V}_{DC\_s}(s) = & \underbrace{\frac{R_{Load}K(s)I(s)G(s)}{R_{Load}+\left(K_{droop}G_f(s)+R_{Load}\right)K(s)I(s)G(s)}}_{G_T(s)} V_{DC\_s\_ref}(s) \\ & + \frac{K_{droop}R_{Load}K(s)I(s)G(s)}{R_{Load}+\left(K_{droop}G_f(s)+R_{Load}\right)K(s)I(s)G(s)} P_{ref}(s) \\ & - \frac{K_{droop}R_{Load}K(s)I(s)G(s)G_f(s)}{R_{Load}+\left(K_{droop}G_f(s)+R_{Load}\right)K(s)I(s)G(s)} \tilde{P}_{ext}(s) \\ & + \frac{R_{Load}}{R_{Load}+\left(K_{droop}G_f(s)+R_{Load}\right)K(s)I(s)G(s)} D(s)\end{aligned} \tag{7-9}$$

The dc-link voltage dynamics with droop feedback given by (7-9) can be represented by the equivalent block diagram in Fig. 7.2(b).

By examining (7-7) and (7-9), the following observations can be made:

1) The open-loop dynamics, represented by the first term in (7-7), has an operating-point-dependent zero. This yields a non-minimum phase dynamics in the rectification mode (i.e., when I_{d0} is negative), which affects the converter performance and stability.
2) A variation in the passive load resistance and equivalent dc-link capacitance remarkably affect the time-constant of the open-loop dynamics.
3) The second, third and fourth terms in (7-7), lumped as $D(s)$, act as dynamic disturbances on the output dc-link voltage and should be effectively rejected by the dc-link voltage controller.
4) The external power disturbance drives the dc-link voltage controller to change the converter operating point; therefore, it affects the plant parameter (I_{d0}) in the first term of (7-7).
5) The converter operating point swiftly changes in dc grid applications, where the converter operating mode and operating point could swiftly change from inversion to rectification and vice versa. Furthermore, fast and harsh variations could be yielded under contingency situation (i.e., converter outage, faults, etc.). A simple proportional-integral (PI) controller can be designed to yield sufficient phase margin at the worst operating condition; however, the closed-loop stability could be lost under fast variation in the operating point as the controller will be working against a time-varying plant.
6) The augmented dynamics in (7-9) is affected by the droop gain and load resistance as long as the aforementioned uncertainties and disturbances associated with the plant transfer function $G(s)$.

7) If a basic dc-link voltage controller is designed to stabilize the nominal plant dynamics, the system stability and performance are not verifiably guaranteed under the occurrence of disturbances and parametric uncertainties. This fact will be illustrated in the following section where a standard PI dc-link voltage controller is designed and used to evaluate the dynamics of the augmented dynamics under uncertainty.
8) If the dc-link voltage controller is designed without considering the dynamics of the droop feedback controller, the stability and performance of the overall dc-link voltage dynamics are not guaranteed due to the additional dynamics imposed by the droop controller.

The aforementioned facts motivate the need for a controller that yields robust stability and performance under fast variation in the operating point, parametric uncertainties and external disturbances.

7.2.3 Model Validation

Before analyzing the dynamic characteristics of the augmented dc-link voltage dynamics with droop feedback control in (7-9), model validation is essential. For this purpose, the model in (7-9) is evaluated at different operating points, and its response is compared to that of the detailed nonlinear time-domain simulation model. Both models have the same parameters (as given in Section 7.6) and are excited by the same disturbances. In both models, a standard PI controller [30] is adopted for dc-link voltage control.

Fig. 7.3 demonstrates acceptable compatibility between the closed-loop responses of the nonlinear plant and the linearized model extracted from the nonlinear plant. In fact, the number and instant of occurrence of the oscillations are very well matched and consistent for both responses. As expected, the dominant dynamics is dictated by the droop controller, which has the slowest dynamics as shown in Fig. 7.3(d). Changes in the droop gain can easily change the location of the dominant eigenvalues and reduce the system stability margins as shown in Fig. 7.3(d). The results reveal the validity of the linearized model for which a robust controller is designed.

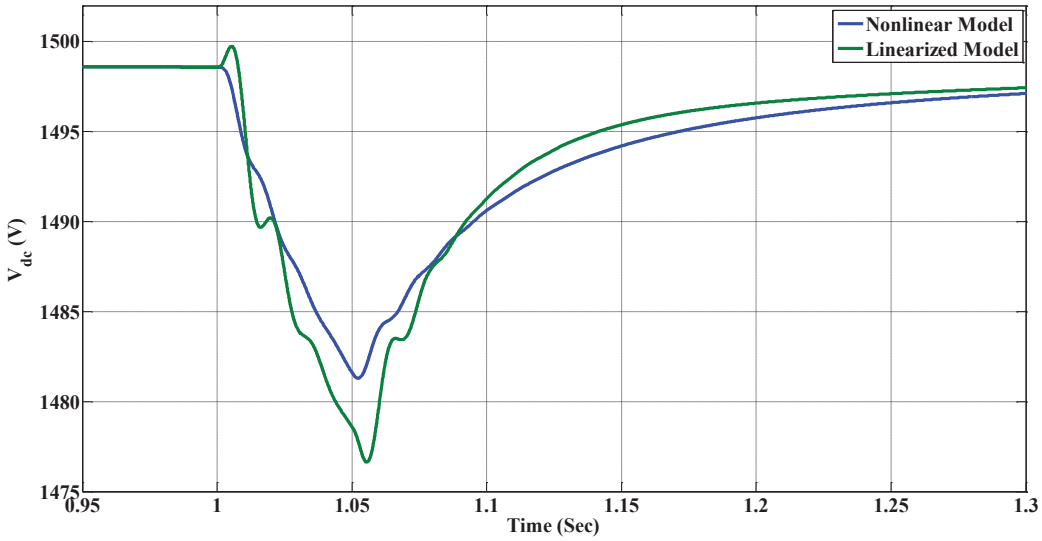
Nonlinear Model
Linearized Model
1500
1495
1490
1485
1480
1475
V_{dc} (V)
0.95
1
1.05
1.1
1.15
1.2
1.25
1.3
Time (Sec)

(a)

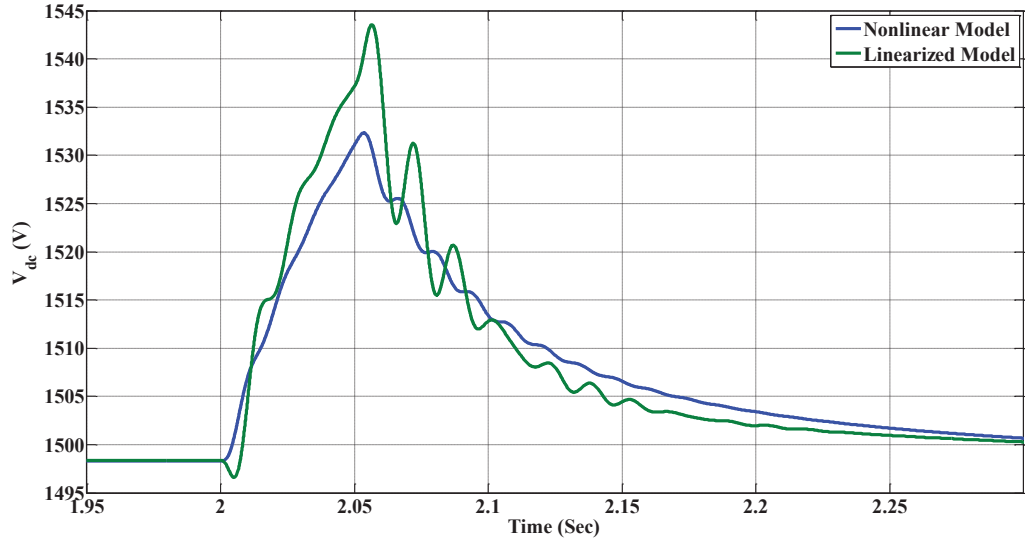
Nonlinear Model
Linearized Model
1545
1540
1535
1530
1525
1520
1515
1510
1505
1500
1495
V_{dc} (V)
1.95
2
2.05
2.1
2.15
2.2
2.25
Time (Sec)

(b)

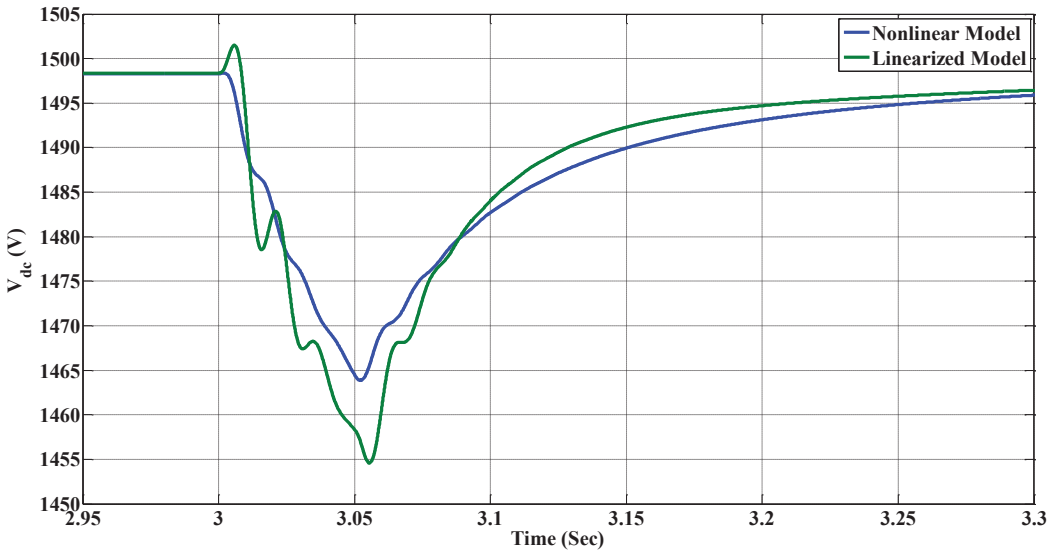

(c)

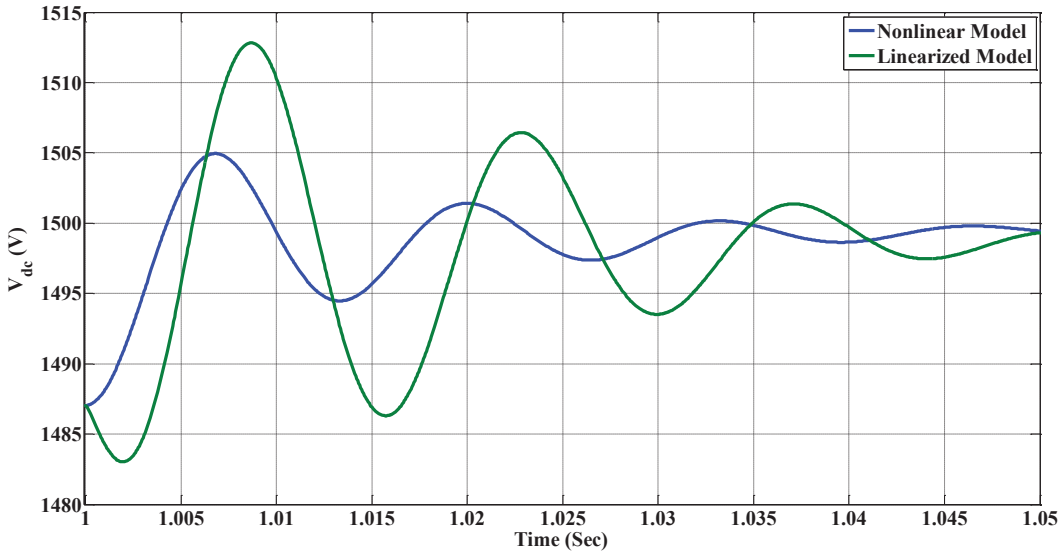

(d)

Fig. 7.3. Model validation results. (a) Converter operating point is changed from +0.1 MW/0.00 Mvar to +0.3 MW/0.0 Mvar in the inversion mode. (b) Converter operating point is changed from 0.3 MW/0.0 Mvar (inversion) to -0.3 MW/0.0 Mvar (rectification). (c) Converter operating point is changed from -0.3 MW/0.0 Mvar (rectification) to +0.3 MW /0.0 Mvar (inversion). (d) Converter droop gain is changed from 13 V/MW to 1.0 V/MW in the rectifier mode with an initial operating point of -1.0 MW/0.0 Mvar.

7.3 Analysis of a DC-Droop-Controlled Grid-Connected VSC

This section presents the eigenvalues analysis of the closed-loop dc-link voltage dynamics under dc grid parameters uncertainty, variable droop gain, and variable converter operating point. The main objective is to characterize the impact of the operating point variation (mainly induced by

the external power imposed on the VSC), uncertainties in the dc grid parameters (e.g., dc grid passive load and dc grid capacitance as reflected to the VSC), and variation in the droop again of the VSC on stability and performance of a grid-connected VSC. As a typical VSC is equipped with a dc-link voltage controller, the dynamic in (7-7) is studied with a standard PI dc-link voltage controller [30]. Also, the dc droop controller in (7-8) is implemented.

Following the detailed design procedure in [30], the PI controller is designed to yield a bandwidth of 20 Hz and a minimum phase margin of 60° phase margin in the worst-case operating point (i.e., when the converter operates in the rectification mode at the rated power), where the phase margin is the lowest due to the minimum phase behaviour.

Using the transfer function of the PI dc-link voltage controller as $K(s)$ in (7-9), the closed-loop system dynamics can be evaluated at different operating points and uncertainties.

Fig. 7.4 shows the pole/zero map of the closed-loop dynamics when the droop gain changes from zero to 20 V/MW. As the droop gain decreases, which is desirable to enhance the voltage regulation and voltage quality in the dc grid, the system stability margin is reduced. Therefore, a strong tradeoff between stability and performance does exist in a grid-connected VSC with dc power droop. The variation in the droop gain does not affect the location of the closed-loop zeros. However, the system has a right-hand-plane zero that is relatively close to the imaginary axis. As expected, the droop loop dictates the behavior of the dominant eigenvalues (closest to the imaginary axis) due to the time and frequency scale separation between the cascaded control loops.

Fig. 7.5 shows the pole/zero map of the closed-loop dynamics when the static load resistance R_{Load} changes from 1 Ω to 250 Ω. As the passive load resistance affects the plant time-constant, uncertainty in the load resistance affects the closed-loop dynamics in a significant way. The higher the load resistance, the lower the damping energy of the VSC system which results in reduced stability margins. Furthermore, variation in the load resistance affects the location of the right-hand zero that becomes dependent on the converter loading level.

Fig. 7.6 shows the pole/zero map of the closed-loop dynamics when the equivalent dc-link capacitance C_{eq} is subjected to uncertainty. The equivalent capacitance affects the open-loop plant time constant and, consequently, it affects the closed-loop dynamics. Increasing C_{eq} results in less stability because it increases the energy stored in the converter system which demands higher damping energy to retain the same stability margins. If both C_{eq} and R_{Load} are increasing,

the system stability margins can be significantly reduced and eventually instability can be yielded under paramedic uncertainty.

Fig. 7.7 shows the pole/zero map of the closed-loop dynamics when the converter active power operating point, or equivalently I_{d0}, changes from the rated positive value to the rated negative value at zero reactive power. As the PI controller is designed at the worst-case operating point (rated negative current corresponding to the rectification mode), the variation in the operating point does significantly affect the location of the closed-loop eigenvalues. It should be noted that if the dc-link PI voltage controller is designed without considering the effect of the converter operating point on the dc-link voltage dynamics (i.e., by ignoring the instantaneous power of the ac filter), which is a very common approach to design the dc-link voltage controller in low-power converters, the dc-link voltage dynamics becomes highly dependent on the converter operating point. Fig. 7.8 shows the closed-loop pole/zero map in this case.

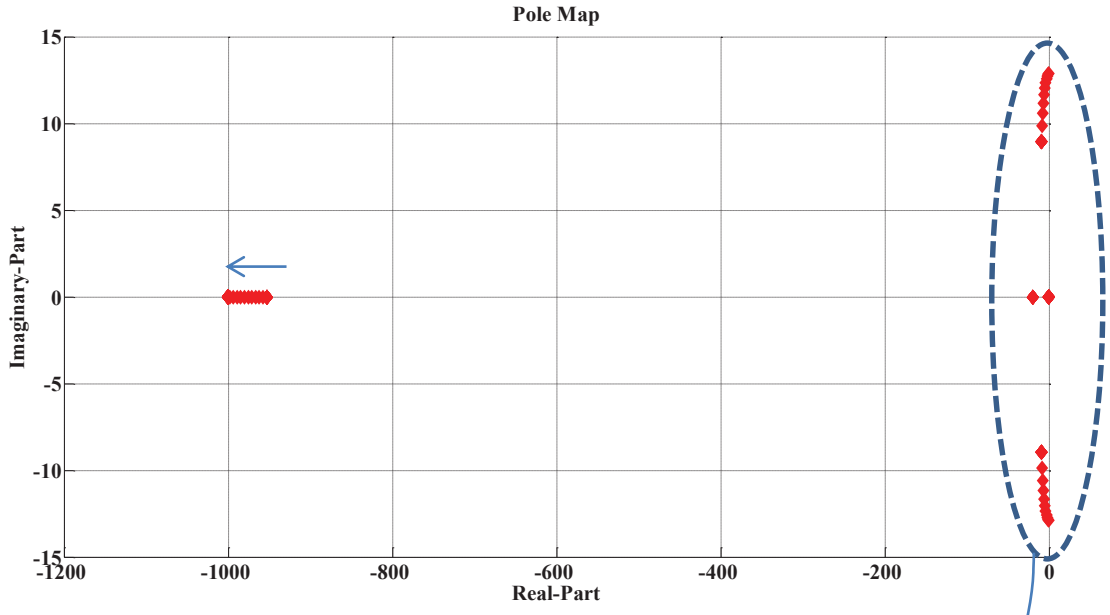

Continued in the Next Page

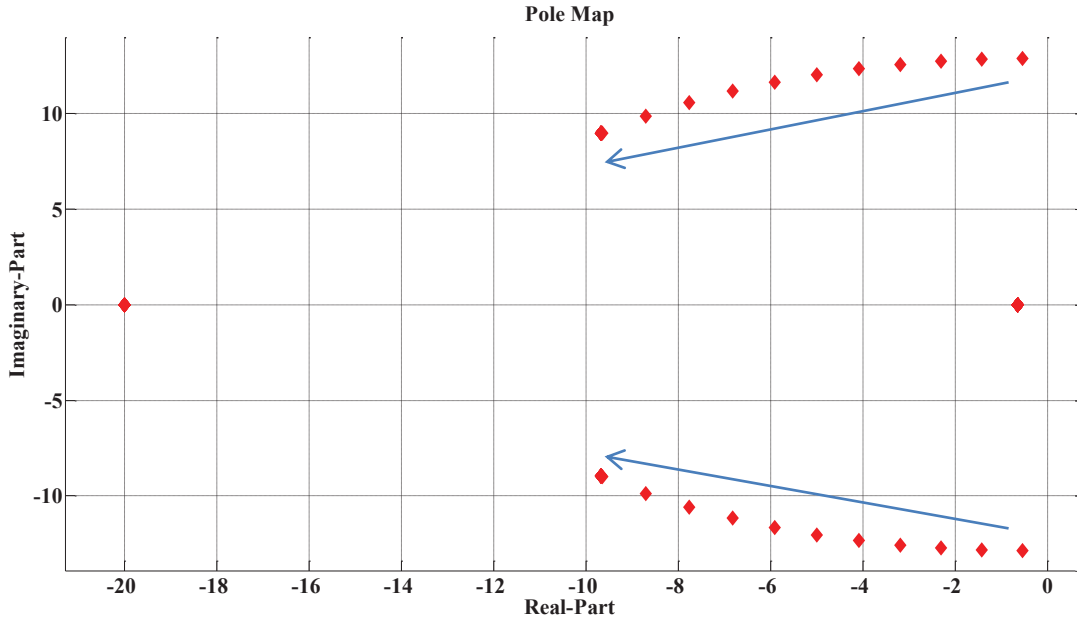

(a)

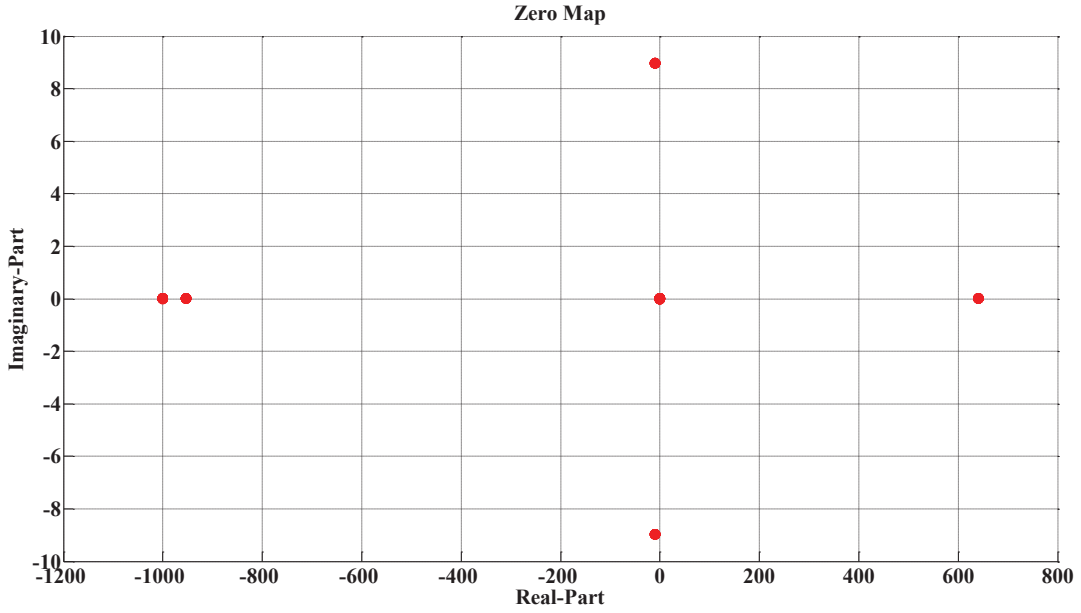

(b)

Fig. 7.4. Pole/Zero map of the clo sed-loop system dynamics with a standard P I controller. K_{droop} changes from 0 to 20 V/MW. (a) Pole map, (b) Zero map.

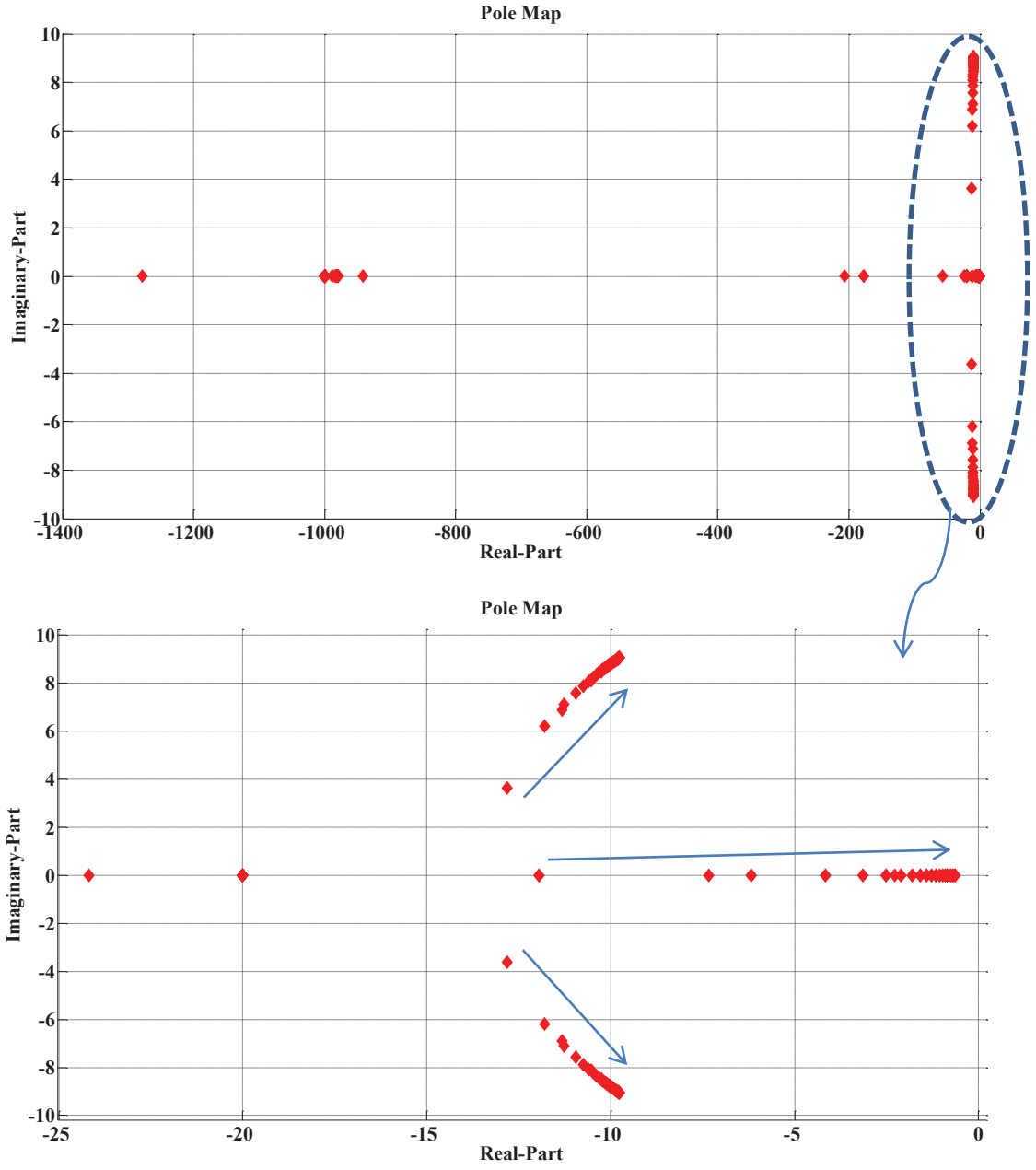
Pole Map
Imaginary-Part
Real-Part
10
8
6
4
2
0
-2
-4
-6
-8
-10
-1400
-1200
-1000
-800
-600
-400
-200
0
Pole Map
Imaginary-Part
Real-Part
10
8
6
4
2
0
-2
-4
-6
-8
-10
-25
-20
-15
-10
-5
0

(a)

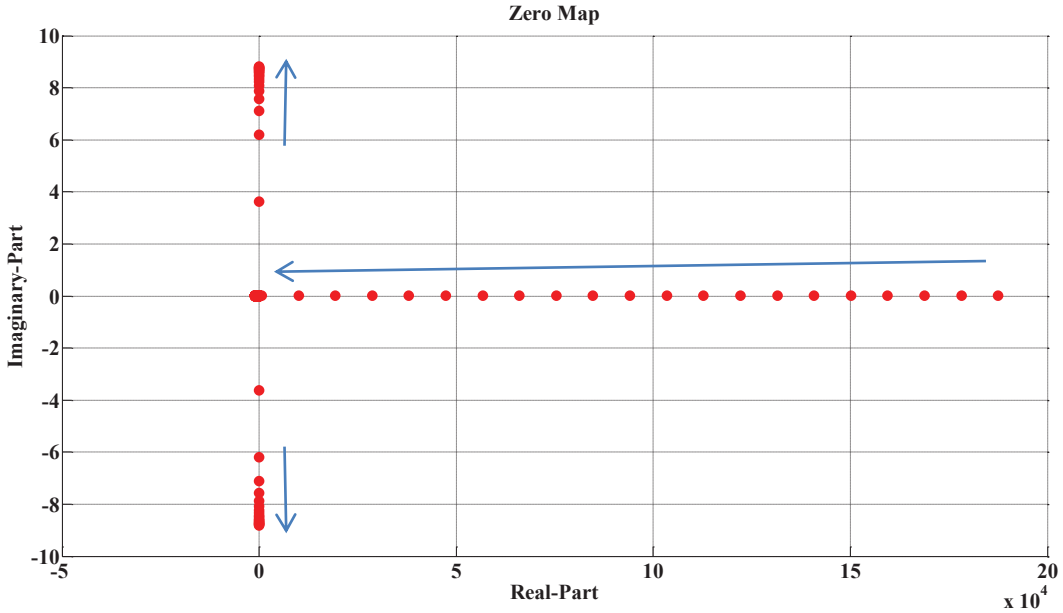

(b)

Fig. 7.5. Pole/Zero map of the clo sed-loop system dynamics with a standard P I controller. R_{Load} changes from 1 Ω to 250 Ω. (a) Pole map, (b) Zero map.

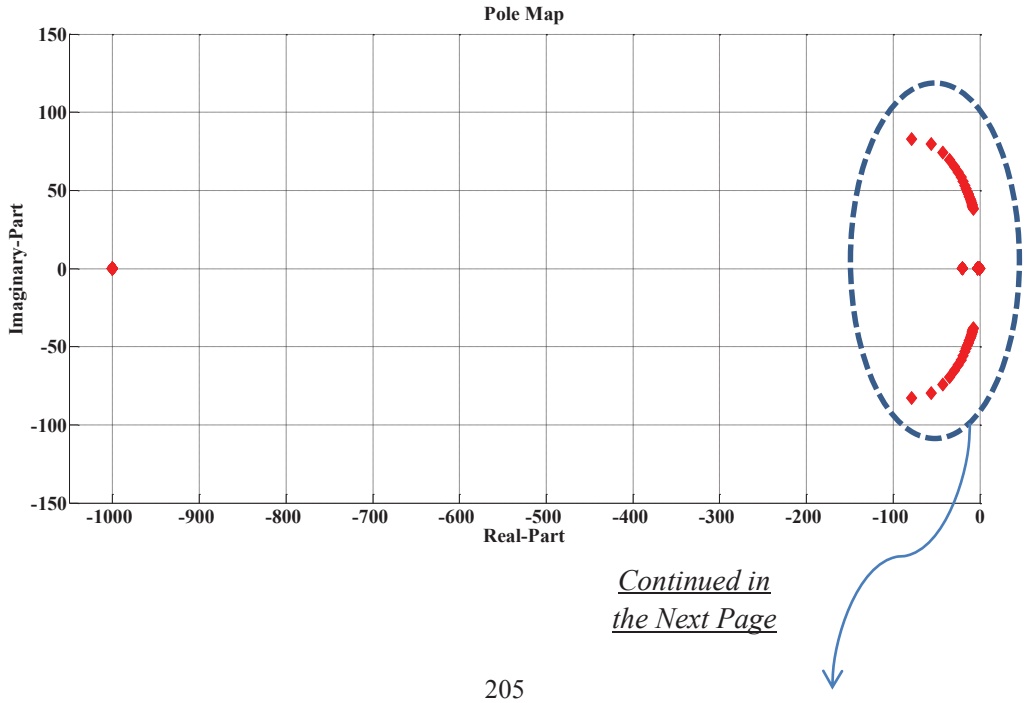

Continued in the Next Page

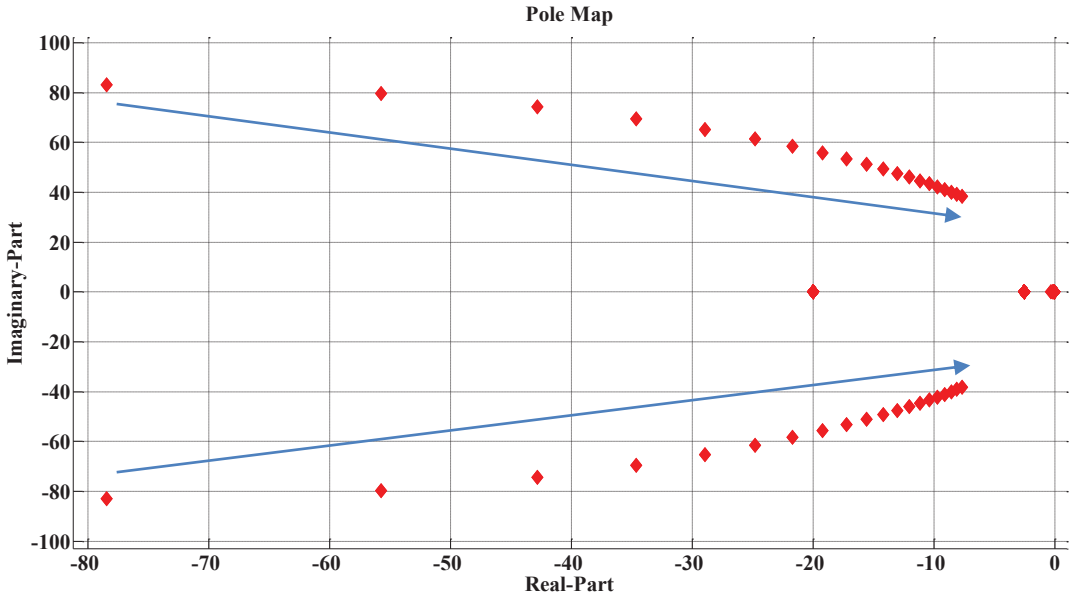

(a)

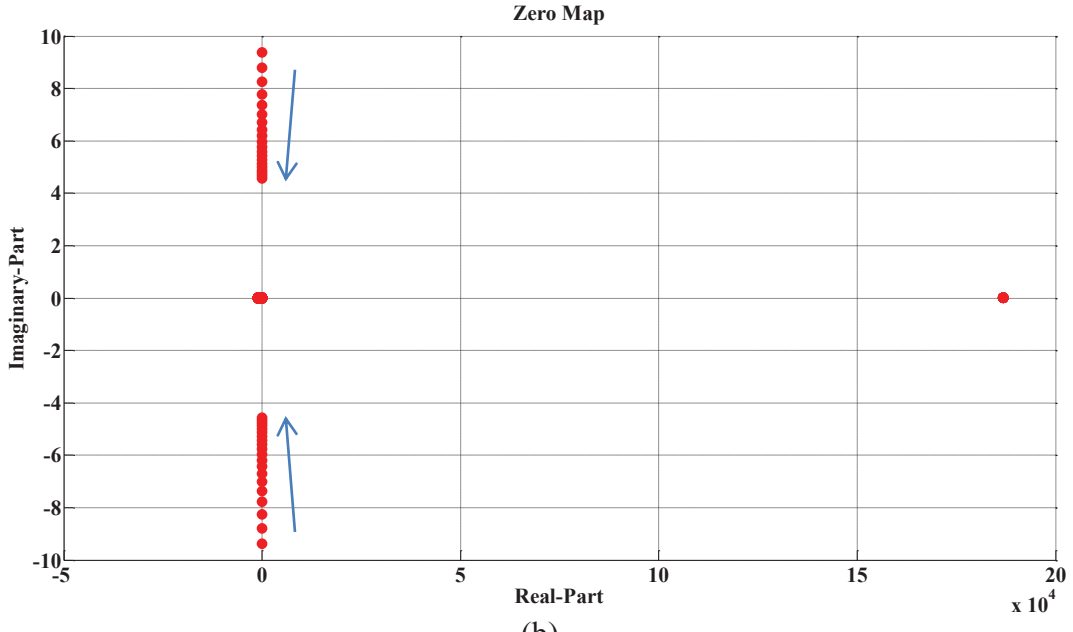

(b)

Fig. 7.6. Pole/Zero map of the clo sed-loop system dynamics with a standard P I controller. C_{eq} changes from 6.25 mF to 100 mF. (a) Pole map, (b) Zero map.

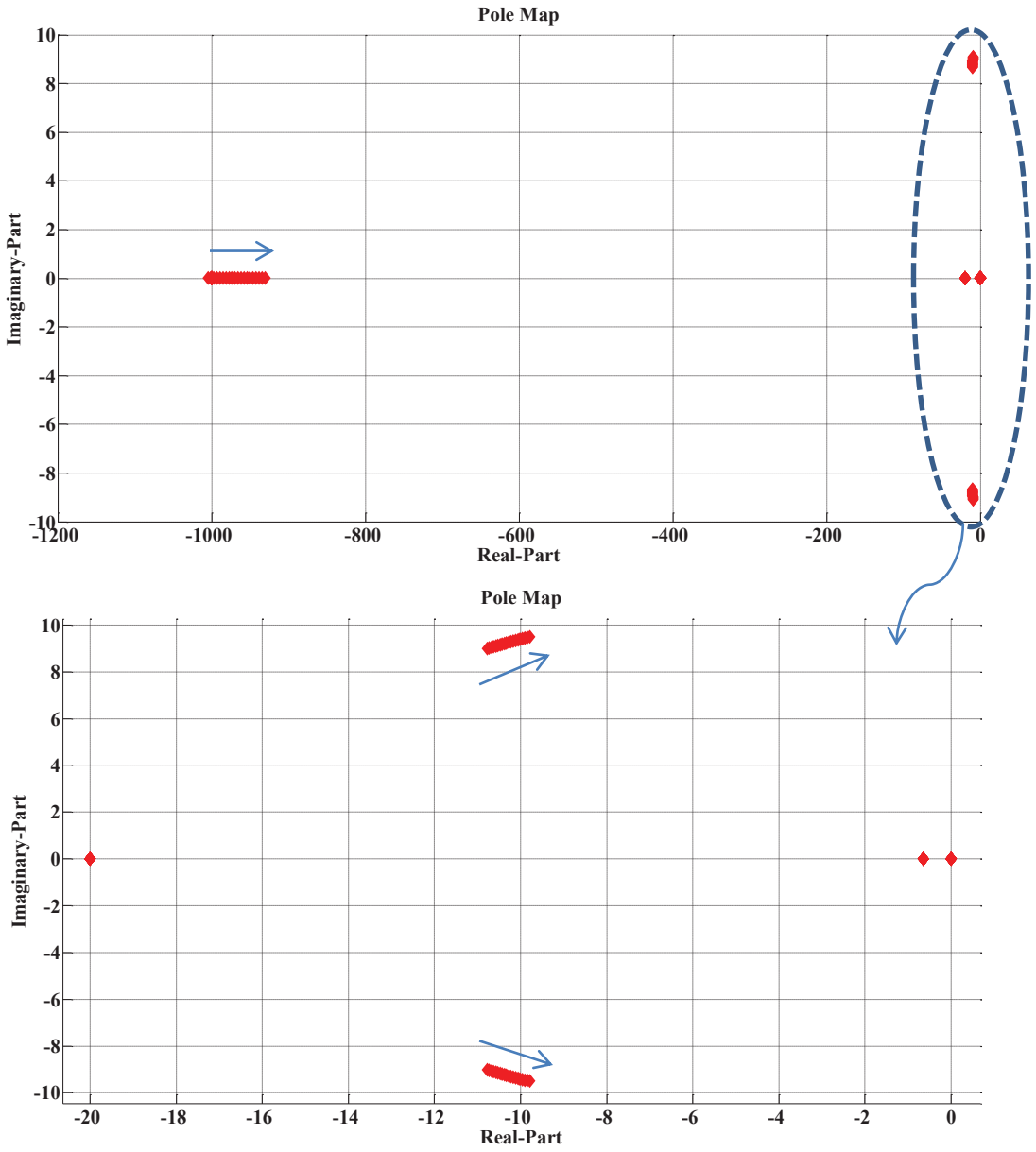
Pole Map
Imaginary-Part
Real-Part
10
8
6
4
2
0
-2
-4
-6
-8
-10
-1200
-1000
-800
-600
-400
-200
0
Pole Map
Imaginary-Part
Real-Part
-20
-18
-16
-14
-12
-10
-8
-6
-4
-2
0

(a)

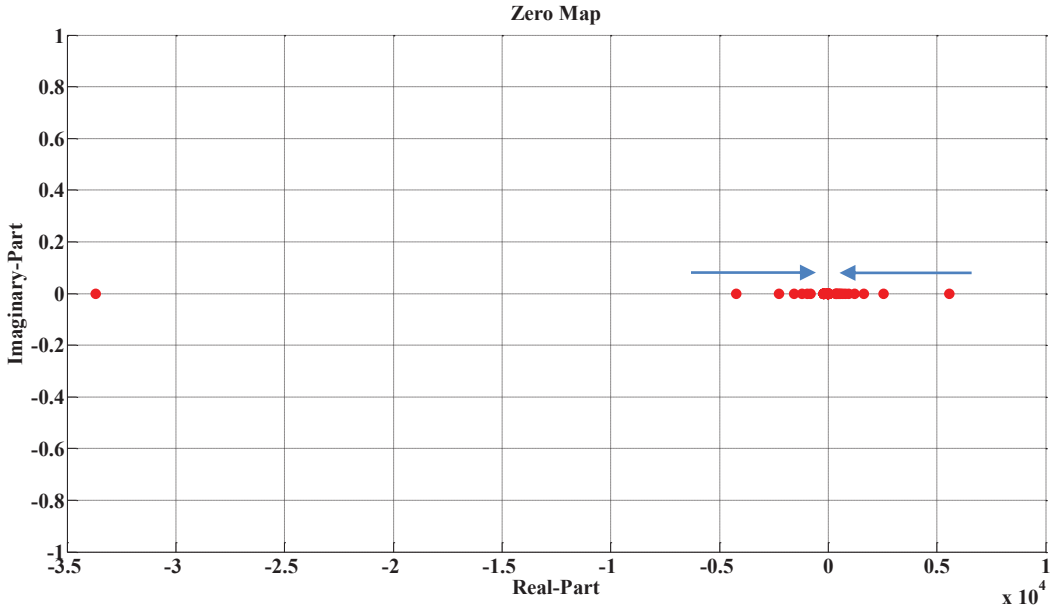

(b)

Fig. 7.7. Pole/Zero map of the clo sed-loop system dynamics with a standard P I controller. I_{d0} changes from the rated positive value to the rated negative value. T he dc-link voltage PI controller is designed to account for the operating point dependency by considering the effect of the instantaneous power of the ac filter. (a) Pole map, (b) Zero map.

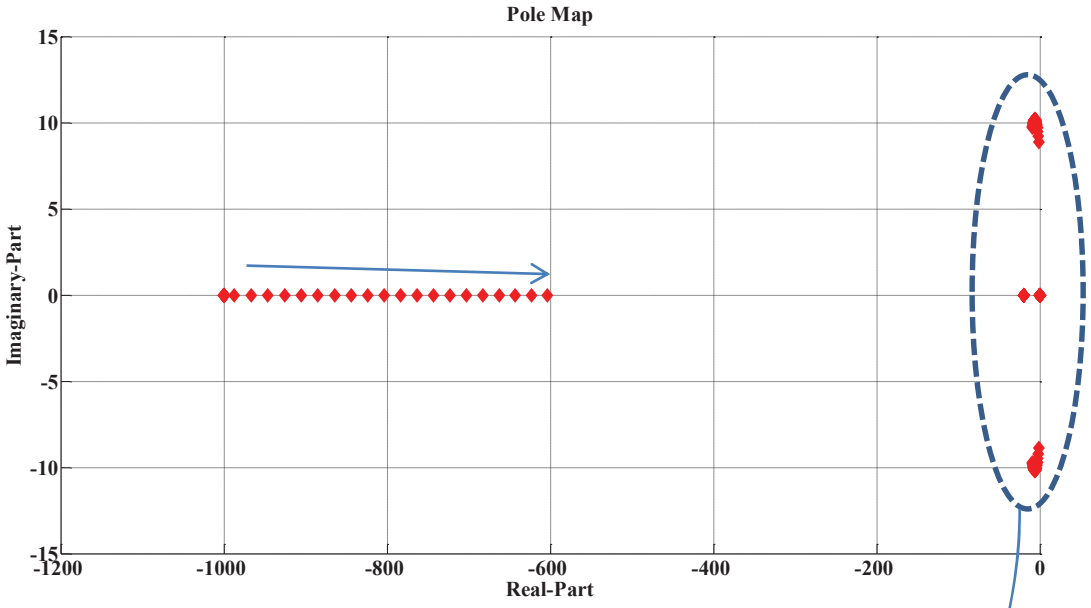

Continued in the Next Page

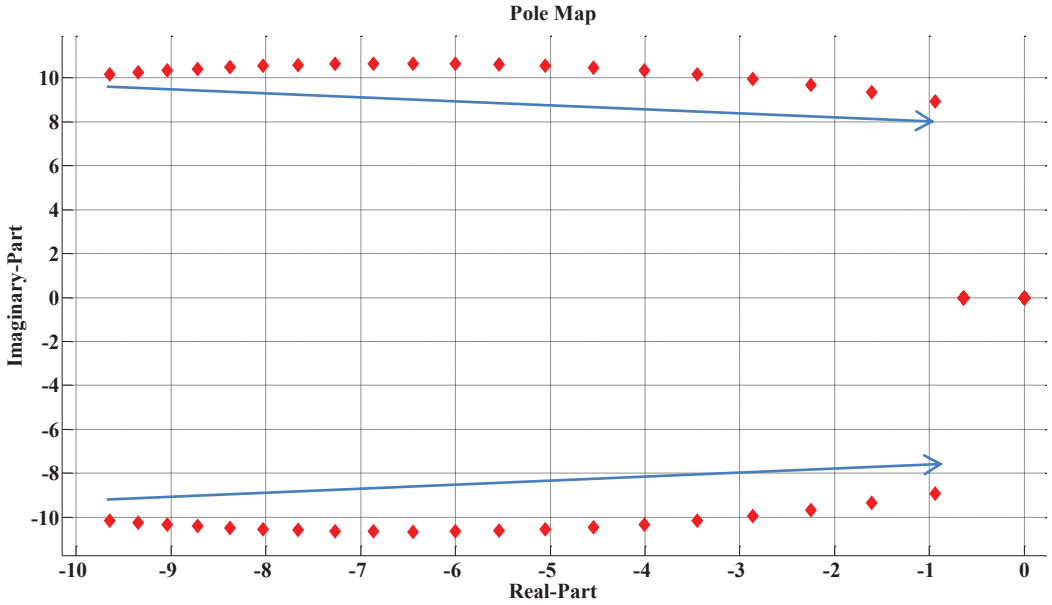

(a)

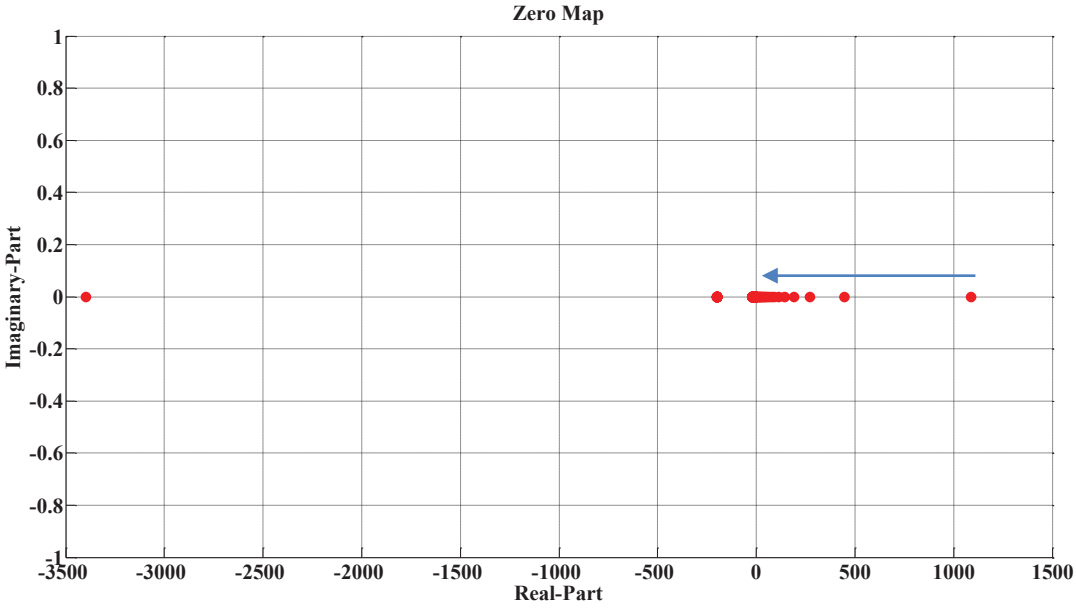

(b)

Fig. 7.8. Pole/Zero map of the closed-loop system dynamics with I_{d0} changes from the rated positive value to the rated negative value. The dc-link voltage PI controller is designed without considering the operating point dependency by ignoring the effect of the instantaneous power of the ac filter. (a) Pole map, (b) Zero map.

7.4 Controller Design

The analysis of the closed-loop dc-link voltage dynamics in a grid-connected VSC with a dc droop function shows that the system stability and performance can be remarkably affected due to 1) ignoring the effect of the outer droop loop on the dc-link voltage dynamics when the dc-link voltage controller is designed, 2) dc grid parametric uncertainties, and 3) variation in the converter operating point. Therefore, a robust control system that addresses these drawbacks is proposed in this chpater.

Several robust control methods are available in the literature. To synthesize a simple robust controller against operating point variation and parametric uncertainties, the polynomial method [86] can be used. However, this method yields an unfeasible solution for the present problem. This is due to the large range of possible operating points and dc grid parameters in a practical VSC. Under these practical conditions, the range of variation of the vertices of the polytopic system generated by the polynomial method is very large so that the linear matrix inequality (LMI) condition is not satisfied [86], [88]. In addition, because the non-minimum phase situation occurs along with unstable modes in the small-signal dynamics of (7-7), it is not possible to benefit from the robust two degree-of-freedom (DOF) control structures that require a plant with stable poles and/or zeros [80]. Furthermore, a switching adaptive controller [69] is not a suitable control candidate owing to the fact that both the operating point and the system parameters are changing, which yields a wide range of plant parameters, and complicates the design of a stable switching controller. Therefore, in this chapter, a robust controller is developed to satisfy the design objectives (i.e., robustness against outer loop droop dynamics with variable droop gain, and robustness against dc grid parameters uncertainties and converter operating point variation). The robust control approach is selected owing to the ability to stabilize and maintain robust control performance, systematic design approach, fixed-order controller, and suitability for industrial applications.

In the present design problem, four uncertain parameters are considered; i.e., K_{droop}, C_{eq}, I_{d0} and R_{Load} as well as the external disturbances $D(s)$ imposed on the output dc-link voltage. Although it is possible to design a robust optimal controller to provide disturbance rejection and robustness against parameter variation, the robust performance cannot be guaranteed under wide range of parameter variation, which is the case in grid-connected VSCs. Furthermore, the

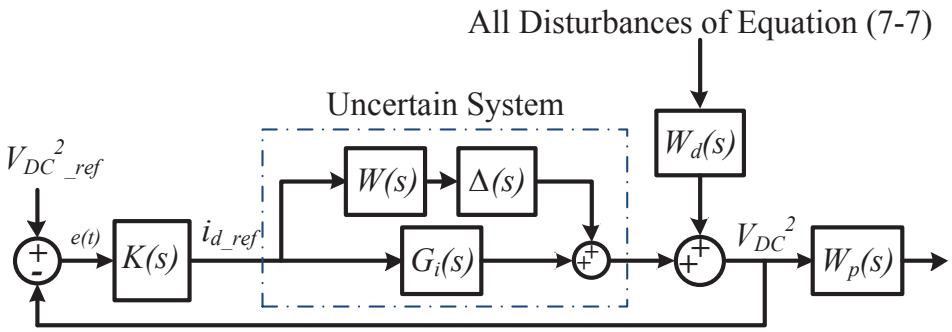

Fig. 7.9. Structure used to design the baseline robust controller.

designed controller will be of a high order which complicates practical implementation. More importantly, the non-minimum phase nature of the plant only allows the consideration of additive uncertainty. Whereas disturbance can be reasonably modeled as additive uncertainty, parametric uncertainties involve both multiplicative and additive [82]. Therefore, a two-stage robust controller is developed in this chapter. In the first stage, a robust optimal controller (baseline controller) is designed to ensure effective disturbance rejection and robustness against operating point variation (i.e., I_{d0} variation) using the dc-link voltage dynamics in (7-7). Then, the augmented dynamics in (7-9) with the designed

baseline controller and droop feedback dynamics are used to retune the baseline controller, via the polynomial method, to ensure that the closed-loop eigenvalues are located in a predetermined region in the complex frequency-domain under parametric uncertainties in K_{droop} and the plant time constant C_{eq} R_{Load}. By this approach, the droop dynamics will be considered in the dc-link voltage controller as well as parametric uncertanities and disturbances.

7.4.1 Stage 1: Controller Synthesis for Disturbance Rejection

One of the best ways to optimally reject the disturbances imposed on the output is minimizing the H_∞ norm from the filtered disturbance signals to the filtered output in the presence of weighted uncertainty using the structured singular values μ-method [81]-[82]. Therefore, a μ-synthesis controller using the *DK*-iteration method is employed to optimally synthesize the baseline dc-link voltage controller.

The employed structure is a controller with one degree of freedom (DOF), and both reference tracking and disturbance rejection are simultaneously achieved. Thus, the controller is synthesized based on the internal model principle to guarantee both reference tracking and

disturbance rejection of step signals at the input and output, respectively [80]. To account for uncertainties associated with unmodelled dynamics and nonlinear effects due to operating point variation, the uncertainties in the dc-link voltage control model are approximated by input multiplicative uncertainties. The applied control structure is shown in Fig. 7.9, where the nominal plant transfer function is $G_i(s)$, the uncertainties weight is $W(s)$, and disturbance and output weights are $W_d(s)$ and $W_p(s)$, respectively.

To have one control structure that models variable operating points, all possible transfer functions have been randomly generated by the Robust Control Toolbox in MATLAB [82]. It is often appropriate to simplify the uncertainty model while approximately retaining its overall variability for optimal feedback design purposes. One hundred and twenty random samples of all possible transfer functions have been generated, and the nominal transfer function and its related unmodeled dynamics have been extracted. The weights Wd(s) and Wp(s) are designed to ensure effective disturbance rejection and good transient response at nominal parameters [81], [84]. Accordingly, the following weight functions are adopted:

$$W(s) = -\frac{1.5R_{Load}LI_{d0}s}{\left(0.5R_{Load}C_{eq}s+1\right)} \times \frac{1}{\tau_i s+1} \tag{7-10}$$

$$W_d(s) = \frac{1\times 10^6 R_{Load}}{(0.5R_{Load}C_{eq})s+1} \times \frac{1}{s+10^{-4}} \tag{7-11}$$

$$W_p(s) = \frac{1}{s+10^{-4}} \tag{7-12}$$

The controller $K(s)$ given by (7-13) has been synthesized using the robust controller design approach via the μ-synthesis and model order reduction tools in the Robust Control Toolbox of MATLAB. As shown in Fig. 7.9, the synthesized controller is a single transfer function employed in the one DOF structure, which simplifies the implementation. In spite of the somewhat high controller order, it is relatively easy to implement using commercial-grade signal processors.

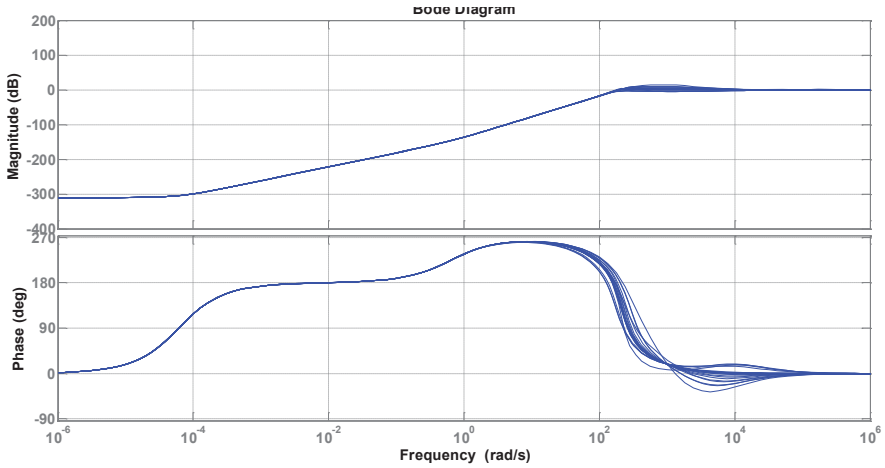

Fig. 7.10. Disturbance rejection performance of the proposed baseline controller.

$$K(s)=\frac{y(s)}{x(s)}=\frac{-4.179\times10^{4}s^{3}-1.711\times10^{7}s^{2}-2.813\times10^{9}s-2.01\times10^{11}}{s^{4}+3.842\times10^{5}s^{3}+2.894\times10^{9}s^{2}+3.389\times10^{5}s+10.79} \tag{7-13}$$

Fig. 7.10 shows the frequency response of the disturbance rejection performance (the response of the d c-link voltage to the disturbance sig nal $D(s)$) with the proposed bas eline controller in (7-13) at d ifferent operating points (r ated power in the re ctification mode to the rated power in the inversion mode). The cont roller offers very effective and robust disturba nce rejection performance at different operating points which yields robustness against disturbances associated with opera ting point variation and el iminates the need for feed-forward control of measured disturbances. The latter features reduce the sensor requirements and enh ance the control system reliability.

7.4.2 Stage 2: Controlle r Synthesis for Robustness against Droop Dynamics and Parameter Variation

In Stage 1, the baseline controller is desig ned to ensure effective disturba nce rejection against external disturbances and uncertainties associ ated with operating point v ariation. Next, in Stage 2, the baseline controller is re-tuned, without compromising the disturbance rejection characteristics, to ensur e robustness against th e outer droop loop d ynamics and variation in system parameters (K_{Droop}

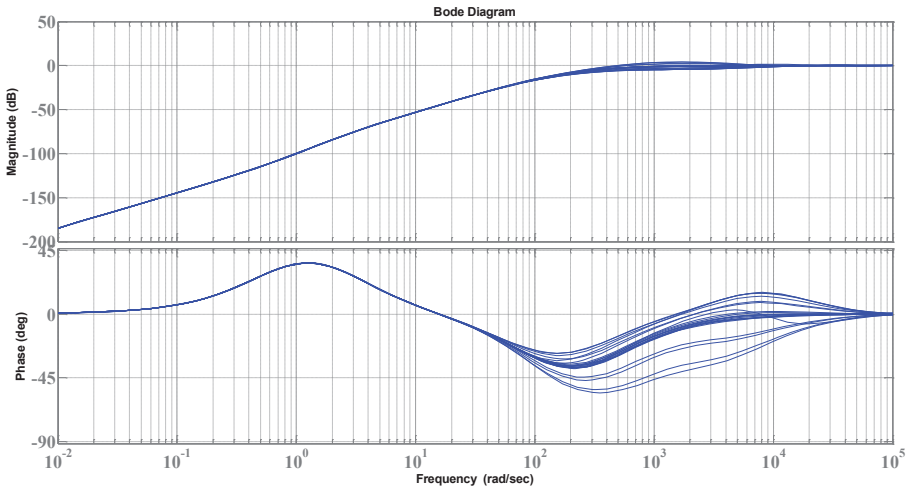

Fig. 7.11. Disturbance rejection performance of the proposed final controller.

and $R_{Load}C_{eq}$). To achieve this objective, the closed-loop dc-link voltage dynamics in (7-9) with the outer loop droop dynamics and the baseline controller as the feedback controller $K(s)$ is used to constrain the location of the augmented system eigenvalues under parametric uncertainties in a predefined location in the complex frequency-domain using the polynomial method. Among the advantages of this method is simplicity and that the resulting controller has the same order, or relatively closer, to the baseline controller. Furthermore, it is an asset to ensure robust stability margins in power networks by ensuring that the closed-loop poles is allocated at a specific pre-determined region in the complex frequency domain even under parametric uncertainties.

Following the design procedure in Section 2.3.3, the controller is modified for induce robust performance against variation in system parameters K_{droop}, C_{eq}, and R_{Load}. The resultant controller is given in (7-14).

$$K(s)=\frac{-9.9734\times10^{-15}s^3-3.3173\times10^{-12}s^2-2.6463\times10^{-10}s-6.5256\times10^{-10}}{2.0123\times10^{-18}s^4+1.2829\times10^{-13}s^3+6.6636\times10^{-10}s^2+5.9627\times10^{-36}s} \tag{7-14}$$

It is worth mentioning that modifying the baseline robust controller to induce closed-loop robustness against parametric uncertainties does not significantly affect the disturbance rejection performance of the baseline controller. This is because the central polynomial in Stage 2 of the controller design is chosen to be the desired nominal closed-loop characteristic polynomial. The latter is generated

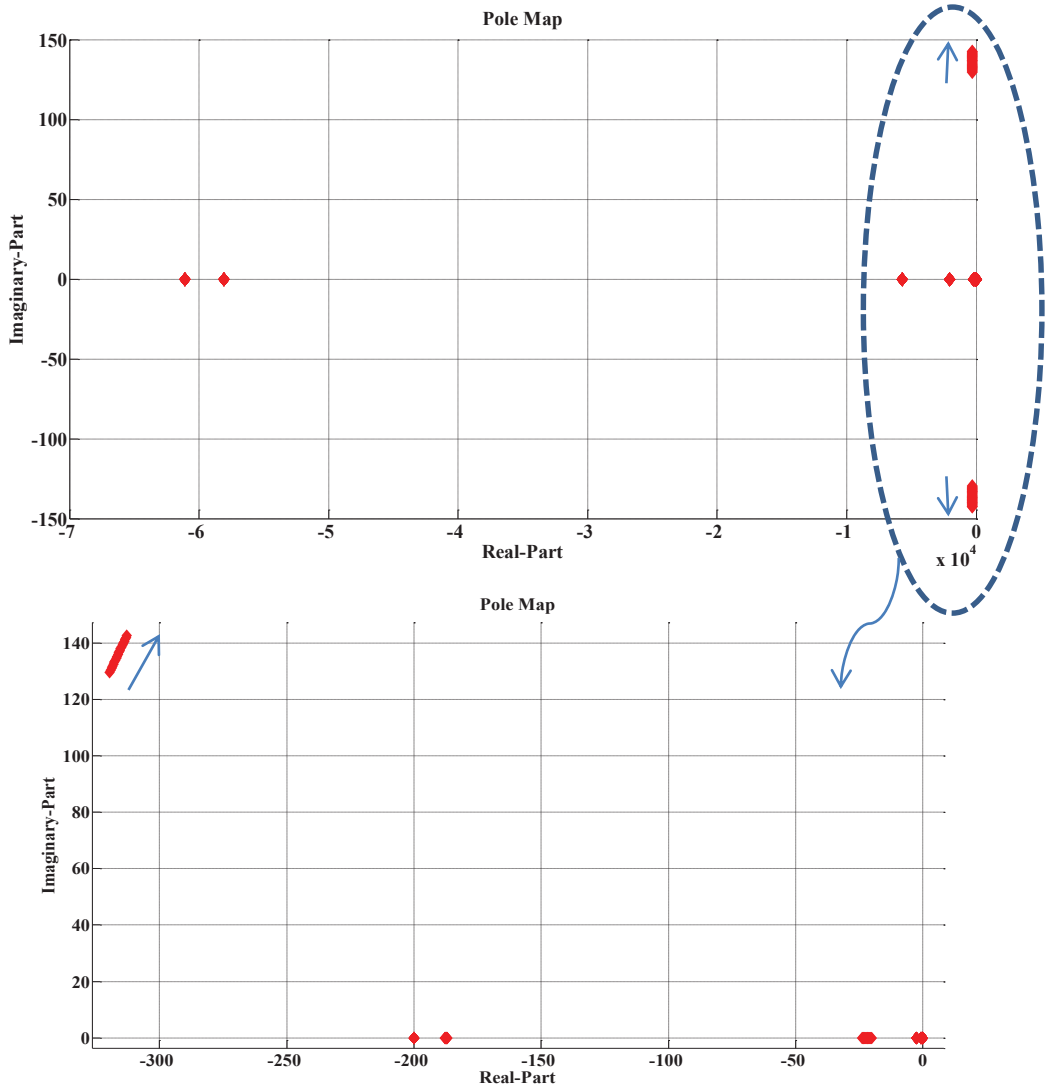

Fig. 7.12. Eigenvalues of the closed-loop system dynamics with the proposed robust controller. K_{droop} is changing from 0 to 20 V/MW.

via minimizing the H_∞ norm of the closed-loop system due to the disturbance input (as detailed in Stage 1). Then, as shown in [86], [88], the closed-loop characteristic polynomials at uncertainty conditions will be close to the central polynomial that has a very effective disturbance rejection performance. Fig. 7.11 shows the frequency response of the disturbance rejection performance with the proposed final controller in (7-14) at different operating points (rated power in the rectification mode to the rated power in the inversion mode). The controller still offers very effective and robust disturbance rejection performance as well as robustness against droop dynamics and parametric uncertainties as shown by the egienvalues analysis in the next subsection.

7.4.1 Analysis of the Closed-Loop Dynamics With the Proposed Controller

To evaluate the performance of the proposed controller, the augmented closed-loop dynamics in (7-9) with the final robust controller in (7-14) is evaluated and used for eigenvalues analysis at variable system parameters and operating points. Fig. 7.12-Fig. 7.15 show the closed-loop eigenvalues with the proposed controller under a wide range of uncertainties in K_{droop}, R_{Load}, C_{eq} and I_{d0}, respectively. As shown in these figures, the proposed controller signficantely increases the robustness of the closed-loop dynamics against parametric uncertainities.

7.5 Simulation Results

A typical multiterminal dc grid with five terminals, as shown in Fig. 7.16, is considered for the simulation study to test the performance of the proposed control system under typical and practical disturbances in modern multiterminal dc grids. The system is simulated in the MATLAB/Simulink environment. The system has five zones. VSCs 1 and 2, in Zones I and II, respectively, are connected to 580 V 60 Hz ac grids on the ac side and are equipped with droop and dc-link voltage control to regulate the dc-link voltage of the dc network with power sharing mechanism. In Zone III, a grid-connected VSC, VSC-PQ, is controlled in the active-reactive power control mode and does not contribute to the dc-link voltage regulation. Zone IV models a 1.0 MW, 500 Vdc dc-micro-grid with an energy storage system (ESS) interfaced to the dc grid via a bi-directional dc/dc converter. Zone V represents a dc micro grid with passive loads/ In Zones I and II, the proposed controller as well as the standard droop with PI dc-link voltage controllers are implemented for performance comparsion. The converter in Zone II employs a standard voltage-oriented PQ control structure with inner PI current control loops in the synchronous *dq*-frame [30]. Zone IV employs a standard PI controller for the bi-directional dc/dc converter. The average model of VSCs in Zones I, II and III is used to reduce the computational burden without loss of accuracy. A switching model of the bi-directional dc/dc converter system in Zone IV is implemented to test the control performance under typical high-frequency disturbances associated with converter switching. The system and controller parameters are given in Section 7.6.

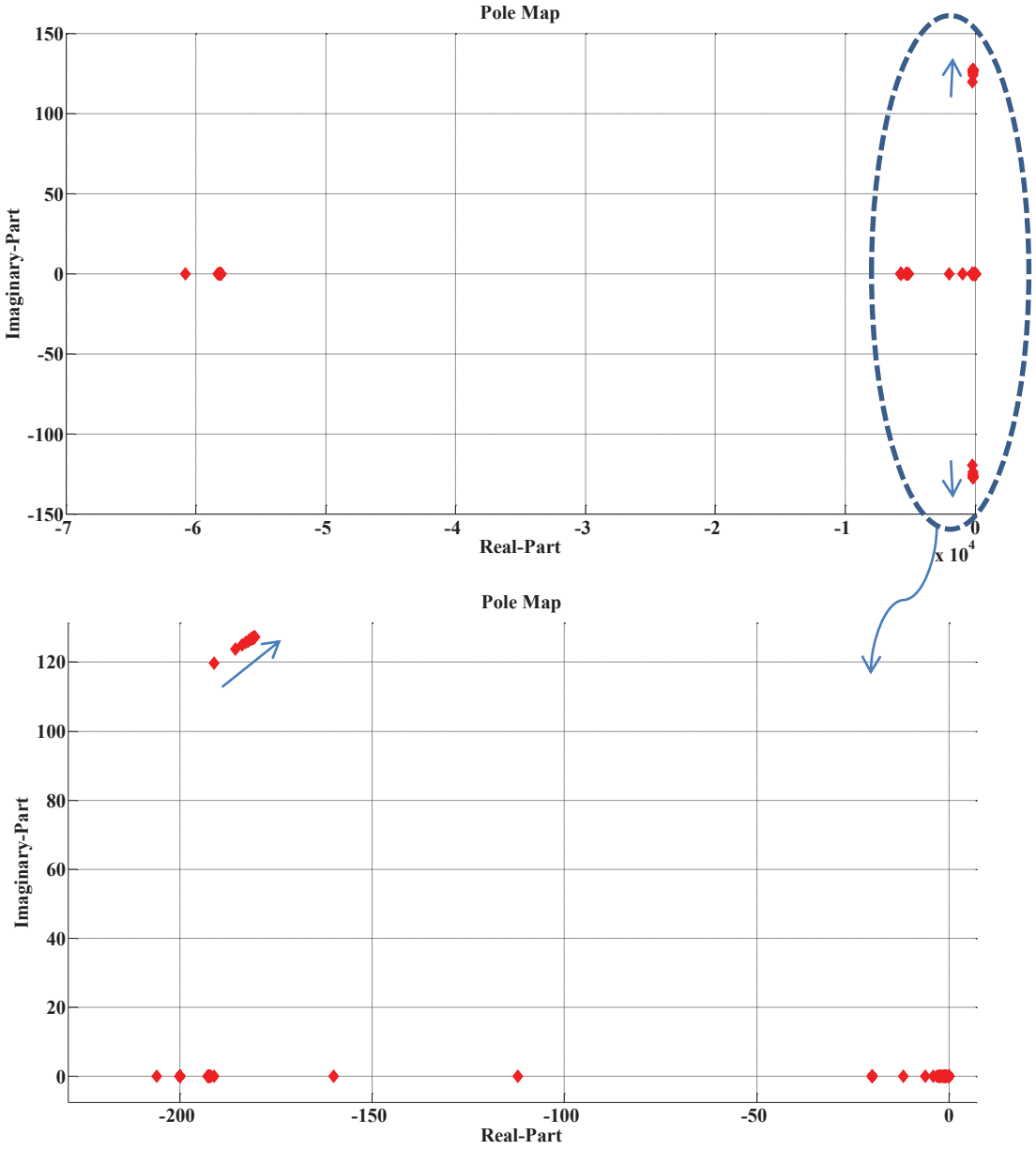

Fig. 7.13. Eigenvalues of the closed-loop system dynamics with the p roposed robust controller. R_{Load} changes from 1 Ω to 250 Ω.

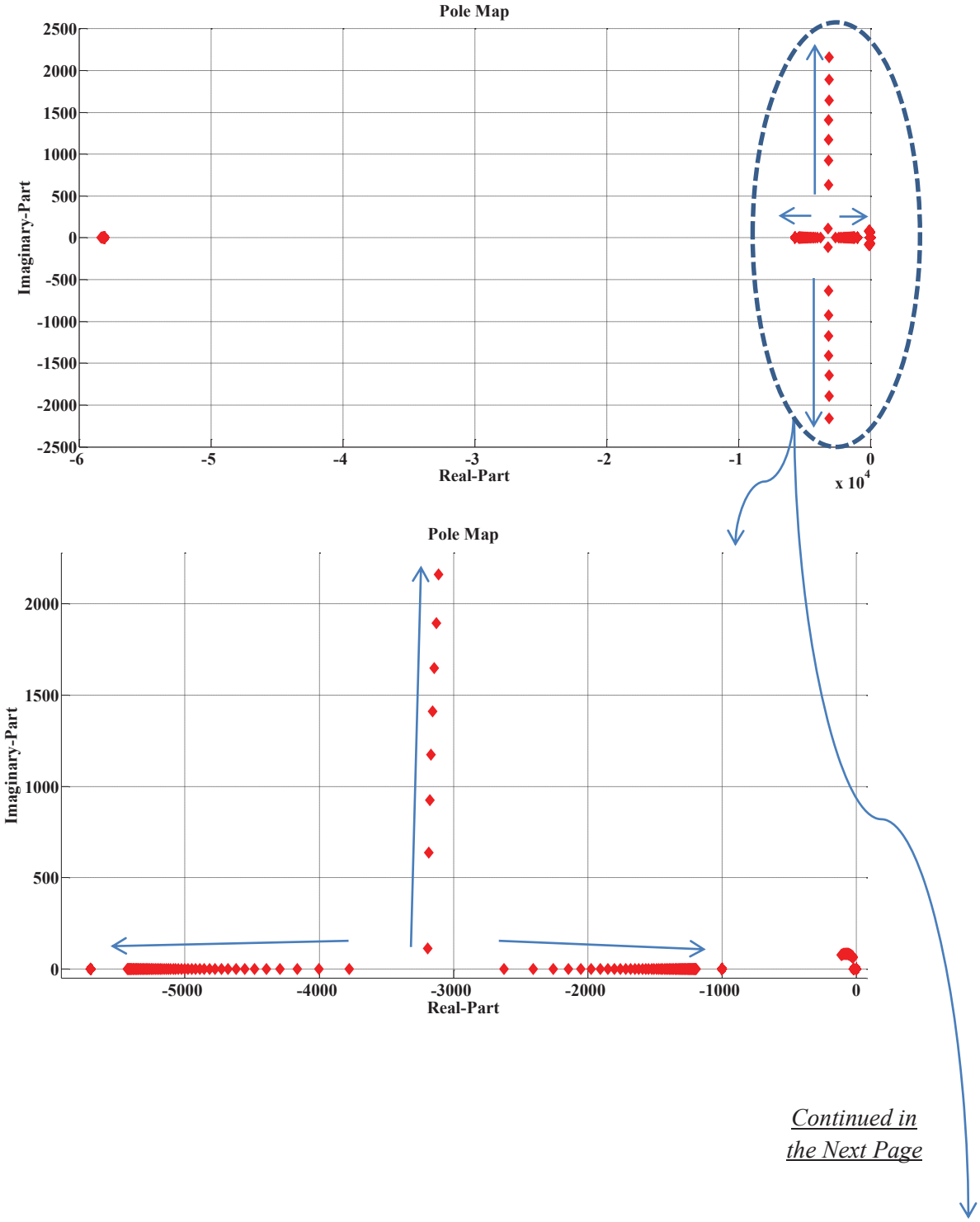

Continued in the Next Page

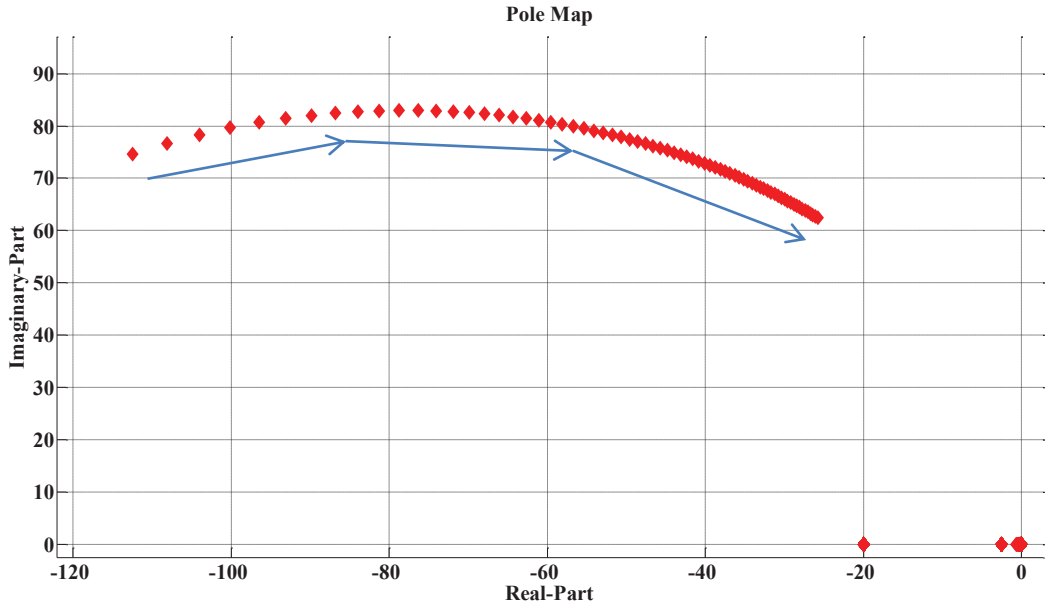

Fig. 7.14. Eigenvalues of the closed-loop system dynamics with the p roposed robust controller. C_{eq} changes from 6.25 mF to 100 mF.

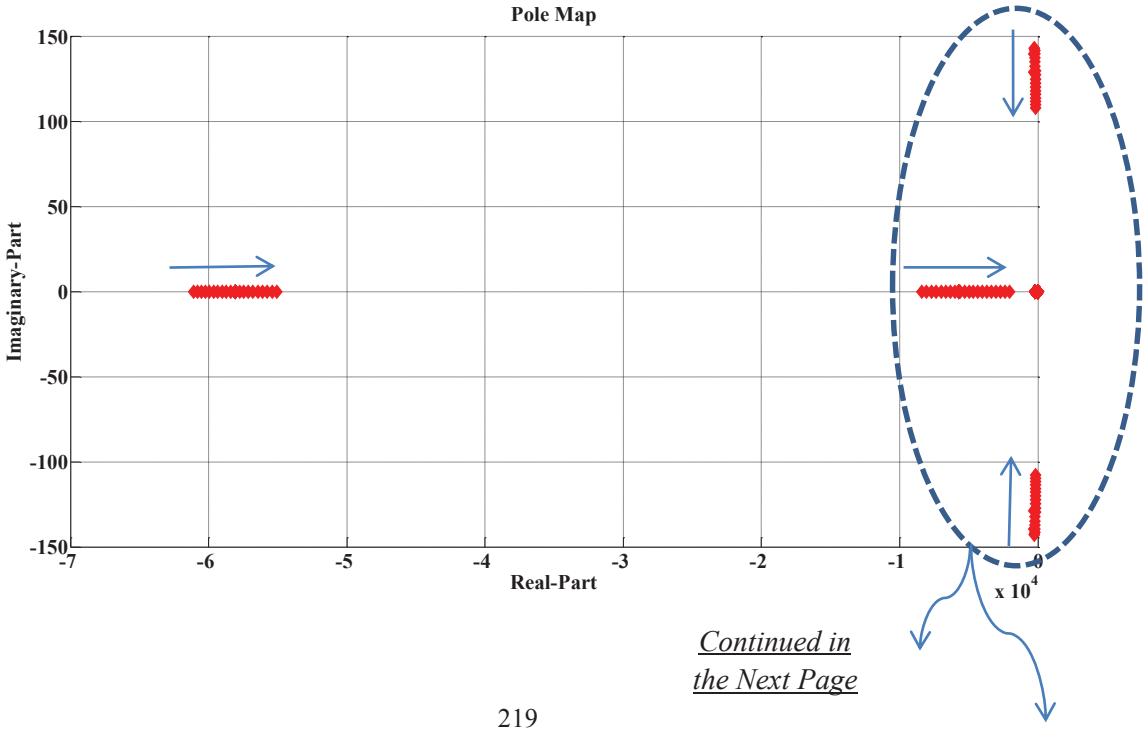

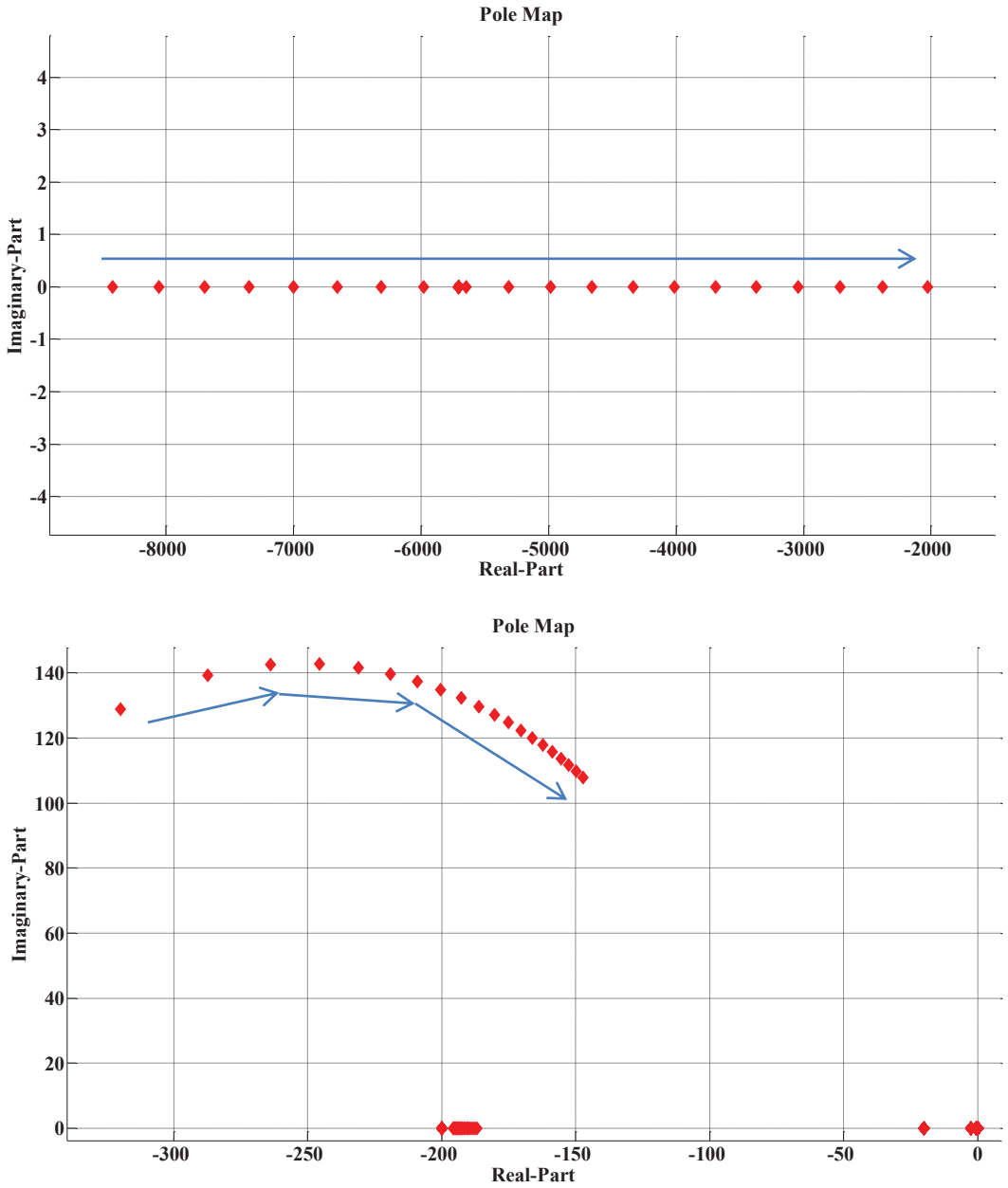

Fig. 7.15. Eigenvalues of the closed-loop system dynamics with the p roposed robust controller. I_{d0} changes from the rated positive value to the rated negative value.

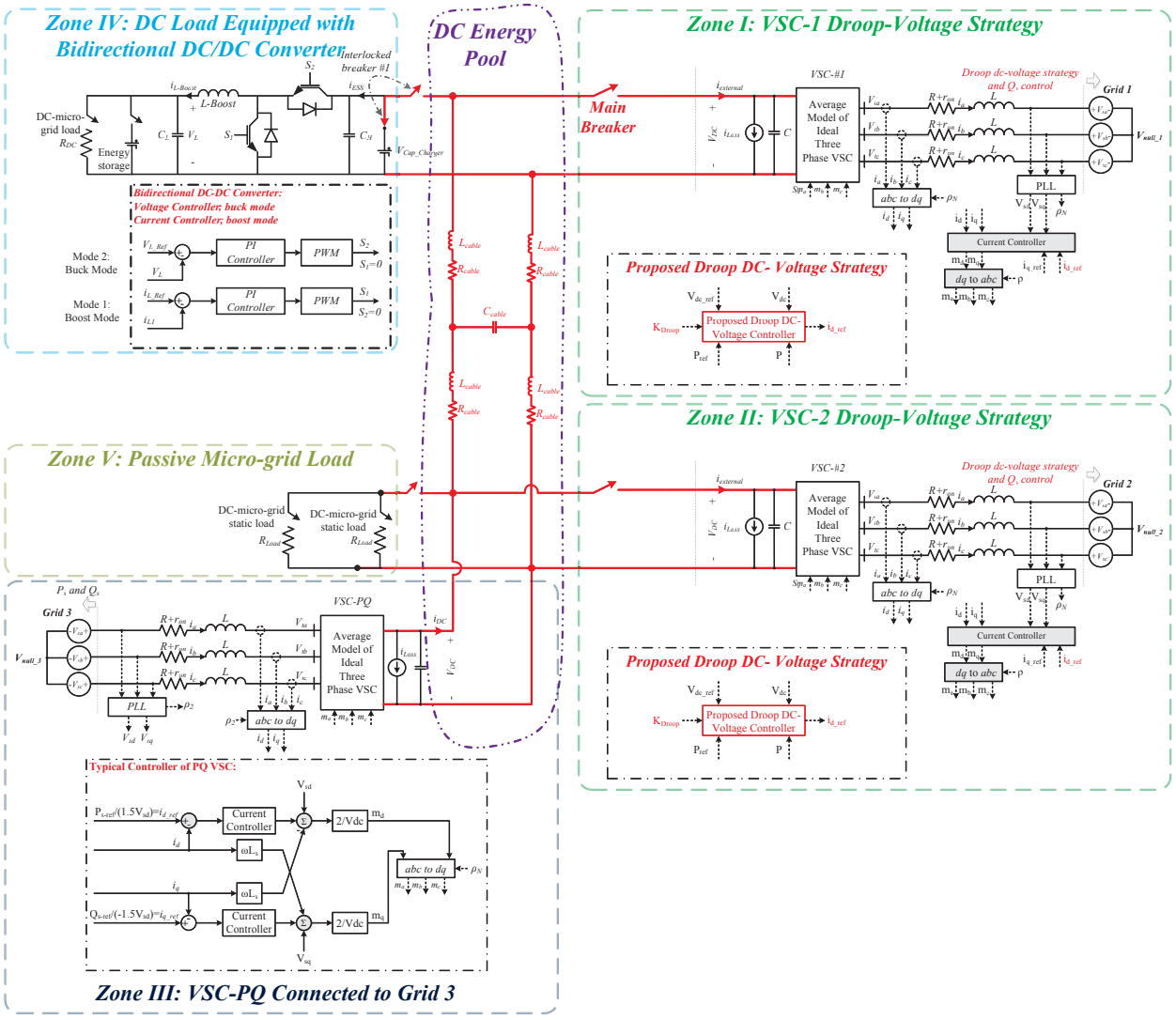

Fig. 7.16. Detailed structure of the simulated network.

Several disturbances and operational scenarios are simulated and studied. Key results are reported as follows. First, the multiterminal grid is energized and all VSCs are connected to the dc link at t=0.17 s. Initially, the droop gain of VSC-1 and VSC-2 is set to 1 V/MW, or equivalently 0.067%/MW. VSC-PQ is commanded to absorb 1.25 MW from the dc grid at t=0.2 s. Then, a 0.75 MW static resistive load, in Zone V, is connected to the dc grid at t=1.25 s. At t=2.25 s another 0.75 MW static resistive load in Zone V is connected to the dc grid. The droop gains in VSCs 1 and 2 are changed to 20 V/MW or equivalently 1.33%/MW, at t=3 s. Afterwards, VSC-PQ is commanded to absorb 2.50 MW from dc grid at t=3.2 s. The droop voltage gain is changed to 1.0 V/MW, or equivalently 0.067%/MW, and 10 V/MW, or equivalently 0.67%/MW, at t=4.0 s and t=5.0 s, respectively. Finally, at t=5.5 s the dc/dc

converter is connected to the dc grid to absorb 0.5 MW. To test the performance of the controllers under harsh disturbances, the dc/dc converter is connected to the dc grid with an initially uncharged capacitor.

Fig. 7.17 shows the system performance with the proposed controller implemented in VSCs 1 and 2 under the aforementioned simulation events. Fig. 7.17(a) shows the dc-link voltage of VSCs 1 and 2. Due to the occurrence of disturbances, transients in the dc-link voltage are generated. However, the effective disturbance rejection ability of the proposed controller limits the magnitude and duration of such disturbances. Due to the variable droop gain operation, the set point of the dc-link voltage varies. In spite of the large variation in the droop gain, e.g., from 20 V/MW to a very small value 1 V/MW that threatens the system stability with a conventional dc-link voltage controller, the proposed controller shows stable and robust control performance. Fig. 7.17(b) shows the corresponding active power response of VSCs 1 and 2. The proposed controller managed to effectively change the converter operating point to regulate the dc-link voltage without overloading the converters. Fig. 7.17(c) shows the active power response of the VSC-PQ converter. It works mainly in the inversion mode. Due to the closed dc-link voltage regulation characteristics yielded by the proposed controller, the VSC-PQ converter operates nearly under a constant dc-link voltage. It is worth mentioning that in multiterminal dc grids, the overall system stability is significantly affected by the converters regulating the dc-link voltage. Other converters demand a regulated dc-link voltage for healthy operation. Fig. 7.17(d) shows the droop voltage of VSCs 1 and 2.

Fig. 7.18 shows the system performance when a conventional PI dc-link voltage controller is used in VSCs 1 and 2 along with the outer loop droop controllers. Under static load disturbances, at t=1.25 s and t=2.25s, the PI controllers yields larger voltage dips/overshoots and larger recovery times as compared with the proposed controller. More importantly, under variable droop gain operation, the PI controller could not maintain the system stability. As predicted by the theoretical analysis, the droop feedback generates dominant eigenvalues that are close to the imaginary-axis. System stability can be easily lost under variable droop gain operation when the droop dynamics are not accounted for in the dc-link voltage control design process.

Second, a converter outage disturbance is tested. A converter outage, .e.g., due to a fault on the dc or the ac side, in a multiterminal dc grid can generate harsh transients and affect the converters operating points. Therefore, the converter controllers should offer robust performance

against such a disturbance. Initially, the droop gains of VSC-1 and VSC-2 are set to 1 V/MW, or equivalently 0.067%/MW. They are kept constant during the outage test to test the controller performance under low values of the droop gain that yield low stability margins. The VSC-PQ converter is commanded to absorb 1.25 MW from the dc grid at t=0.2 s. Then, a 0.75 MW static resistive load is connected to the grid at t=1.25 s. At t=2.0 s, VSC-2 experienced a three phase fault at its ac side, and at t=2.042 s, or equivalently 2.5 cycle after fault occurrence, VSC-2 is disconnected by opening its ac and dc breakers.

Fig. 7.19 shows the system performance with the proposed controller under the converter outage test. The dc-link voltage, shown in Fig. 7.19(a), has damped oscillations that decay in 60 ms. The minimum and maximum voltages during the outage disturbance are 0.88 and 1.02 per-unit, respectively. The active power response of VSC-1 is shown in Fig. 7.19(b). Due to the converter outage, VSC-1 supplies the dc grid load by suddenly increasing its operating power by approximately 1.2 MW in the rectification model. In spite of the large variation in the operating point and circuit transients imposed by the converter outage, the proposed controlled managed to effectively control the dc-link voltage. The active power responses of VSC-2 and VSC-PQ are shown in Fig. 7.19(c) and Fig. 7.19 (d), respectively.

Fig. 7.20 shows the system performance with the conventional PI dc-link voltage controller under the converter outage test. The system remains stable with the PI controller; however, the voltage overshoot exceeds 1.04 pu with a recovery time approximately 100 ms.

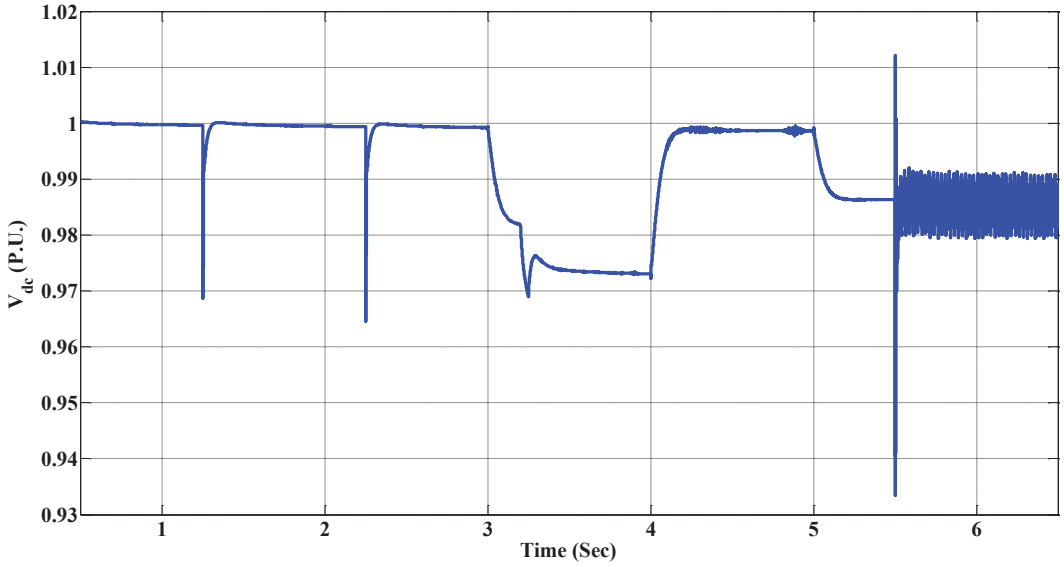
1.02
1.01
1
0.99
0.98
0.97
0.96
0.95
0.94
0.93
V_{dc} (P.U.)
1
2
3
4
5
6
Time (Sec)

(a)

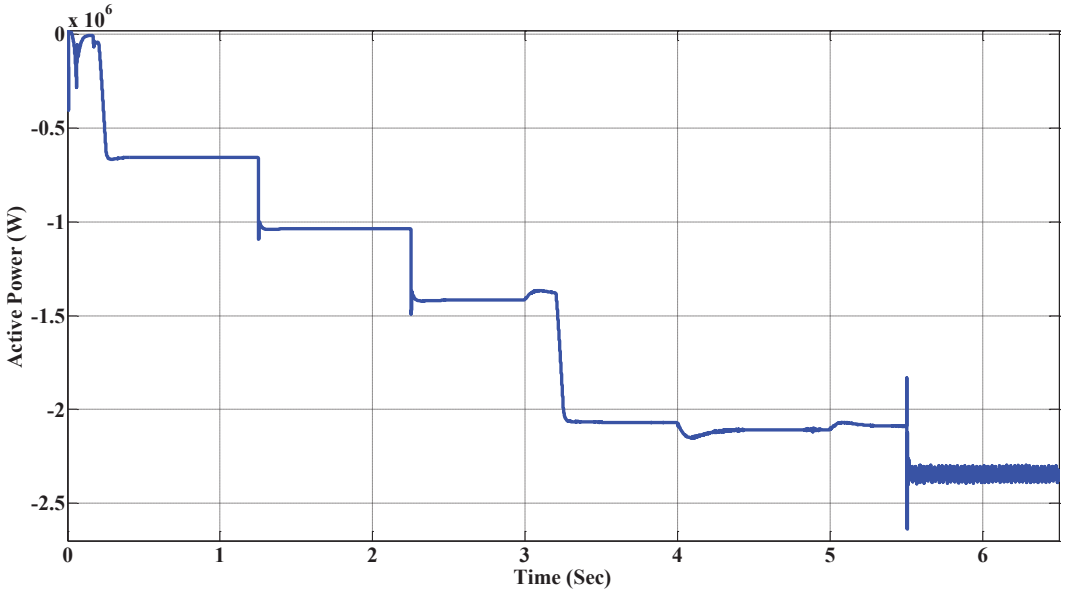
x 10^6
0
-0.5
-1
-1.5
-2
-2.5
Active Power (W)
0
1
2
3
4
5
6
Time (Sec)

(b)

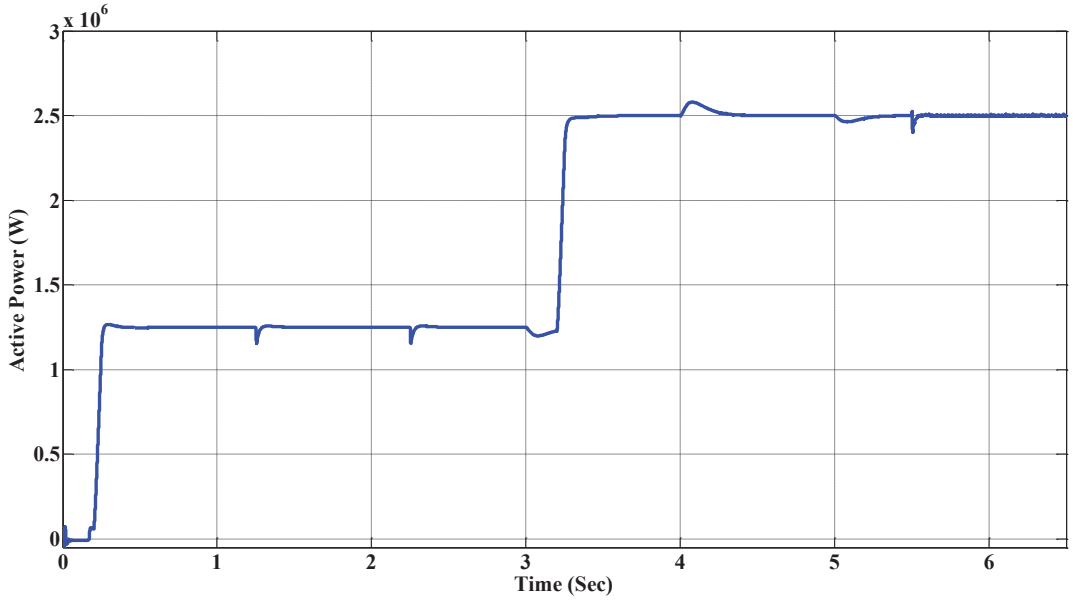

(c)

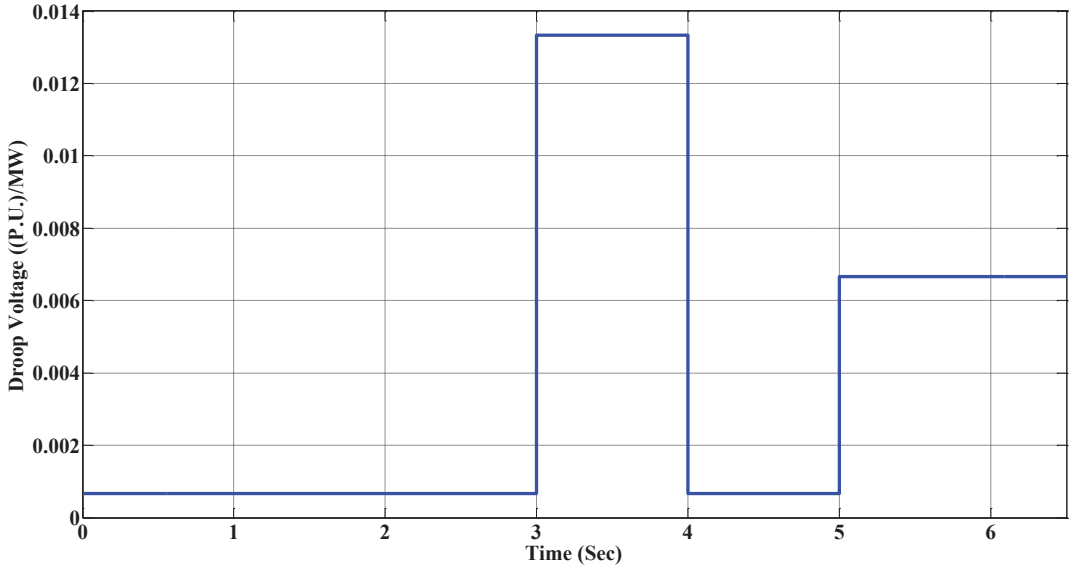

(d)

Fig. 7.17. System performance with the proposed controller. (a) DC-link voltage of VSC-1 and VSC-2, (b) Active power of VSC-1 and VSC-2, (c) Active power of VSC-PQ. (d) Droop voltage of VSC-1 and VSC-2.

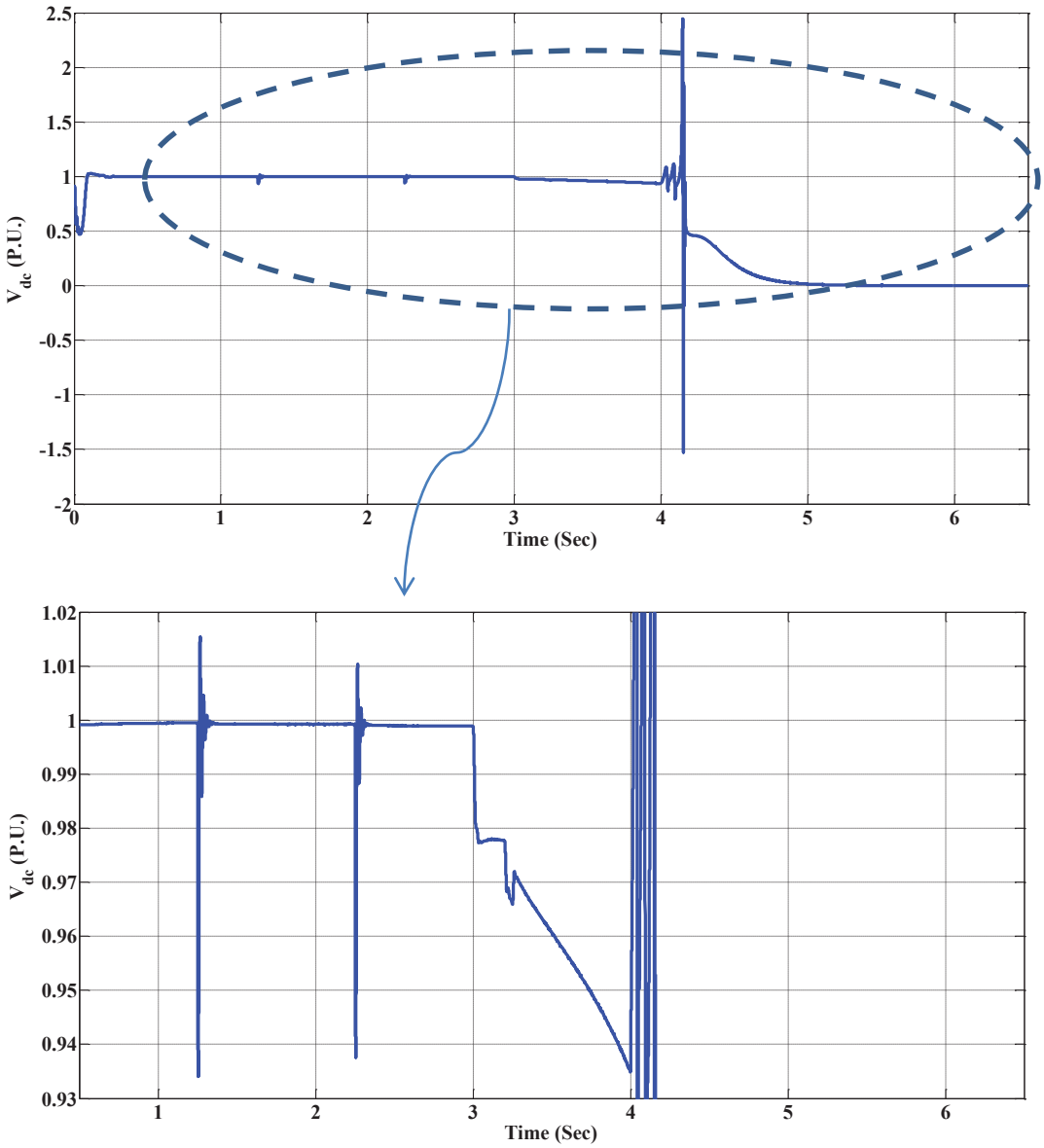

Fig. 7.18. DC-link voltage of VSC 1 and VSC 2 with the conventional PI controller.

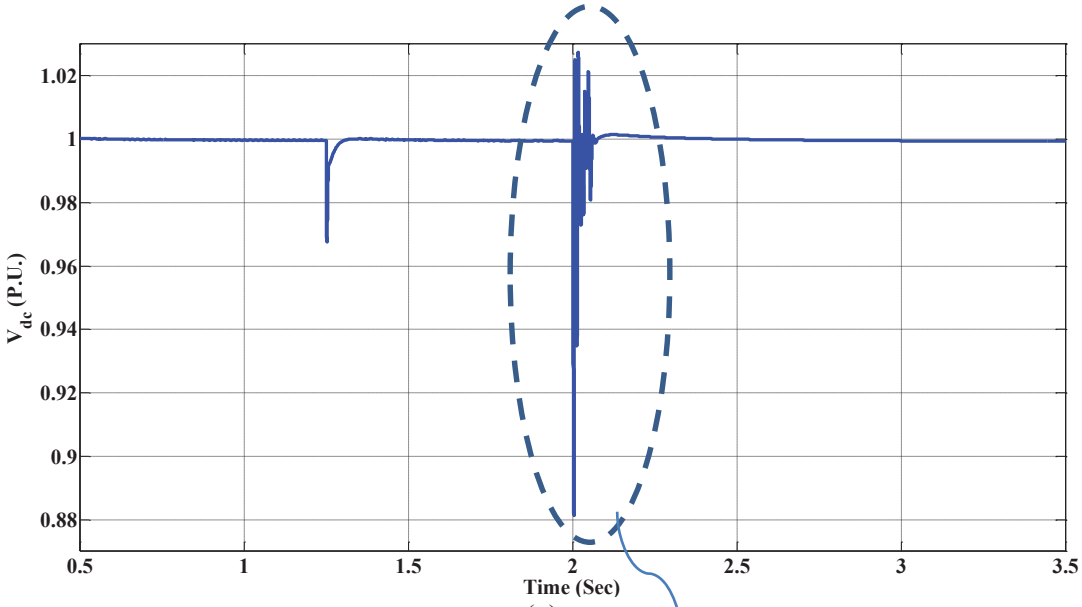
1.02
1
0.98
0.96
0.94
0.92
0.9
0.88
V_{dc} (P.U.)
0.5
1
1.5
2
2.5
3
3.5
Time (Sec)

(a)

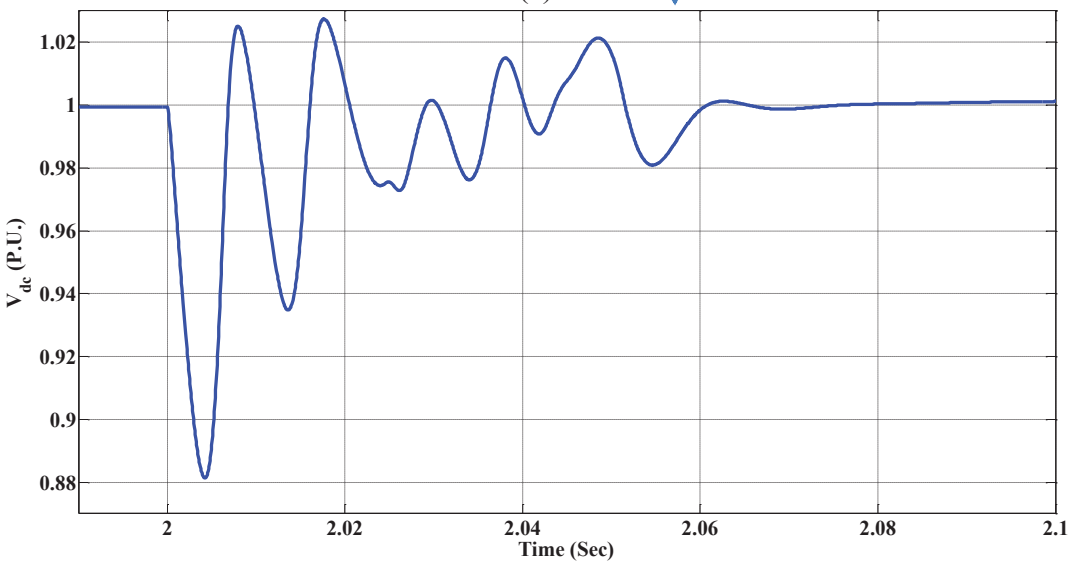
1.02
1
0.98
0.96
0.94
0.92
0.9
0.88
V_{dc} (P.U.)
2
2.02
2.04
2.06
2.08
2.1
Time (Sec)

(b)

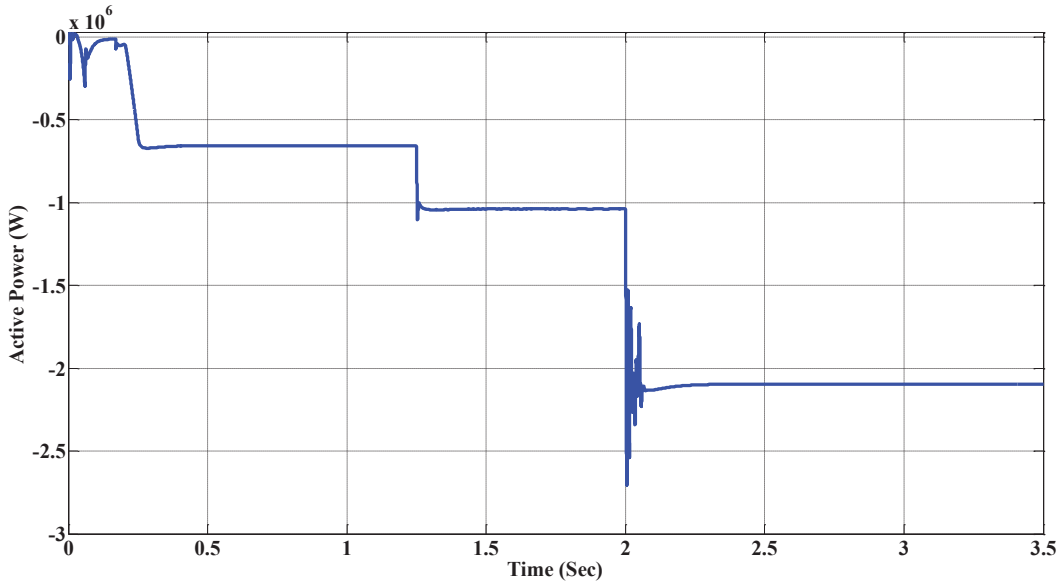
x 10^6
0
-0.5
-1
-1.5
-2
-2.5
-3
Active Power (W)
0
0.5
1
1.5
2
2.5
3
3.5
Time (Sec)

(c)

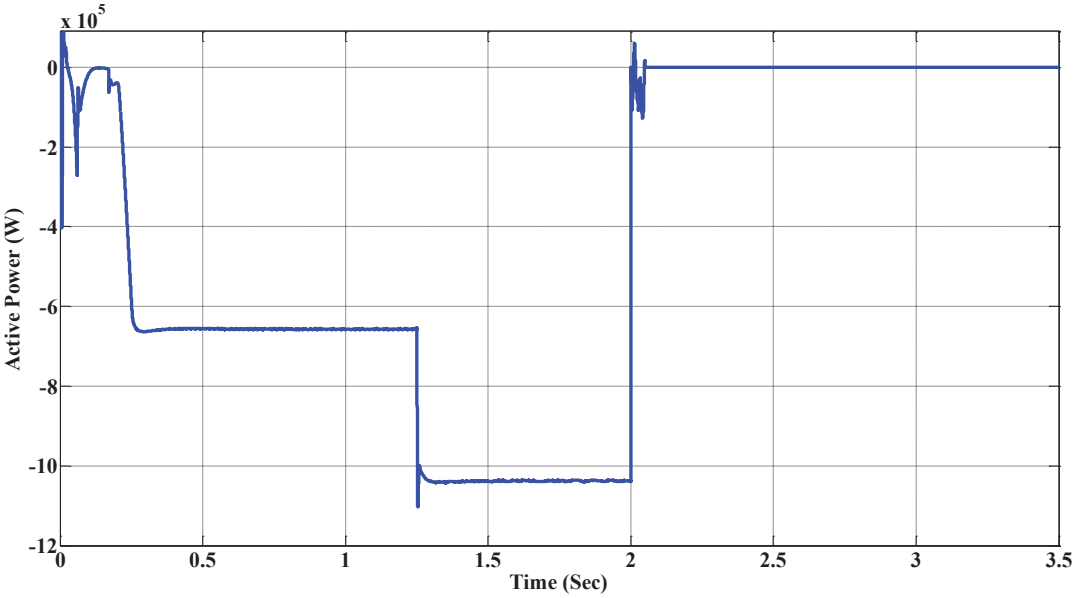
x 10^5
0
-2
-4
-6
-8
-10
-12
Active Power (W)
0
0.5
1
1.5
2
2.5
3
3.5
Time (Sec)

(d)

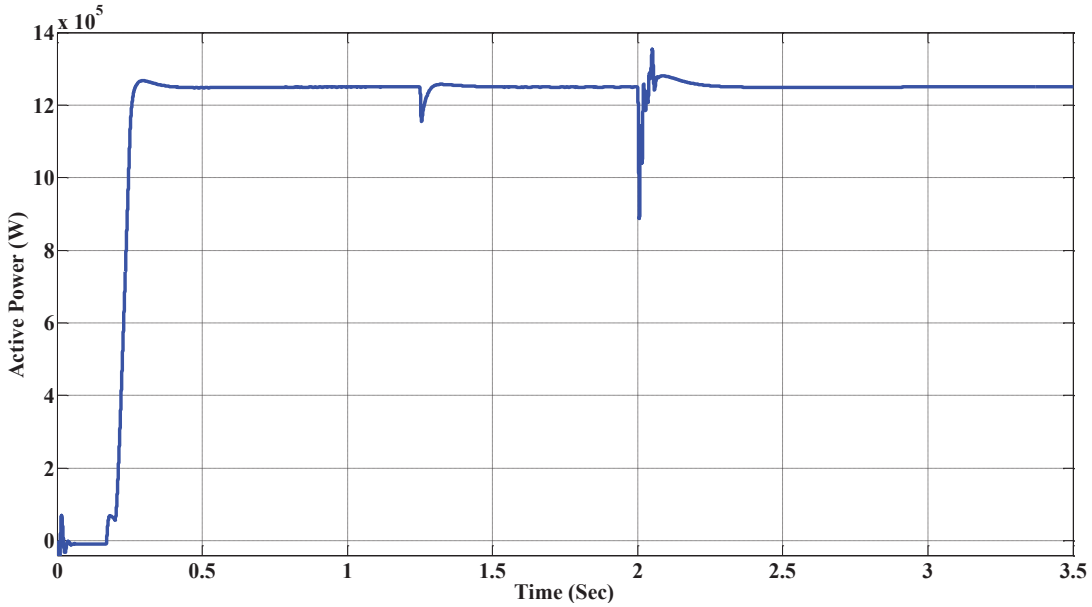

(e)

Fig. 7.19. System performance with the proposed controller under converter VSC-2 outage. (a) DC-link voltage of VSC-1, (b) Magnified view of the dc-link voltage of VSC-1, (c) Active power of VSC-1. (d) Active power of VSC-2. (e) Active power of VSC-PQ.

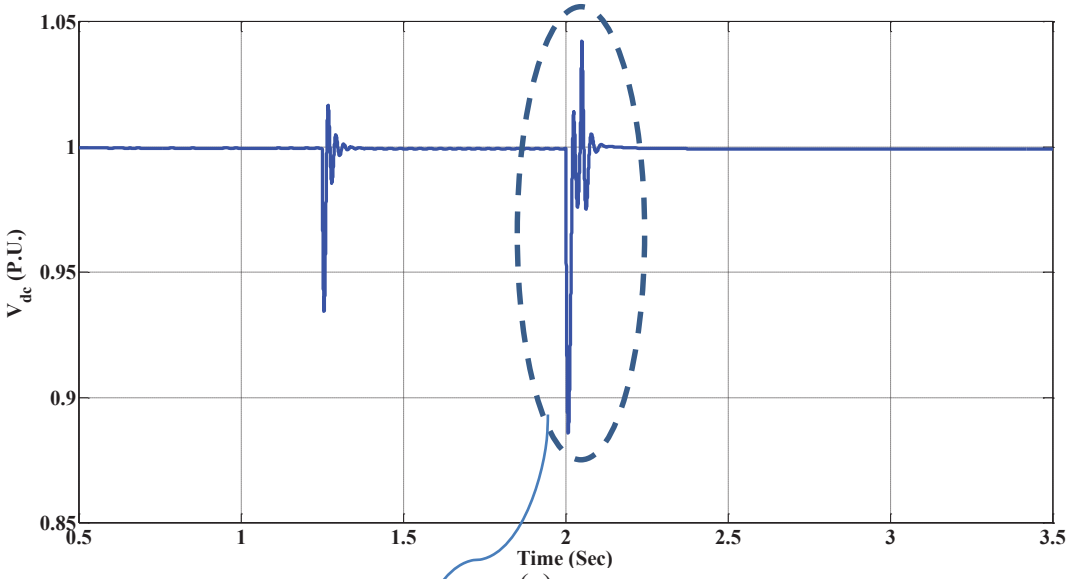

(a)

Continued in the Next Page

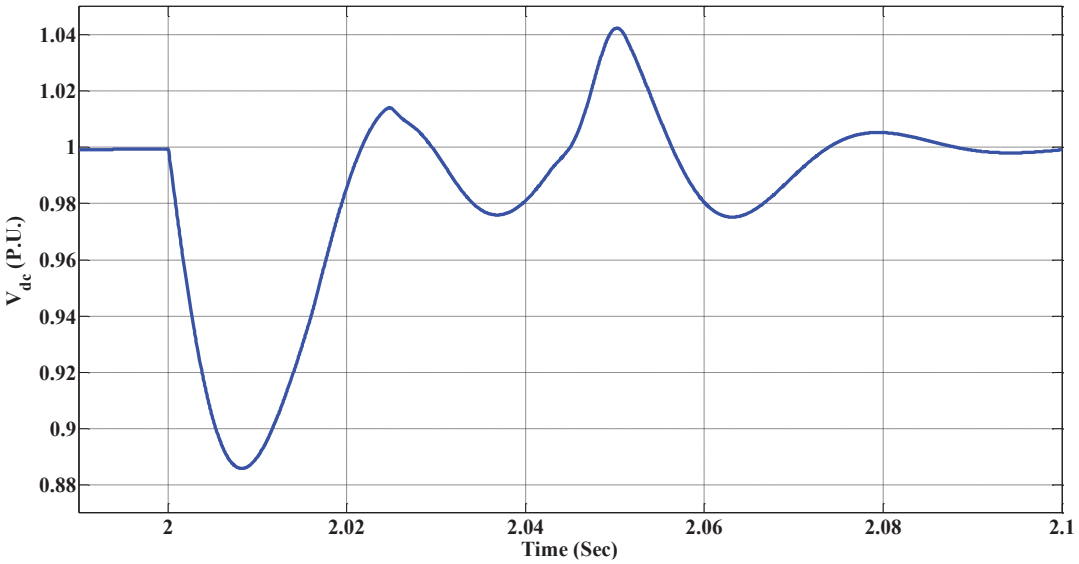

(b)

Fig. 7.20. System performance with the conventional PI controller under converter VSC-2 outage. (a) DC-link voltage of VSC-1, (b) Magnified view of the dc-link voltage of VSC-1.

7.6 Parameters of Simulated System, Fig. 7.16

Zones I and II, Grid voltage 580 V at 60 Hz, *VSC-1 and VSC-2*: Rated Power=2.5 MVA; C_{eq}=6.25 *m*F, Switch resistance=1.0 mΩ; Diode Resistance=1.0 mΩ; Current Controller: K_p=0.3 Ω; K_i=3.5 Ω/s.

Range of parameter variation and uncertainties used in the robust controller design: 1 Ω < R_{Load} < 250 Ω, 0 < K_{droop}< 20 V/MW, 6.25mF < Ceq < 18.75 mF

Zone III. VSC-PQ: Rated Power=2.5 MVA; C_{eq}=6.25 *m*F, Switch resistance=1.0 mΩ; Diode Resistance=1.0 mΩ; Current Controller: K_p=0.3 Ω; K_i=3.5 Ω/s.

Zone IV: Power Rating = 0.5 MW, load voltage 500 V-dc, C_L=1000 μF, C_H=6000 μF, L_1=100 mH, R_{DC}=0.5Ω, K_p= 0.0133, K_i= 0.0533.

Zone V. Passive Micro-grid Load: 0.75 MW (each one)

DC grid: Rated Voltage=1,500 V, dc-cable Length=10 km, R_{cable}=0.82 mΩ/km, C_{cable}= 0.014 μF/km, L_{cable}=1 μH/km

7.7 Conclusion

A robust dc-bus voltage controller for VSCs in a multiterminal dc grid governed by droop dc-voltage control has been proposed in this chapter. A detailed mathematical model of the dc-link

voltage dynamics in the presence of the droop control dynamics, the effect of the instantaneous power of the ac-side filter, and the effect of the equivalent dc grid-related uncertainties has been developed. Then, to ensure robust stability and performance under parametric uncertainties has been developed. The proposed controller has a simple structure with fixed-order and does not require any adaptation, which makes it attractive for industrial applications. Furthermore, it provides excellent performance in rejecting wide range of system uncertainties and disturbances without a priori knowledge of the dc grid components and dynamics. These features positively contribute to the stability and robustness enhancements of multiterminal grids. A mathematical analysis and simulation results have validated the effectiveness of the proposed controller.

Chapter 8

Conclusions and Future Work

In this chapter, the main findings of the thesis are summarized, and suggestions for future work are presented.

8.1 Thesis Conclusions and Contributions

The electric energy sector is moving toward extensive integration of renewable and clean energy resources, energy storage units, and modern loads via highly efficient and flexible multiterminal dc grids integrated within the traditional ac grid infrastructure. A VSC is the major technology enabling the interconnection of dc and ac grids. In this thesis, dynamics, robust control, and power management of VSCs in hybrid multiterminal ac/dc grids are comprehensively addressed.

In Chapter 2, a robust controller with a simple fixed-parameter low-order structure has been proposed for the dc-energy-pool-based ac/dc multiterminal micro-grids. The salient features of the proposed controller are: 1) robust disturbance rejection performance under wide range of large and fast dynamic changes in the converter operating points and large-signal disturbances (e.g., power reversal at rated and over-load (contingency) conditions; low-impedance unsymmetrical fault conditions; and connection/disconnection of loads/sources in the dc-energy pool); 2) the controller eliminates the need of using external power disturbance feed-forward control, which improves the reliability and cost measures by creating a dc-power (or dc-current) sensor-less robust disturbance rejection controller; 3) robust control performance under possible variation in the equivalent dc-link capacitance due to connection/disconnection of dc loads and/or sources in the dc-energy pool; and 4) simple fixed-parameter low-order linear control structure with robust performance in spite of the highly nonlinear dc-link voltage control dynamics. With these features, the proposed controller remarkably contributes to the stability and reliability of multiterminal ac/dc networks. A theoretical analysis and comparative simulation and experimental results have shown the robustness and effectiveness of the proposed controller.

In Chapter 3, dynamics and control of VSCs considering the instantaneous power of both ac-side filter and uncertain dc-side inductor have been addressed. Uncertainty in the dc-side component parameters, including filter capacitance and dc-side inductance, affects the stability and performance of the converter owing to connecting/disconnecting electric devices to/from the dc grid. Furthermore, small-signal dynamic analysis has shown that the dc-link voltage dynamics are highly dependent on the converter operating point. When operating point variation is combined with possible parametric uncertainties, unstable open-loop dynamics along with non-minimum phase behavior can be easily generated in grid-connected converters. To overcome those difficulties, Chapter 3 has presented a robust optimal dc-link voltage controller is designed. The proposed controller has yielded excellent tracking performance, robust disturbance rejection, and robust performance against operating point and parameter variation with a simple fixed-parameter controller. Comparative simulation studies and experimental results have validated the theoretical results and demonstrated the effectiveness of the proposed control structure.

In Chapter 4, a dc-link voltage controller has been designed based on the average nonlinear dynamics of the master VSC employed in multiterminal dc grids, and the control efforts have been synthesized using general switching functions. Consequently, the synthesized controller has not suffered from small-signal control design issues, and the global stability has been guaranteed. Besides, the conventional power-balance and cascaded control-structure has been avoided; therefore, unmodeled nonlinear dynamics associated with a power balance framework and presence of inner loop current controller has inherently been mitigated. The controller has been synthesized using passivity-based criteria, and it has been implemented via sigma-delta modulation to induce sliding regiment required for the variable structure nature of the VSC. As a result, the existing equilibrium-to-equilibrium maneuver of the proposed controller can handle the dependency of the controlled dynamics on the operating point variation. Finally, the global stability has been guaranteed using the simultaneous convergence of all states, including V_{dc}, to their equilibrium points. The performance of the proposed controller has also been compared with a PI-lead controller under the same test conditions. The proposed controller provides excellent tracking and disturbance rejection performances, and it offers very effective fault-ride-thorough performance against ac- as well as dc-side faults. These features remarkably enhance the reliability of the dc-link voltage which is essential to stabilize the performance of multiterminal ac/dc grids. Besides, simulation and experimental results have been provided to

verify the validity and effectiveness of the proposed controller.

In Chapter 5, a robust vector-controlled VSC that facilitates full converter power injection at weak and very weak grid conditions has been developed. To realize the controller, firstly, a detailed dynamic model for the ac-bus voltage dynamics, including the PLL dynamics, has been developed and validated in Chapter 5. Secondly, the model has been used to optimally design a robust ac-bus voltage controller to stabilize the dynamics under operating point variation and grid impedance uncertainty. A theoretical analysis and comparative simulation and experimental results have shown the effectiveness of the proposed controller. The proposed controller has the following characteristics.

1) Because the developed model includes the PLL dynamics, the developed controller inherently stabilizes the negative impact of the PLL on the converter stability.
2) By the proposed approach, the need to change the structure and/or the parameters of the standard vector controllers (e.g., current controller, PLL, and dc-link voltage controller) to facilitate very weak grid integration is eliminated.
3) The controller gives a robust control performance against operation point variation and uncertainties in the grid inductance.
4) The controller has a systematic design approach and simple fixed-order structure; therefore, it can be easily implemented in commercial-grade digital signal processors.

In Chapter 6, a robust parallel distributed controller has been proposed for a dc-link-voltage controlled full-scale wind turbine in a dc grid. The controller offers the following characteristics. 1) Robust performance against large variation in the operating point associated with variation of the wind turbine characteristic curve which is affected by pitch angle, wind speed, and control lever itself (i.e., the rotational speed of the PMSG. 2) Robust performance against static as well as dynamic load variation (e.g., power converters or dc machines connected to the dc-link. 3) The effective rejection of disturbances associated with dynamic load variations as well as wind speed changes to enhance the performance of the closed-loop system. Furthermore, because the control lever is not affected by power changes in the ac sides of other VSCs connected to the dc grid, the dc voltage dynamics is not affected by the unsymmetrical condition (e.g., faults or unbalance) in the ac grids of other VSCs connected to the dc grid. Therefore, the controller enhances the reliability and performance of dc grids and provides excellent fault-ride-through performance.

In Chapter 7, a robust dc-bus voltage controller for VSCs in a multiterminal dc grid governed by droop dc-voltage control has been proposed. A detailed mathematical model of the dc-link voltage dynamics in the presence of the droop control dynamics, the effect of the instantaneous power of the ac-side filter, and the effect of the equivalent dc grid-related uncertainties has been developed. Then, to ensure robust stability and performance under parametric uncertainties has been developed. The proposed controller has a simple structure with fixed-order and does not require any adaptation, which makes it attractive for industrial applications. Furthermore, it provides excellent performance in rejecting wide range of system uncertainties and disturbances without a prior knowledge of the dc grid components and dynamics. These features positively contribute to the stability and robustness enhancements of multiterminal grids. A mathematical analysis and simulation results have validated the effectiveness of the proposed controller.

8.2 Suggestions for Future Work

The following research directions can be followed as an extension out of this thesis:

1) Extending the applicability of the developed controllers to MTDC grids with synchronous machines.
2) Developing energy management controllers to optimize the economic aspects of MTDC grids operation.
3) Investigating the integration of other renewable resources, such as photovoltaic farms, into dc grids.

Bibliography

[1] *The War of the Currents: AC vs. DC Power*, US De partment of Energy website: http://energy.gov/articles/war-currents-ac-vs-dc-power.

[2] R. Rudervall, J.P. Charpentier and R. Sharma, "High Voltage Direct Current (HVDC)Transmission Systems Technology Review Paper," *Energy Week 2000, Washington, D.C, USA, March 7-8, 2000.*

[3] N.G. Hingorani, "High Voltage DC Transmission: A powe r electronics workhorse," *IEEE Spectrum,* pp. 63-72, April 1996.

[4] E. M. Lightner and S. E. Widergren, "An Orderly Transition to a Transf ormed Electricity System," *IEEE Trans. Smart Grids*, vol. 1, pp. 3-10, June 2010.

[5] P. Fairley, "Germany jump-starts the super grid," *IEEE Spectrum*, vol. 50, pp. 3 6-41, May 2013.

[6] P. Wang, L. Goel, X. Liu, and F.H. Choo, "Harmonizing AC and DC: A Hybrid AC/DC Future Grid Solution," *IEEE Power and Energy Magazine*, vol. 11, pp. 76-83, April 2013.

[7] Philips company News Center, "Empire State Building gives gift to New York City – and the world – with its first-ever LED Tower Light Show fe aturing Alicia Keys," [Online]. Available: http://www.newscenter.philips.com/us_en/standard/news/press/2012/20121127-Empire-State-Building.wpd#.UYb9BLXvuCn, November 2012.

[8] S. Moon, G.- B. Koo, and G.-W. Moon, "A New Control Method of Interleaved Single-Stage Flyback AC–DC Converter for Outdoor LED Lighting Systems," *IEEE Trans. Power Electronics*, vol. 28, pp. 4051-4062, August 2013.

[9] C. K. Lee, S. Li, and S. Y. (Ron) Hui, " A Design Methodology for Smart LED Lighting Systems Powered By Weakly Regulated Renewable Power Grids," *IEEE Trans. Smart Grids*, vol. 2, pp. 548-554, September 2011.

[10] Y. Kheng Tan, T. Phuong Huynh, and Z. Wang, "Smart Personal Sensor Network Control for Energy Saving in DC Grid Powered LED Lighting System," *IEEE Trans. Smart Grids*, vol. 4, pp. 669-676, June 2013.

[11] J. Dong, A. Pandharipande, W. van Driel, and G. Zhang, "Diagnosing Lumen Depreciation in LED Lighting Systems: An Estimation Approach," *IEEE Trans. Signal Processing*, vol. 60, pp. 3796-3808, July 2012.

[12] A. Radwan and Y. A-R I. Mohamed, "Linear Active Stabilization of Converter-Dominated DC Microgrids," *IEEE Trans. Smart Grids*, vol. 3, pp. 203-216, March 2012.

[13] A. Kwasinski and C. N. Onwuchekwa, "Dynamic behavior and stab ilization of DC microgrids with instantaneous constant-power loads," *IEEE Trans. Power Electronics*, vol. 26, pp. 822-834, March 2011.

[14] A. Kwasinski, "Quantitative evaluation of DC microgrids availability: Effects of system architecture and converter topology design choices," *IEEE Trans. Power Electronics*, vol. 26, pp. 835-851, March 2011.

[15] R. S. Balog, W. W. Weaver, and P. T. Krein, "The load as an en ergy asset in a dist ributed DC smartGrid architecture," *IEEE Trans. Smart Grids*, vol. 3, pp. 253-260, March 2012.

[16] R. S. B alog and P. T. Krein, "Bus selection in multibus DC microgr ids," *IEEE Trans. Power Electronics*, vol. 26, pp. 860-867, March 2011.

[17] D. Chen and L. Xu, "Autonomous DC voltag e control of a DC microgrid with mult iple slack terminals," *IEEE Trans. Power Systems*, vol. 27, pp. 1897-1905, November 2012.

[18] H. Kakigano, Y. Miura, and T. Ise, "Configuration and Control of a DC Microg rid for Residential Houses," in *Proc. IEEE Transmission & Distribution Conference & Exposition: Asia and Pacific*, 2009, pp. 1-4.

[19] H. Kakigano, Y. Miura, T. Ise, and R. Uc hida, "DC micro-grid for super hig h quality distribution-system configuration and control of distributed generations and energy storage devices," in *Proc. 37th IEEE Power Electronics Specialists Conference* (*PESC*), 2006, pp. 1-7.

[20] H. Kakigano, Y. Miura, T. Ise, and R. Uchida, "DC voltage control of the DC micro -grid for super high quality distribution," in *Proc. Power Conversion Conference* (*PCC*), 2007, pp. 518-525.

[21] J. Lee, B. Han, and N. Choi, "DC micro-grid operational analysis with detailed simulation model for distributed generation," in *Proc. IEEE Energy Conversion Congress and Exposition* (*ECCE*), 2010, pp. 3153-3160.

[22] X. She, S. L ukic, and A. Q.Huan g, "DC zonal micro-grid architecture and control ," in *Proc. IEEE 36th Annual Conference on Industrial Electronics Society* (*IECON*), 2010, pp. 2988-2993.

[23] Y. Zhu, Z. Yin, and J. Tian, "Microgrids-based on DC-energy pool," in *Proc. IEEE Energy 2030 Conference*, 2008, pp. 1-2.

[24] M. Saeedifard, M. Graovac, R.F. Dias, and R. Iravani, "DC power systems: challenges and opportunities," in *Proc. IEEE Power and Energy Society General Meeting*, 2010, pp. 1-7.

[25] K. Shenai and K. Shah, "Smart DC micro- grid for efficient utilization of distributed renewable energy," in *Proc. IEEE Energytech*, 2011, pp. 1-6.

[26] Christian M. F ranck, "HVDC Circuit B reakers: A Review Identifying Future Research Needs," *IEEE Trans. Power Delivery*, vol. 26, no. 2, April 2011, pp. 998-1007.

[27] A. Radwan and Y. A.-R. I. Mohamed, "Assessment and mitigation of interaction dynamics in hybrid AC/DC distributed generation networks," *IEEE Transactions on Smart Grid*, vol. 3, no. 3, pp. 1382 – 1393, 2012.

[28] X. Liu, P. W ang, and P. Chiang Loh, "A hybrid AC/DC microgrid and its coordination control," *IEEE Trans. Smart Grids*, vol. 2, pp. 278-286, June 2012.

[29] Y. Zhu, J. Tian, and Z. Yin, "AC & DC hy brid supplying system with distribu ted generation based on energy pool," in *Proc. International Conference on Sustainable Power Generation and Supply* (*SUPERGEN*), 2009, pp. 1-3.

[30] A. Yazdani and R. I ravani, *Voltage-Sourced Converters in Power Systems*, 1st ed., John Wiley & Sons, 2010.

[31] A. Yazdani and R . Iravani, "An a ccurate model for the DC -side voltage control of the neutral point diode clamped converter," *IEEE Trans. Power Del.*, vol. 21, pp. 185-193, Jan. 2006.

[32] *1321 Power Conditioning Products*, Publication 1321-TD001O-EN-P, Technical Data by Rockwell Automation, pp. 1 -26, September 2012. [Online] Available: http://literature.rockwellautomation.com/idc/groups/literature/documents/td/1321-td001_-en-p.pdf

[33] J. Dai, S. Woo Nam, M. Pande, G. Esmae ili, "Medium Voltage Current S ource Converter Drives for Marine Propulsion System using a Dual-winding Synchronous Machine," *IEEE*

Transactions on Industry Applications, to be published , [Online]. Available: http://ieeexplore.ieee.org/stamp/stamp.jsp?tp=&arnumber=6786332

[34] D. Jovcic and W. Lin, "Multiport High-Power LCL DC Hub for Use in DC Transmission Grids," *IEEE Transactions on Power Delivery*, vol. 29, no. 2, pp. 760-768, April 2014.

[35] F. Zheng Peng, "Z-Source Inverter," *IEEE Transactions on Industry Applications*, vol. 39, no. 2, pp. 504-510, March/April 2003.

[36] M. P. Kazmierkowski and L. Malesani, " Current Control Techniques for Three-Phase Voltage-Source PWM Converters: A Survey," *IEEE Trans. Industrial Electronics*, vol. 45, pp. 691-703, Oct. 1998.

[37] M. Karimi-Ghartemani, S. A. Khajehoddin, P. Jain, and A. Bakhshai, "A Systematic Approach to DC -Bus Control Design in Single-Phase Grid-Connected Renewable Converters," *IEEE Trans. Power electronics*, vol.28, no.7, pp. 3158,3166, July 2013.

[38] L. Zhang, L. Harnefors, and H.-P. Nee, "Power-synchronization control of grid-connected voltage-source converters," *IEEE Trans. Power Syst.*, vol. 25, no. 2, pp. 809-820, May 2010.

[39] P. Mitra, L. Zhang, L. Harnefors, "Offshore wind integration to a weak grid by VSC-HVDC links using power-synchronization control: A case study," *IEEE Trans. Power Del.,* vol.29, no.1, pp.453-461, Feb. 2014.

[40] N.P.W. Strachan, D. Jovcic, "Stability of a variable-speed permanent magnet wind generator with weak AC grids," *IEEE Trans. Power Del.*, vol.25, no.4, pp.2779-2788, Oct. 2010.

[41] J. Zhou, D. Hui, S. Fan, Y. Zhang, and A. M. Gole, "Impact of short-circuit ratio and phase-locked-loop parameters on the small-signal behavior of a VSC-HVDC converter," *IEEE Trans. Power Del.*, vol.29, no.5, pp.2287-2296, Oct. 2014.

[42] A. E.-Alvarez, S. Fekriasl, F. Hassan, and O. G.-Bellmunt, "Advanced vector control for voltage source converters connected to weak grids," *IEEE Trans. Power Syst.*, vol. 30, no. 6, pp. 3072-3081, Nov. 2015.

[43] D. Dong, B. Wen, D. Boroyevich, P. Mattavelli, and Y. Xue, "Analysis of phase-locked loop low-frequency stability in three-phase grid-connected power converters considering impedance interactions," *IEEE Trans. Ind. Electron.*, vol. 62, no. 1, pp. 310-321, Jan. 2015.

[44] Y. Huang, X. Yuan, J. Hu, P. Zhou, “Modeling of VSC connected to weak grid for stability analysis of DC-link voltage control,” *IEEE J. Emerg. Sel. Topics Power Electron*., in press, available online on IEEE Xplore.

[45] M. Durrant, H. Werner, and K. Abbott, “Model of a VSC HVDC terminal attached to a weak ac system,” in *Proc. IEEE Conf. Control Applications*, vol. 1, p p. 178-182, June 2003.

[46] L. Zhang, L. Harnefors, and H.-P. Nee, “Interconnection of two very weak ac systems by VSC-HVDC links using power-synchronization control,” *IEEE Trans. Power Syst.*, vol. 26, no. 1, pp. 344-355, Feb. 2011.

[47] L. Harnefors, M. Bongiorno, S. Lundberg, "Input-Admittance Calculation and Shaping for Controlled Voltage-Source Converters," *IEEE Trans. Ind. Electron.*, vol.54, no.6, pp. 3323-3334, Dec. 2007.

[48] D.-W. Gu, P. Hr. Petkov and M. M. Konstantino v, *Robust Control Design with MATLAB*, Springer, 2005.

[49] D.R. Wilburn, "Wind Energy in the United Stat es and M aterials Required for the Land-based Wind Turbine Industry from 2010 through 2030," U.S. Geological Survey Scientific Investigations Report.

[50] F. Blaabjerg,, M. Liserre, and Ke Ma, "Power Electronics Converters for Wind Turbine Systems," *IEEE Trans. Ind. Applicat.*,vol.48, no.2, pp.708, 2012

[51] X. Yuan, et. al., "DC-link Voltage Control of a Full Power Converter for Wind Generator Operating in Weak-Grid Systems," IEEE Trans. Power Electron, vol. 24, pp. 2178-2192, September 2009.

[52] K.-H. Kim, Y.-C. J eung, D.-C. Lee, and H.- G. Kim, "L VRT Scheme of PMSG Win d Power Systems Based on Feedback Linearization," *IEEE Trans. Power Electron*., vol. 27, pp. 2376-2384, May 2012.

[53] E. Prieto-Araujo, F. D. Bianchi, A. Junyent-Ferré, and O. Gomis-Bellmunt, "Methodology for Droop Control D ynamic Analysis of Mult iterminal VSC-HVDC Grids for Offshore Wind Farms," *IEEE Trans. Power Delivery*, vol. 26, pp. 2476-2485, October 2011.

[54] D. Jovcic, "Interconnecting offshore wind farms using multiterminal VSC-based HVDC," *Power Engineering Society General Meeting*, 2006. IEEE, 2006

[55] T. M. Haileselassie and K. Uhlen, " Precise control of power flow in multiterminal VSC-HVDCs using DC voltage droop control," *Power and Energy Society General Meeting*, 2012 IEEE, 2012, pp. 1-9.

[56] R. T. Pinto, et al., " Comparison of direct voltage control methods of multiterminal DC (MTDC) networks through modular dynamic models," *Power Electronics and Applications* (EPE 2011), Proceedings of the 2011-14th European Conference on, 2011, pp. 1-10.

[57] T. K. Vrana, et al., " A Classification of DC Node Voltage Control Methods for HVDC Grids," *Electric Power Systems Research*, 2012.

[58] D. Van Hertem and M. Ghandhari, "Multiterminal VSC HVDC for the European supergrid: Obstacles," *Renewable and sustainable energy reviews*, vol. 14, pp. 3156-3163, 2010.

[59] C. Gavriluta, I. Candela, A. Luna, A. Gomez-Exposito, and P. Rodriguez, "Hierarchical control of HV-MTDC systems with droop-based primary and OPF-based secondary," *IEEE Trans. Smart Grid*., vol.6, no.3, pp.1502-1510, May 2015.

[60] K. Rouzbehi, A. Miranian, A. Luna, and P. Rodriguez, "DC voltage control and power sharing in multiterminal DC grids based on optimal DC power flow and voltage-droop strategy," *IEEE Journal of Emerging and Selected Topics in Power Electronics*, vol.2, no.4, pp.1171-1180, Dec. 2014.

[61] N. Chaudhuri, and B. Chaudhuri, "Adaptive droop control for effective power sharing in multiterminal dc (MTDC) grids," *IEEE Trans. Power Systems*, vol.28, no.1, pp.21-29, Feb. 2013.

[62] J. Xiao, L. Setyawan, P. Wang, and C. Jin, "Power-capacity-based bus-voltage region partition and online droop coefficient tuning for real-time operation of dc microgrids," *IEEE Trans. Energy Convers*., in press, available online.

[63] M. Davari and Y. A.-R. I. Mohamed, "Robust Multi-Objective Control of VSC-Based DC-Voltage Power Port in Hybrid AC/DC Multiterminal Microgrids," *IEEE Trans. Smart Grids*, vol. 4, pp. 1597-1612, September 2013.

[64] M. Davari and Y. A.-R. I. Mohamed, "Variable-Structure-Based Nonlinear Control for the Master VSC in DC -Energy-Pool Multiterminal Grids," *IEEE Trans. Power Electronics*, vol. 29, pp. 6196 - 6213, November 2014.

[65] J. Blau, "Europe plans a north sea grid," *IEEE Spectrum*, vol. 47, no.3, pp. 12–13, 2010.

[66] T.M. Haileselassie and K. Uhlen, "Power System Security in a Meshed North Sea HVDC Grid," *Proceedings of the IEEE*, vol. 101, issue: 4, pp. 978 – 990, April 2013.

[67] IEEE Standards Association (IEEE-SA), "A Call for Participation: IEEE Plan for DC in the Home," [Online]. Available: http://standards.ieee.org/email/2013_10_cfp_dchome_web.html, November 2013.

[68] Jean-Jacques E. Slotine and W eiping Li, *Applied Nonlinear Control*, Prentice Hall, NJ, 1991.

[69] K. S. Na rendra and J. Balakrishnan, "Adaptive Control Using Multiple Models," *IEEE Trans. Automatic Control*, vol. 42, no. 2, pp. 171-187, Feb. 1997.

[70] Zhou, J.Z.; Ding, H.; F an, S.; Z hang, Y.; Gole, AM., "I mpact of Short -Circuit Ratio and Phase-Locked-Loop Parameters on the Small -Signal Behavior of a VSC-HVDC Converter," *IEEE Trans. Power Delivery*, vol. 29, pp. 2287-2296, October 2014.

[71] D.R. Wilburn, "Wind Energy in the United Stat es and M aterials Required for the Land-based Wind Turbine Industry from 2010 throu gh 2030," *U.S. Geological Survey Scientific Investigations Report* [Online]. Available: http://pubs.usgs.gov/sir/2011/5036, pp. 1-22, June 2011.

[72] X. Yang, Y. Song , G. Wang, and W . Wang, "A Comprehensive Review on the Development of Sustainable Energy Strategy and Implementation in China," *IEEE Trans. Sustainable Energy*, vol. 1, pp. 57-65, July 2010.

[73] F. D. Kanellos and N. D . Hatziargyriou, "The Effect of Variable-Speed Wind Turbines on the Operation of W eak Distribution Ne tworks," *IEEE Trans. Energy Conversion*, vol. 17, pp. 543-548, December 2002.

[74] R. Biernatzki, J. Bechthold, and W. Stauss, "Small Wind Turbines Applie d to Rural Areas for Independent Power Supply," in *Proc. Universities Power Engineering Conference (UPEC)*, *47th International Conference*, 2012, pp. 1-4.

[75] D. L. Hoffman and T. S. Molinski, " How New Technology Developments Will Lower Wind Energy Costs," in Proc . *CIGRE/IEEE PES Joint Symposium of Integration of Wide-Scale Renewable Resources Into the Power Delivery System*, 2009. pp. 1-6.

[76] K. Sunderland and M. F. Conlon, " Estimating the Yield of Micro W ind Turbines in an Urban Environment: *A Methodolog*," in *Proc. Universities Power Engineering Conference (UPEC)*, *45th International Conference*, 2010, pp. 1-6.

[77] K. Nigim, F. Ahmed, H. Reiser, O. Ramahi, and A. Mous a, "Strategies for Rapid Development of Renewable Energy Technologies Infrastructures," in *Proc. IEEE International Energy Conference and Exhibition (EnergyCon),* 2010, pp. 652-657.

[78] Z. Litifu and K. Nagasaka, "A Research on Planning and Installing Scattered Power into a Local Power System," in *Proc. International Conference on Advanced Mechatronic Systems*, 2012, pp. 54-59.

[79] M. Treuer, T. Weissbach, a nd V. Ha genmeyer, "Flatness-based feed-forward in a two-degree-of-freedom control of a pumped storage power plant," *IEEE Trans. Control Systems Technology*, vol. 19, pp. 1540-1548, Nov. 2011.

[80] G. C. Goodwin, S. F . Graebe, and M. E. Salg ado, *Control System Design*, Prentice Hall, 2000.

[81] J. C. Do yle, B. A. Francis, and A. R. Tannenbaum, "Uncertainty and Robustness," in *Feedback Control Theory*, Macmillan Publishing Company, 1992, ch. 4, pp. 45-62.

[82] MATLAB R2012a Documentation, Robust Control Toolbox, "Robust controller design using μ-synthesis," MathWorks. [Online]. Available: http://www.mathworks.com/help/toolbox/robust/ref/dksyn.html

[83] MATLAB R2012a Do cumentation, Robust Con trol Toolbox, "Application of H_∞ and Mu to Active Suspension Control," MathWorks. [Online]. Available: http://www.mathworks.com/help/toolbox/robust/gs/f6-44171.html

[84] D.-W. Gu, P. Hr. Petkov and M. M. Konstantino v, *Robust Control Design with MATLAB*, Springer, 2005.

[85] W. Zhang, Y. Hou, X. Liu, and Y. Z hou, "Switched control of thre e-phase voltage source PWM rectifier under a wide range rapidly varying active load," *IEEE Trans. Power electronics*, vol. 27, pp. 881-890, Feb. 2012.

[86] D. Henrion, M. ˇSebek, and V. Kuˇcera, "Positive polynomials and robust stabilization with fixed-order controllers," *IEEE Trans. Automatic Control*, vol. 48, pp. 1178-1186, July. 2003.

[87] S. P. Bhattacharyya, H. Chapellat, L. H. Keel, "Multilinear interval systems: the mapping theorem," in *Robust Controller, The Parametric Approach*, Prentice Hall, 1995, pp. 432 - 459.

[88] F. Yang, M. Gani, and D. Henrion, "Fixed-order robust H_∞ controller design with regional pole assignment," *IEEE Trans. Automatic Control*, vol. 52, pp. 1959-1963, Oct. 2007.

[89] Johan Löfberg (2004), "YALMIP: A free MATLAB Toolbox for rapid prototyping of optimization problems," [Online]. Available: http://users.isy.liu.se/johanl/yalmip/

[90] Y. A.-R. I. Mohamed, "Mitigation of dynamic, unbalanced and harmonic voltage disturbances using grid-connected inverters with *LCL* filter" *IEEE Trans. on Industrial Electronics*, vol. 58, no. 9, pp. 3914-3924, Sept. 2011.

[91] Y. A.-R. I. Mohamed, "Design and implementation of a robust current control scheme for a PMSM vector drive with a simple adaptive disturbance observer," *IEEE Trans. on Industrial Electronics*, vol. 54, no. 2, pp. 1981-1988, Aug. 2007.

[92] A. A. Rockhill, M. Liserre, R. Teodorescu, and P. Rodriguez, "Grid-filter design for a multimegawatt medium-voltage voltage-source inverter," *IEEE Trans. Ind. Electron.*, vol. 58, no. 4, pp. 1205–1217, Apr. 2011.

[93] H. Sira-Ramirez and S. K. Agrawal, *Differentially Flat Systems*, CRC Press, 2004.

[94] R. Ortega, A. J. van der Schaft, I. Mareels, and B. Maschke, "Putting Energy Back in Control," *IEEE Control Systems Magazine*, April 2001, pp 18-31.

[95] R. Ortega, A. van der Schaft, and B. Maschke, G. Escobar, "Interconnection and damping assignment passivity-based control of port-controlled Hamiltonian systems," *Automatica*, vol. 38, pp. 585-596, April 2002.

[96] R. Ortega and E. Garcia-Canseco, "Interconnection and Damping Assignment Passivity-Based Control: A Survey," *European Journal of Control* vol. 10, pp. 432–450, 2004.

[97] J.-Hwan Kim, S.-Ki Sul, and P. N. Enjeti, "A Carrier-Based PWM Method With Optimal Switching Sequence for a Multilevel Four-Leg Voltage-Source Inverter," *IEEE Trans. Industry Applications*, vol. 44, pp. 1239-1248, July/August 2008.

[98] B.-Kuk Lee and M. Ehsani, " A Simplified Functional Simulation Model for Three-Phase Voltage-Source Inverter Using Switching Function Concept," *IEEE Trans. Industrial electronics*, vol. 48, pp. 309-321, April 2001.

[99] H. Sira-Ramirez, "On the generalized PI sliding mode control of DC-to-DC power converters: a tutorial," International Journal of Control,vol. 76, pp. 1018–1033, 2003.

[100] H. Sira-Ramirez, "Sliding mode Δ modulators and generalized proportional integral control of linear systems," Asian J of Control, vol. 5, pp. 467-475, 2003.

[101] J. A. J u´arez-Abad, J. Linares-Flores, E. G uzman-Ram´ırez, and H. Sira-Ramirez, "Generalized Proportional Integral Tracking Controller for a Sing le Phase Multilevel Cascade Inverter: A FPGA Implementation," *IEEE Trans. Industrial Informatics*, vol. 10, pp. 256-266, February 2014.

[102] J. Linares-Flores, J. L. Barahona-Avalos, H. Sira-Ramíre z, and M. A. Contrera s-Ordaz, "Robust Passivity-Based Control of a Buck–Boost-Converter/DC-Motor System: An Active Disturbance Rejection Approach," *IEEE Trans. Industry Applications*, Vol. 48, pp. 2362-2371, Nov./Dec. 2012.

[103] M. Davari, B. Abdi, H. Nafisi, G. B. Gharehpetian, H.R. Karshenas, "State Feedback Control of B oost Converter Using S1-ΣΔ PWM Method", in *Proc. the 2nd IEEE International Conference on Power and Energy Conference* (*PECon2008*), pp. 208-212, Dec., 2008.

[104] M. Davari, I. Salabeigi, G.B. Gharehpetian, S.H. F athi, J. Milimonfared, "Multifunction Current Controller for Inverter-Based Distributed Generation using Combined P I-Sliding Mode Controller via Sigma-Delta Modulation," in *Proc. IEEE International Symposium on Industrial Electronics* (*ISIE*'09), pp. 1803-1808, July, 2009.

[105] B. Jacob and M. R. Baiju, "Vector-Quantized Space-Vector-Based Spread Spectrum Modulation Scheme for Multilevel Inverters Using the Principle of Oversampling ADC," *IEEE Trans. Industrial Electronics*, vol. 60, pp. 2969-2977, August 2013.

[106] C.-Hsi Chang, F.-Yu Wu, and Y.-Ming Chen, "Modularized Bidirectional Grid-Connected Inverter With Constant-Frequency Asynchronous Sigma–Delta Modulation," *IEEE Trans. Industrial Electronics*, vol. 59, pp. 4088-4100, Nov. 2012.

[107] Shiang-Hwua Yu and Ming-Hun g Tseng, "Use of Sliding-Mode Modulation in Switch-Mode Power Amplification," *IEEE Trans. Industrial Electronics*, vol. 55, pp. 4022-4028, Nov. 2008.

[108] H. Sira-Ramirez, C. Nunez, and N. Visai ro, "Robust sigma-delta generalized proportional integral observer based control of a 'buck' converter with uncertain loads," *International Journal of Control*, vol. 83, No. 8, pp. 1631–1640, 2010.

[109] S.-K. Chung "A phase trackin g system for three phase utilit y interface inverters", *IEEE Trans. Power Electron.*, vol. 15, no. 3, pp. 431-438, May 2000.

[110] A. Arani and Y. Mohamed "Analysis and Impacts of Implementing Droop Control in DFIG-Based Wind Turbines on Micro grid/Weak-Grid Stability," *IEEE Trans. on Power Systems*, vol.30, no.1, pp.385,396, Jan. 2015.

[111] Osman S. Senturk, Lars Helle, Stig Munk-Nielsen, Pedro Rodriguez, and Remus Teodorescu, "Converter Structure-Based Power Loss and Static Thermal Modeling of The Press-Pack IGBT Three-Level ANPC VSC Appli ed to Multi -MW Wind Turbines," *IEEE Trans. Industry Applications*, vol. 47, pp. 2376-2384, May 2012.

[112] MATLAB R2013a Documentation, Wind Turbine, SimPowerSystem Toolbox, "Implement model of v ariable pitch wind tu rbine," MathWorks. [Online]. Available: http://www.mathworks.com/help/physmod/powersys/ref/windturbine.html

[113] W. Pedrycz and F . Gomide, "Functional (Local) Fuzzy Models, Rule -Based Fuzzy Models," in *Fuzzy Systems Engineering: Toward Human-Centric Computing*, Wiley-IEEE Press, 2007, ch. 11, sec. 5, pp. 312-318.

[114] K. Tanaka and H. Wang, "Takagi-Sugeno Fuzzy Model and Parallel Distributed Compensation," in *Fuzzy Control Systems Design and Analysis*, John Wiley & Sons, 2001, ch. 2, pp. 4-48.

[115] G. Zhang, Z. Xu, and Y. Cai, "An equivalent model for simulating VSC based HVDC," i*n Proc. IEEE/Power Eng. Soc. Transm. Distrib. Conf. Expo.*, 2001, vol. 1, pp. 20–24.